

Summer 1978

Design, Calibration, and Application of a Sensor for Measuring Time Dependent Angle of Attack of Helicopter Blades

Weiyuan Henry Liu
Old Dominion University

Follow this and additional works at: https://digitalcommons.odu.edu/mae_etds



Part of the [Mechanical Engineering Commons](#)

Recommended Citation

Liu, Weiyuan H.. "Design, Calibration, and Application of a Sensor for Measuring Time Dependent Angle of Attack of Helicopter Blades" (1978). Doctor of Philosophy (PhD), Dissertation, Mechanical & Aerospace Engineering, Old Dominion University, DOI: 10.25777/zyr8-1g85
https://digitalcommons.odu.edu/mae_etds/259

This Dissertation is brought to you for free and open access by the Mechanical & Aerospace Engineering at ODU Digital Commons. It has been accepted for inclusion in Mechanical & Aerospace Engineering Theses & Dissertations by an authorized administrator of ODU Digital Commons. For more information, please contact digitalcommons@odu.edu.

DESIGN, CALIBRATION, AND APPLICATION
OF A SENSOR FOR MEASURING
TIME DEPENDENT ANGLE OF ATTACK
OF HELICOPTER BLADES

by

Weiyan Henry Liu

B.E. June 1970, Chung Yuan College of
Science and Engineering, Taiwan
M.S. June 1973, Southern Illinois University

A Dissertation Submitted to the Faculty
of Old Dominion University in Partial
Fulfillment of the Requirements for the Degree of

DOCTOR OF PHILOSOPHY
MECHANICAL ENGINEERING
Old Dominion University

August, 1978

Approved by:

John M. Kuhlman (Chairman)

U

ABSTRACT

DESIGN, CALIBRATION AND APPLICATION OF A SENSOR FOR MEASURING TIME DEPENDENT ANGLE OF ATTACK OF HELICOPTER BLADES

By

Weiyuan Henry Liu

Old Dominion University, 1978

Director: John M. Kuhlman

Various pressure probes were designed and tested which could be attached to helicopter blades when a helicopter is in flight. The pressure probes consisted of spherical heads which were held in place by cylindrical shanks. Built inside the heads were transducers to measure the pressure differential between pressure ports which were located on the front portion of the spherical head facing the airstream. Data was obtained over a range of airstream velocity of 11.6 to 88.4 m/s (38 to 290 ft/sec), corresponding to Reynolds numbers of 0.24 to 1.84×10^5 based on the sphere diameter. Both static and dynamic tests were performed. For the dynamic testing

cases, the probe oscillating frequency was varied from 1.59 to 5.20 Hz., covering the range of frequencies typical of helicopter blade motion.

Two potential flow theories were developed and correlated with the experimental data: Theory I was based on the instantaneous superposition of the airstream velocity vector with the instantaneous probe motion vector, and Theory II was based on unsteady potential flow. Two computer programs were developed, based on these two theories to obtain the numerical solution of the unsteady probe motion. Both theories were found suitable for prediction of time dependent angle of attack from pressure differential data. Experimental static test results were found in agreement with the theoretical analyses for 3 of the probes tested. The dynamic test results for one of these 3 probes were also in reasonable agreement with the prediction of both Theory I and Theory II.

The time dependent angle of attack can be calculated from the recorded pressure differential outputs in conjunction with the theories. The resulting predicted time dependent angle of attack was found to deviate no more than 2-3 degrees from the experimental data over the range mentioned frequency and velocity ranges.

ACKNOWLEDGEMENTS

The author would like to express his sincere thanks to professor P. Stephen Barna of the Old Dominion University; professor Barna served as the chairman of the Dissertation Committee for two years before he retired in May, 1977. Most of the experimental apparatus in this research were designed by professor Barna, and he also gave much valuable advice in the experimental phase of this work. The author is also appreciative of the fact that NASA Langley Research Center provided the financial support (Grant Number NSG-1143) to carry on this project.

TABLE OF CONTENTS

	Page
ABSTRACT	i
TITLE PAGE	iii
ACKNOWLEDGEMENTS	iv
TABLE OF CONTENTS	v
LIST OF TABLES	viii
LIST OF FIGURES	ix
LIST OF SYMBOLS	xiv
 I. INTRODUCTION	 1
1.1 Literature Survey	1
1.2 Justification For Present Work	6
II. THEORY	7
2.1 Theory For Steady State Flow Field	7
2.2 Superposition Of The Velocity Vectors	9
2.3 Unsteady Flow Equations	13
2.4 Application Of Theory I To Probe ODU2 Under Oscillating Test Motion	 25
2.5 Application Of Theory II To Probe ODU2 Under Oscillating Test Motion	 25
2.6 R-Equation Model	30
III. INSTRUMENTATION AND TEST APPARATUS	35
3.1 Pressure Probes	35

	Page
3.2 Transducer Description And Calibration .	43
3.3 Wind Tunnel Employed In Measurements . .	47
3.3.1 The Free Air Intake Induction Tunnel	47
3.3.2 The Open End Wind Tunnel	55
3.4 Drive Mechanism	60
3.4.1 Conventional Mechanism	60
3.4.2 Scotch Yoke	63
IV. TEST PROCEDURES AND RESULTS	69
4.1 Static Test On Sphere	69
4.2 Static Test	71
4.3 Oscillating Probe Test Procedures	82
4.4 Oscillating Probe Test Results	84
4.5 Time Lag Phenomenon	84
V. TEST RESULTS ANALYSIS AND DISCUSSION	97
5.1 Static Test	97
5.1.1 Determination Of Probe Coefficient From Steady Flow Results	98
5.1.2 Direct Comparison Between Theory And Static Test Results For Deter- mination Of Static Angle Of Attack	107
5.2 Oscillating Probe Test	110
5.2.1 Oscillating Probe Data Analysis .	110
5.2.2 Comparison Between Experiments And Theories	119

	Page
5.3 Theoretical Prediction Of Time Dependent Angle Of Attack	131
VI. CONCLUSIONS	137
APPENDIXES	
A. TEST ON HEMISPHERICAL YAWMETERS	141
B. COMPUTER PROGRAM FOR THEORY I	151
C. POTENTIAL FLOW SOLUTION PAST A TRANSLATING SPHERE	157
D. COMPUTER PROGRAM FOR THEORY II	162
E. ANALYTIC CALCULATION OF THE OSCILLATING PROBE MOTION	167
F. EFFECTS OF A CYLINDER BEHIND A SPHERE	172
G. OSCILLATING PROBE TEST RESULTS	179
REFERENCES	186

LIST OF TABLES

Table		Page
3.1	Transducer Characteristics	51
G.1	Oscillating Probe Test Results	180

LIST OF FIGURES

Figure	Page
2.1 Definition sketch for flow past a sphere . . .	8
2.2 Schematic diagram of superposition of the velocity vectors	11
2.3 Definition sketch for a sphere under trans- lating motion in X-direction	17
2.4 Typical plot of equation (2.3-23), $f=5.0$ Hz, $a=0.0016$ m, $U=100$ m/s, and $u_1/U=\sin(2\pi ft)$. .	21
2.5 Definition sketch for a sphere under trans- lating motion in Y-direction	22
2.6 Definition sketch for a sphere under rota- tional motion	23
2.7 Variation of non-dimensional pressure quantity with oscillating angle under constant airspeed but different frequencies, Theory II	28
2.8 Variation of non-dimensional pressure quantity with probe position angle under constant oscillating frequency but various airspeeds, Theory II	31
3.1 Schematic showings of pressure probes, dimen- sions in meter	36
3.2 Existing pressure probes	39
3.3 Sectional view of Patterson gage	44

Figure		Page
3.4	Steady state transducer calibration set-up .	46
3.5	Calibration chart for gage T1	48
3.6	Calibration chart for gage T2	49
3.7	Test procedure for transducer calibration . .	50
3.8	Determination of transducer's settling time .	52
3.9	Velocity distribution profiles, induction wind tunnel	54
3.10a	General features of the induction wind tunnel	56
3.10b	Schematic diagram of the test section, induction wind tunnel	57
3.11a	General features of the open end tunnel . . .	58
3.11b	Photograph of the open end wind tunnel test section	59
3.12a	Schematic diagram of mechanism producing oscillating motion	61
3.12b	Test set-up for parallel flow of air, oscil- lating probe	62
3.13a	Schematic diagram of Scotch Yoke	64
3.13b	Photograph of Scotch Yoke mechanism	65
3.13c	Comparison of oscillating motion for Scotch Yoke with and without spring	66
3.14	Comparison of probe oscillating motion curve with sine curve	67
4.1	Pressure distribution around a sphere	70
4.2	Pressure distribution around a sphere with and without cylinder tailfitted	72

Figure		Page
4.3	Schematic sketch of static test set-up . . .	73
4.4	Static test procedures	74
4.5	Variation of non-dimensional pressure differential with angle quantity	75
4.6	Variation of pressure differential ratio with probe angle	79
4.7	Experimental procedures for dynamic test . .	83
4.8	Data reduction procedures	85
4.9	Stripchart outputs for probe ODU2	86
4.10	Variation of non-dimensional pressure differential with probe position angle	88
4.11	Variation of pressure differential ratio with probe angle	92
4.12	Variation of time lag with oscillating frequency (probe ODU2 and $U=30.5$ m/s)	94
4.13	Illustration of time lag phenomenon	95
5.1	Comparison of static test results with static potential flow theory	99
5.2	Non-dimensional comparison of the probe coefficient	104
5.3	Variation of probe coefficients with Reynolds number, Tunnel 1 - Induction wind tunnel, Tunnel 2 - Open end wind tunnel	108
5.4	Variation of pressure differential ratio with airstream angle	111

Figure		Page
5.5	Variation of output angle with input angle, probe NASA60	114
5.6	Variation of non-dimensional pressure differ- ential, $\Delta P_{23}/q$, with probe position angle θ under different frequencies, probe ODU2 . . .	116
5.7	Experimental data on $\Delta P/q$ variation, probe ODU2	117
5.8	Comparison of experiment and theories, $\Delta P_{12}/q$ versus θ	120
5.9	Comparison of experiment and theories, $\Delta P_{23}/q$ versus θ	122
5.10	Comparison of experiment and theories, R versus θ	128
5.11	Theoretical prediction of R value as a func- tion of θ , $R_e=0.635 \times 10^5$, $b_{12}=2.03$, and $b_{23}=1.79$	133
5.12	Theoretical prediction of angle of attack, α_a , $R_e=0.635 \times 10^5$, $b_{12}=2.03$, and $b_{23}=1.79$. .	134
5.13	Theoretical prediction of angle of attack, α_a , $R_e=0.635 \times 10^5$, $f=1.84$ Hz, $b_{12}=2.03$, and $b_{23}=1.79$	136
A.1	Definition sketch of a 5-porthole hemispher- ical yawmeter	144
A.2	Variation of pressure differential with yaw angle for hemispherical yawmeter	145

Figure		Page
A.3	Variation of pressure differential with pitch angle θ for hemispherical yawmeter . .	148
E.1	Comparison of probe motion curves with the true sine curve	171
F.1	Definition sketches of a 0.0635 m sphere with support and with cylinder tailfitted	175
F.2	Pressure distribution around a sphere with and without cylinder tailfitted	176
F.3	Static pressure distribution of porthole number 2, Reynolds number $R_e = 1.4 \times 10^5$	177
F.4	Static pressure distribution of porthole number 3, Reynolds number $R_e = 1.4 \times 10^5$	178
G.1	Experimental data on $\Delta P/q$ variation, probe ODU2	181

LIST OF SYMBOLS

a	radius of spherical probe head
b	probe coefficient for a real fluid flow
b_o	probe coefficient for ideal flow, $b_o=9/4$
b_{ij}	probe coefficient based on portholes i and j
b_{12} , b_{23} , b_{13}	probe coefficients based on portholes 1 and 2, 2 and 3, and 1 and 3 respectively
b_r	the ratio of b_{23} and b_{12} , $b_r=b_{23}/b_{12}$
C_{pi}	pressure coefficient at point i on the surface of a sphere
D	sphere diameter
e_{12} , e_{23}	functions that represent the dynamic effect for ΔP_{12} and ΔP_{23}
f	frequency, Hz
g	gravitational acceleration, 9.81 m/s^2
G	function of U , f , and θ
h	dimension measured vertically upward
H	function of time, $H(t)$
k	reduced frequency, $k=2\pi f D/U$
L_p	distance between the probe head front end to the center of oscillation
M	Mach number
P_1 , P_2 , P_3	static pressures at portholes 1, 2, and 3 respectively
P_i	static pressure at point i on a sphere

P_j	static pressure at point j on a sphere
P_t	total pressure
P_∞	free stream static pressure
ΔP	pressure difference
ΔP_{ij}	pressure differential between two points i and j
$\Delta P_{12}, \Delta P_{23}, \Delta P_{13}$	pressure differentials between portholes 1 and 2, 2 and 3, and 1 and 3 respectively
q	dynamic pressure head, $q = (1/2) \rho U^2$
q_r	relative q
q_r^*	new quantity of q_r , used in equation (2.3-31)
r	radial direction in the spherical coordinates
R	ratio of ΔP_{23} to ΔP_{12} , $R = \Delta P_{23} / \Delta P_{12}$
R_e	Reynolds number
R_o	radius of circular arc, used in Appendix E
S	stagnation point
t	time, second
t_1	reference time
t^*	time at a specific instant
Δt_s	transducer's response time
U	airstream velocity, m/s
U_∞	free stream velocity, m/s
u_1	horizontal component of the instantaneous probe velocity
u, v, w	velocity components in X, Y, and Z directions respectively

\vec{V}	velocity in vector form
$ \vec{V} $	absolute value of \vec{V}
v	vertical component of the instantaneous probe velocity
V_p	probe velocity under oscillating motion, m/s
W	combined weight of the steel plate and parallel steel rods in Scotch Yoke mechanism
X, Y, Z	cartesian coordinates
α	half of the amplitude angle, degrees
α_a	angle of attack, degrees
β	yaw angle, degrees
γ	angle between side port and center port
η	instantaneous change of angle due to the probe oscillating motion
η_r	relative η
η_r^*	new quantity of η_r , used in equation (2.3-30)
θ	probe position angle, degrees
θ_D	displacement angle, degrees
θ_{in}	input angle, degrees
θ_L	lowermost probe position angle, degrees
θ_{out}	output angle, degrees
θ_U	uppermost probe position angle, degrees
θ_2	angle between undisturbed free stream velocity and porthole number 2 on the spherical head
θ_3	angle between undisturbed free stream velocity and porthole number 3 on the spherical head

$\theta', \theta'_i, \theta'_j$	angle quantities used in article 2.3
μ	dynamic viscosity
ρ	density
ϕ	velocity potential
ψ	stream function
ω	angular velocity

DESIGN, CALIBRATION AND APPLICATION OF A SENSOR
FOR MEASURING TIME DEPENDENT ANGLE OF
ATTACK OF HELICOPTER BLADES

I. INTRODUCTION

Pressure-sensing devices commonly used in aeronautical and turbomachinery research for measuring flow direction, velocity and static pressure in three-dimensional flows consist of various combinations of tube, conical and spherical type probes. Unfortunately, most existing probes are suitable only for static determination of flow velocity direction and magnitude. Development of a rigid probe able to determine the time dependent flow properties and characteristics in a field test is of great interest to turbomachinery and helicopter researchers since hot-wire probe systems would be too fragile for use on helicopter blades or turbine blades.

1.1 Literature Survey

Lavender (Ref. 1) found that the mean wind direction could be determined by means of a pressure direction-meter. This device made use of the experimental fact that the pressure

given by a total-head tube falls off as the axis of the head of the tube is inclined to the wind (Ref. 2). The direction and velocity meter had two pairs of fine total-head tubes, one pair in a horizontal plane and the other pair in the vertical plane. The axes of the two holes of each tube were nearly at the angle of maximum sensitivity to the axis of the instrument. The fifth tube was a central tube with its opening sheltered by the apex of the cone. The accuracy of such a pressure direction-meter was about $1/10$ degree in angle and $1/2$ percent in velocity.

Bryer, Walshe and Garner (Ref. 3) indicated that the 5-tube Conrad probe, which embodied a central tube to which side tubes were attached and their forward ends chamfered to form a point, could be used to determine the flow direction and magnitude. For probe operating angles of up to 20 degrees, the accuracy was found to be within 4 percent.

Martinot-Lagarde, Fauquet and Frenkiel (Ref. 4) developed the IMFL anemoclinometer, an instrument for the investigation of a fluctuating velocity vector. The principle part of an IMFL anemoclinometer was a spherical head fixed on a tubular socket. The probe was held rigidly in the wind during the recording of data. Three pressure differences were obtained, from which the velocity vector could be found. IMFL anemoclinometers have been applied to measurements in wind-tunnels, jets, and on airplanes.

Reichle (Ref. 5) found that the pressure distribution on the hemisphere-cylinder varies as a strong function of Mach

Number. For low Mach Number ($M=0.4$), the pressure distribution was found to be close to the inviscid, incompressible theory for the front portion of the sphere. As M increased, the pressure distribution became more like a cosine squared function.

A "six-channel" three-dimensional yawmeter has been used at the Central Aero and Hydrodynamics Institute, USSR (Ref. 6). This instrument is called the "six-channel" because it incorporates six pressure channels. The head is hemispherical with five orifices. The central orifice measured total head, while the other four holes were symmetrically spaced around it to measure air stream direction in two mutually perpendicular planes.

A spherical type flow-direction probe was used for measuring yaw in both vertical and horizontal planes in Ref. 7. Theoretical and actual values of $\Delta P/q$ for a spherical yawhead were compared and the calibrations were found independent of Reynolds Number from speed of 17.9 to 53.6 m/s (58.7 to 176 ft/sec) under standard air test conditions.

Nowack (Ref. 8) made a detailed experimental study of a five-hole spherical pitot tube. A calibration method was described for this probe by which the direction of a velocity vector was fixed by two cartesian angles, one lying in the horizontal equatorial plane and the other in a vertical meridian plane containing the velocity vector. The spherical head was of 0.0147 m (0.0484 ft) diameter and contained five radially drilled holes of 0.001 m (0.0033 ft) diameter. Mea-

surements were possible within the range of 65 degrees half cone angle from the probe axis. It was found that the error in velocities over the whole velocity and angle range was approximately 4 percent, while for the static pressure the error was approximately 5 percent.

Thurtell, Tanner and Wesely (Ref. 9), following the idea of the anemoclinometer described by Martinot-Lagarde et al., made their own three-dimensional pressure-sphere anemometer (PSA) system. The anemometer system consisted of a spherical probe head with pressure ports drilled into its surface. The pressures developed at these ports were transmitted through small tubes and measured by pressure transducers. The response of the transducer was limited by the size and length of tubing and the effective internal volume of the transducers. Later Wesely, Tanner and Thurtell (Ref. 10) improved their PSA system with one center port and four side ports, each 22.5 degrees from the center port rather than 45 degrees, and thus having larger angular acceptance than the earlier model. Thurtell et al. found this new pressure sphere anemoclinometer with a probe coefficient, b , defined as the slope of non-dimensional pressure differential quantity against non-dimensional angle quantity within the linear range, of 1.79 had a wider acceptance angle than the IMFL anemoclinometer. Also it was more easily constructed. It was stated that the total wind vector magnitude estimated was accurate within 2 percent for angles less than 25 degrees.

Montoya (Ref. 11) developed a hemispherical head angle-of-attack-angle-of-sideslip sensor. The sensors were strut-mounted on a nose boom with pitot head. Three sensor configurations mounted off the nose boom were tested in wind tunnels over a Mach number range of 0.2 to 3.6. The hemispherical head had four portholes. It was found that:

1) Angular measurements accurate to 0.25 deg. were possible for angles up to 8 degrees at high supersonic speeds; 2) A single calibration curve for determining both angle of attack and angle of sideslip could have been used in conjunction with appropriate bias error corrections; 3) Reynolds number effects were found negligible for the range of values tested (3.28 to 65.6×10^6 per meter of wind tunnel dimension).

Yap, Black and Oke (Ref. 12) constructed a yaw sphere thermometer (YST) system following the design of Tanner and Thurtell. The yaw sphere had a diameter of 0.05 m (0.164 ft) and five ports arranged identical to the probe developed by Thurtell et al. (Ref. 10). A new probe coefficient, $b=1.57$, was obtained based on a series of measurements with Reynolds number which ranged from 6,000 to 20,000 based on the sphere diameter.

Barna and Liu (Ref. 13) made a preliminary investigation on three hemispherical yawmeters which were similar to the three-dimensional yawmeter in Ref. 5 but without the static holes. Static results for these three hemispherical yawmeters are detailed in Appendix A.

Bennett (Ref. 14) investigated the effects of velocity fluctuation on yawmeter measurements.

tuations on data for a five-hole hemispherical probe. He found the fluctuations contributed to the mean pressures at the probe itself because of the nonlinear character of the probe response; hence, the fluctuations affected both response of the probe and the subsequent interpretation of the results.

1.2 Justification for Present Work

None of the previous investigators have considered constructing a pressure probe with built-in pressure transducers. Further, no direct measurements of pressure differentials have been made under oscillating probe conditions. The present investigation was therefore undertaken with the primary objectives being to investigate the unsteady state characteristics of a three-hole spherical velocity vector sensor and to develop an instrument to predict the time dependent angle of attack when a flying body is under periodic oscillatory motion. One possible application of such a device is measurement of the time dependent flow properties in a rotating helicopter rotor blade system.

Chapter II of this work considers the basic theories for both steady and unsteady state potential flow developed in the present work. Chapter III describes the instrumentation and test apparatus. Chapter IV presents the test results. Chapter V and VI are devoted to test result analysis, comparison of theory and experiment, discussion of results and conclusions.

II. THEORY

2.1 Theory for Steady State Flow Field

The static theory of the spherical head pressure probe is based on the mechanical energy equation between a point in the free stream and a point on the surface of a sphere. According to the Bernoulli equation, which applies for an ideal fluid, or a potential flow, the pressure on the sphere surface at any point i (see figure (2.1)) is, neglecting any potential energy changes,

$$P_i + (1/2) \rho |\vec{V}|^2 = P_\infty + (1/2) \rho U_\infty^2 \quad (2.1-1)$$

From the potential flow theory (Ref. 15) for flow past a sphere, it is known that

$$P_i = P_\infty + (1/2) \rho U_\infty^2 \left(1 - \frac{9}{4} \sin^2 \beta_i \right) \quad (2.1-2)$$

or

$$P_i = P_t - b_o q \sin^2 \beta_i \quad (2.1-3)$$

where

$P_t = P_\infty + (1/2) \rho U_\infty^2$, is the total pressure,

$q = (1/2) \rho U_\infty^2$, is the free stream dynamic pressure,

$b_o = 9/4$,

and β_i is the central angle between point i and the stagnation point S . Consider a sphere in a steady, uniform flow field. If i, j are two points on the sphere surface, from

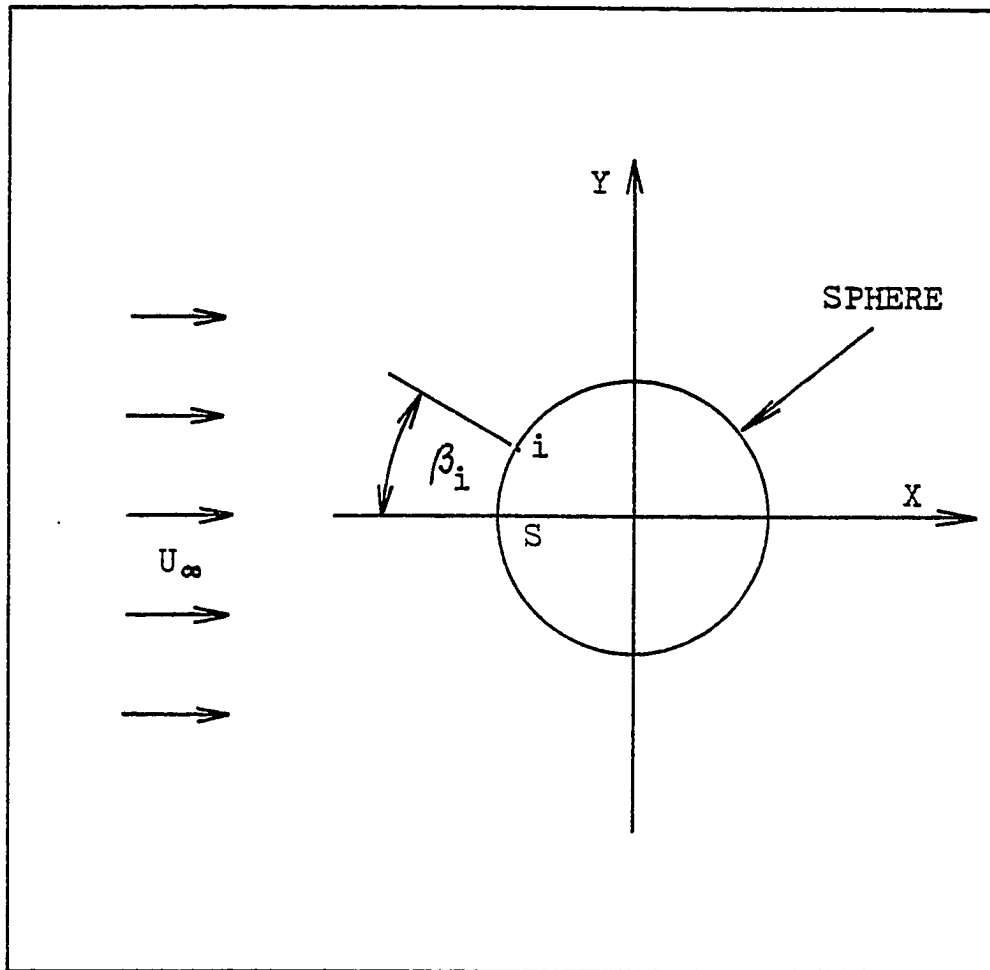


Figure 2.1 Definition sketch for flow past a sphere

equation (2.1-3) one obtains

$$P_t = P_i + b_o q \sin^2 \beta_i$$

and

$$P_t = P_j + b_o q \sin^2 \beta_j$$

After subtraction

$$\begin{aligned} P_i - P_j &= b_o q (\sin^2 \beta_j - \sin^2 \beta_i) \\ &= b_o q (\sin \beta_j + \sin \beta_i) (\sin \beta_j - \sin \beta_i) \end{aligned}$$

By using the trigonometric identities

$$\sin \beta_j + \sin \beta_i = 2 \sin \left(\frac{\beta_j + \beta_i}{2} \right) \cos \left(\frac{\beta_j - \beta_i}{2} \right)$$

and

$$\sin \beta_j - \sin \beta_i = 2 \sin \left(\frac{\beta_j - \beta_i}{2} \right) \cos \left(\frac{\beta_j + \beta_i}{2} \right)$$

one obtains the pressure difference between points i and j as

$$P_i - P_j = b_o q \sin (\beta_j + \beta_i) \sin (\beta_j - \beta_i) \quad (2.1-4)$$

Hence, once the central angles β_i and β_j are known, the pressure differential may be obtained from equation (2.1-4).

2.2 Superposition of the Velocity Vectors

Instantaneous superposition of the free stream velocity vector and the probe head motion vector is now considered. Assume the spherical probe head is a point and the probe is under a periodic, oscillating motion with a frequency f .

Let the initial probe position angle with respect to the horizontal axis be θ_D , and the oscillating half amplitude angle be α , so that the oscillating instantaneous position angle θ in a sinusoidal motion is

$$\theta(t) = \theta_D - \alpha \sin(2\pi f t) \quad (2.2-1)$$

Consider that the probe head velocity vector V_p be instantaneously added to the free stream velocity vector \vec{U}_∞ (see figure (2.2)), and assume that the resultant vector produces the pressure differences $\Delta P_{ij} = P_i - P_j$. If the probe head oscillates with respect to a center of rotation with a radius L_p , then the instantaneous probe head surface velocity at point i is

$$V_p = L_p \frac{d\theta}{dt} \quad (2.2-2)$$

From equation (2.2-1), differentiating with respect to time t , one obtains

$$V_p = -L_p 2\pi f \alpha \cos(2\pi f t) \quad (2.2-3)$$

This instantaneous tangential velocity may be resolved into two components: the horizontal component $V_p \cos \theta$ may be added to the horizontal free stream velocity U_∞ , while the transverse component $V_p \sin \theta$ becomes the vertical component. Hence the resultant velocity magnitude is

$$|\vec{V}| = \left[(U_\infty + V_p \cos \theta)^2 + (V_p \sin \theta)^2 \right]^{\frac{1}{2}} \quad (2.2-4)$$

The relative angle of \vec{V} with respect to the horizontal reference axis is

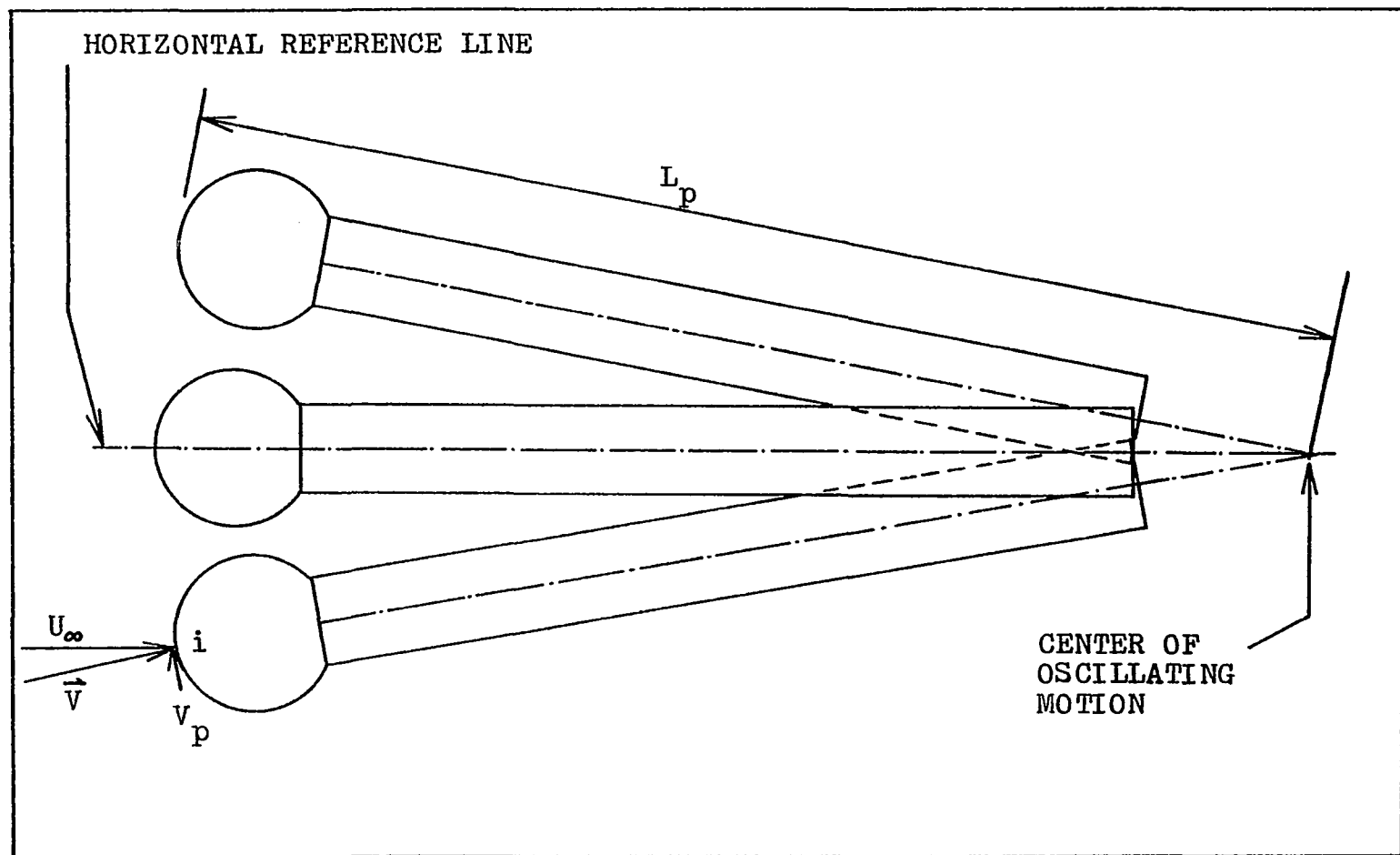


Figure 2.2 Schematic diagram of superposition of the velocity vectors

$$\eta = \tan^{-1} \left[V_p \sin \theta / (U_\infty + V_p \cos \theta) \right] \quad (2.2-5)$$

The instantaneous angle of attack, the angle between the probe longitudinal axis and the resultant velocity, is

$$\alpha_a = \theta + \eta \quad (2.2-6)$$

We now assume that the pressure distribution on the sphere adjusts instantaneously to the velocity changes due to probe oscillating motion. This approximation would be most accurate at low oscillating frequencies. That is, denoting P_i as the instantaneous pressure at a point i on the probe head front surface with an instantaneous angle of attack α_a ,

$$P_i = P_t - b_o q(t) \sin^2(\alpha_a)_i$$

Here P_t is the total pressure, b_o is the theoretical probe coefficient and $q(t)$ is the local dynamic pressure term $(1/2) \rho V_i^2$ where

$$V_i^2 = (U_\infty + V_p \cos \theta)^2 + (V_p \sin \theta)^2$$

Hence, the pressure differential between two points i and j on the probe head surface is

$$P_i - P_j = b_o q(t) (\sin^2(\alpha_a)_j - \sin^2(\alpha_a)_i) \quad (2.2-7)$$

where $q(t)$, $(\alpha_a)_i$ and $(\alpha_a)_j$ are all functions of time t . Hence the pressure differential $P_i - P_j$ varies with time as the probe oscillates. A computer program has been written to calculate and plot the pressure difference from this

equation, which is described in Appendix B.

2.3 Unsteady Flow Equations

Consider the X component of the Navier-Stokes equation,

$$\frac{\partial u}{\partial t} + u \frac{\partial u}{\partial x} + v \frac{\partial u}{\partial y} + w \frac{\partial u}{\partial z} = -g \frac{\partial h}{\partial x} - \frac{1}{\rho} \frac{\partial P}{\partial x} + \frac{\mu}{\rho} \left(\frac{\partial^2 u}{\partial x^2} + \frac{\partial^2 u}{\partial y^2} + \frac{\partial^2 u}{\partial z^2} \right), \quad (2.3-1)$$

where h is measured vertically upward.

For irrotational flow

$$\frac{\partial w}{\partial y} = \frac{\partial v}{\partial z}, \quad \frac{\partial u}{\partial z} = \frac{\partial w}{\partial x}, \quad \frac{\partial v}{\partial x} = \frac{\partial u}{\partial y}.$$

Hence, equation (2.3-1) can be written as

$$\frac{\partial u}{\partial t} + \frac{\partial}{\partial x} \left(\frac{u^2 + v^2 + w^2}{2} \right) = -g \frac{\partial h}{\partial x} - \frac{1}{\rho} \frac{\partial P}{\partial x} + \frac{\mu}{\rho} \frac{\partial}{\partial x} \left(\frac{\partial u}{\partial x} + \frac{\partial v}{\partial y} + \frac{\partial w}{\partial z} \right)$$

Since for incompressible flow

$$\frac{\partial u}{\partial x} + \frac{\partial v}{\partial y} + \frac{\partial w}{\partial z} = 0$$

one obtains

$$\frac{\partial u}{\partial t} + \frac{\partial}{\partial x} \left(\frac{v^2}{2} \right) + g \frac{\partial h}{\partial x} + \frac{1}{\rho} \frac{\partial P}{\partial x} = 0 \quad (2.3-2a)$$

where

$$v^2 = u^2 + v^2 + w^2$$

Similarly, for the Y and Z components of the Navier-Stokes

equation, one obtains for irrotational incompressible flow

$$\frac{\partial v}{\partial t} + \frac{\partial}{\partial y} \left(\frac{v^2}{2} \right) + g \frac{\partial h}{\partial y} + \frac{1}{\rho} \frac{\partial P}{\partial y} = 0 \quad (2.3-2b)$$

$$\frac{\partial w}{\partial t} + \frac{\partial}{\partial z} \left(\frac{v^2}{2} \right) + g \frac{\partial h}{\partial z} + \frac{1}{\rho} \frac{\partial P}{\partial z} = 0 \quad (2.3-2c)$$

For three dimensional, irrotational flow one may define the velocity potential, ϕ , by

$$u = \frac{\partial \phi}{\partial x}, \quad v = \frac{\partial \phi}{\partial y}, \quad w = \frac{\partial \phi}{\partial z}.$$

The time derivatives of the velocity components become

$$\frac{\partial u}{\partial t} = \frac{\partial^2 \phi}{\partial t \partial x}, \quad \frac{\partial v}{\partial t} = \frac{\partial^2 \phi}{\partial t \partial y}, \quad \frac{\partial w}{\partial t} = \frac{\partial^2 \phi}{\partial t \partial z}$$

Therefore, equation (2.3-2) may be written

$$\frac{\partial}{\partial x} \left(\frac{\partial \phi}{\partial t} \right) + \frac{\partial}{\partial x} \left(-\frac{v^2}{2} + g h + \frac{P}{\rho} \right) = 0 \quad (2.3 -3a)$$

$$\frac{\partial}{\partial y} \left(\frac{\partial \phi}{\partial t} \right) + \frac{\partial}{\partial y} \left(-\frac{v^2}{2} + g h + \frac{P}{\rho} \right) = 0 \quad (2.3 -3b)$$

$$\frac{\partial}{\partial z} \left(\frac{\partial \phi}{\partial t} \right) + \frac{\partial}{\partial z} \left(-\frac{v^2}{2} + g h + \frac{P}{\rho} \right) = 0 \quad (2.3 -3c)$$

Ignoring gravitational effects, one obtains upon integration

$$\frac{\partial \phi}{\partial t} + \frac{v^2}{2} + \frac{P}{\rho} = H(t). \quad (2.3-4)$$

This equation is known as the unsteady Bernoulli equation.

In general, an object moving through a fluid may be translating, rotating and deforming. Hence the velocity of a fluid element on the surface of the object, may in general be a function of position on the surface of the body and

time. The theory of an object moving through an ideal fluid can be found in Refs. 16, 17, 18. The aim here is to determine the velocity potential of a fluid motion resulting from the motion of a solid body that was initially in a state of rest.

Consider a reference coordinate system and describe the surface of the body as

$$F(\vec{X}, t) = 0 \quad (2.3-5)$$

where \vec{X} is the position vector and t is time. Let ϕ be the velocity potential and determine ϕ as the solution of the Laplace equation

$$\nabla^2 \phi = 0 \quad (2.3-6)$$

The boundary condition is

$$\frac{\partial F}{\partial t} + \nabla \phi \cdot \nabla F = 0 \text{ on } F(\vec{X}, t) = 0 \quad (2.3-7)$$

Furthermore, the components of the velocity $\vec{u} = \nabla \phi$ should vanish as the distance from the body tends to infinity. The boundary condition can be expressed in the form

$$\frac{\partial \phi}{\partial n} = \nabla \phi \cdot \vec{n} = \vec{u}(\vec{X}, t) \cdot \vec{n} \text{ on } F(\vec{X}, t) = 0 \quad (2.3-8)$$

or

$$\nabla \phi \cdot \nabla F = \vec{u}(\vec{X}, t) \cdot \nabla F \text{ on } F(\vec{X}, t) = 0 \quad (2.3-9)$$

where \vec{n} is the unit vector pointing outward normal to the body surface. This states that at every point on the surface of the body the component of the fluid velocity normal to the body is equal to the normal component of the body

velocity. In other words, there may be no flow through or separation from the surface of the body. Once the velocity potential is determined, the pressure at any point is given by equation (2.3-4) as

$$P(\vec{X}, t) = -\rho \left[\frac{\partial \phi}{\partial t} + (1/2) (\nabla \phi)^2 \right] + H(t) \quad (2.3-10)$$

where $H(t)$ is a function of time only. Denoting the pressure at infinity as P_∞ and using the boundary condition at infinity, the relation for the pressure may be written as

$$P(\vec{X}, t) = P_\infty - \rho \left[\frac{\partial \phi}{\partial t} + (1/2) (\nabla \phi)^2 \right] \quad (2.3-11)$$

For a general problem, the motion of a rigid body can be resolved into translation and rotation. First, consider the translating rigid sphere problem. This problem was solved first by Lamb (Ref. 16) considering a sphere under an uni-directional translating motion. As the sphere translates through the fluid, the velocity of the sphere is time dependent; that is, the sphere is in accelerating motion. In a spherical coordinate system (r, θ, φ) , let the center of the sphere be the origin of the coordinate system and the axis from which θ is measured is chosen opposite to the sphere velocity \vec{u}_1 , as shown in figure (2.3) where a is the radius of the sphere.

Because of this uni-directional motion, one expects the velocity potential ϕ to be independent of the coordinate φ , or the motion to be axisymmetric. Hence we have for a time dependent system

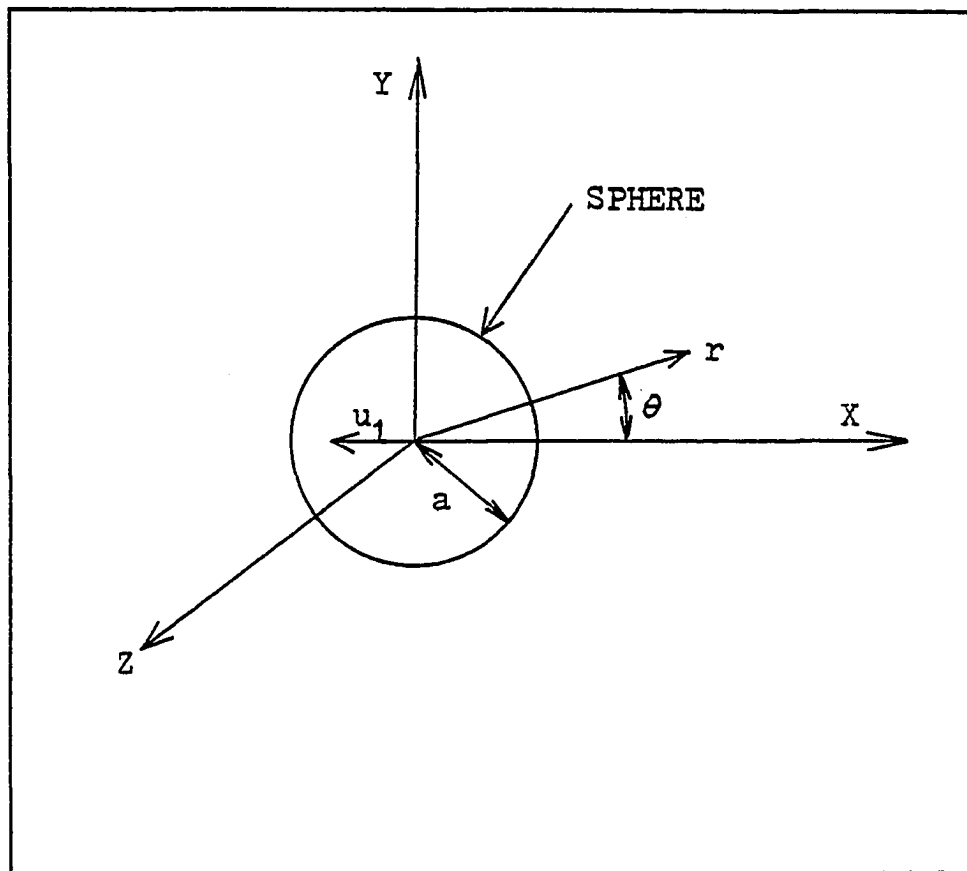


Figure 2.3 Definition sketch for a sphere under translating motion in X-direction

$$\phi = \phi(r, \theta, t)$$

The equation for the potential (2.3-6) becomes

$$\frac{\partial}{\partial r} \left(r^2 \sin \theta \frac{\partial \phi}{\partial r} \right) + \frac{\partial}{\partial \theta} \left(\sin \theta \frac{\partial \phi}{\partial \theta} \right) = 0 \quad (2.3-12)$$

The boundary condition on $r=a$ is

$$\text{grad } \phi \cdot \vec{e}_r = \vec{u}_1 \cdot \vec{e}_r \quad (2.3-13)$$

where \vec{u}_1 is the instantaneous horizontal speed and \vec{e}_r is the unit vector in the r -direction. Equation (2.3-13) can be simplified to

$$\frac{\partial \phi}{\partial r} = - \vec{u}_1 \cos \theta \quad (2.3-14)$$

The solution for ϕ is known to be (see Appendix C)

$$\phi(r, \theta, t) = u_1(t) a^3 \cos \theta / (2 r^3) \quad (2.3-15)$$

since the motion is axisymmetric, and the equation for a streamline in any axial plane is

$$\psi(r, \theta, t) = \text{constant}$$

Along a streamline $\psi = \text{constant}$, so one has the relation

$$d\psi = - r \sin \theta u_\theta dr + r^2 \sin \theta u_r d\theta = 0 \quad (2.3-16)$$

with

$$u_\theta = \frac{1}{r} \frac{\partial \phi}{\partial \theta} = \frac{u_1 a^3 \sin \theta}{2 r^3} \quad (2.3-17a)$$

and

$$u_r = \frac{\partial \phi}{\partial r} = - \frac{u_1 a^3 \cos \theta}{r^3} \quad (2.3-17b)$$

After integration of (2.3-16) with substitution of (2.3-17a, 17b), the stream function is given by

$$\psi(r, \theta, t) = -\frac{u_1 a^3 \sin^2 \theta}{2r} + \text{constant} \quad (2.3-18)$$

The pressure on the surface of the sphere can be obtained from equation (2.3-11) as

$$\begin{aligned} P(a, \theta, t) &= P_\infty - \rho \left[\frac{\partial \phi}{\partial t} - \vec{u}_1(t) \cdot \nabla \phi + \frac{1}{2} (\nabla \phi)^2 \right]_{\text{at } r=a} \\ &= P_\infty + \frac{\rho}{2} \left[\frac{u_1^2(t)}{4} (9 \cos^2 \theta - 5) \right. \\ &\quad \left. - a \frac{d u_1(t)}{dt} \cos \theta \right] \end{aligned} \quad (2.3-19)$$

If the sphere is moving with a constant velocity, i.e., $u_1 = \text{constant}$, the pressure distribution on the sphere becomes

$$P(a, \theta) = P_\infty + \frac{\rho u_1^2}{8} (9 \cos^2 \theta - 5) \quad (2.3-20)$$

Now, consider the sphere under a one dimensional sinusoidal motion in the X-direction; i.e.,

$$u_1(t) = V_p(t) \sin \beta(t) \quad (2.3-21)$$

The pressure at any point i on the sphere can be expressed as

$$\begin{aligned} P(a, \theta_i, t) &= P_\infty + \frac{\rho}{2} \left[\frac{u_1^2(t)}{4} (9 \cos^2 \theta_i - 5) \right. \\ &\quad \left. - a \frac{d u_1(t)}{dt} \cos \theta_i \right] \end{aligned} \quad (2.3-22)$$

where θ_i is the angle between the $u_1(t)$ direction and a radius through point i. The pressure differential between two points i and j on the sphere surface under one dimensional motion is

$$\begin{aligned}
P(a, \theta_i, t) - P(a, \theta_j, t) = & (9/8) \rho u_1^2(t) (\cos^2 \theta_i - \\
& \cos^2 \theta_j) - \frac{\rho a}{2} \frac{d u_1(t)}{dt} \\
& (\cos \theta_i - \cos \theta_j) \quad (2.3-23)
\end{aligned}$$

A typical example to illustrate equation (2.3-23) is shown in figure (2.4).

Next, consider a sphere of radius a under a one-dimensional, sinusoidal motion in the Y -direction only. With

$$V(t) = V_p(t) \cos \beta(t) \quad (2.3-24)$$

and let θ' denote the new angular quantity as shown in figure (2.5). The pressure at any point on the surface can be expressed as

$$\begin{aligned}
P(a, \theta', t) = P_\infty + \frac{\rho}{2} \left[\frac{v^2(t)}{4} (9 \cos^2 \theta' - 5) - a \frac{dv(t)}{dt} \cos \theta'(t) \right] \\
(2.3-25)
\end{aligned}$$

The pressure differential between two points i and j on the sphere surface under this sphere motion is

$$\begin{aligned}
P(a, \theta'_i, t) - P(a, \theta'_j, t) = & \frac{9}{8} \rho v^2(t) (\cos^2 \theta'_i - \cos^2 \theta'_j) \\
& - \frac{\rho a}{2} \frac{dv(t)}{dt} (\cos \theta'_i - \cos \theta'_j) \\
(2.3-26)
\end{aligned}$$

Finally, consider the effect due to the free stream velocity and the rotational motion as shown in figure (2.6). The sphere surface velocity at point i is $a \cdot (d\beta/dt)$ and the relative angle with respect to the free stream velocity U_∞ direction is

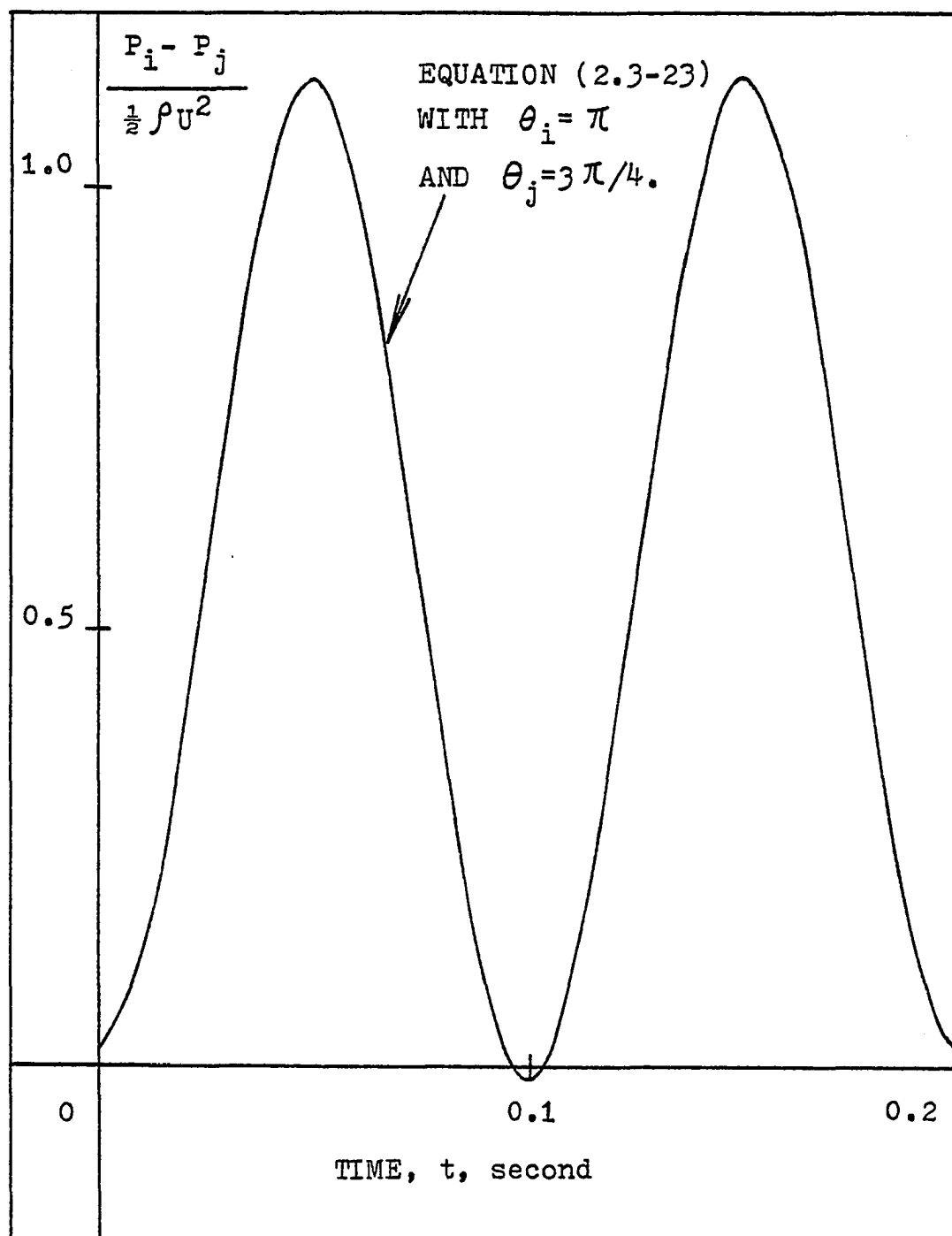


Figure 2.4 Typical plot of equation (2.3-23),
 $f = 5.0$ Hz, $a = 0.0016$ m, $U = 100$ m/s,
 and $u_1/U = \sin(2\pi ft)$.

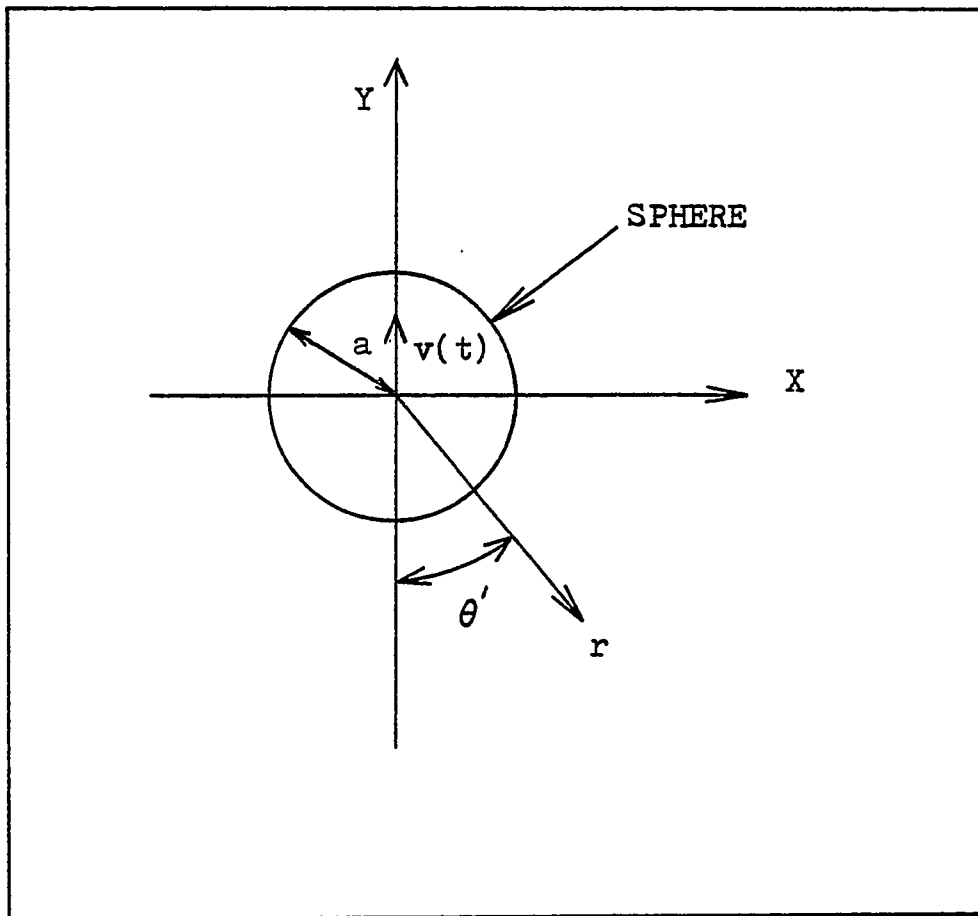


Figure 2.5 Definition sketch for a sphere under translating motion in Y-direction

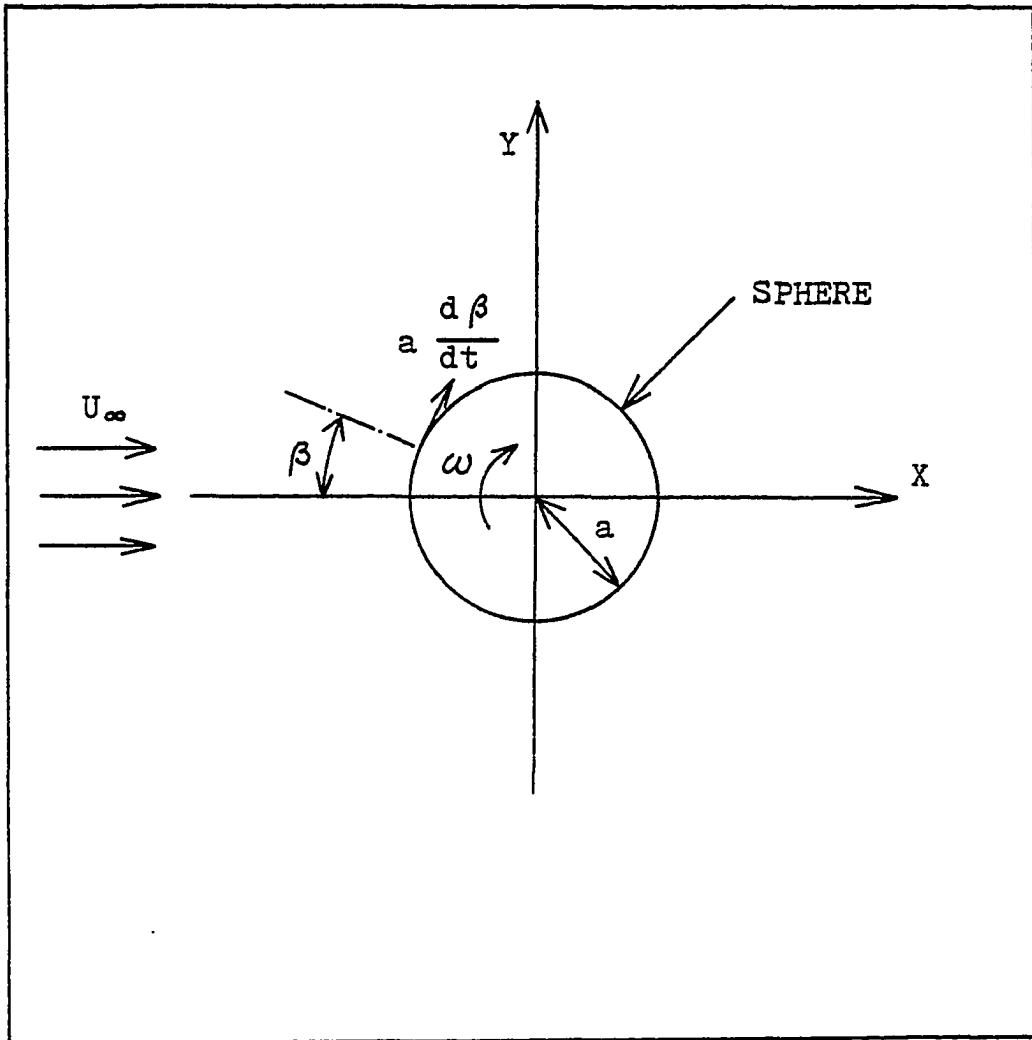


Figure 2.6 Definition sketch for a sphere under rotational motion

$$\eta_r = \tan^{-1} \left[a \frac{d\beta}{dt} \cos \beta / (U_\infty + a \frac{d\beta}{dt} \sin \beta) \right] \quad (2.3-27)$$

and the total dynamic head is

$$q_r = \frac{\rho}{2} \left[(U_\infty + a \frac{d\beta}{dt} \cos \beta)^2 + (a \frac{d\beta}{dt} \sin \beta)^2 \right] \quad (2.3-28)$$

By using equation (2.2-7), the pressure differential between two points i and j on the sphere surface can be expressed as

$$P_i - P_j = b_o q_r (\sin^2(\beta_j + \eta_r) - \sin^2(\beta_i + \eta_r)) \quad (2.3-29)$$

To solve for the combined effects due to the horizontal oscillation, vertical oscillation, and rotational motion,

η_r must be revised to include $u_1(t)$ and $v(t)$.

Upon denoting the new angle quantity

$$\eta^* = \tan^{-1} \left[\frac{v(t) + a \frac{d\beta}{dt} \cos \beta}{U_\infty + u_1(t) + a \frac{d\beta}{dt} \sin \beta} \right] \quad (2.3-30)$$

and the new dynamic head

$$q^* = \frac{\rho}{2} \left[(U_\infty + u_1(t) + a \frac{d\beta}{dt} \sin \beta)^2 + (v(t) + a \frac{d\beta}{dt} \cos \beta)^2 \right] \quad (2.3-31)$$

Hence, the new pressure differential becomes

$$P_i - P_j = b_o q^* [\sin^2(\beta_j + \eta^*) - \sin^2(\beta_i + \eta^*)] \quad (2.3-32)$$

So, the total pressure differential between two points i and j on the sphere surface is the superposition of equations

(2.3-23), (2.3-26), and (2.3-32). A computer program has been written to calculate the pressure difference from these three equations, which is described in Appendix D.

These two theoretical analyses of the unsteady, potential flow over a sphere will be compared in Chapter V with the experimental data to be described in Chapter IV.

2.4 Application of Theory I to Probe ODU2 Under Oscillating Test Motion

From equation (2.2-7), the pressure differential between two portholes i and j on a spherical probe head can be written in the following form:

$$\frac{\Delta P_{12}}{q(t)} = b_{12} (\sin^2(\alpha_a)_2 - \sin^2(\alpha_a)_1) \quad (2.4-1)$$

and

$$\frac{\Delta P_{23}}{q(t)} = b_{23} (\sin^2(\alpha_a)_3 - \sin^2(\alpha_a)_2) \quad (2.4-2)$$

where subscripts 1, 2 and 3 are porthole numbers on the probe ODU2, $q(t)$ is the effective dynamic head, and b_{12} and b_{23} are probe coefficients which will be determined experimentally in Chapter IV and discussed in Chapter V. These probe coefficients are defined as the slopes, over the linear response range, of the corresponding probe pressure difference versus the angle curves.

2.5 Application of Theory II to Probe ODU2 Under Oscillating Test Motion

The theory derived in article 2.3 can be applied to the pressure probe ODU2 as follows. The pressure differential caused by the translating and rotational motion is given by equations (2.3-23, 26 and 32). Consider the case of $P_1 - P_2$ and substitute $\theta_1 = \pi$ and $\theta_2 = (3/4)\pi$ into equation (2.3-23), to obtain

$$P_1 - P_2 \Big|_{\text{due to } u_1} = \frac{b_{12}}{4} u_1^2(t) + \frac{2 - \sqrt{2}}{9} b_{12} \rho a \frac{du_1(t)}{dt} \quad (2.5-1a)$$

Substitute $\theta'_1 = (3/2)\pi$ and $\theta'_2 = (5/4)\pi$ into equation (2.3-26), so that

$$P_1 - P_2 \Big|_{\text{due to } v} = \frac{-b_{12}}{4} \rho v^2(t) - \frac{\sqrt{2}}{9} b_{12} \rho a \frac{dv(t)}{dt} \quad (2.5-1b)$$

Also, equation (2.3-32) becomes

$$P_1 - P_2 \Big|_{\text{due to rotation}} = b_{12} q^* (\sin^2(\theta + \eta^* - \frac{\pi}{4}) - \sin^2(\theta + \eta^*)) \quad (2.5-1c)$$

where

$$q^* = \frac{\rho}{2} \left[(U_\infty + u_1(t) + a \frac{d\theta}{dt} \cos \theta)^2 + (v(t) + a \frac{d\theta}{dt} \sin \theta)^2 \right],$$

$$\eta^* = \tan^{-1} \left[(v(t) + a \frac{d\theta}{dt} \sin \theta) / (U_\infty + u_1(t) + a \frac{d\theta}{dt} \cos \theta) \right],$$

$$\theta = \theta_D - \alpha \sin(2\pi f t),$$

$$u_1(t) = L_p \frac{d\theta}{dt} \sin \theta,$$

and

$$v(t) = L_p \frac{d\theta}{dt} \cos \theta.$$

Similarly, by substituting appropriate quantities for θ_2 ,

θ_3 , θ'_2 and θ'_3 into equations (2.3-23, 26 and 32), one obtains equations (2.5-2a, 2b and 2c) respectively as follows:

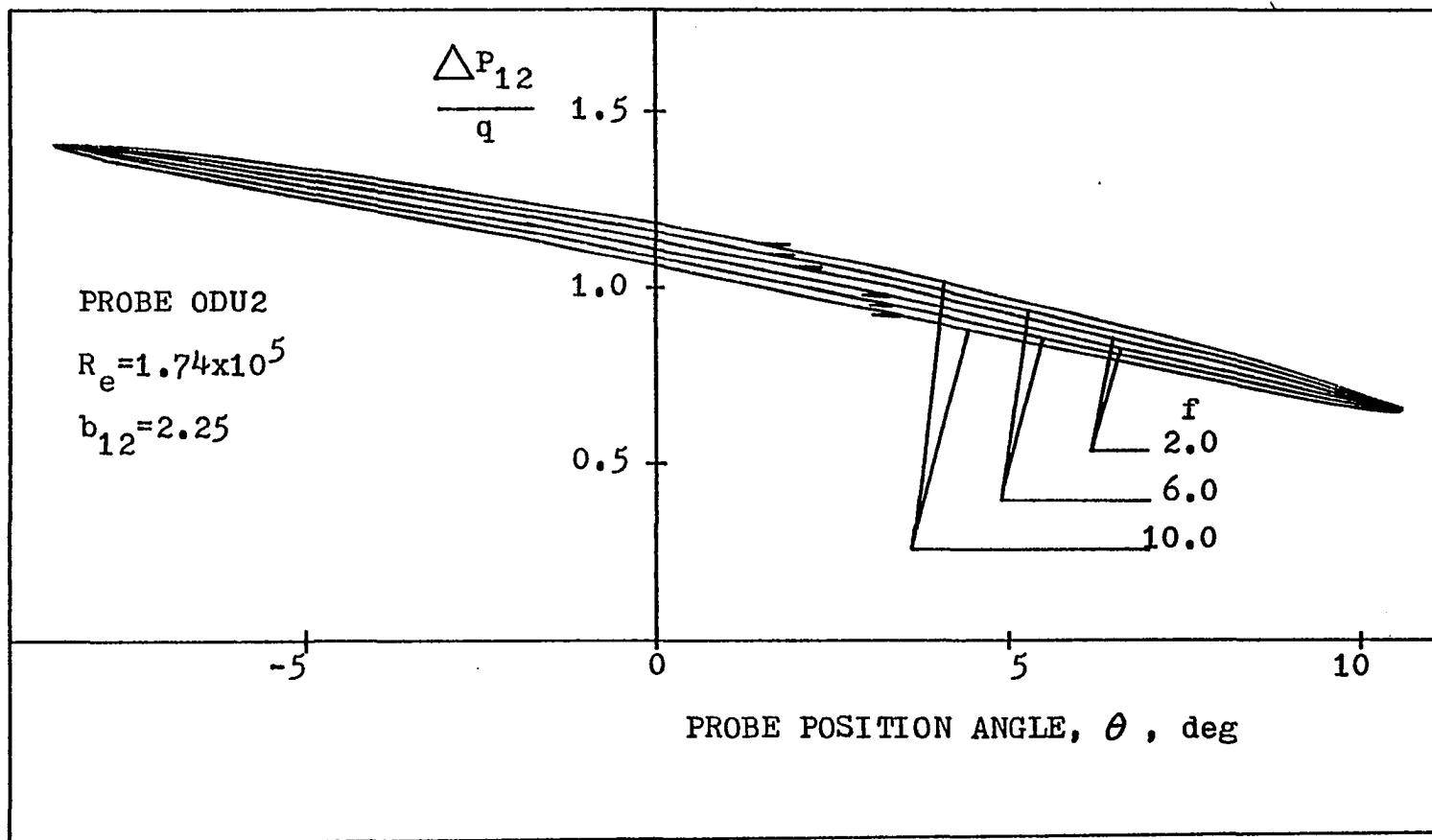
$$P_2 - P_3 \Big|_{\substack{\text{due to} \\ u_1}} = \frac{b_{23}}{4} \rho u_1^2(t) \quad (2.5-2a)$$

$$P_2 - P_3 \Big|_{\substack{\text{due to} \\ v}} = \frac{b_{23}}{4} \rho v^2(t) - \frac{2}{9} b_{23} \rho a \frac{dv(t)}{dt} \quad (2.5-2b)$$

$$P_2 - P_3 \Big|_{\substack{\text{due to} \\ \text{rotation}}} = b_{23} q^* \left(\sin^2 \left(\theta + \eta^* - \frac{\pi}{4} \right) - \sin^2 \left(\theta + \eta^* + \frac{\pi}{4} \right) \right) \quad (2.5-2c)$$

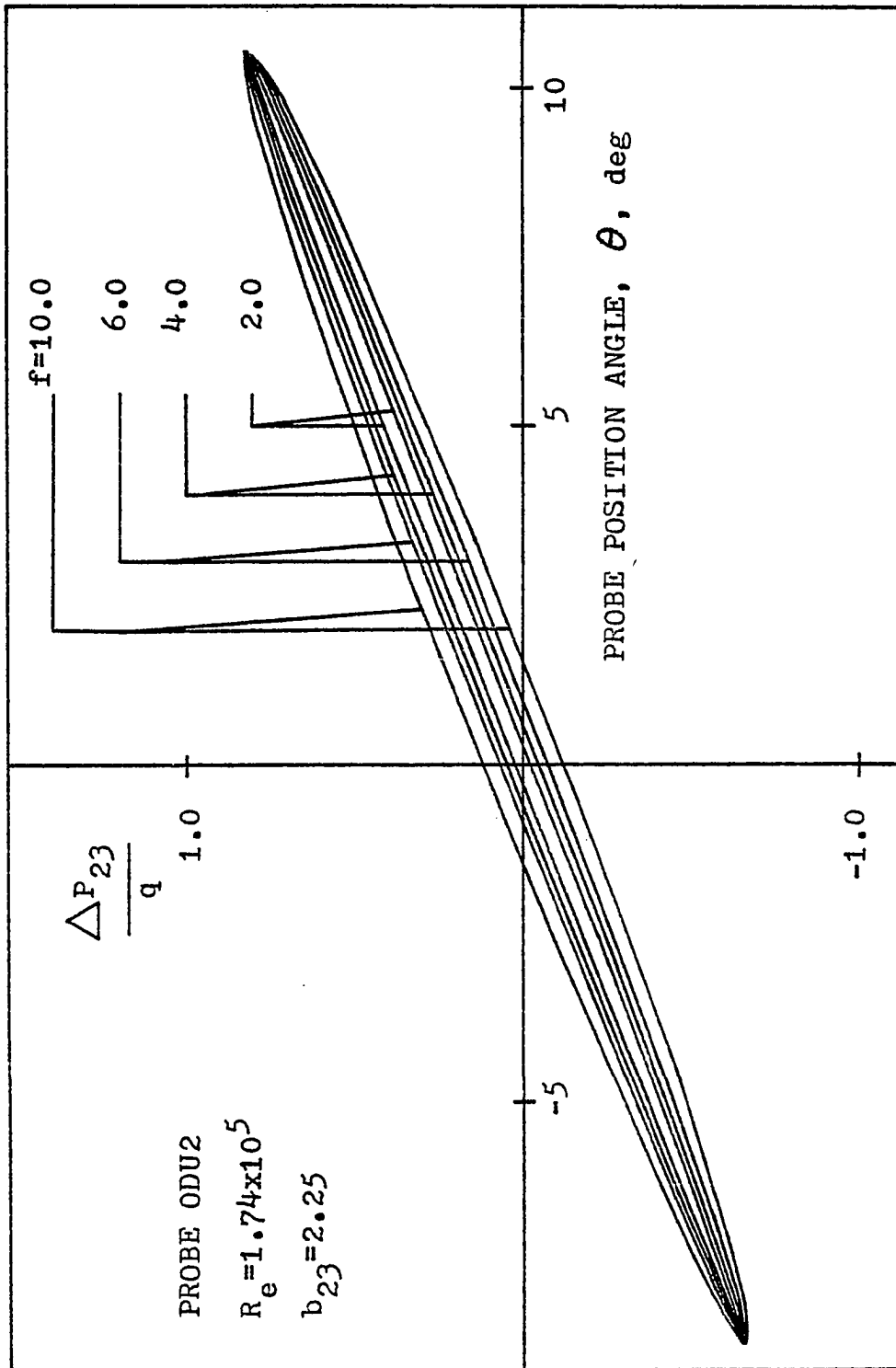
where q^* , η^* , θ , u_1 , and v are defined as in equation (2.5-1c). The probe coefficients b_{12} and b_{23} have been defined in 2.4.

The combined effects of equations (2.5-1a, 1b and 1c) for an oscillating probe are determined by two major factors: the oscillating frequency, f , and the airstream velocity, U . First, consider the case with various oscillating frequencies but constant airstream velocity. Figure (2.7a) shows the prediction by Theory II of the variation of non-dimensional pressure differential $\Delta P_{12}/q$ with oscillating frequency and probe position angle. The airspeed has been held fixed at $U=83.5$ m/s, corresponding to a value of $Re=1.74 \times 10^5$. At lower frequencies, the pressure differential loops are narrower than at higher frequencies; i.e., the pressure differential varies less between the upward and downward probe motion at lower oscillating frequencies. Figure (2.7b) shows the variation of $\Delta P_{23}/q$ with the probe angle θ at



(a) $\Delta P_{12}/q$ versus θ

Figure 2.7 Variation of non-dimensional pressure quantity with oscillating angle under different frequencies, Theory II.



(b) $\Delta P_{23}/q$ versus θ

Figure 2.7 Concluded

various oscillating frequencies. As the frequency, f , is increased, the difference between $\Delta P_{23}/q$ for upward and downward motion at the same probe position angle is again increased, except at the two extreme positions.

Now, consider the case of constant oscillating frequency and oscillation amplitude but various airstream velocities. As the Reynolds number was increased, i.e., the airstream velocity increased, the loops of predicted $\Delta P_{12}/q$ and $\Delta P_{23}/q$ variation became narrower as shown in figures (2.8a, b) respectively. Hence, the effects of U and f were predicted by Theory II to be opposite to one another. That is, an increase of U and a decrease of f have similar effects on the probe output response. Similar trends were predicted by Theory I.

2.6 R-Equation Model

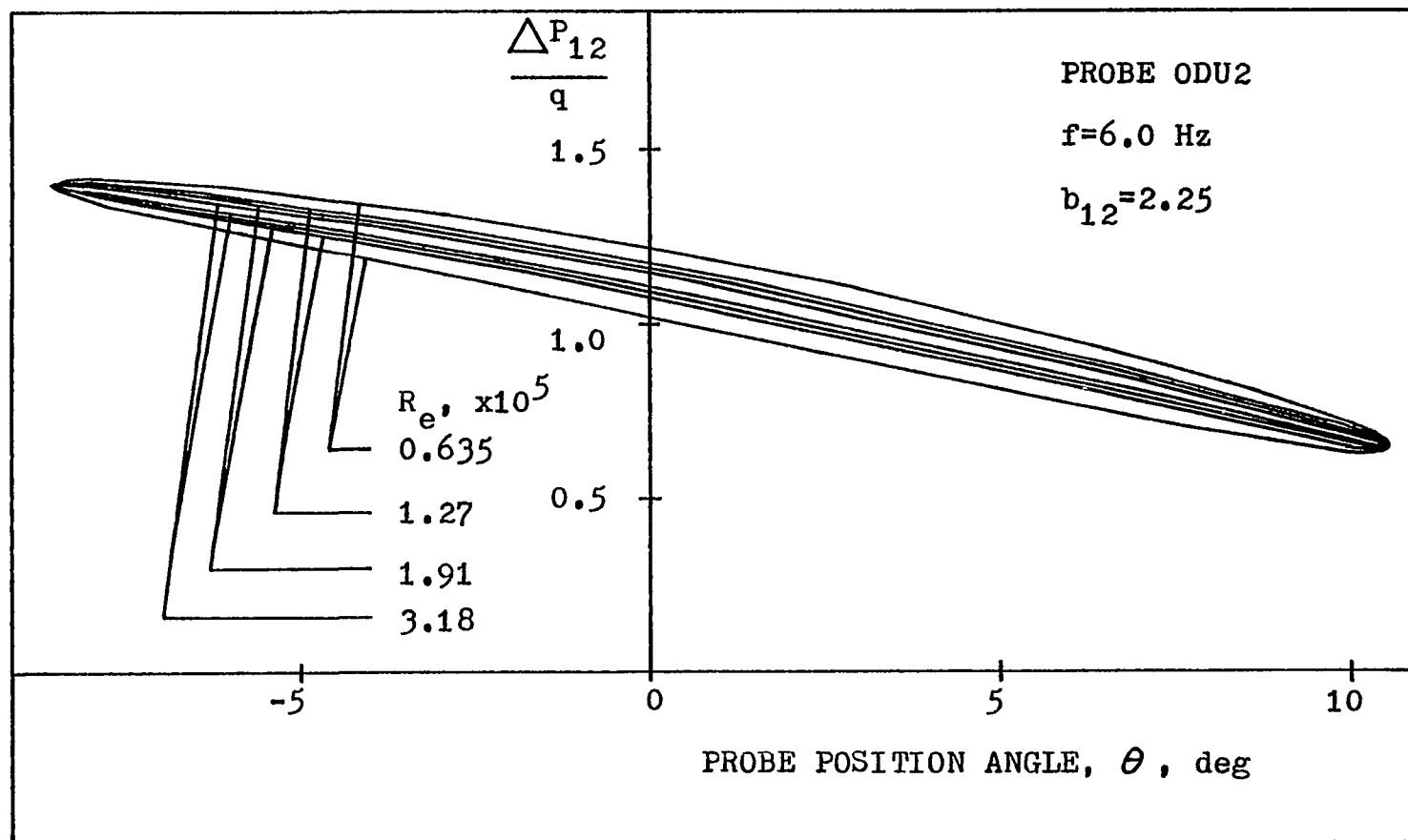
Consider the unsteady state Bernoulli equation, (2.2-4):

$$\frac{\partial \phi}{\partial t} + \frac{1}{2} (\nabla \phi)^2 + \frac{P}{\rho} = H(t).$$

Since this equation holds for the entire field of motion, at a specific time $t=t^*$, one may write for port 2 and port 3

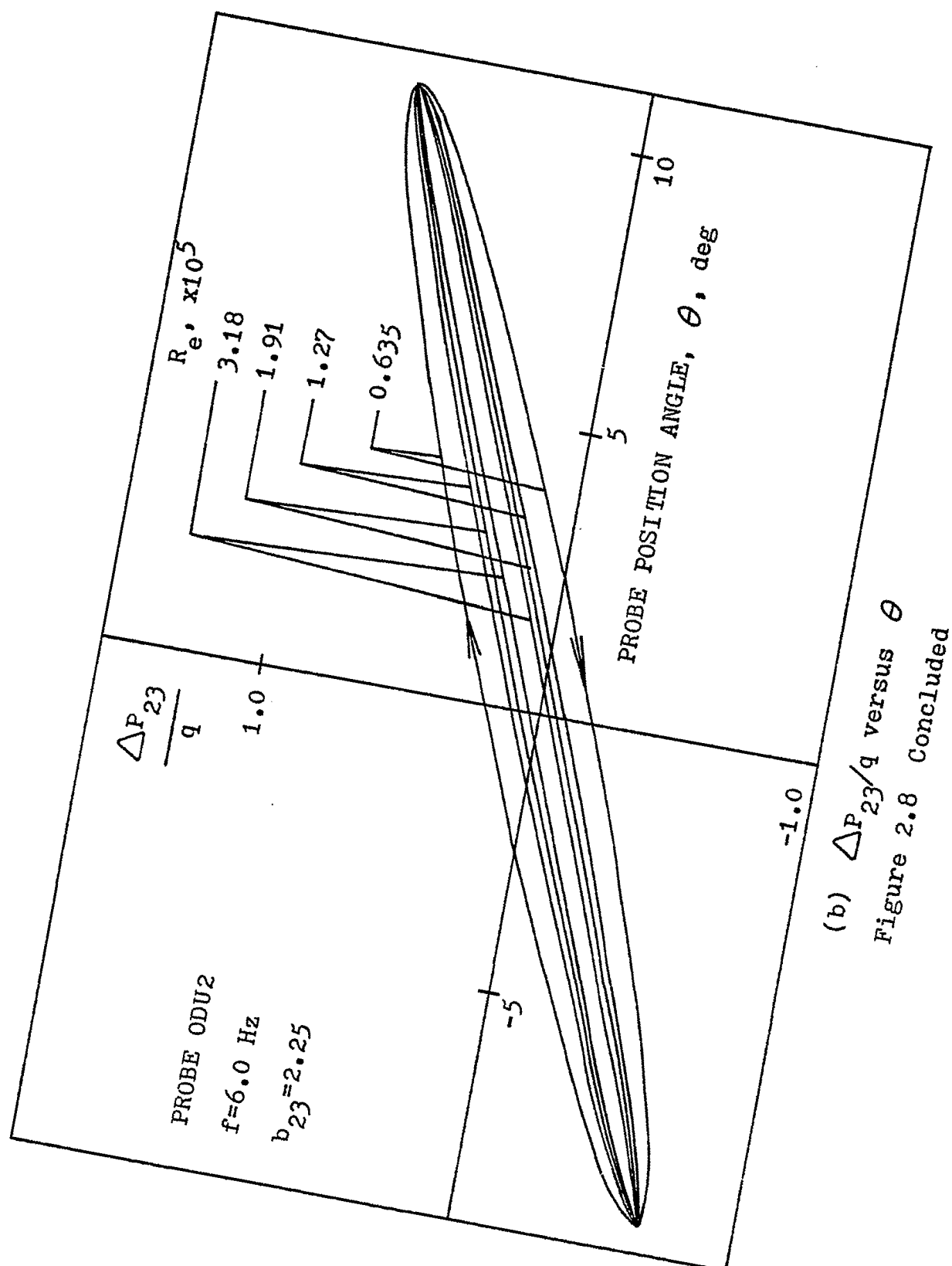
$$\left(\frac{V^2}{2} + \frac{P}{\rho} \right)_2 - \left(\frac{V^2}{2} + \frac{P}{\rho} \right)_3 = \left(\frac{\partial \phi}{\partial t} \right)_3 - \left(\frac{\partial \phi}{\partial t} \right)_2 \quad (2.6-1)$$

Thus the instantaneous pressure differential between ports 2 and 3 becomes



(a) $\frac{\Delta P_{12}}{q}$ versus θ

Figure 2.8 Variation of non-dimensional pressure quantity with probe position angle under constant oscillating frequency but various airspeeds, Theory II.



$$\frac{P_2 - P_3}{\rho} = \frac{1}{2} (v_3^2 - v_2^2) + \left[\left(\frac{\partial \phi}{\partial t} \right)_3 - \left(\frac{\partial \phi}{\partial t} \right)_2 \right]$$

or

$$\Delta P_{23} = \frac{\rho}{2} (v_3^2 - v_2^2) + \rho \left[\left(\frac{\partial \phi}{\partial t} \right)_3 - \left(\frac{\partial \phi}{\partial t} \right)_2 \right] \quad (2.6-2)$$

The first term on the right-hand-side of equation (2.6-2) is the same as the static result, while the second term is the additional term due to the unsteady effect.

Denoting a new function

$$e_{23}(U, f) = \frac{2 \left[\left(\frac{\partial \phi}{\partial t} \right)_3 - \left(\frac{\partial \phi}{\partial t} \right)_2 \right]}{b_{23} U_\infty^2 \sin(2\theta)} \quad (2.6-3)$$

equation (2.6-2) can be rewritten as

$$\Delta P_{23} = b_{23} q \left[1 + e_{23}(U, f) \right] \sin(2\theta) \quad (2.6-4)$$

where $q = (1/2) \rho U_\infty^2$.

Similarly, the pressure differential ΔP_{12} can be expressed as

$$\Delta P_{12} = b_{12} q \left[1 + e_{12}(U, f) \right] \sin(\pi/4 - 2\theta) / \sqrt{2}. \quad (2.6-5)$$

For the static case, $e_{12}(U, f) = 0$ and $e_{23}(U, f) = 0$.

From equations (2.6-4, 5), the pressure differentials can be combined by taking the ratio of two pressure differentials, i.e., $\Delta P_{23} / \Delta P_{12}$, to form a one equation model:

$$\frac{\Delta P_{23}}{\Delta P_{12}} = \frac{b_{23}}{b_{12}} \frac{1 + e_{23}(U, f)}{1 + e_{12}(U, f)} \frac{\sqrt{2} \sin(2\theta)}{\sin(\pi/4 - 2\theta)} \quad (2.6-6)$$

By defining $R = \Delta P_{23} / \Delta P_{12}$, one can rewrite equation (2.6-6)

as

$$R = b_r G(U, f, \theta) \quad (2.6-7)$$

where $b_r = b_{23}/b_{12}$, and G is a function of U , f and θ .

By combining equations (2.4-1, 2) or (2.5-1, 2) with equation (2.6-7), one may obtain a set of curves through systematic variation of U , f , and θ . These curves may be applied to the pressure probe in actual flight, and may be subsequently used to predict the instantaneous angle of attack α_a . More detailed discussion is presented in article 5.3.

III. INSTRUMENTATION AND TEST APPARATUS

3.1 Pressure Probes

There were altogether 5 pressure probes used in the present investigation, which were denoted as NASA1, ODU1, ODU2, NASA2, and NASA60. The NASA1 probe consisted of a two-port-hole probe of spherical shape, where each port enclosed a 45-degree central angle with respect to the probe longitudinal axis. The ODU1, ODU2, and NASA2 probes were three-port-hole probes. Their outer appearances were identically the same as the NASA1 probe, but with a center port located on the longitudinal axis. The NASA60 probe was constructed in such a way that its upper and lower ports enclosed a 45-degree central angle with respect to the probe axis but port 1 was shifted downward to form a 15-degree central angle (see figures (3.1a to d)). For the measurements of pressure differences, all the probes embodied highly sensitive transducers, which were mounted inside the spherical probe body. The NASA1 probe utilized only one transducer, while the other four probes used two built-in transducers. Figure (3.1e) shows a schematic diagram of the ODU2 probe arrangement, while figure (3.1f) shows a photograph of probe NASA60. Figures (3.2a to f) show some of the existing pressure probes

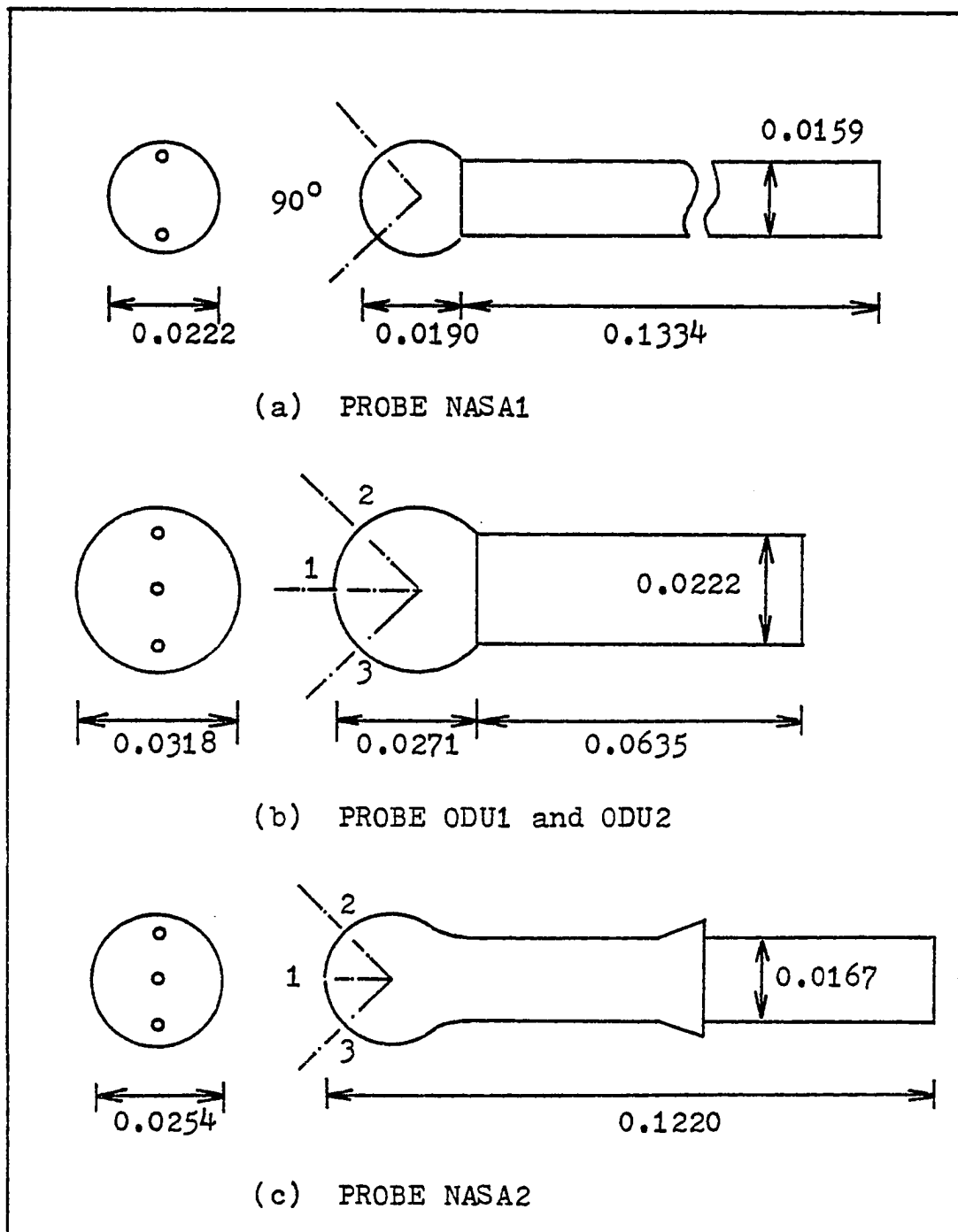


Figure 3.1 Schematic showings of pressure probes,
dimensions in meters.

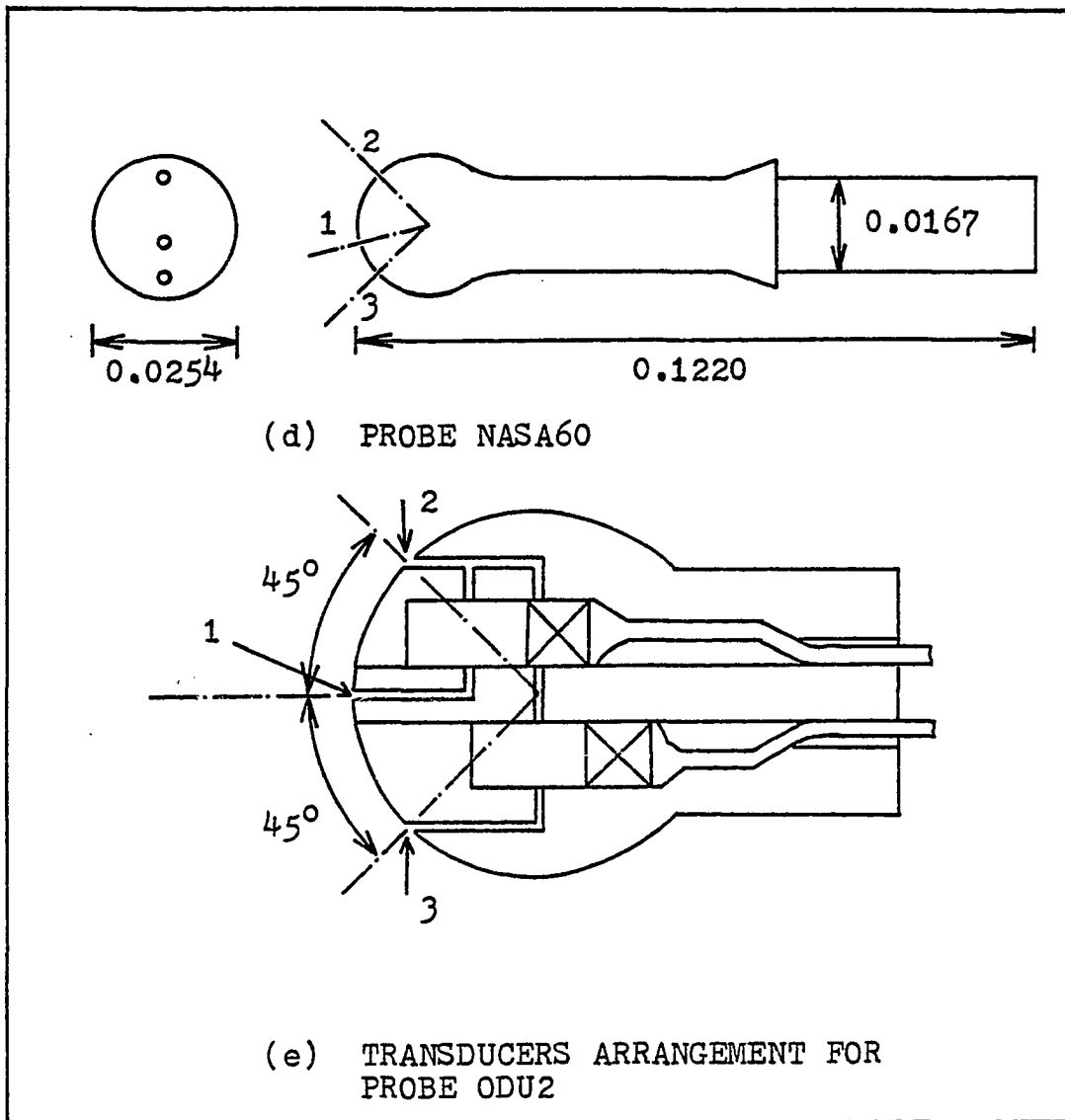
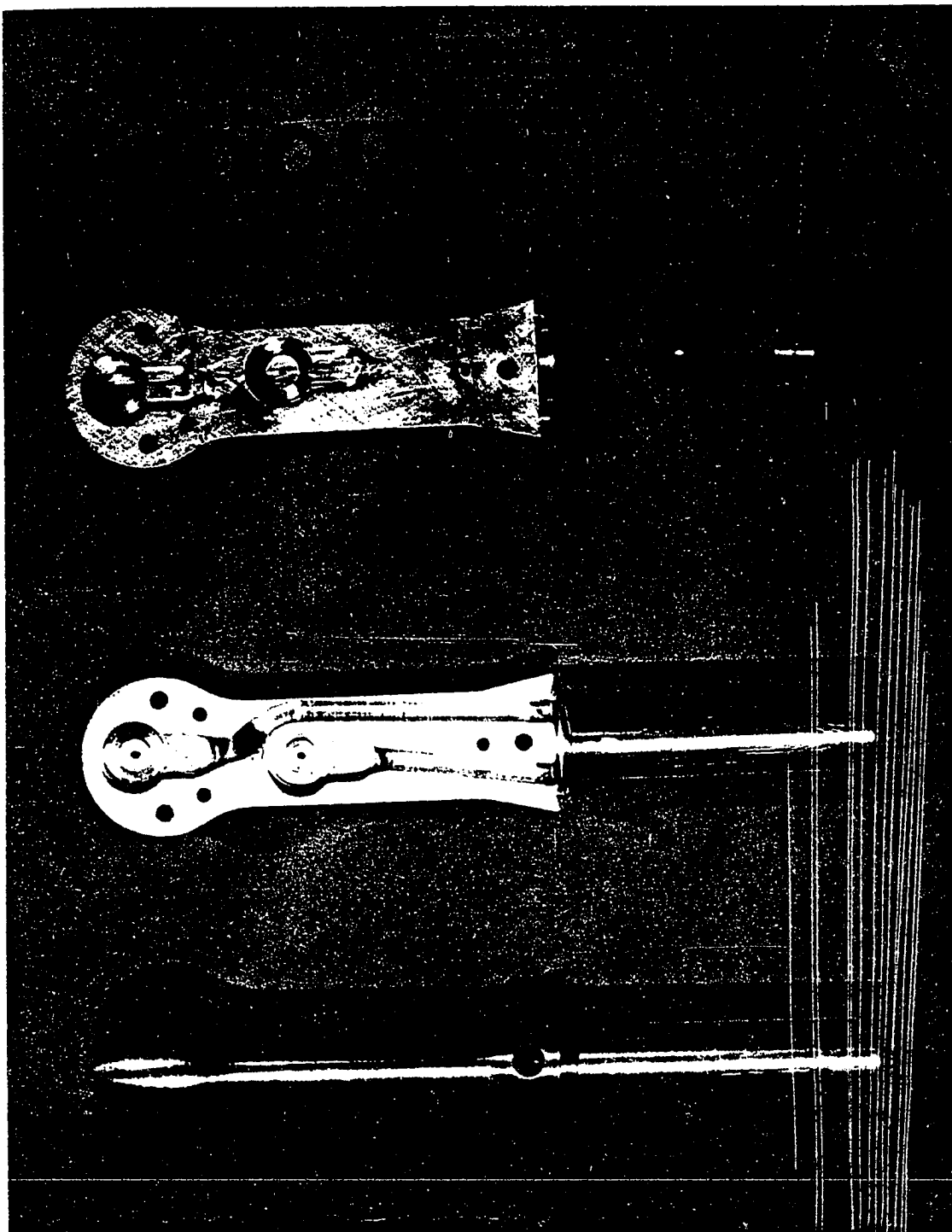
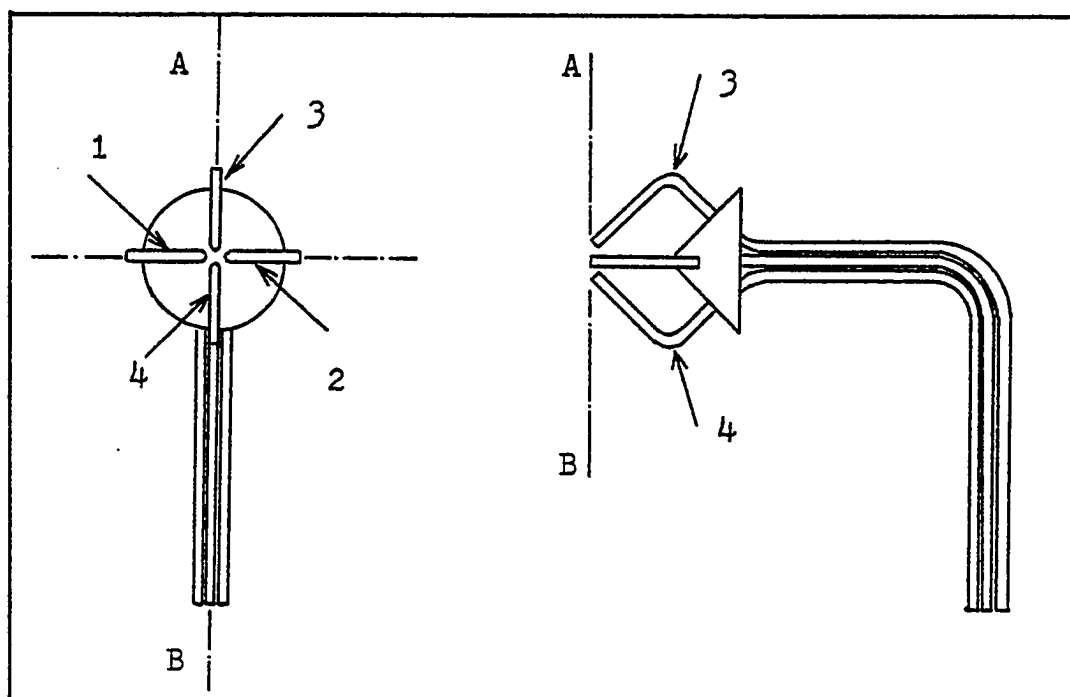


Figure 3.1 Continued

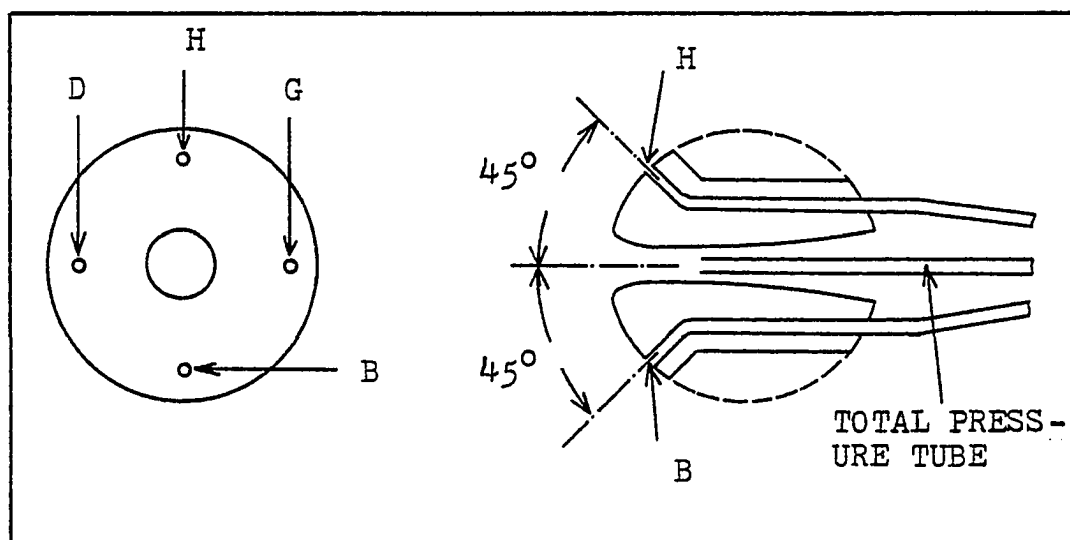


(f) PHOTOGRAPH OF PROBE NASA60

Figure 3.1 Concluded

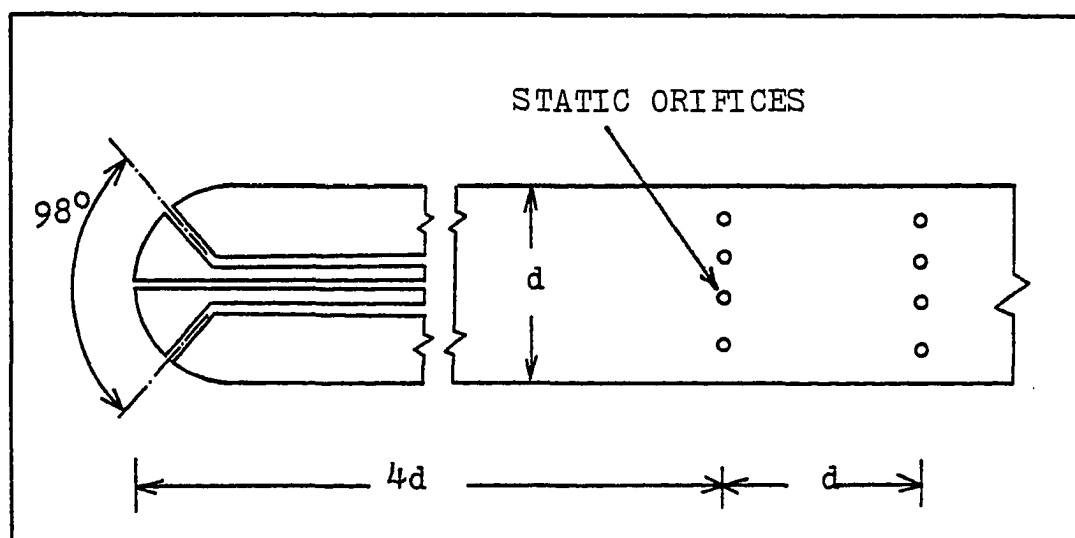


(a) SCHEMATIC SKETCH OF PRESSURE DIRECTION-METER (REF.1)

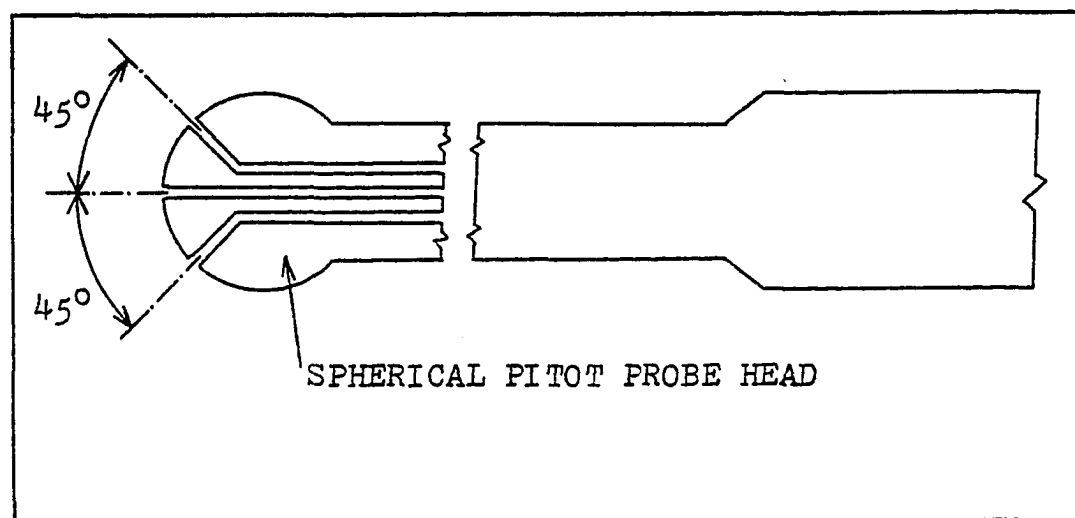


(b) SCHEMATIC SKETCH OF IMFL ANEMOCLINOMETER (REF.4)

Figure 3.2 Existing pressure probes

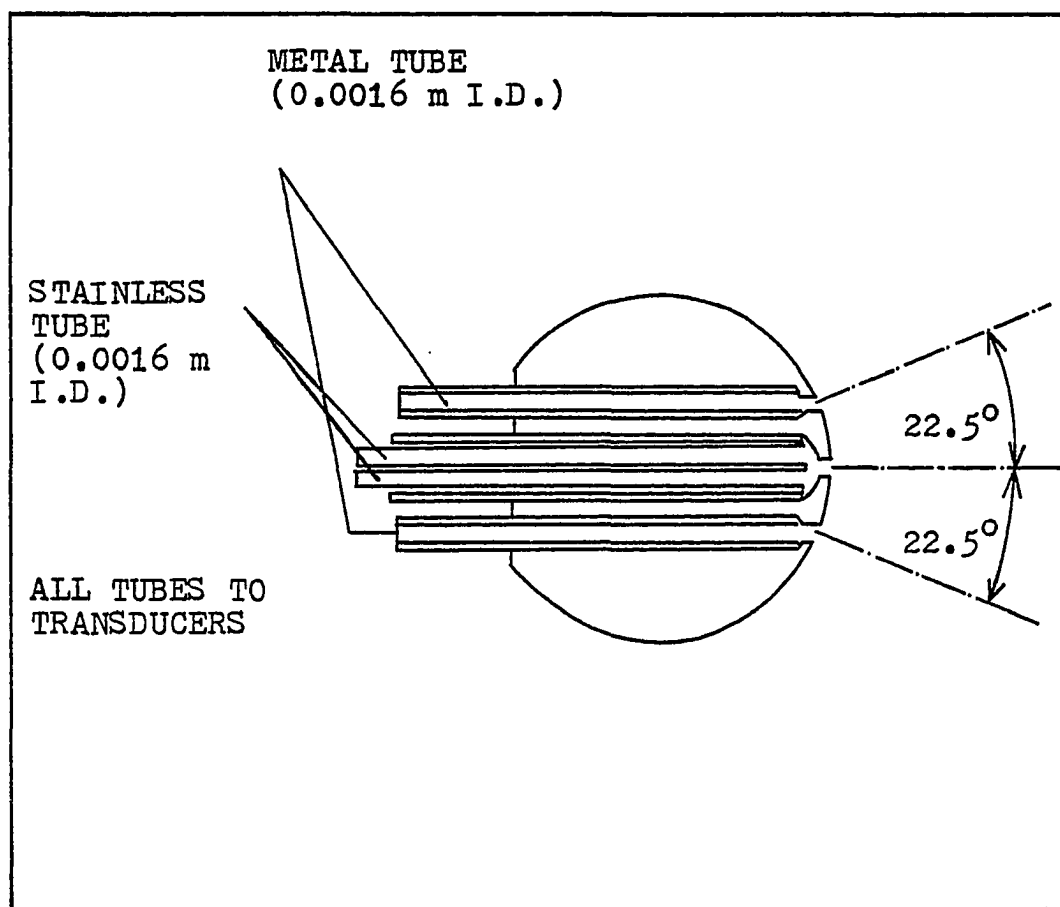


(c) SIX-CHANNEL PROBE, USED AT THE CENTRAL AERO AND HYDRODYNAMICS INSTITUTE (REF.6)



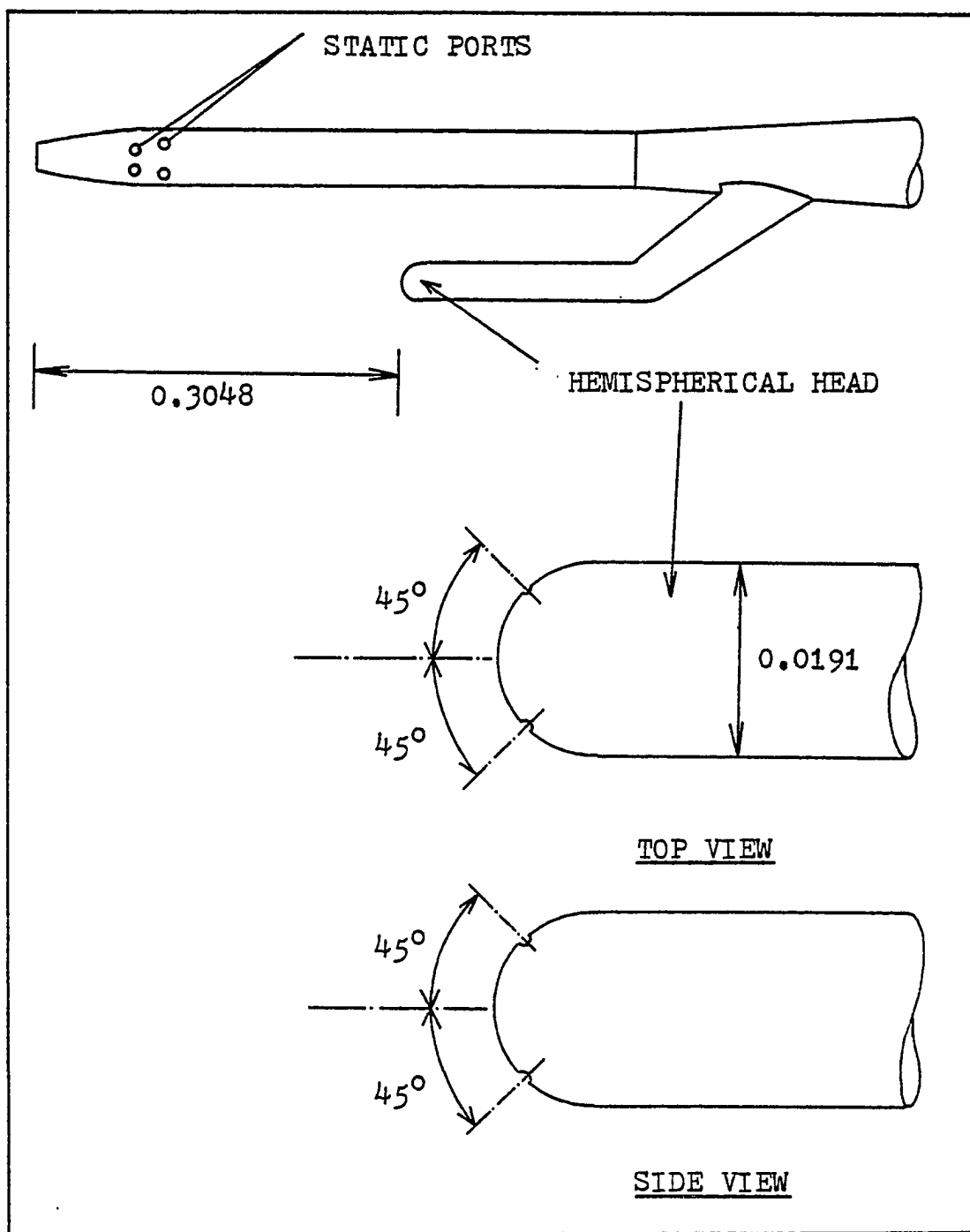
(d) SPHERICAL PITOT PROBE (REF.8)

Figure 3.2 Continued



(e) SCHEMATIC DIAGRAM OF THE 5-HOLE P.S.A.(REF.10)

Figure 3.2 Continued



(f) THREE-VIEW DRAWING OF HEMISPHERICAL HEAD
ANGULARITY SENSOR. DIMENSIONS IN METERS. (REF.11)

Figure 3.2 Concluded

mentioned in Chapter I (Reference 1-12). The current probes are most nearly like those of Ref. 8, shown in figure (3.2d), except that Nowack did not place the transducers inside the probe head.

3.2 Transducer Description and Calibration

The following tests were performed for the determination of transducer properties. The transducers employed in these pressure probes were gages originally designed by J. Patterson (Ref. 19). These gages are of the variable-air-gap type with electrical inductance, of about 0.0111 m in diameter and 0.0064 m in thickness. The gage was primarily designed to measure pressures fluctuating at high frequencies, but it was also capable of measuring static pressures with errors of less than 1 percent of full scale. A detailed sectional view of the pressure gage is shown in figure (3.3).

The main reasons for choosing the "Patterson" gage were as follows:

- 1) The gages were compact.
- 2) The gages were "rugged". From Patterson's report, the effect of accelerating force normal to the diaphragm was of the order of one percent of full scale per 100 g. Accelerations of 5000 g or lower parallel to the diaphragm therefore have negligible effect.
- 3) The frequency response of the transducer alone is approximately that of a single-degree-of-freedom system having a

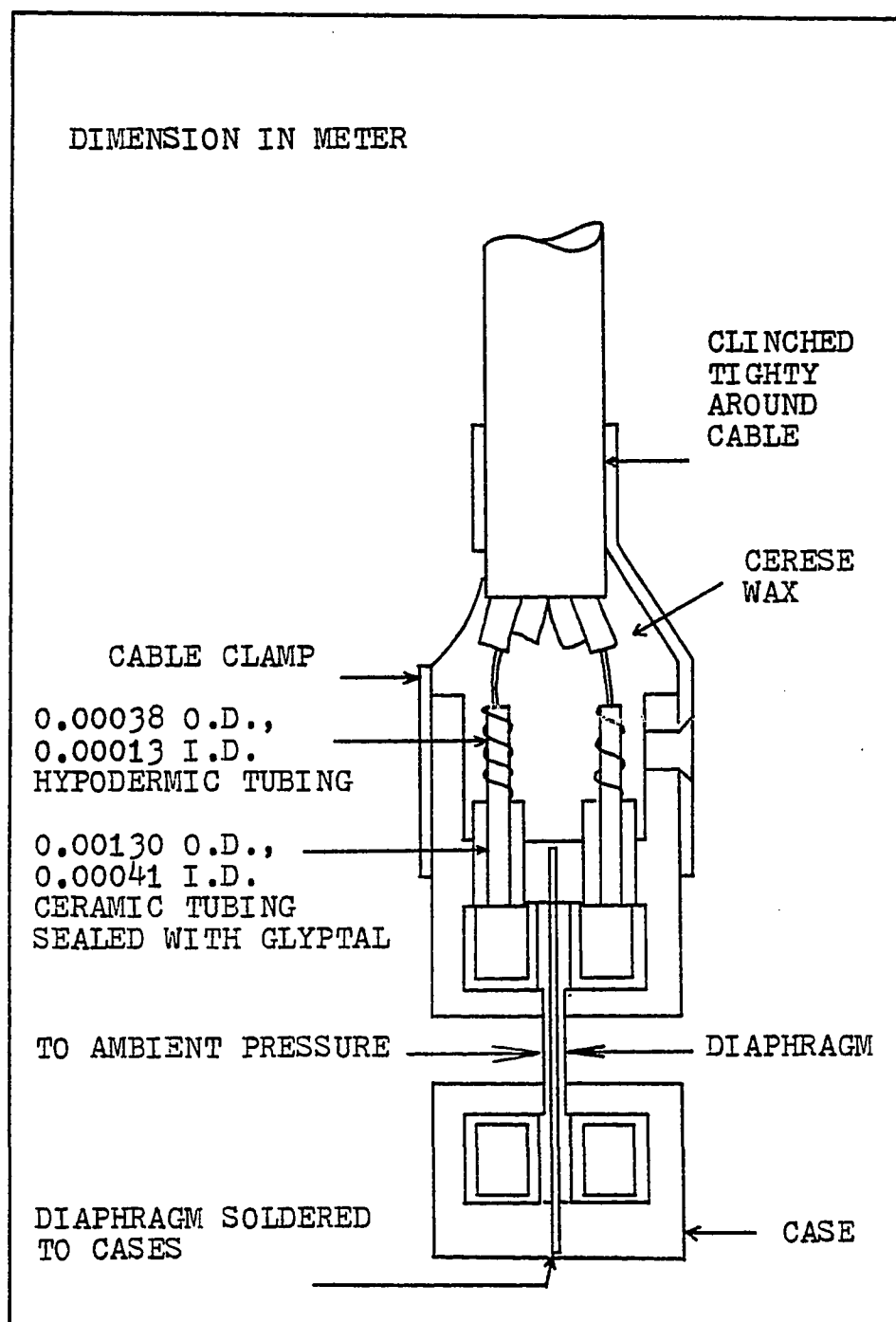


Figure 3.3 Sectional view of Patterson gage

natural frequency of 4000 cycles per second and a damping ratio of about 0.1.

4) The gages were almost independent of temperature. Temperature errors in the range of -50°F to 200°F normally are less than 0.03 percent of full scale per degree and may be corrected.

5) The gages are adequately reliable. However, over-all accuracy when measuring static or low-frequency pressure oscillations is usually somewhat limited by hysteresis errors, which are normally less than one percent of full scale.

The steady-state pressure calibration test set-up is shown in figure (3.4). 0.0064 m diameter plastic tubes were used to connect the pressure generator, manometer, and transducer. The pressure generator employed was a standard apparatus capable of compressing or expanding the air inside a chamber to cause a pressure difference between ambient pressure and the air contained inside the chamber. The transducer was connected to a carrier and amplifier unit. A two-channel BRUSH220 chart recorder was used to record the pressure difference signals, in terms of millivolts, on a recorder. In other words, for a given pressure difference, $P - P_{\text{room}}$, the manometer indicated a liquid level difference, Z , and the chart recorder recorded a corresponding value of mv. A sequence of tests were made in the pressure difference range of ± 0.65 m of water at room temperature. Transducer calibration charts in terms of pressure difference output in

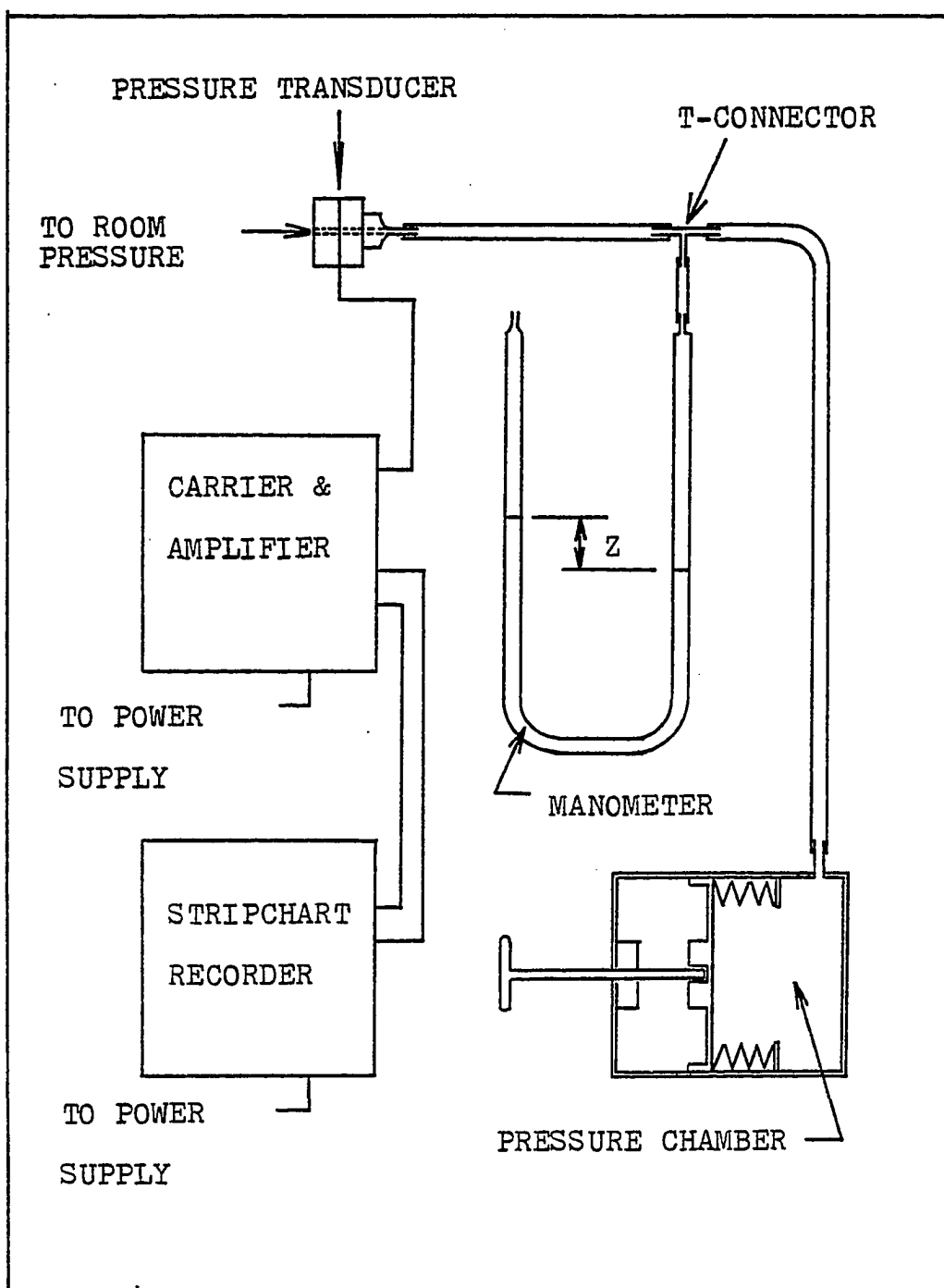


Figure 3.4 Steady state transducer calibration set-up.

mv versus manometer readings are shown in figures (3.5) and (3.6) for 2 different transducers. Figure (3.7) shows the experimental procedure for the transducer calibration and table 3.1 gives a comparison between these transducers.

These steady-state calibration results were used in the probe steady-state experiments conducted for finding the probe coefficients b_{12} , b_{23} , and b_{13} (discussed in article 5.2).

An experiment was performed to investigate the response time for these transducers. The transducer was connected as shown in figure (3.8a). The distance between the transducer side and the connector was 0.0254 m. For time $t \leq t_1$ (t_1 used here as a reference time), the transducer was given a pressure difference ΔP ; at $t > t_1$, the connector was removed suddenly and the transducer responded accordingly. The response curve indicated that there was a measurable time interval, Δt_s , for transducer to reach another steady pressure reading. In figure (3.8b), the transducer tested was gage T1, $\Delta P = 109$ newtons/m² and $\Delta t_s = 0.032$ seconds. This indicates that the pressure gages used in the current study had a bandwidth on the order of 30 Hz, assuming that the time required to remove the pressure difference, ΔP , was not the limiting factor in this experiment.

3.3 Wind Tunnels Employed in Measurements

3.3.1 The Free Air Intake Induction Tunnel

The air stream was introduced into the tunnel by suction

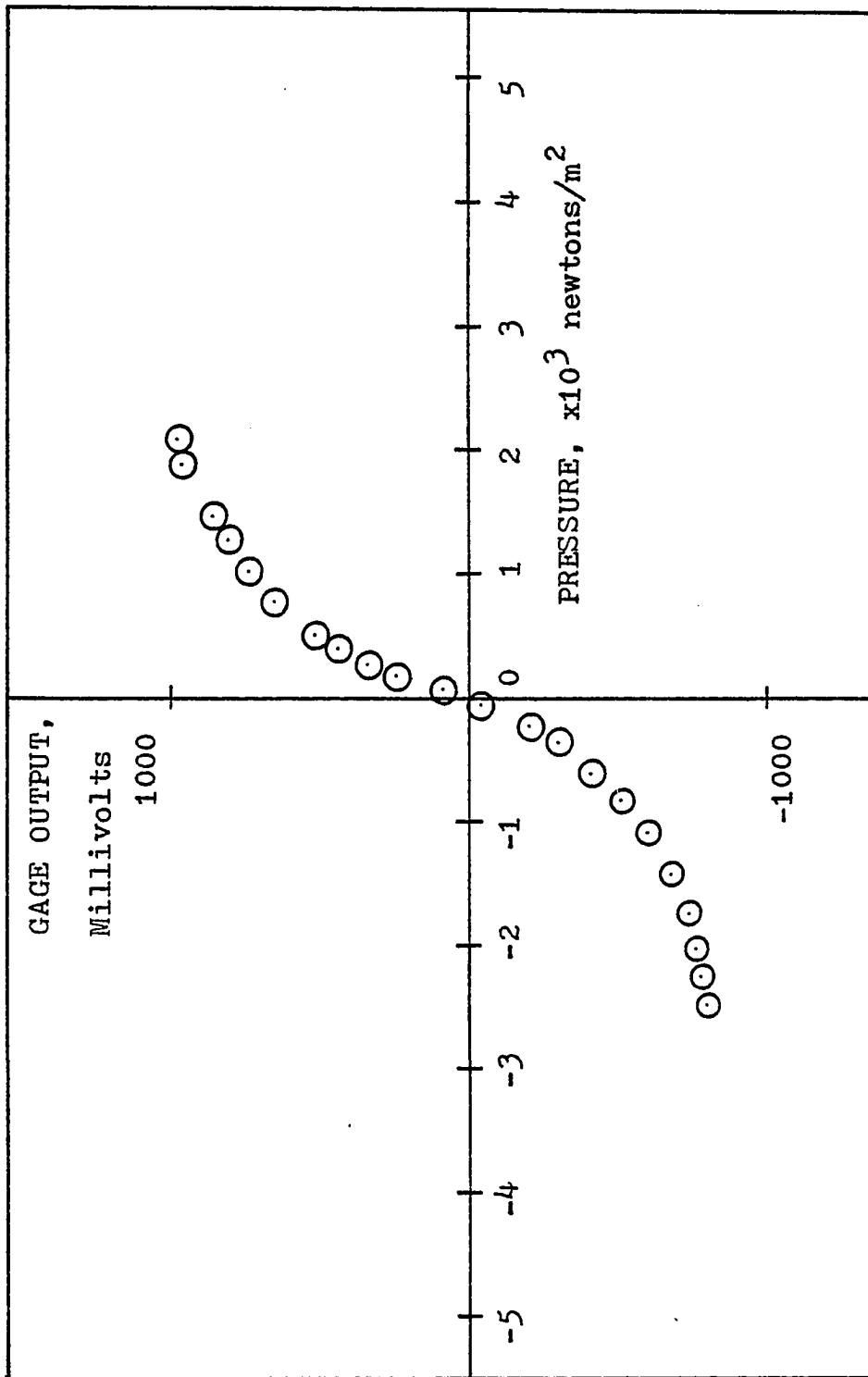


Figure 3.5 Calibration chart for gage T1.

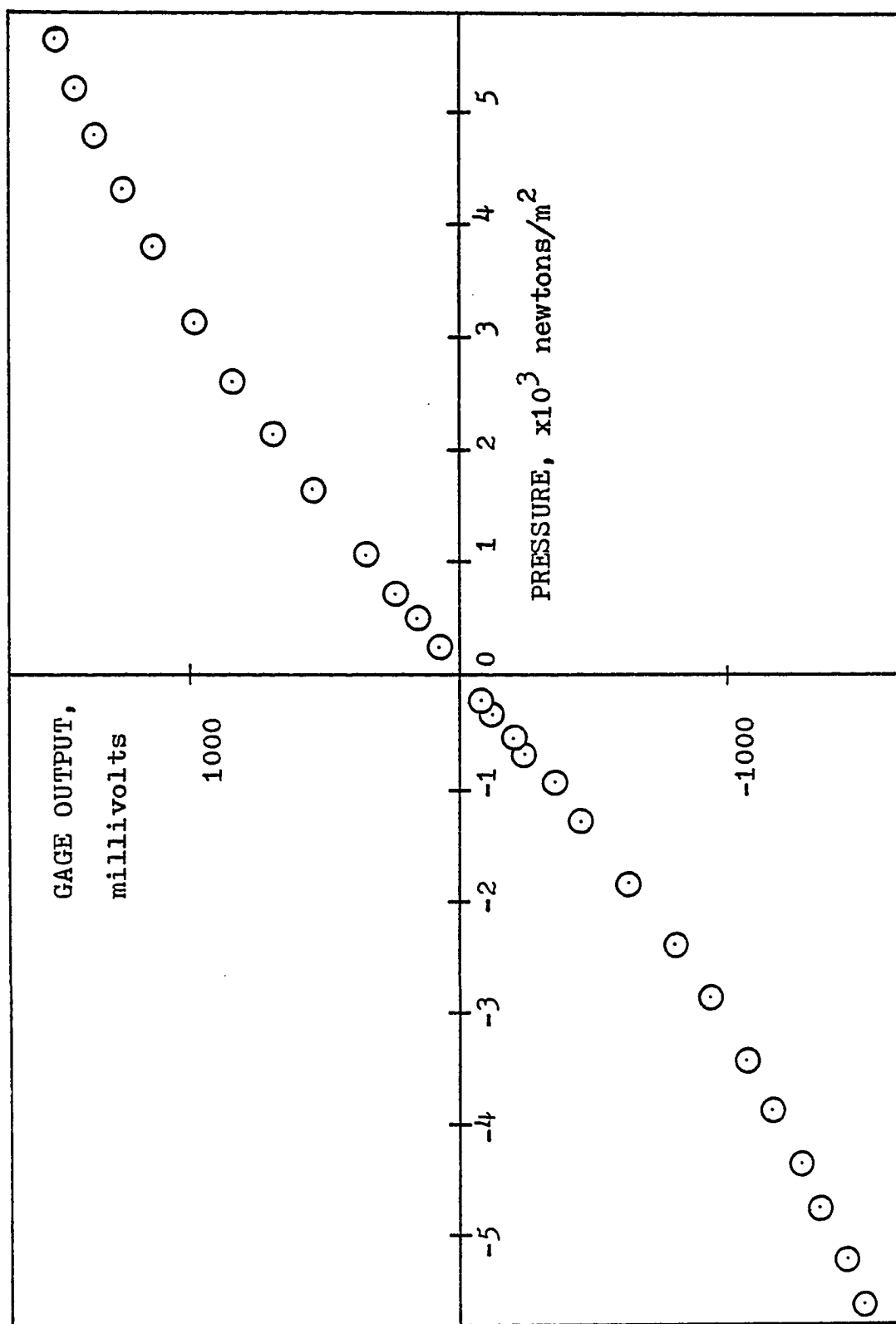


Figure 3.6 Calibration chart for gage T2.

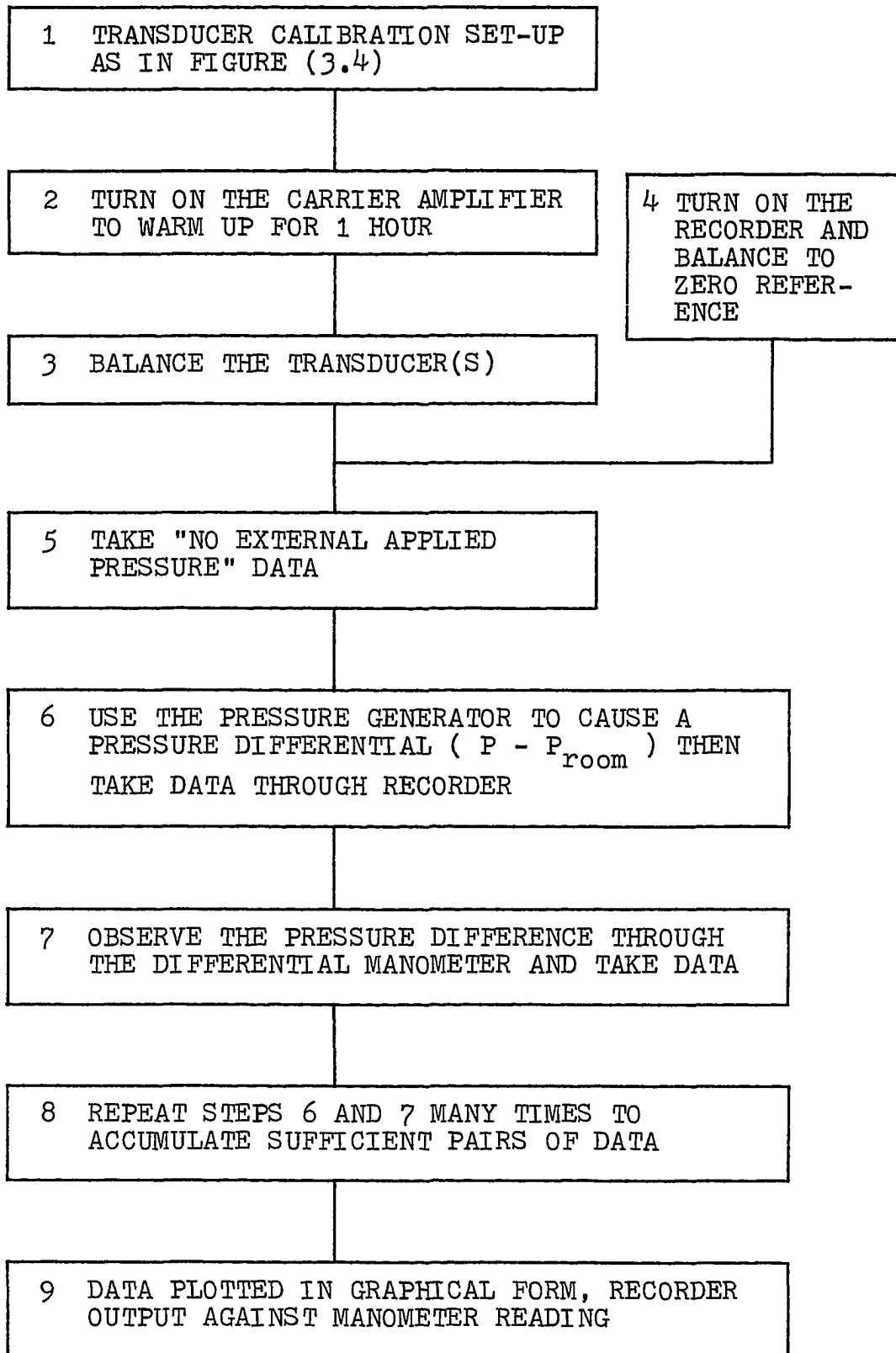
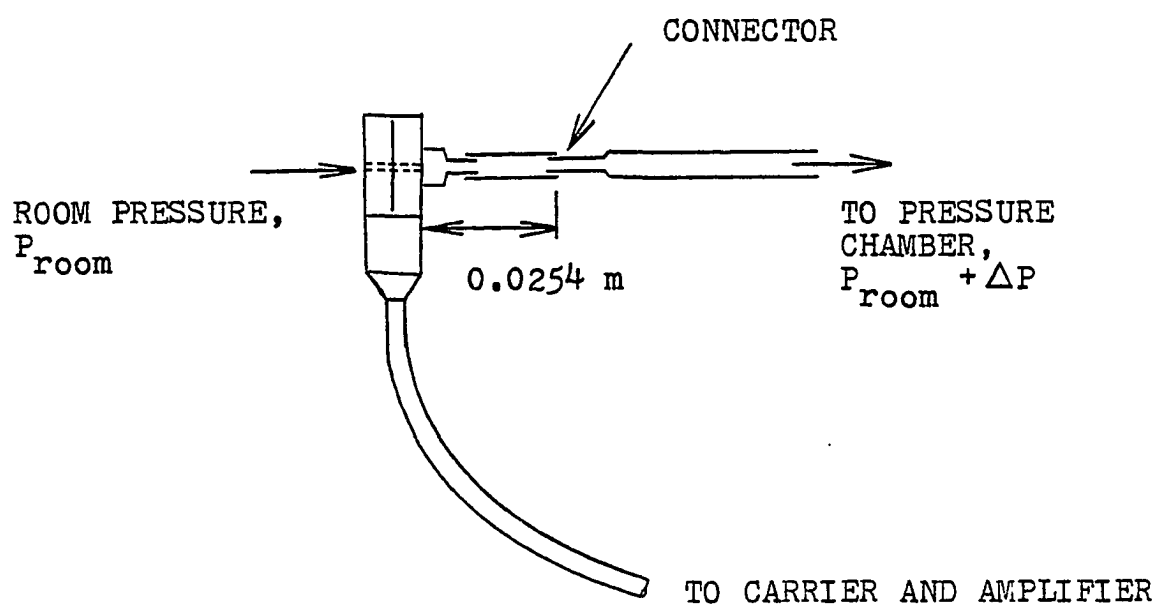


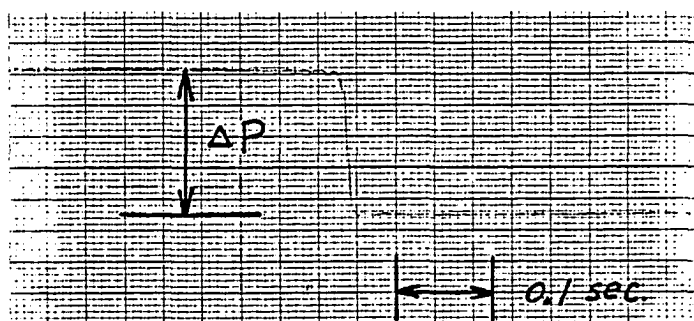
Figure (3.7) Test procedures for transducer calibration

Table 3.1 Transducer Characteristics

Gage number	Employed in the probe	Used for pressure difference	Number of ports on spherical head	Linear range, newtons/m ²
T1	NASA1	ΔP_{23}	2	-192 to 431
T2	ODU1	ΔP_{12}	3	-1179 to 2633
T3		ΔP_{23}		-575 to 575
T4	ODU2 and NASA2	ΔP_{12}	3	-2011 to 3352
T5		ΔP_{23}		-479 to 479
T6	NASA60	ΔP_{12}	3	-2633 to 1915
T7		ΔP_{23}		-479 to 814



(a) TEST SET-UP



(b) RESPONSE CHART FOR TRANSDUCER UNDER A STEP CHANGE OF PRESSURE DIFFERENCE

Figure 3.8 Determination of transducer's response time

produced by a centrifugal blower which was powered by a 4-stage motor rated at 15 hp. The intake produced a uniform velocity field in the test section as shown in figure (3.9). The contraction walls were bent into a bell shape to prevent unwanted air separation at the tunnel inlet. The wind tunnel contraction was constructed in two sections. The first section was designed to have parallel top and bottom walls but converging side walls, while the second section had two parallel side walls, but converging top and bottom walls. A 0.102 m thick honeycomb with mesh size 0.0048 m was inserted at the intake to reduce fluctuations in the approaching air stream. The 0.305 m long test section of 0.152x0.203 m cross section consisted of 0.025 m thick plexiglas walls. A diffuser followed the test section and joined the suction side of the blower. To prevent vibration of the test section, a foam rubber isolator was inserted between the test section exit and diffuser entrance. The tunnel test section was provided with a probe holder of special design which consisted of two parallel discs which fitted flush into the recessed top and bottom plexiglas plates. Since the discs could rotate about a common axis they served the purpose of a turntable. The discs were interconnected by a vertical rod which held the probe. The discs could be turned together with a common handle from the outside of the wind tunnel, so that the spherical probe head could be set to a certain angle of attack with respect to the incoming air stream. Angle of attack was set by a protractor made from polar graph

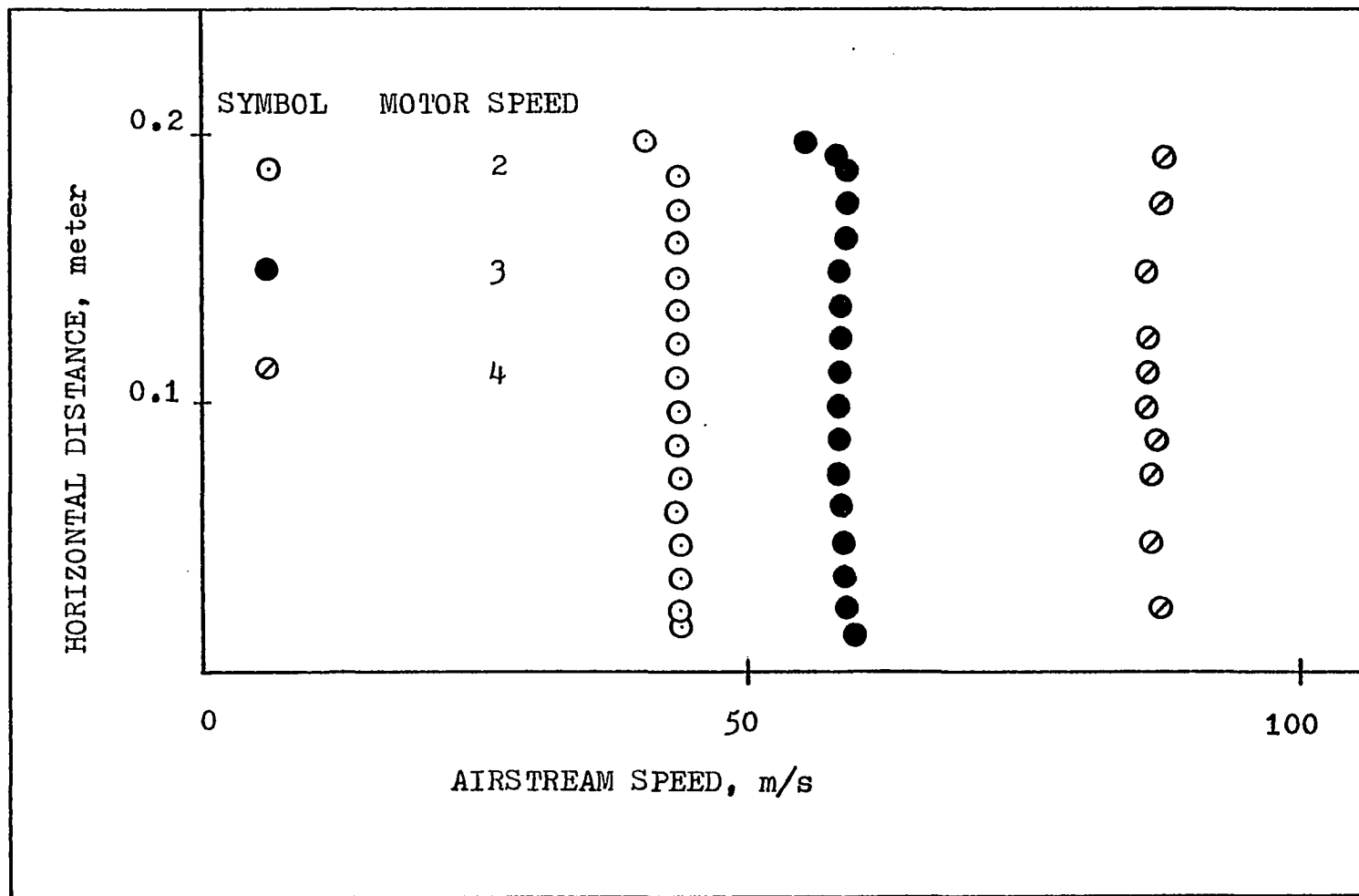


Figure 3.9 Velocity distribution profiles, induction wind tunnel.

paper. The general features of the induction wind tunnel are shown in figures (3.10a, b). The mean velocity distributions horizontally across the working test section are illustrated in figure (3.9) for three motor speeds. The maximum mean velocity was about 88.4 m/s or 290 ft/sec.

3.3.2 The Open End Wind Tunnel

The open end tunnel consisted of an axial fan, a diffuser, a settling chamber contraction, and a test section. A steel frame furnished with the oscillatory mechanism was fitted to its open end. The general features are shown in figure (3.11a). Figure (3.11b) shows the probe, cylinder and steel frame in the test section.

The tunnel was powered by a GE 4-stage motor which rated at 15 hp. A circular "floating" shaft was connected by both ends to the motor and the axial fan. A guide-vane ring served the purposes of supporting the shaft as well as to guide the intake air flow. Following the conical diffuser, a honeycomb was used to reduce the flow fluctuations.

Immediately following the contraction, there was a parallel wall transition which changed the tunnel passage from circular cross section to a rectangular cross section. The soft connection section was mainly used to isolate the vibration effects due to the motor-axial fan system. The parallel test section had a rectangular cross section of 0.546x0.608 m. A pitot-static tube was mounted on the side wall for measuring air velocity. A free-rotation cylinder was also

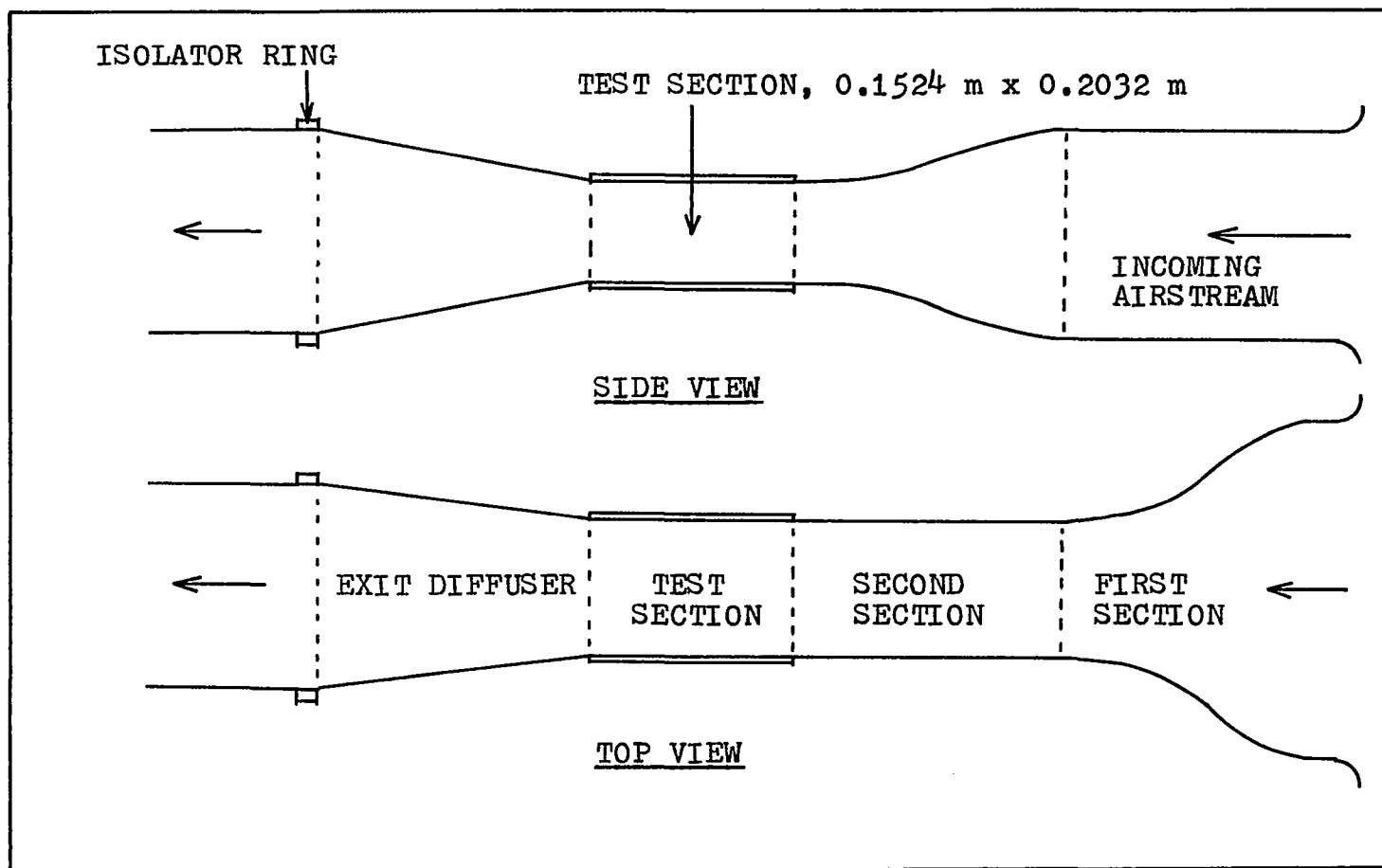


Figure 3.10a General features of the induction wind tunnel.

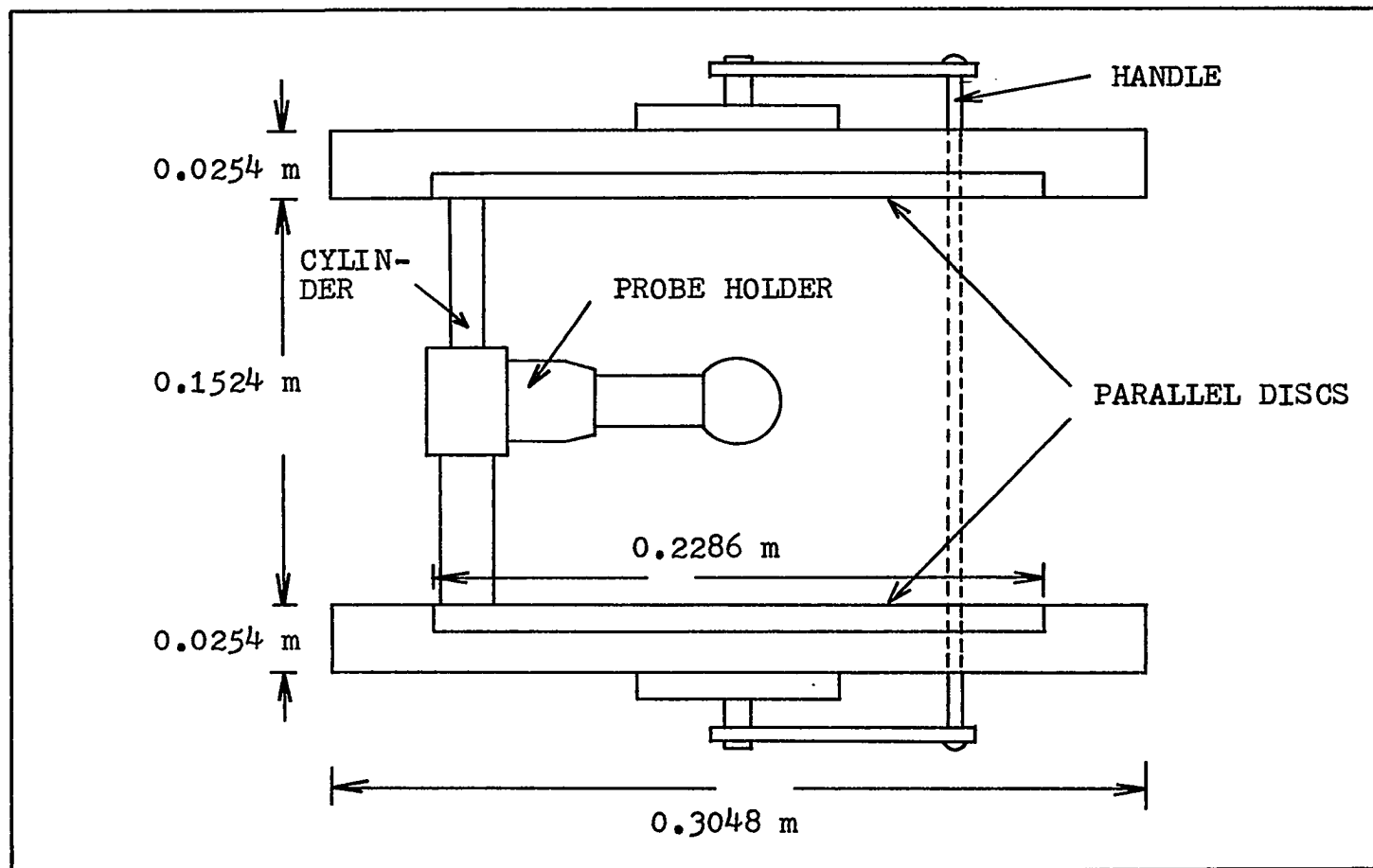


Figure 3.10b Schematic diagram of the test section, induction wind tunnel.

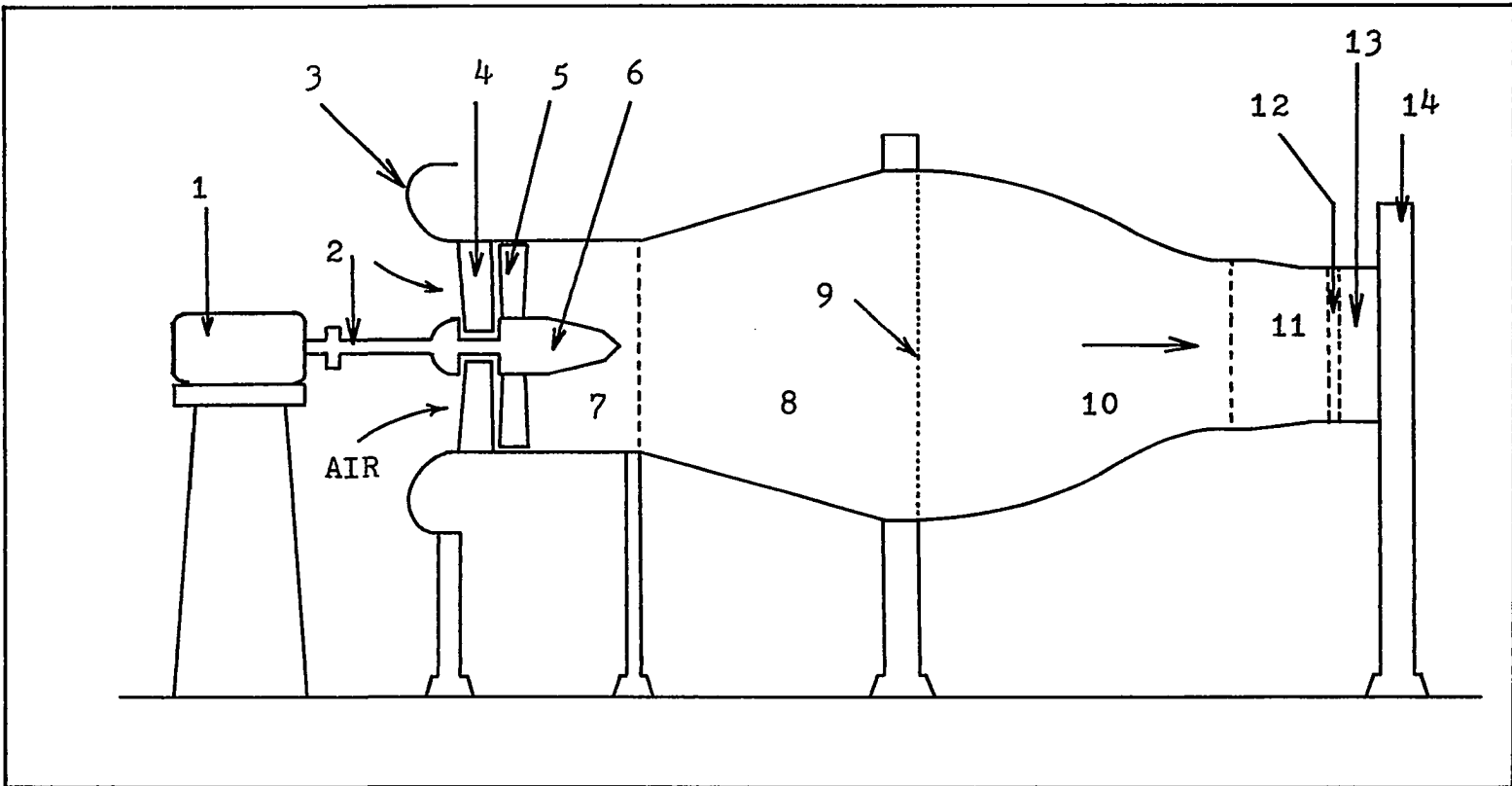


Figure 3.11a General features of the open end tunnel

- | | | |
|---------------------|------------------|--------------------|
| 1 motor | 2 circular shaft | 3 intake shape |
| 4 stator | 5 rotor | 6 straightener |
| 7 circular section | 8 conical shape | 9 honeycomb |
| 10 contraction | 11 transition | 12 soft connection |
| 13 parallel section | 14 frame | |

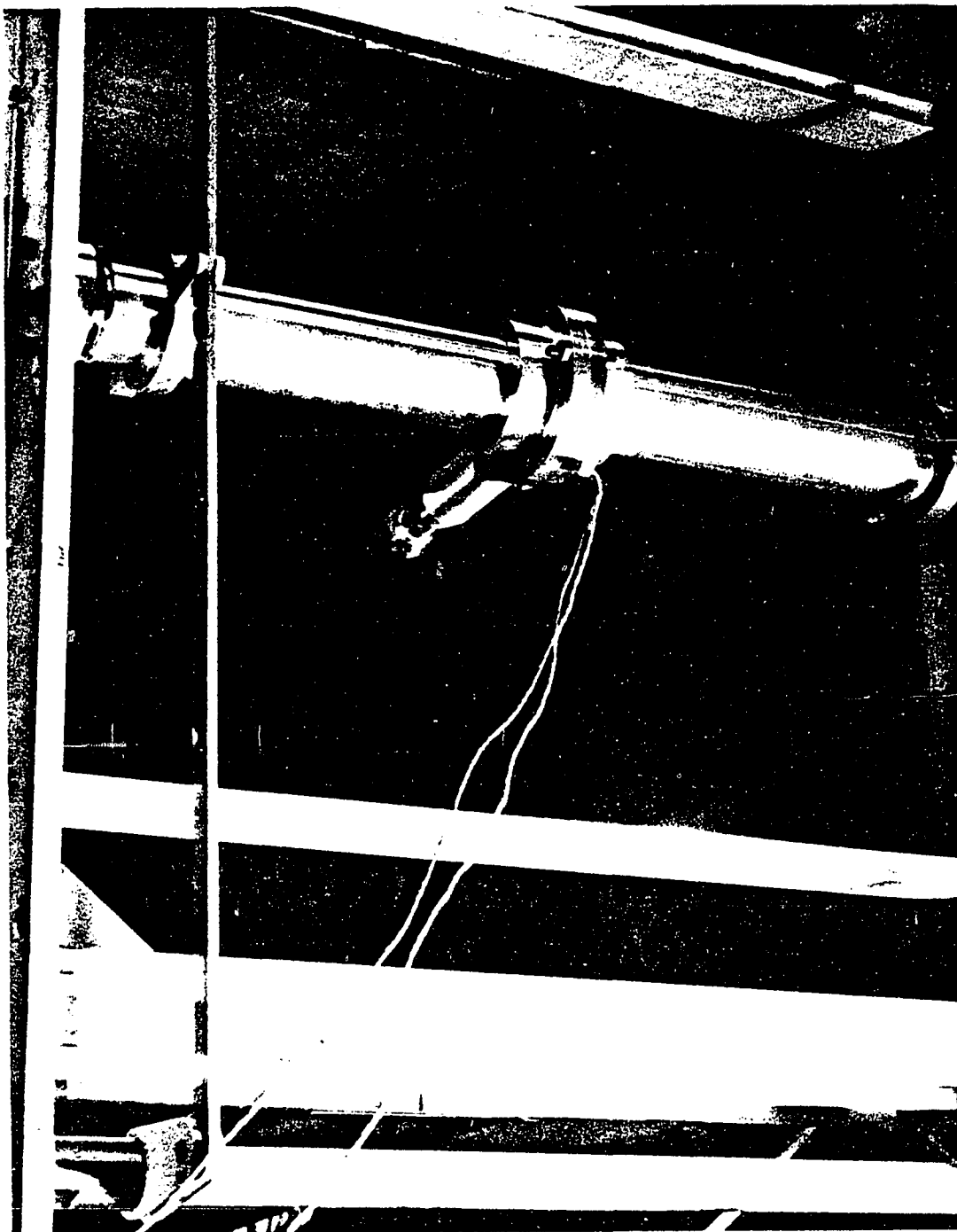


Figure 3.11b Photograph of the open end wind tunnel test section.

mounted across the side walls.

A steel frame was connected to the test section exit. This frame was furnished with (i) the oscillatory mechanism which is discussed in article 3.4; and (ii) a DC variable-speed motor which supplies the power to drive the oscillatory mechanism. This frame may be seen in figure (3.11b).

3.4 Drive Mechanism

The two kinds of drive mechanisms used to cause the oscillating motion of the spherical pressure probes will now be described.

3.4.1 Conventional Mechanism

The mechanism which produced the oscillatory motion of the probe consisted of a crank, connecting link, and a bar, as shown in figure (3.12). Rotation of the crank was provided by a variable speed electric motor. A pivot was located at crank radius r which fitted into the bearing at one end of the link while the other end connected to the bar. The bar was pivoted at a distance of R_0 from the link end. When the crank revolved, one end of the link followed a circle while the other end moved on a circular arc with a central angle 2α . Thus, while the crank revolved with a central angular speed ω , the bar oscillated with an angular speed changing with time. Since the crank radius r was variable by design, the amplitude of the probe oscillation could be arbitrarily

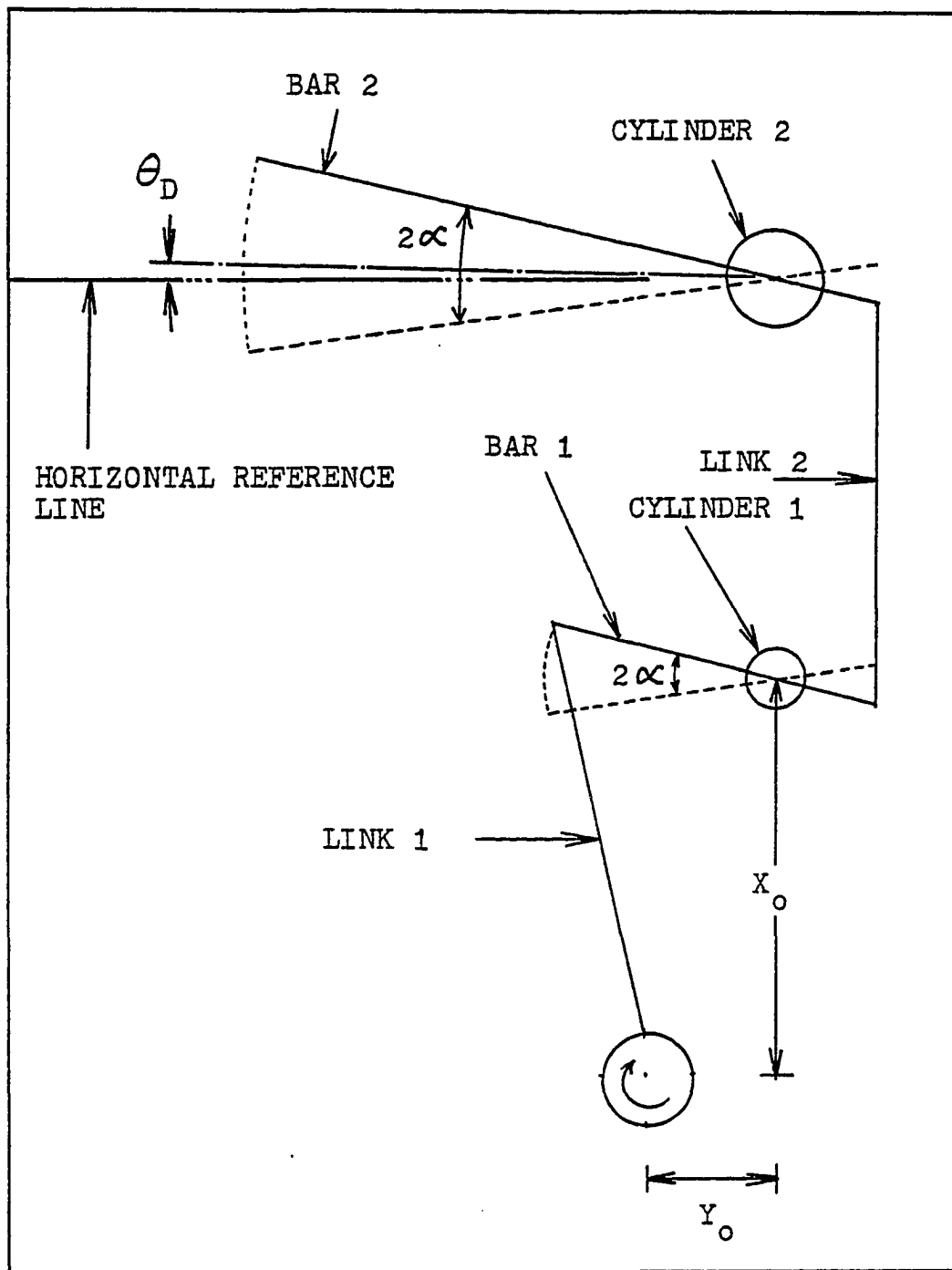


Figure 3.12a Schematic diagram of mechanism producing oscillating motion.

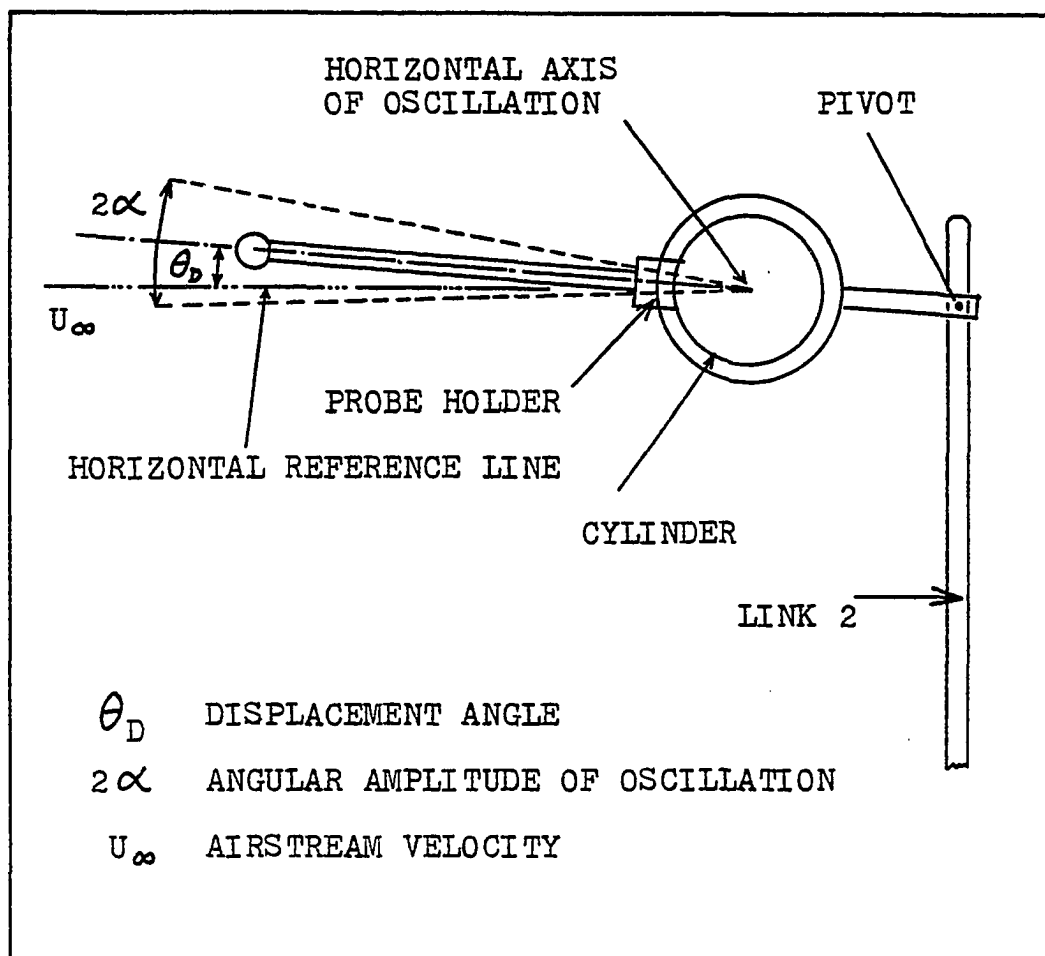


Figure 3.12b Test set-up for parallel flow of air, oscillating probe.

changed. The detailed description of this mechanism is discussed in Appendix E.

Although this mechanism gave oscillatory motion, it did not give purely sinusoidal oscillation. Hence, a second Scotch Yoke mechanism was constructed.

3.4.2 Scotch Yoke

In a Scotch Yoke mechanism, the circular motion of a pivot is transformed into a reciprocating motion. The pivot is inserted into an elongated slot cut into a crosshead provided with two parallel guides. As the pivot rotates the slot translates parallel to itself.

Because of the combined weight W of the steel plate and parallel steel rods of the actual mechanism, the resulting motion was not truly sinusoidal; i.e., the upward movement was slower than the downward movement. When the pivot moved upward, a portion of the force was balanced by the weight W , but when the pivot moved downward, the weight W also worked on the pivot. Hence, a pair of springs were used to create a balancing effect so that the effect of weight W could be balanced. Four specially designed ball bearing were used to minimize the friction between the bearings and the parallel rods. The general features of the Scotch Yoke arrangement are shown in figures (3.13a) and (3.13b); figure (3.13c) shows the comparison of oscillation motion for the Scotch Yoke with and without springs. Figure (3.14) compares the experimental motion with the true sine curve under a speci-

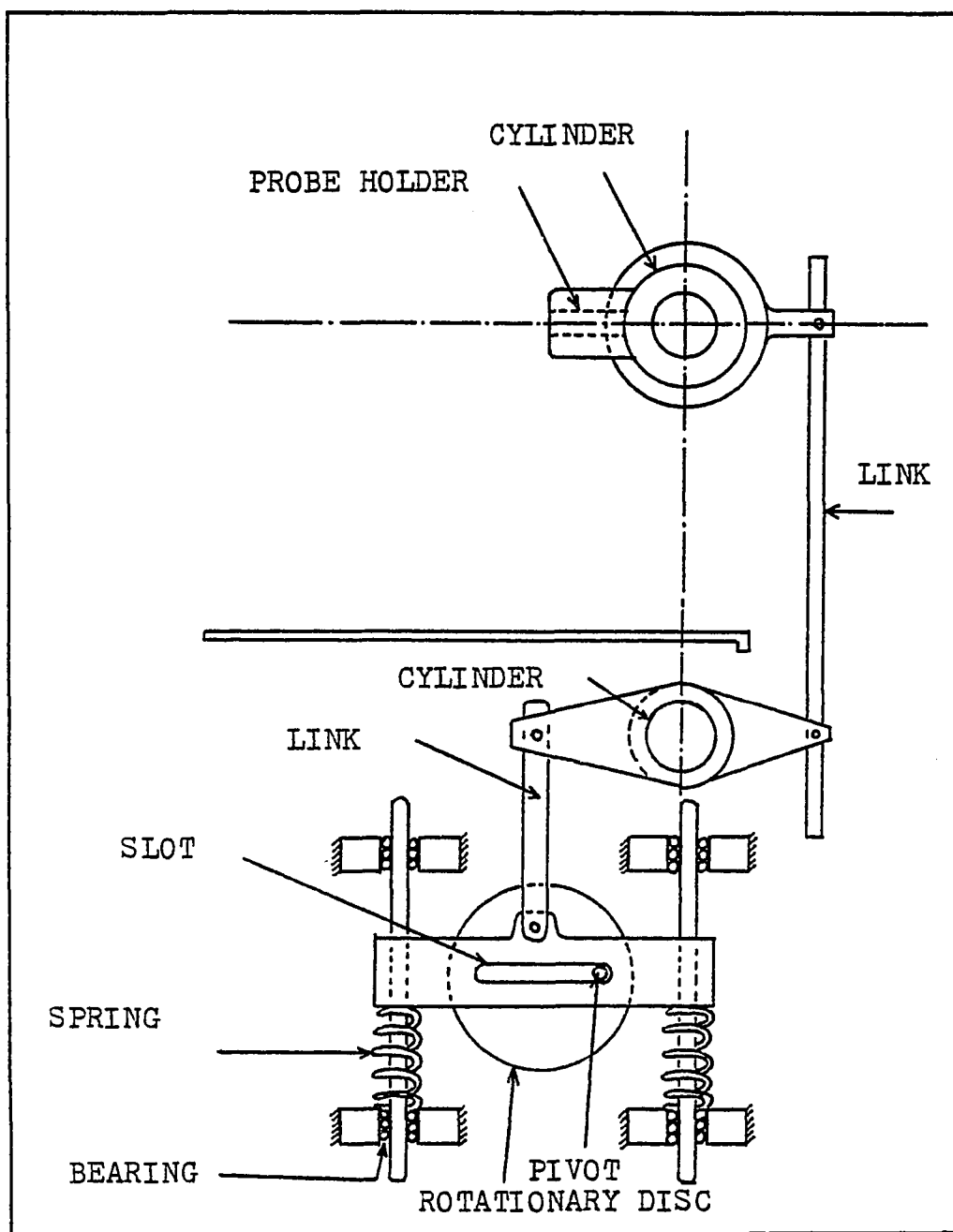


Figure 3.13a Schematic diagram of "Scotch Yoke".

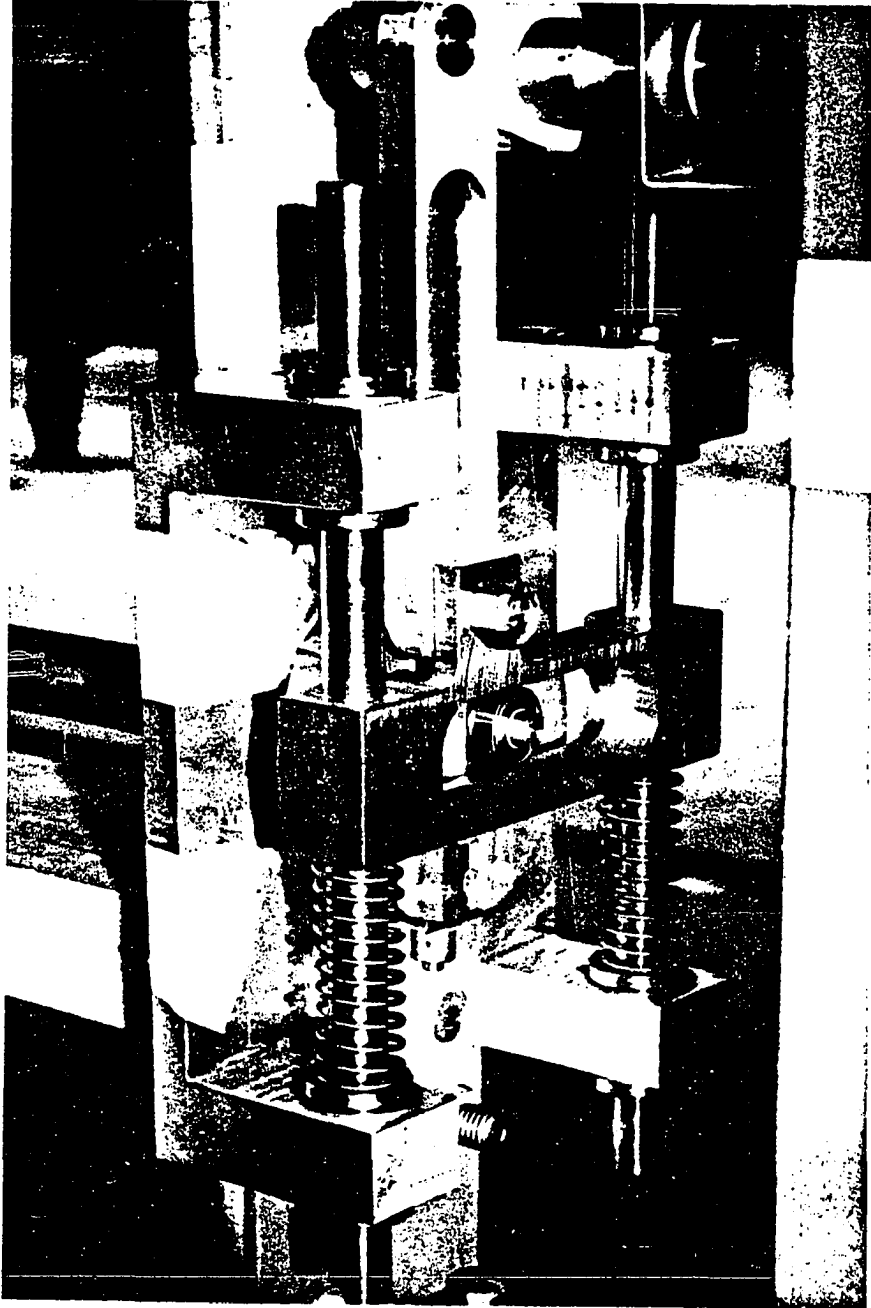


Figure 3.13b Photograph of Scotch Yoke mechanism.

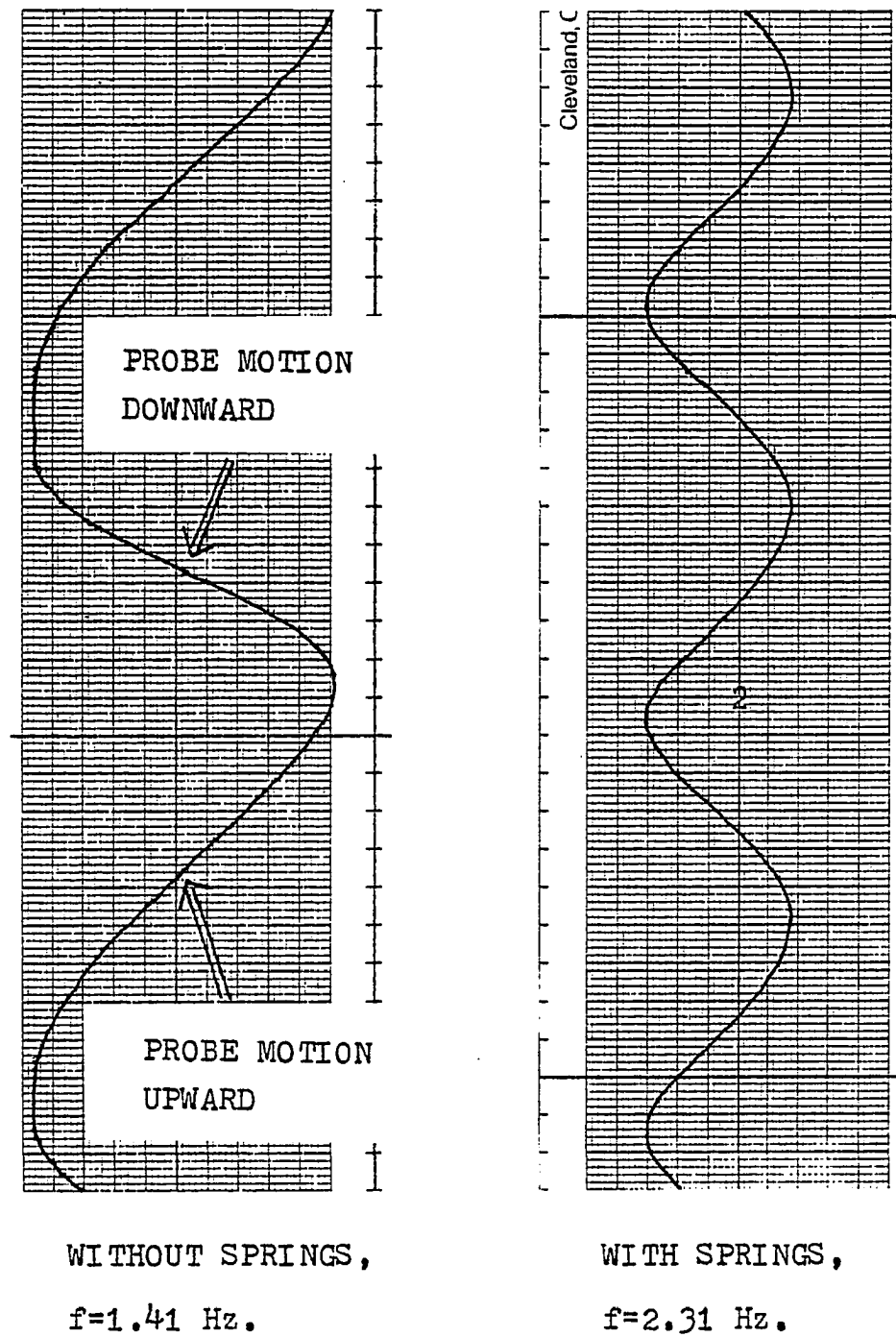


Figure 3.13c Comparison of oscillating motion for Scotch Yoke with and without springs.

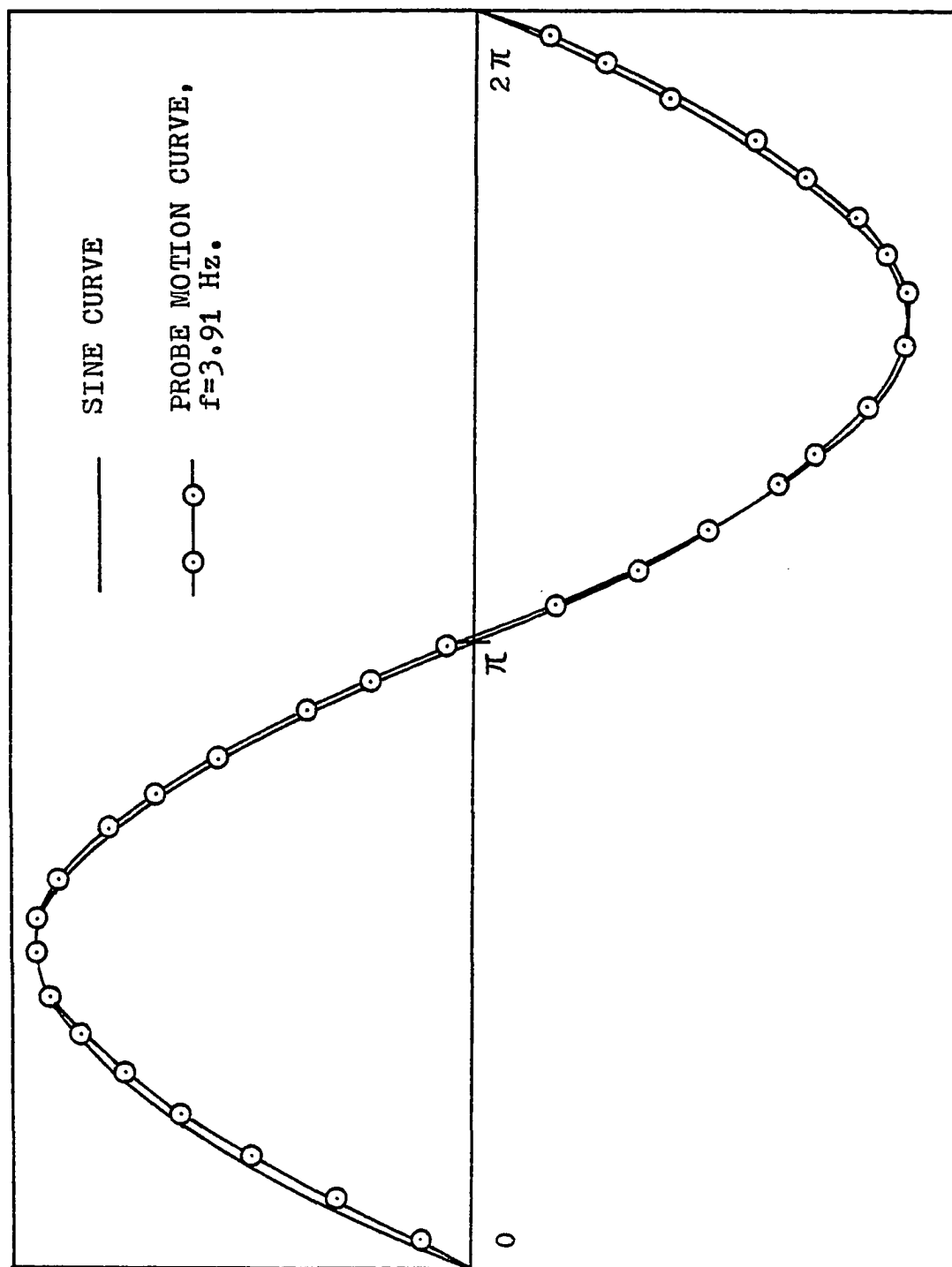


Figure 3.14 Comparison of probe oscillating motion curve with sine curve.

fied oscillating frequency of 3.91 Hz. It is seen that the two curves are quite close.

IV. TEST PROCEDURES AND RESULTS

Both static and dynamic test procedures and results are presented in this chapter.

4.1 Static Test on A Sphere

An isolated sphere was tested in the open end wind tunnel test section to determine the static pressure distribution around the front portion of the sphere. Figure (4.1) shows the non-dimensional static pressure distribution around the sphere for angle θ up to 70 degrees, where data for Reynolds numbers of 4.24 and 1.57×10^5 were taken from experiments done on a 0.153 m sphere from Ref. 2, while current data for $R_e = 1.39 \times 10^5$ were test results for a 0.0635 m sphere performed at 0.D.U. The solid line represents the potential flow theory for a sphere which gives the static pressure distribution over the sphere as

$$P - P_{\infty} = \frac{1}{2} \rho U_{\infty}^2 \left(1 - \frac{9}{4} \sin^2 \theta \right) \quad (4.1-1)$$

where θ denotes the angle from the forward stagnation point.

In order to investigate the effect of the cylinder attached to the rear portion of the sphere, an experiment was per-

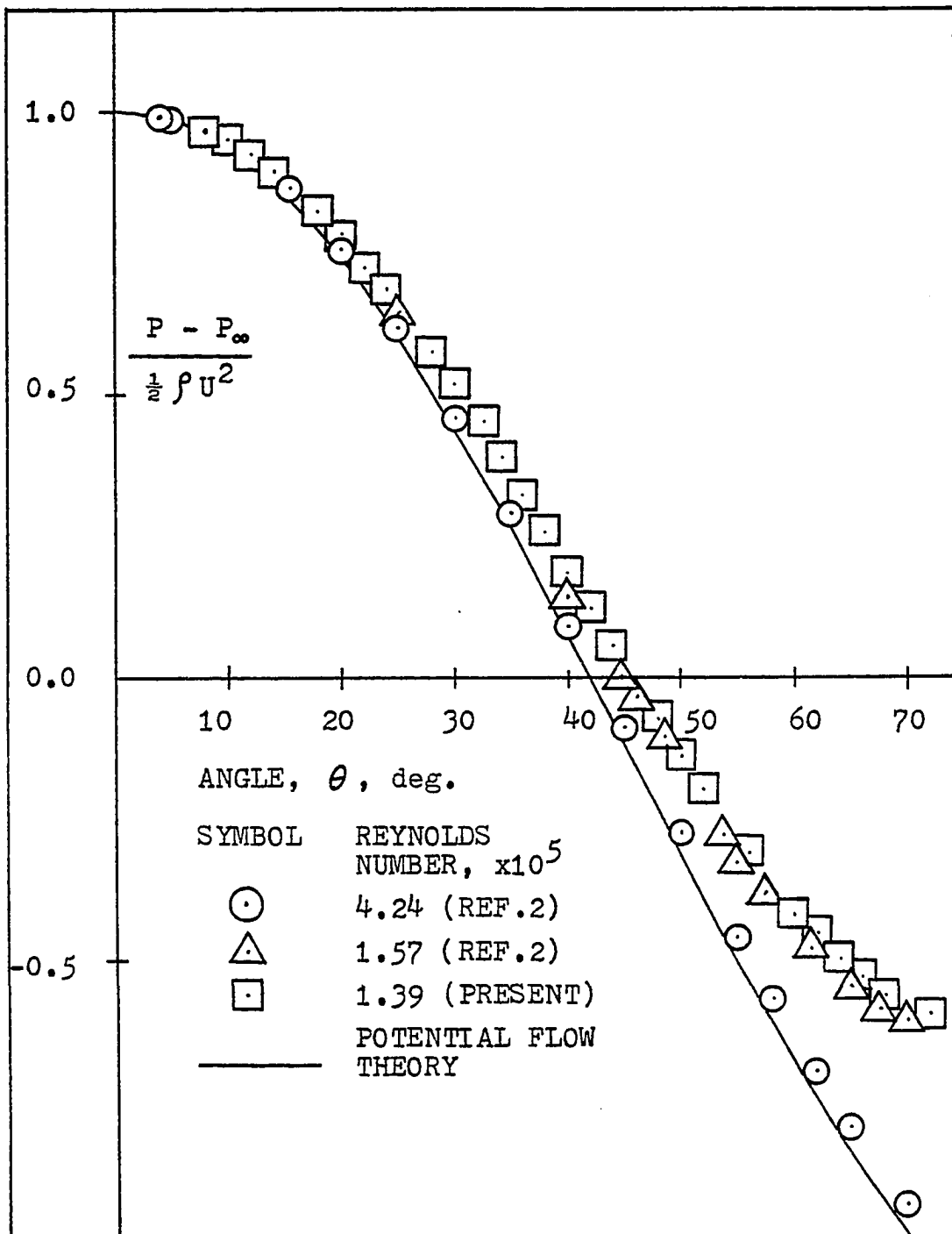


Figure 4.1 Pressure distribution around a sphere.

formed in which a 0.0445 m diameter, 0.152 m long cylinder was tailfitted onto the rear portion of the sphere and the static pressures were measured for θ from -80 to +80 degree. The experimental results for two cases, a sphere and a sphere with cylinder tailfitted, are shown in figure (4.2). For a more detailed discussion refer to Appendix F, but it is noted that the cylinder has a considerable effect upon the pressure distribution.

4.2 Static Test

The probe was rigidly supported in the wind tunnel test section, and its response automatically recorded through a two channel BRUSH220 recorder. The general features of the static test set-up are shown in figure (4.3). The probe was mounted in the test section facing the airstream and rotated until the pressure difference between ports 2 and 3 was zero. The probe was then judged to be at zero angle of attack. Then the probe was rotated to form an angle θ and data was taken for the angle range under consideration. The static test procedures are shown in figure (4.4).

Sample results of static tests are shown in figures (4.5) and (4.6). In figure (4.5), the pressure differentials non-dimensionalized by $(1/2)\rho U_\infty^2$ were plotted against probe angle. Probe angle is the same as angle of attack under static test conditions. In figure (4.6), the pressure difference ratios, R , were plotted against probe angle θ for

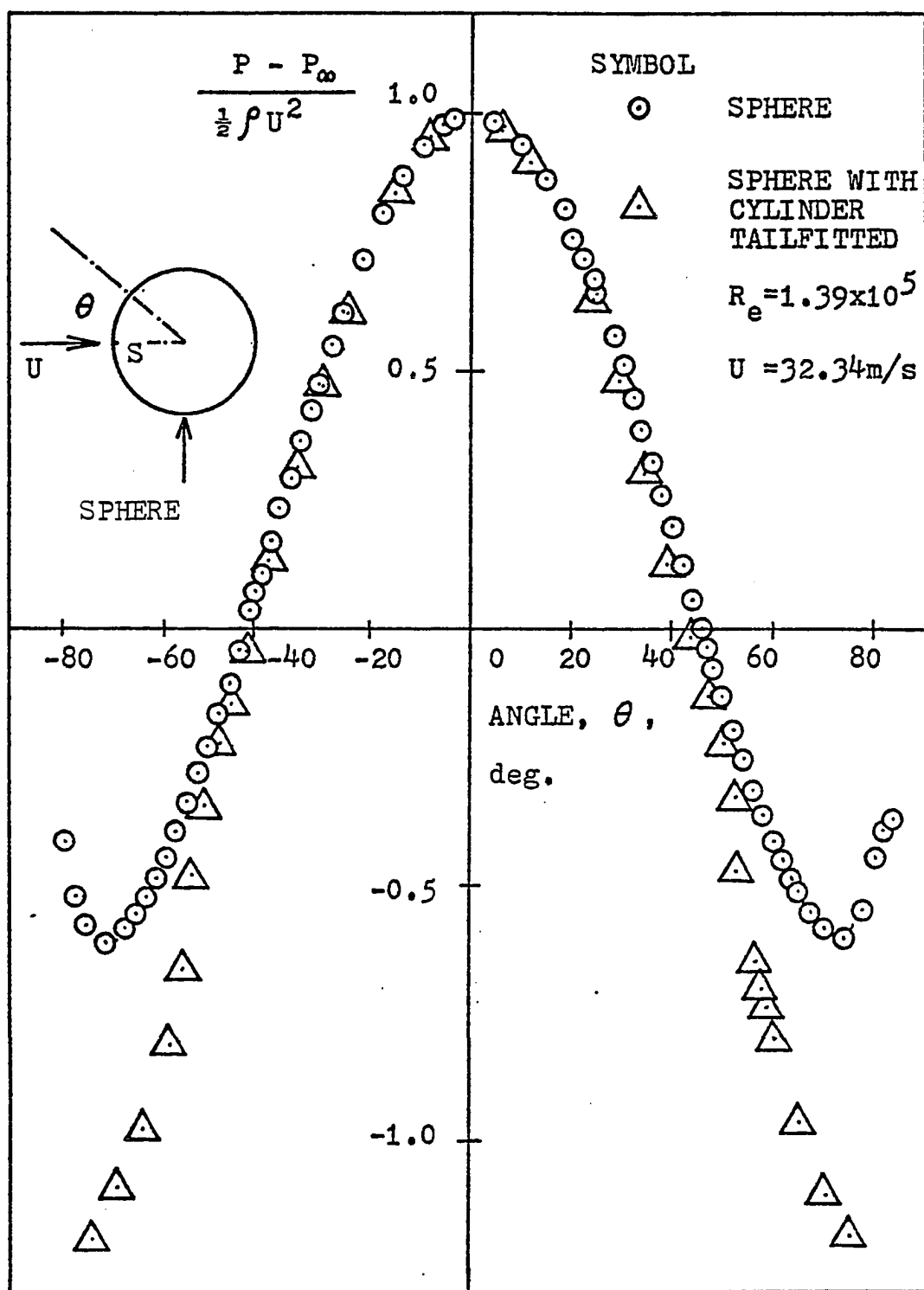


Figure 4.2 Pressure distribution around a sphere with and without cylinder tailfitted.

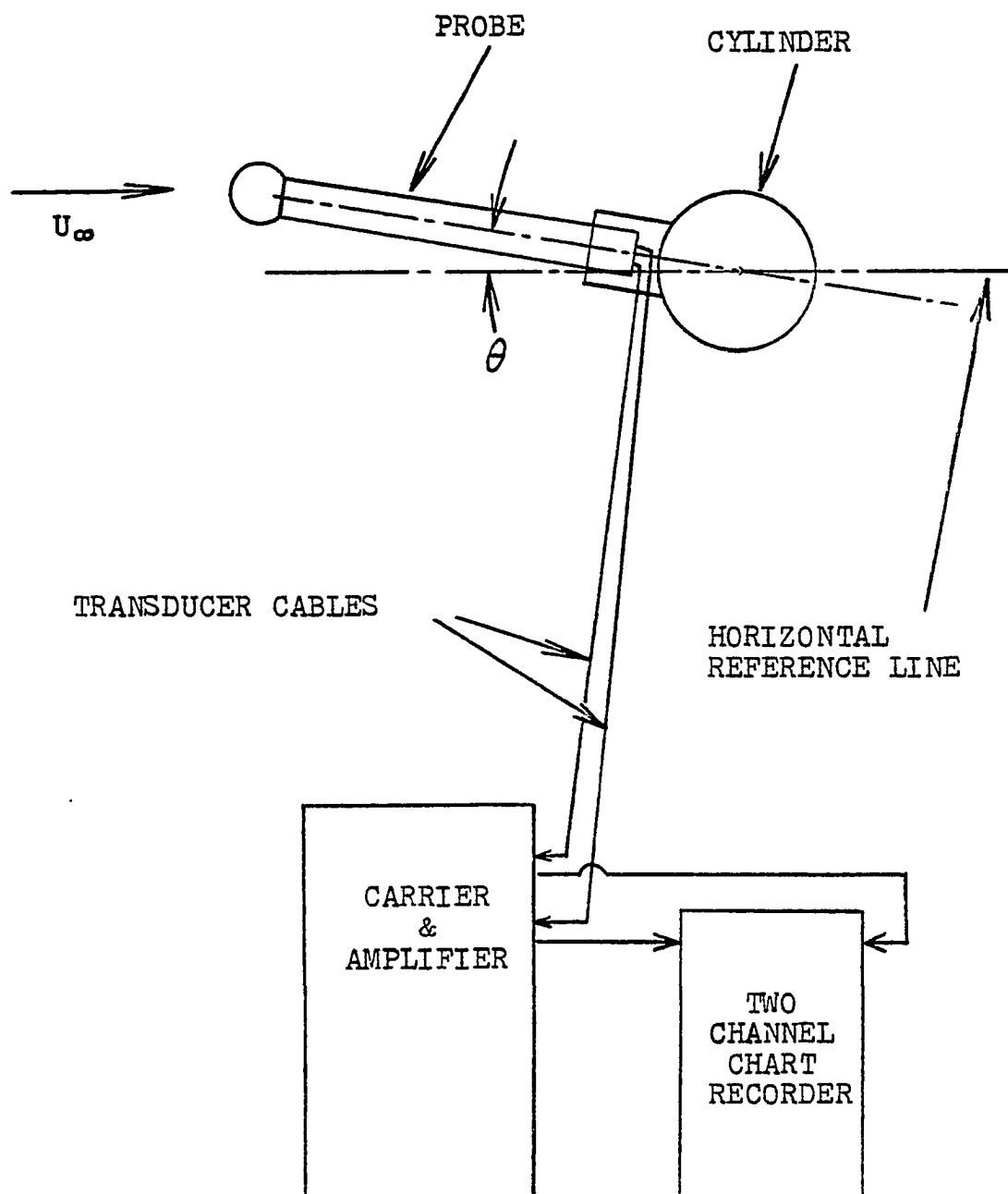


Figure 4.3 Schematic sketch of static test set-up

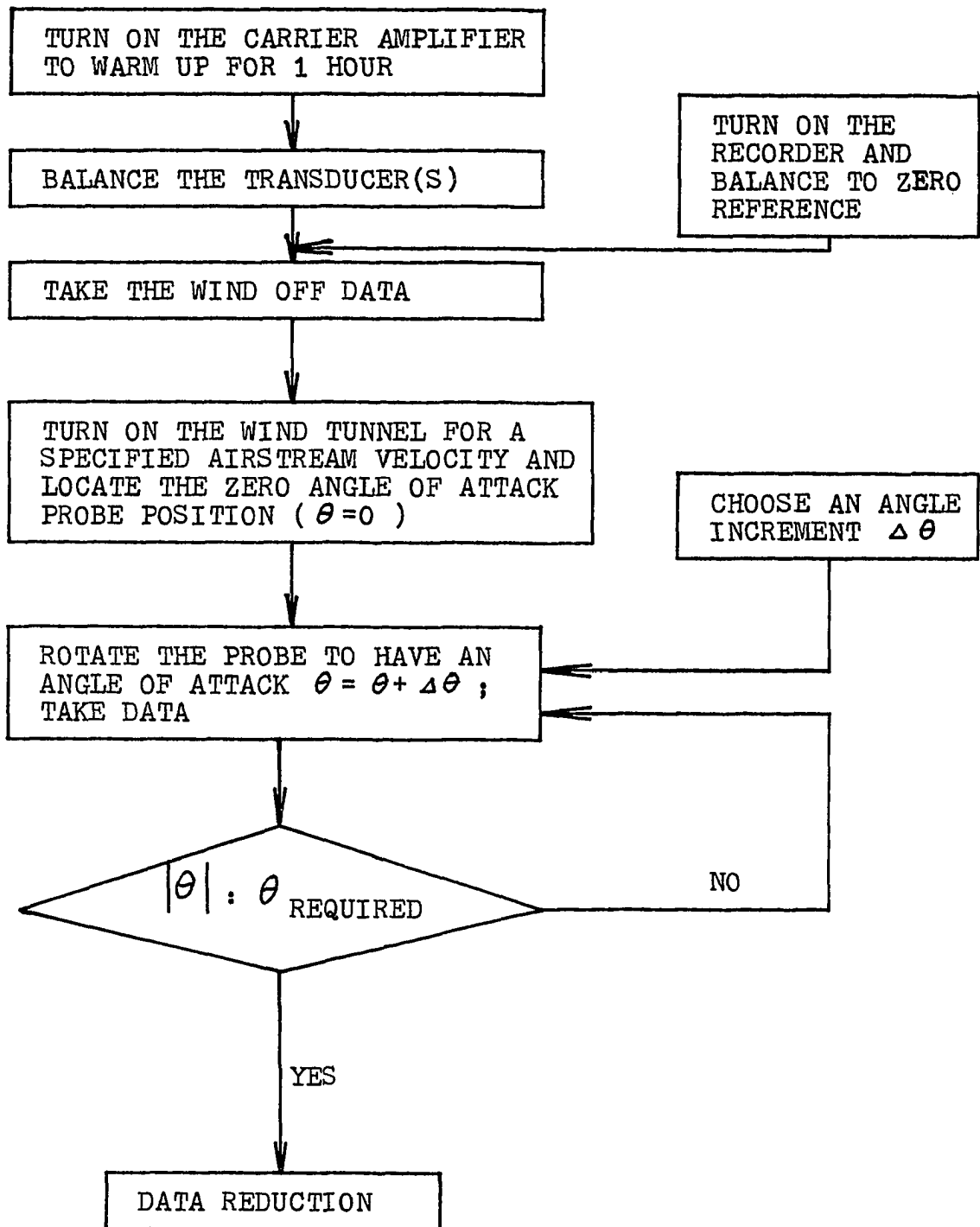
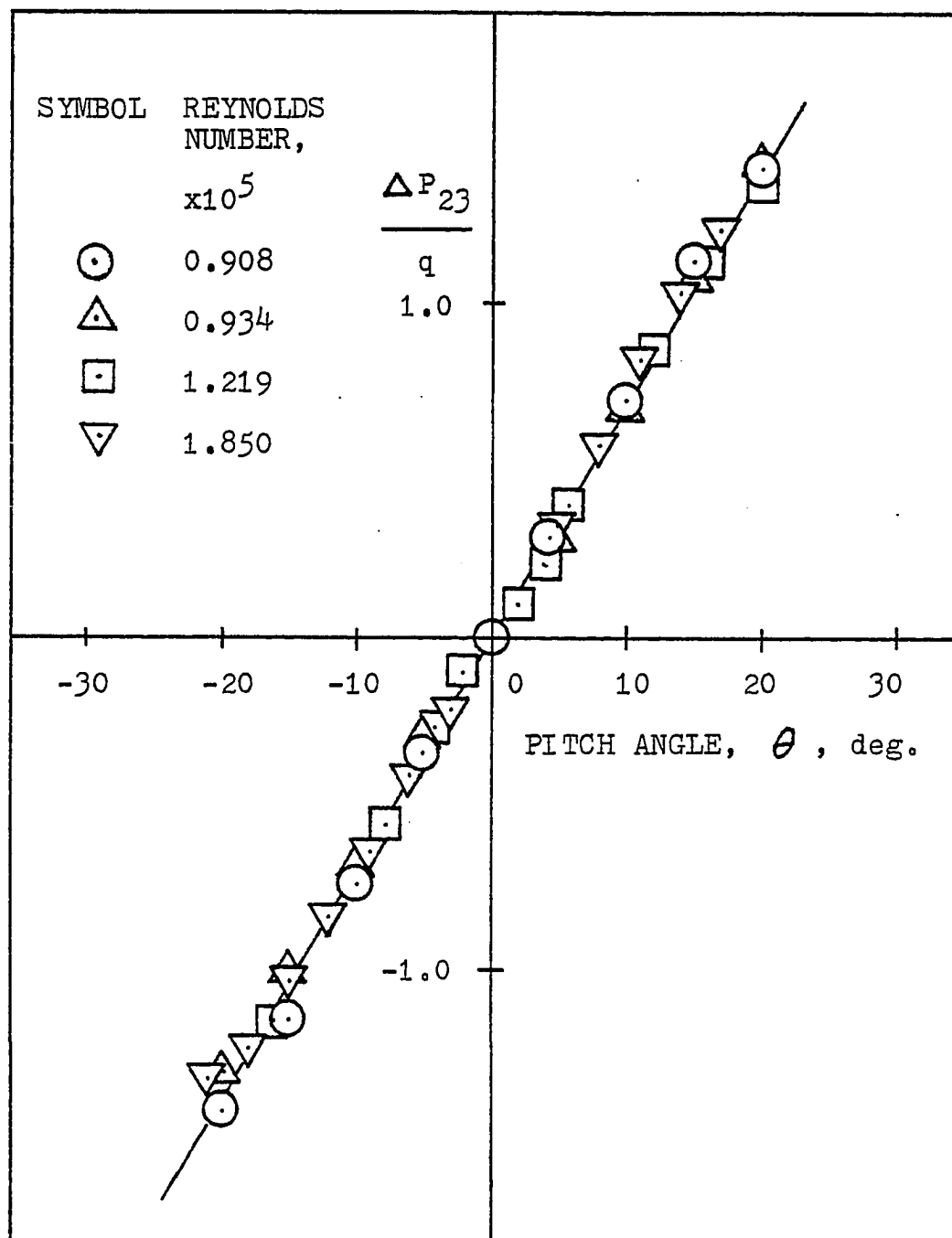
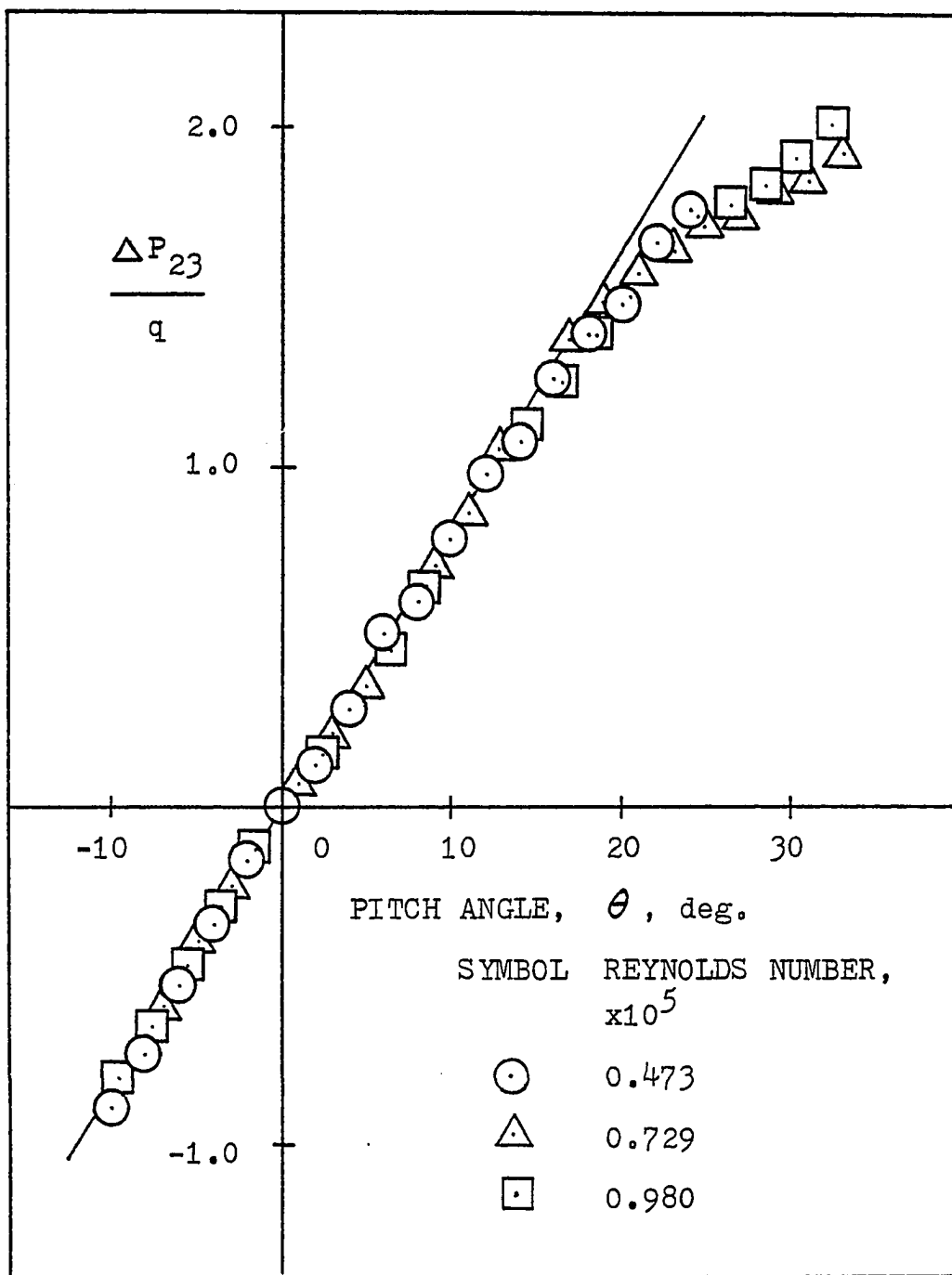


Figure 4.4 Static test procedures



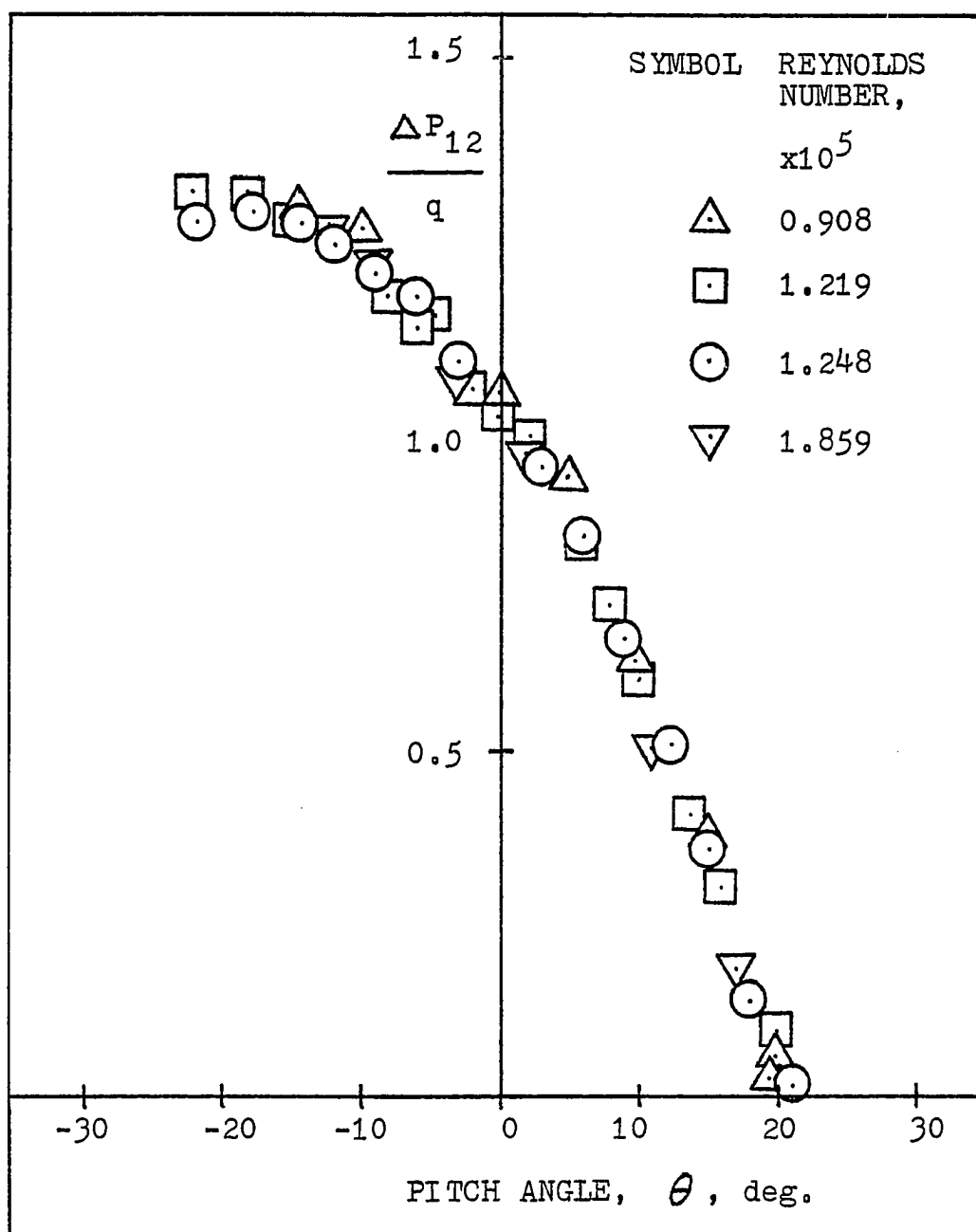
(a) PROBE ODU2, $\Delta P_{23}/q$ versus θ .

Figure 4.5 Variation of non-dimensional pressure differential with angle quantity



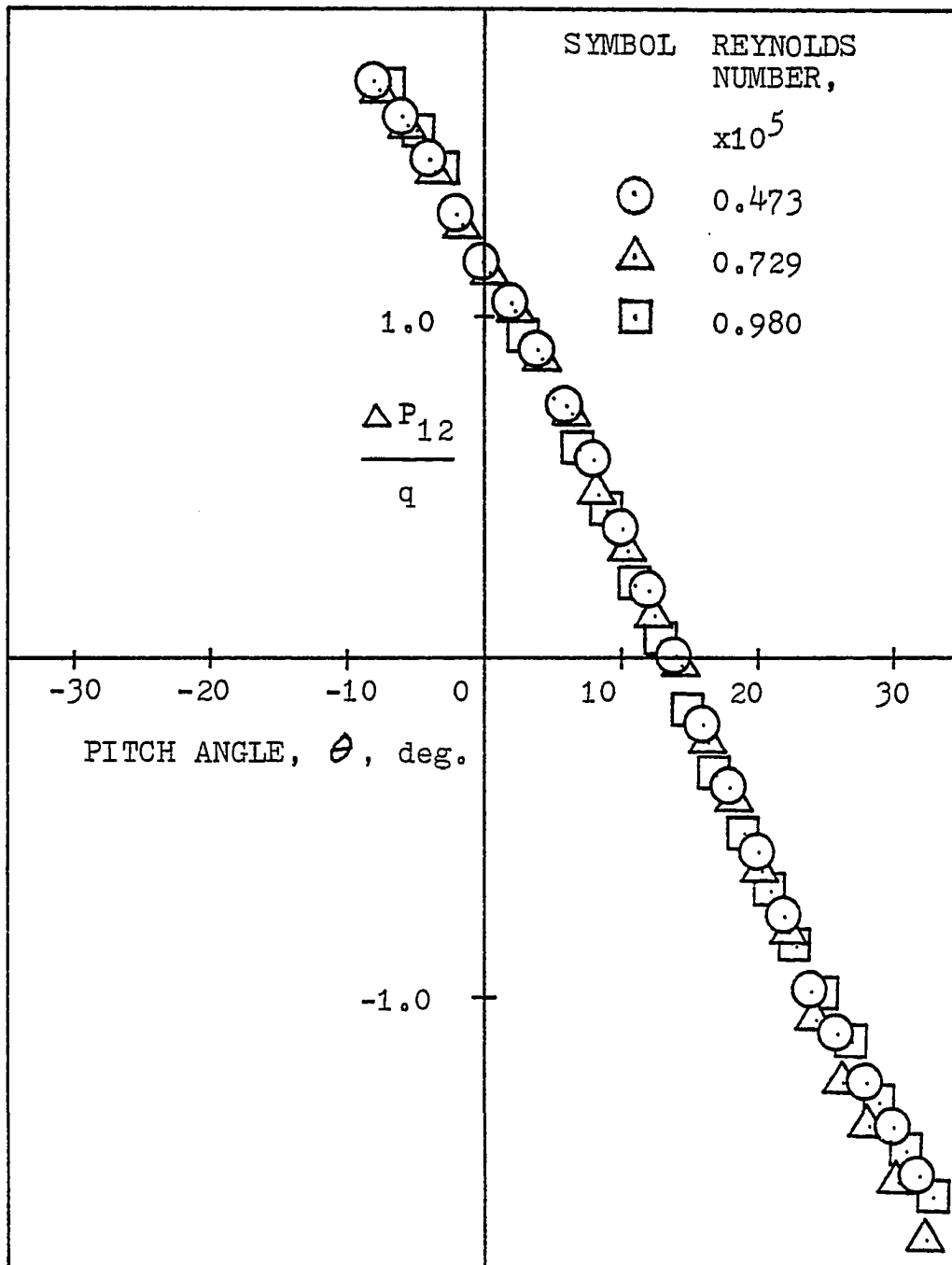
(b) PROBE NASA60, $\Delta P_{23}/q$ versus θ .

Figure 4.5 Continued



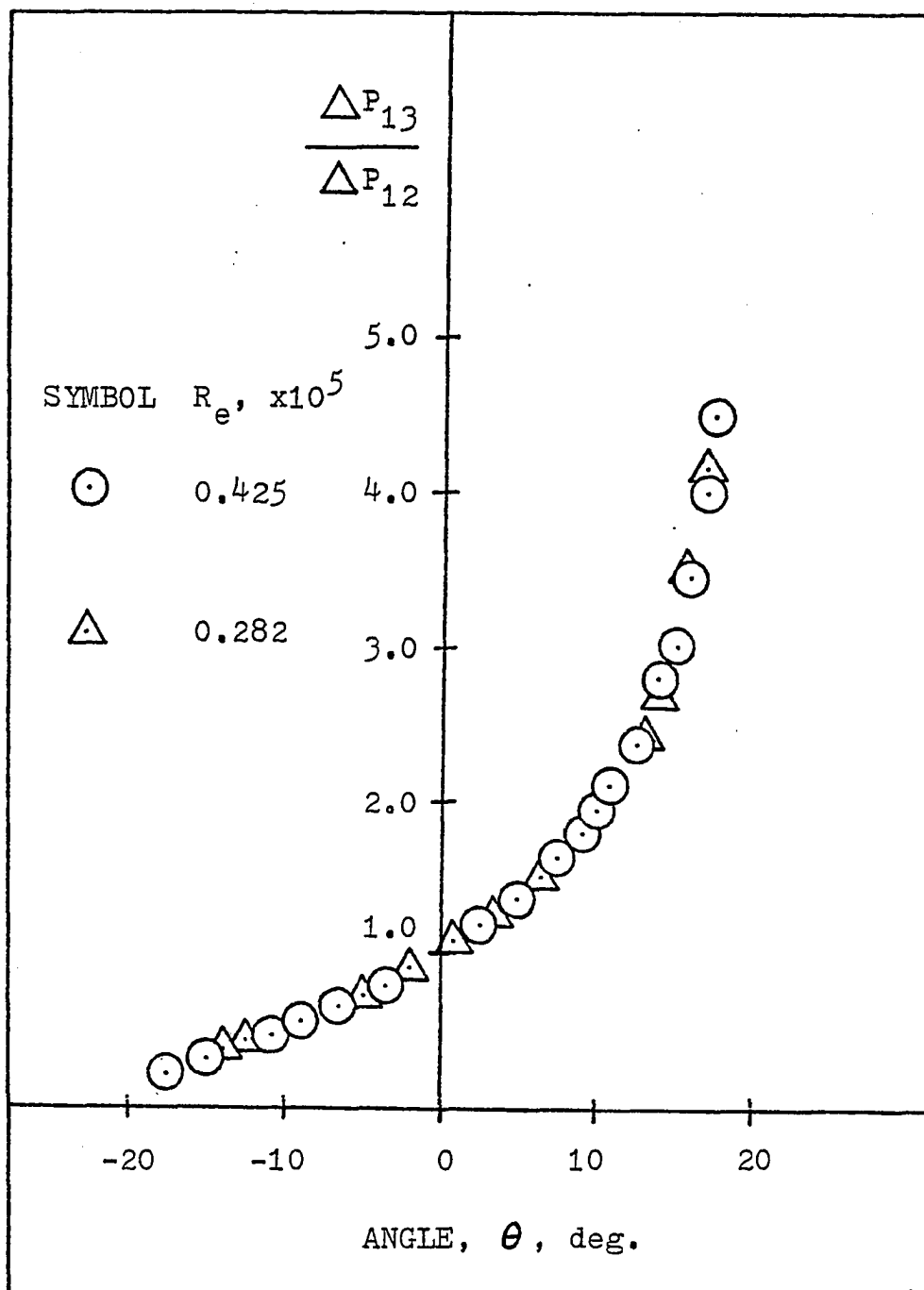
(c) PROBE ODU2, $\Delta P_{12}/q$ versus θ .

Figure 4.5 Continued



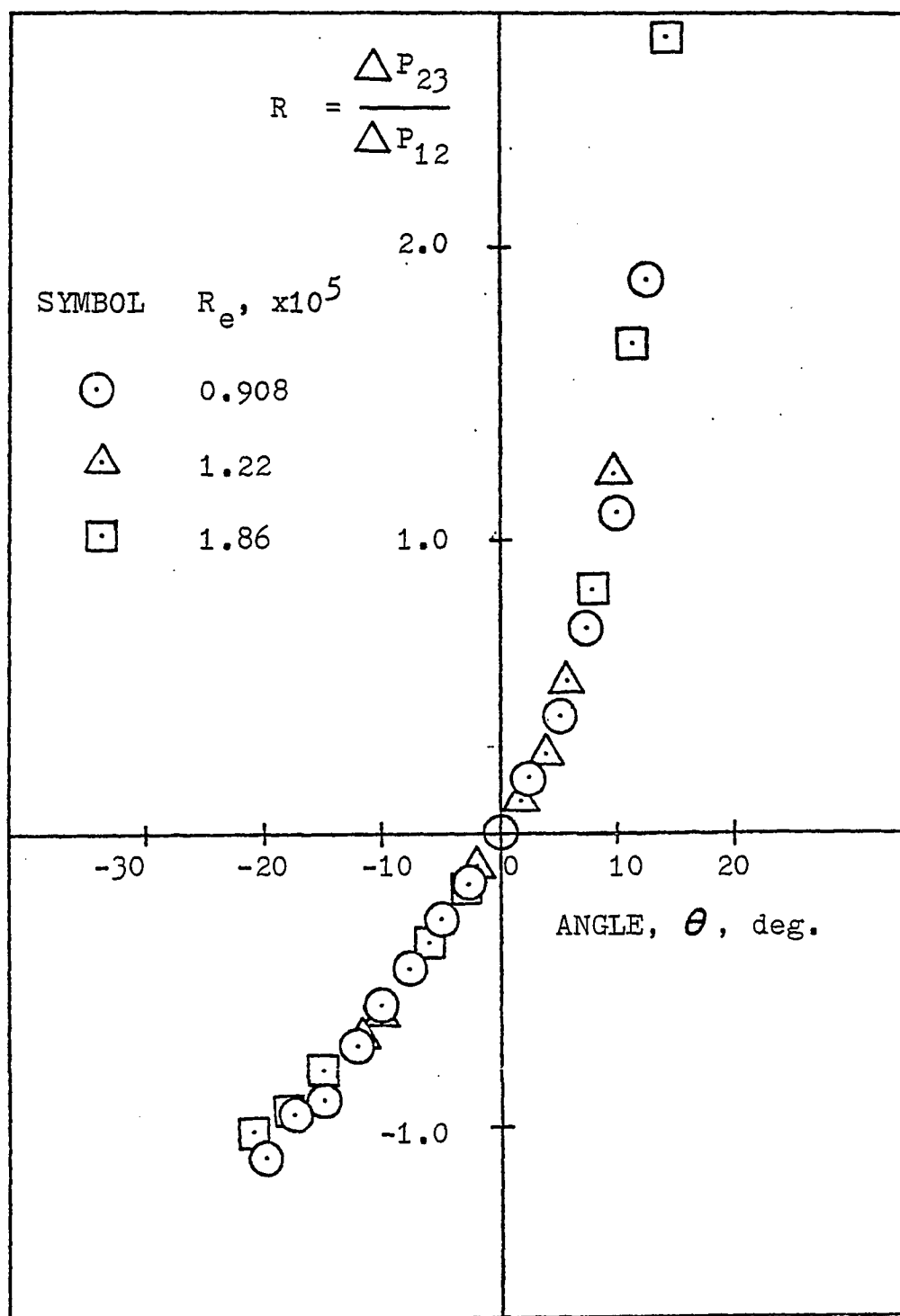
(d) PROBE NASA60, $\Delta P_{12}/q$ versus θ .

Figure 4.5 Concluded



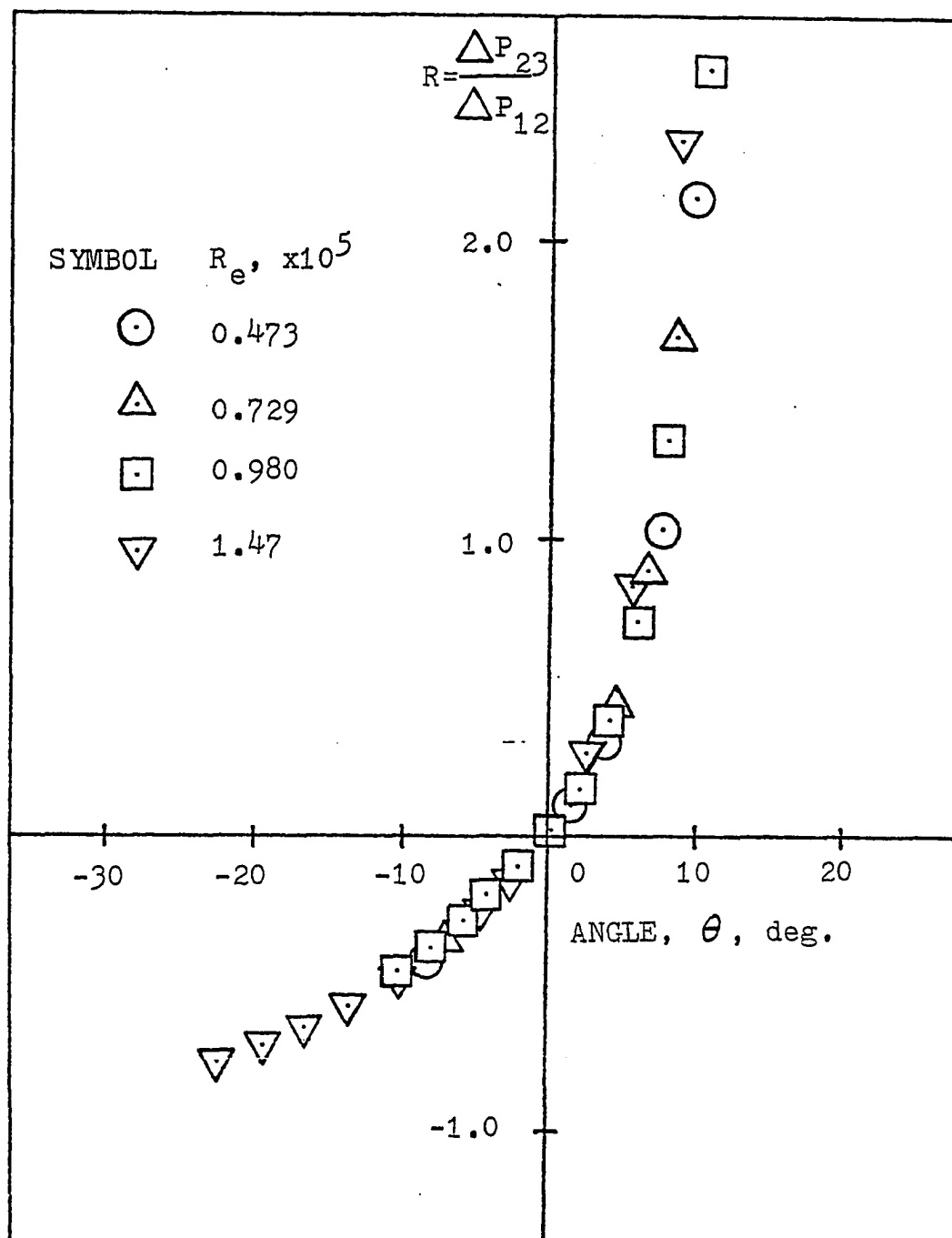
(a) PROBE ODU1

Figure 4.6 Variation of pressure differential ratio with probe angle



(b) PROBE ODU2

Figure 4.6 Continued



(c) PROBE NASA60

Figure 4.6 Concluded

probes ODU1, ODU2 and NASA60. These test results will be analyzed and discussed in Chapter V.

4.3 Oscillating Probe Test Procedures

The transducers inside the probe were balanced and the probe was fitted into the probe holder located on the rotational cylinder. Subsequently the upward maximum and the downward maximum angles, i.e., θ_U and θ_L , were measured by a clinometer with an accuracy of ± 0.1 degree. The wind off reference datum lines were taken using the chart recorder. After having chosen a specific oscillatory frequency, f , as well as a reference airstream velocity, U_∞ , the fan was turned on and adjusted.

The probe response was automatically recorded through the two-channel chart recorder. Channel 1 was used to record the pressure differential $\Delta P_{23} = P_2 - P_3$ or $\Delta P_{12} = P_1 - P_2$; channel 2 was utilized for recording the probe angle variation through use of a potentiometer. The variables for this dynamic test were airstream velocity, U_∞ , oscillating frequency, f , and the oscillating probe position angle, θ . By keeping two variables out of three (U_∞ , f , θ) constant, a series of experiments were conducted, varying the third variable. The results were reduced into plots of $\Delta P/q$ versus θ , to analyze the unsteady effects. The experimental procedures for dynamic tests are outlined in figure (4.7) and the data reduction procedures are outlined in

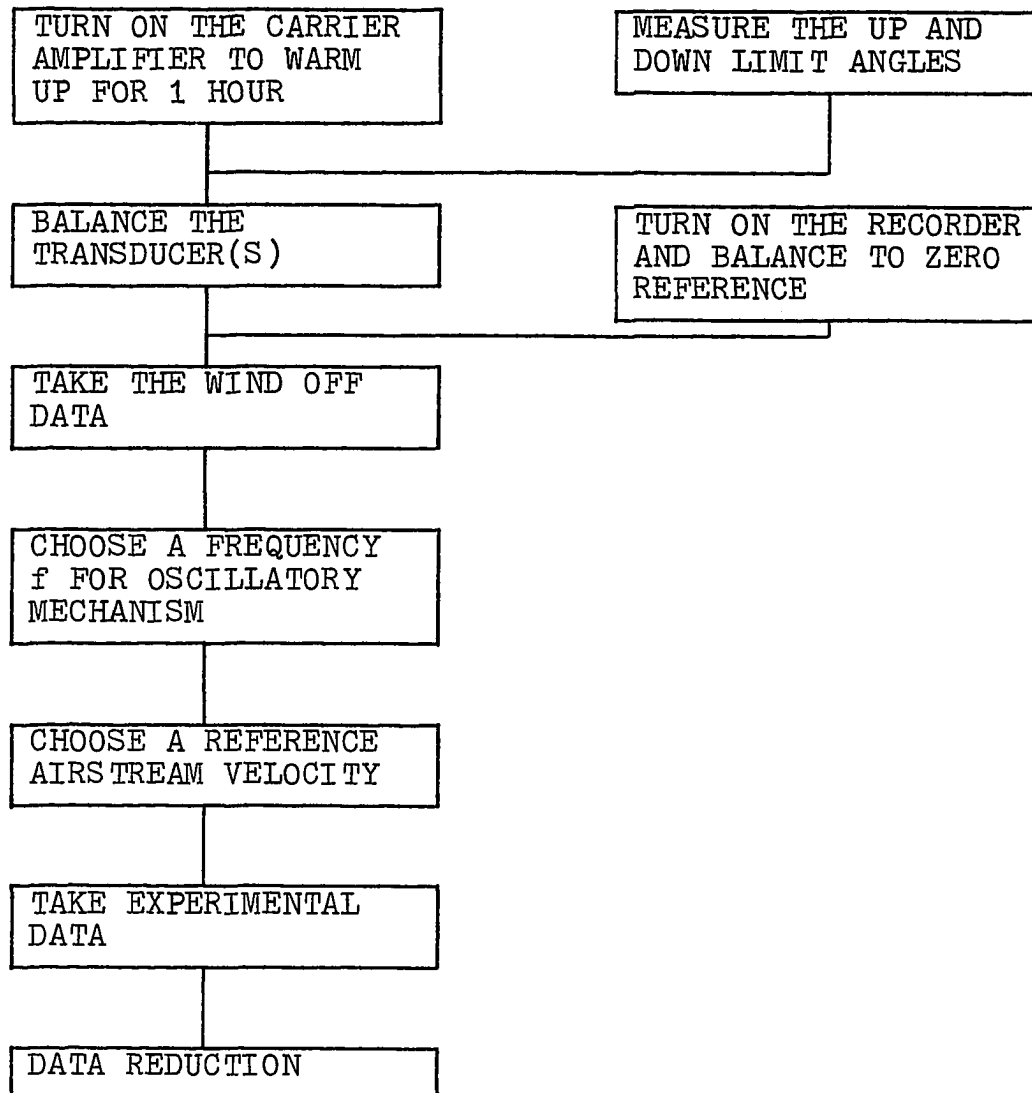


Figure 4.7 Experimental procedures for dynamic test

figure (4.8). Typical stripchart outputs for probe ODU2 are shown in figure (4.9).

4.4 Oscillating Probe Test Results

For different ranges of oscillating probe angles, oscillating frequencies, and airstream velocities, a series of data were obtained using probe ODU2 and plotted as $\Delta P/q$ versus θ . Figure (4.10) shows some representative non-dimensional pressure differential versus probe angle plots. The rest of these results are shown in Appendix G. Figure (4.11) shows the variation of pressure differential ratio R , defined as $\Delta P_{23}/\Delta P_{12}$, with probe angle θ under different probe operating conditions. These dynamic results will be compared with theoretical predictions in Chapter V.

4.5 Time Lag Phenomenon

A time lag phenomenon was observed from the stripchart outputs, such as those shown in figure (4.9). The potentiometer response curves which represented the variation of the probe position angle were not in phase with the pressure differential output curves. For airstream velocity $U=30.5$ m/s (100 ft/sec), the time lag varied with oscillating frequency, f , as shown in figure (4.12).

For example, see figure (4.13), for probe ODU2 under the conditions $U=30.5$ m/s, $f=3.88$ Hz, where probe position angle

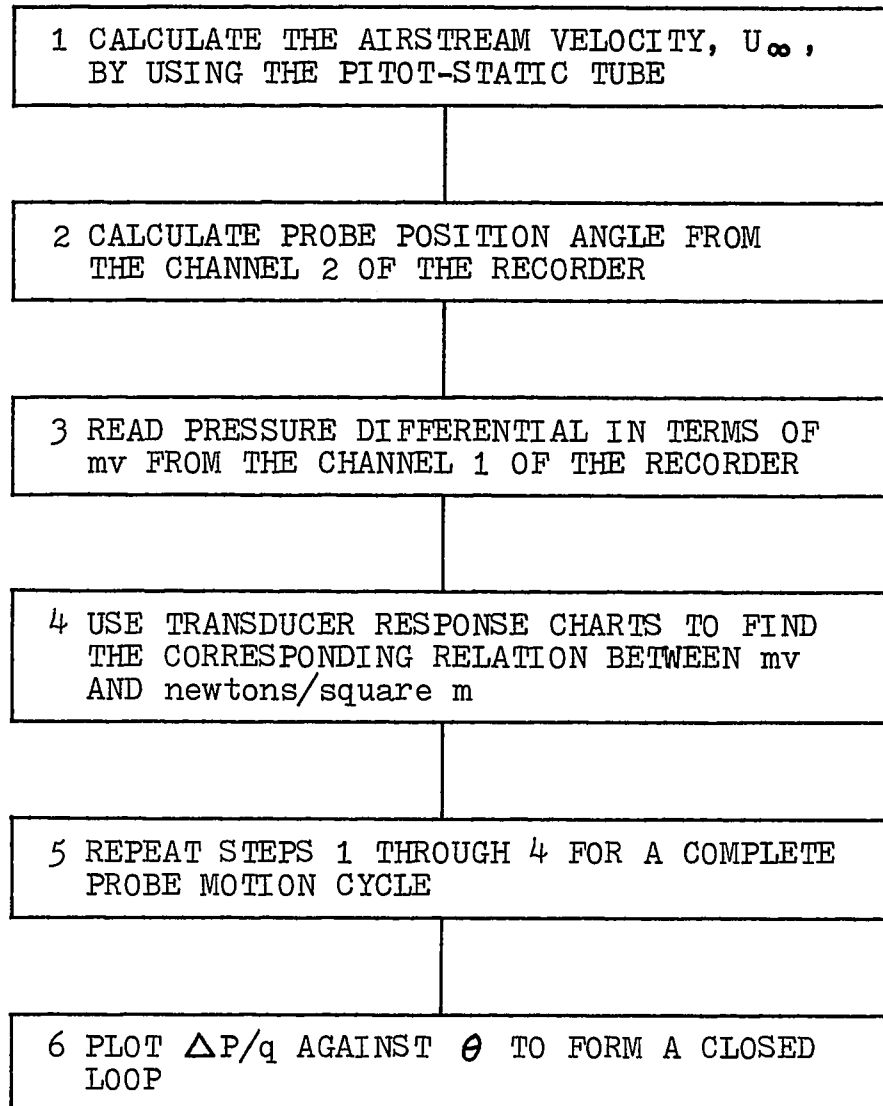
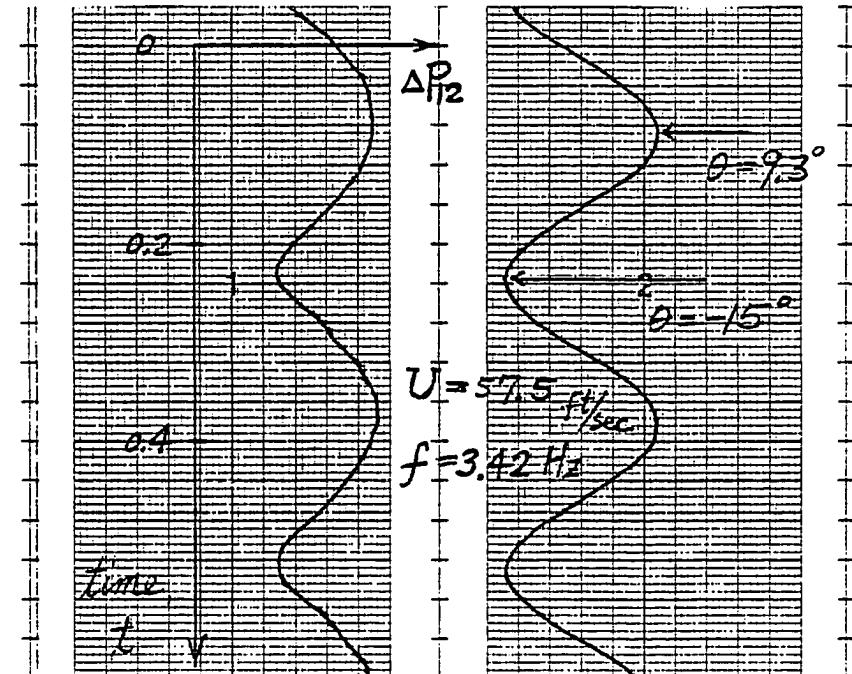
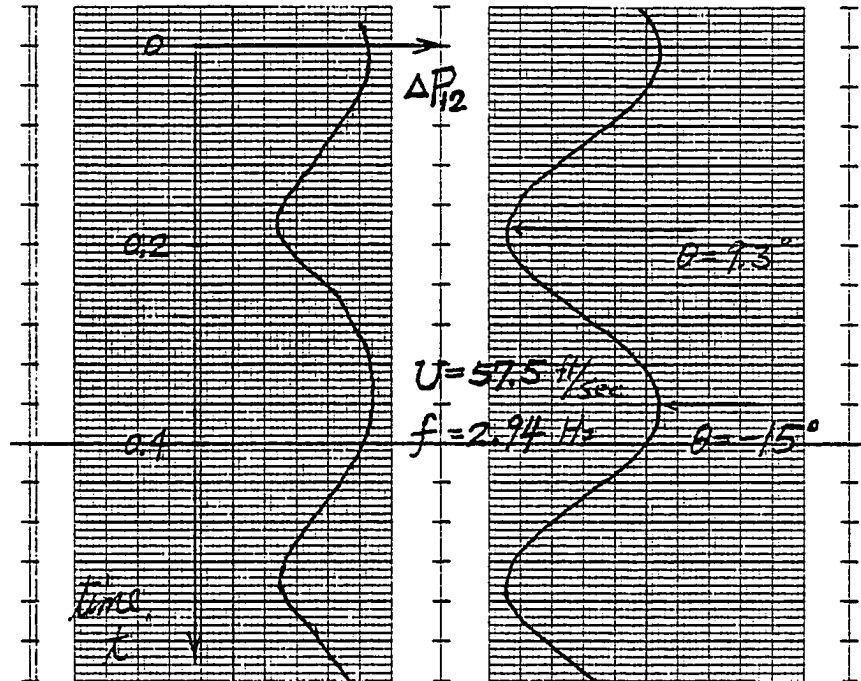
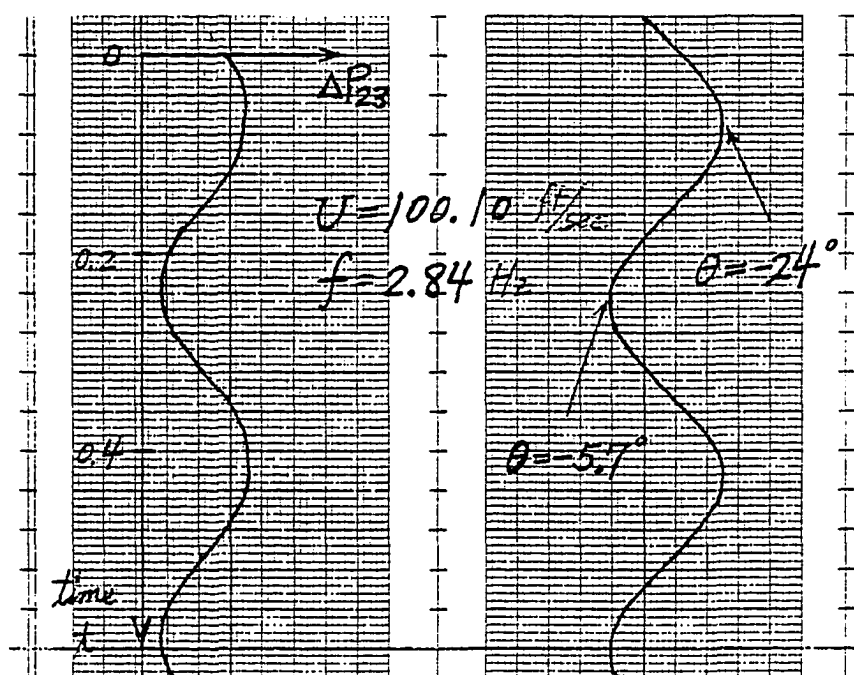
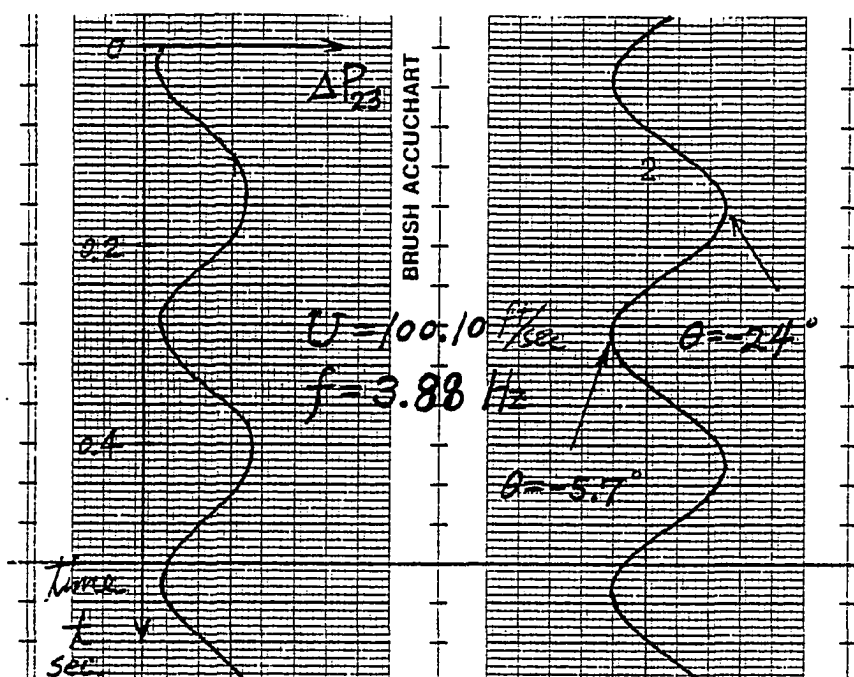


Figure 4.8 Data reduction procedures



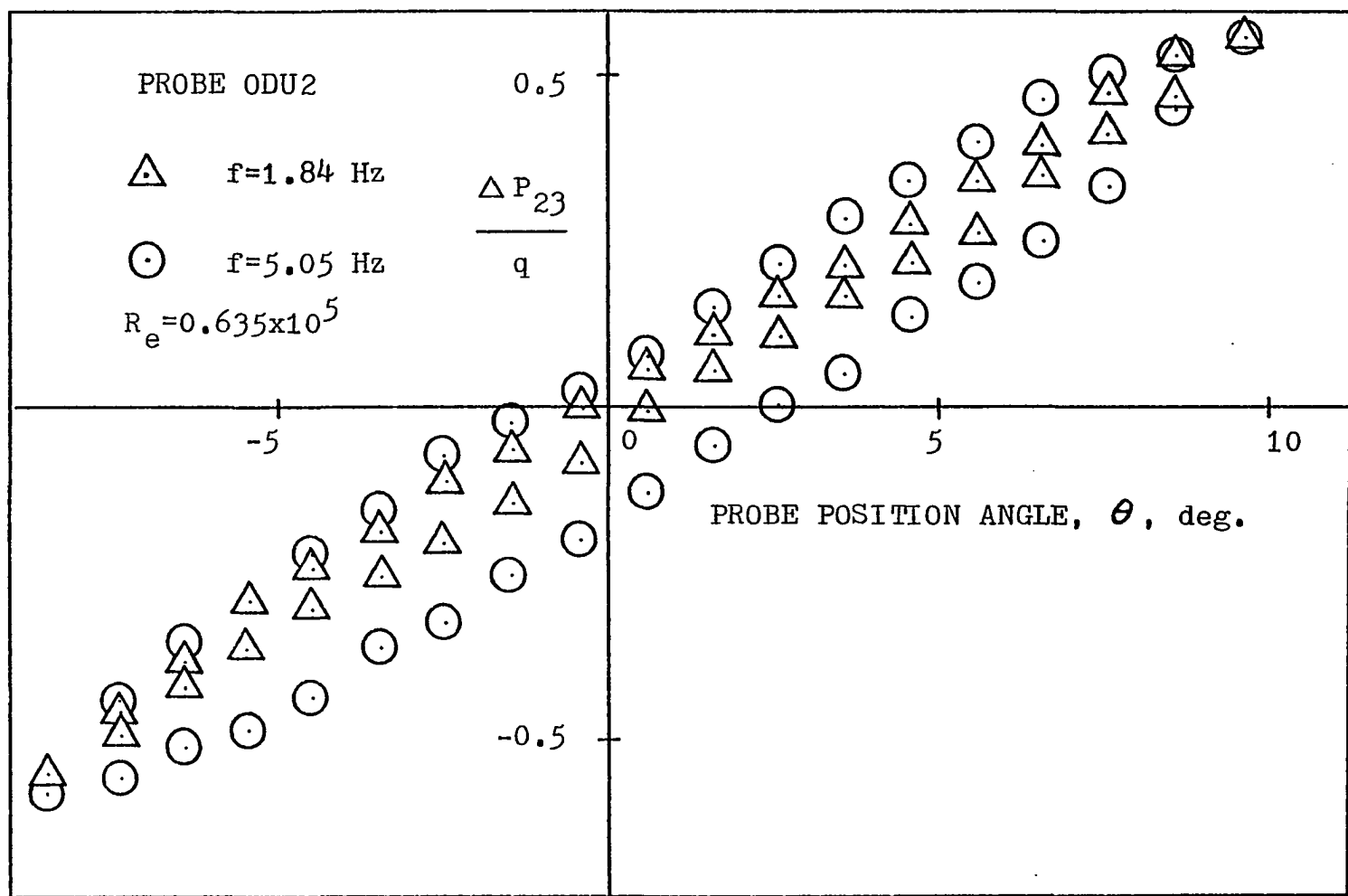
(a) STRIPCHART OUTPUTS FOR ΔP_{12}

Figure 4.9 Stripchart outputs for probe ODU2



(b) STRIPCHART OUTPUTS FOR ΔP_{23}

Figure 4.9 Concluded



(a) $\Delta P_{23}/q$ versus θ

Figure 4.10 Variation of non-dimensional pressure differential with probe position angle

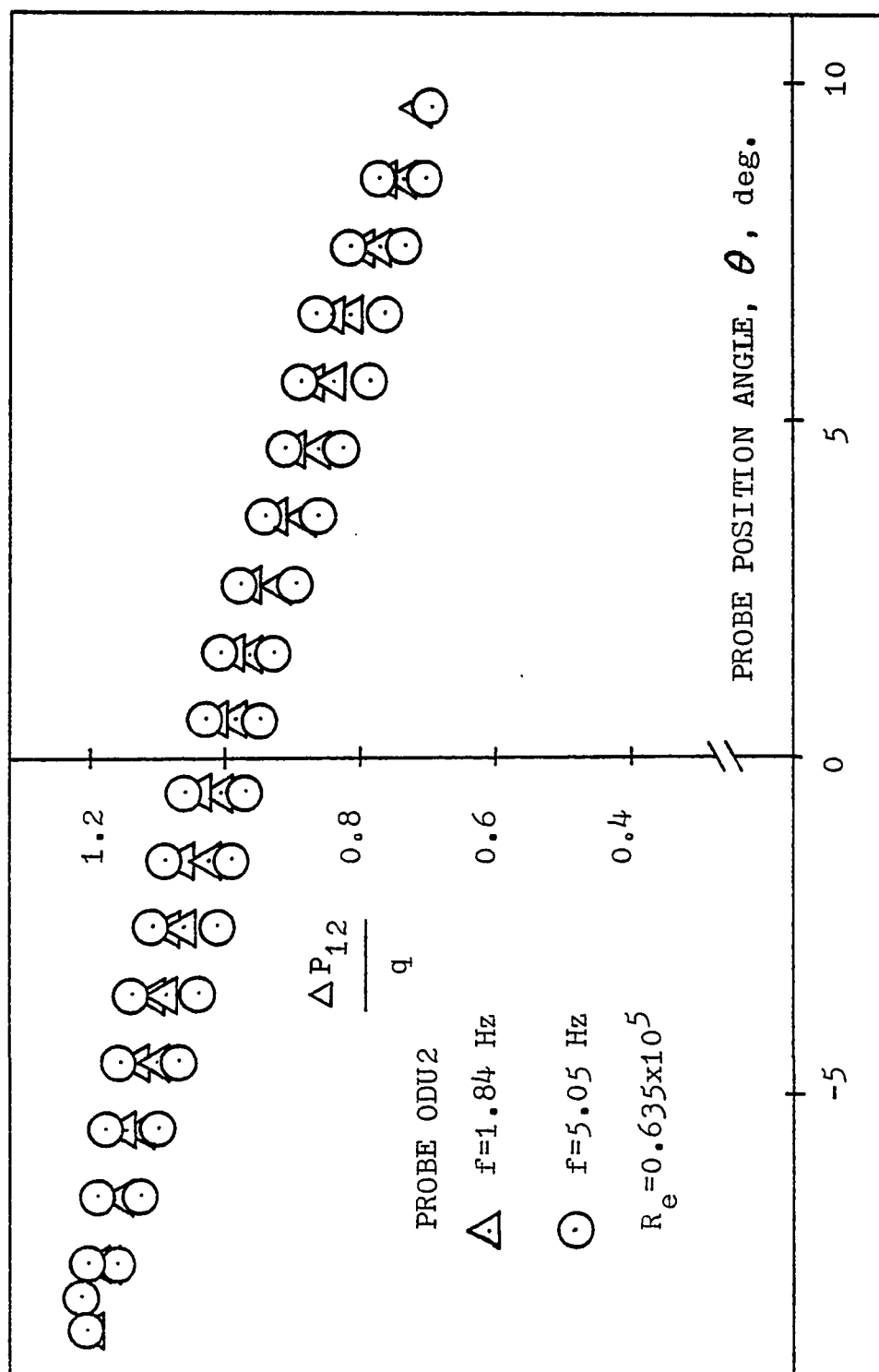
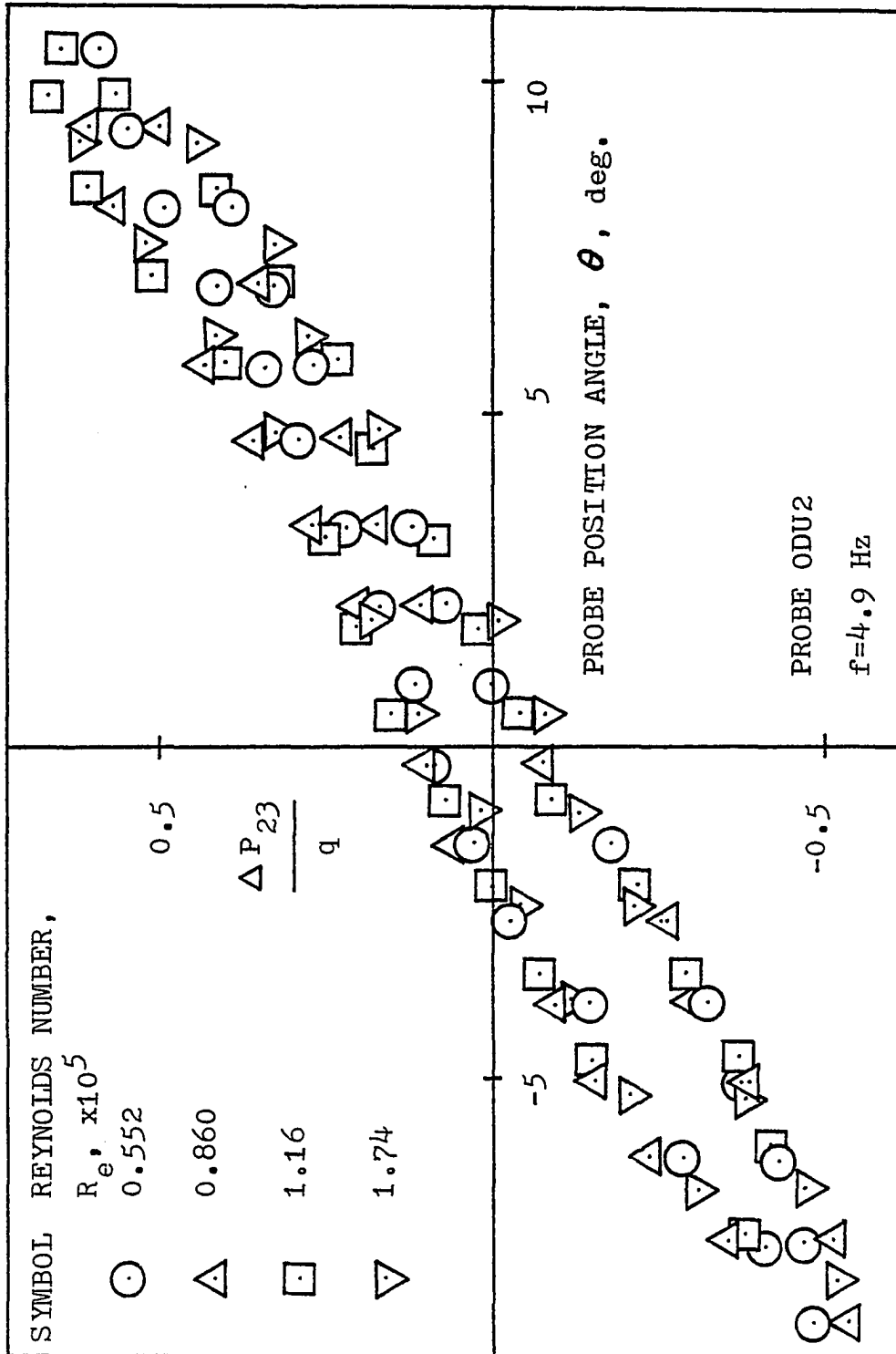
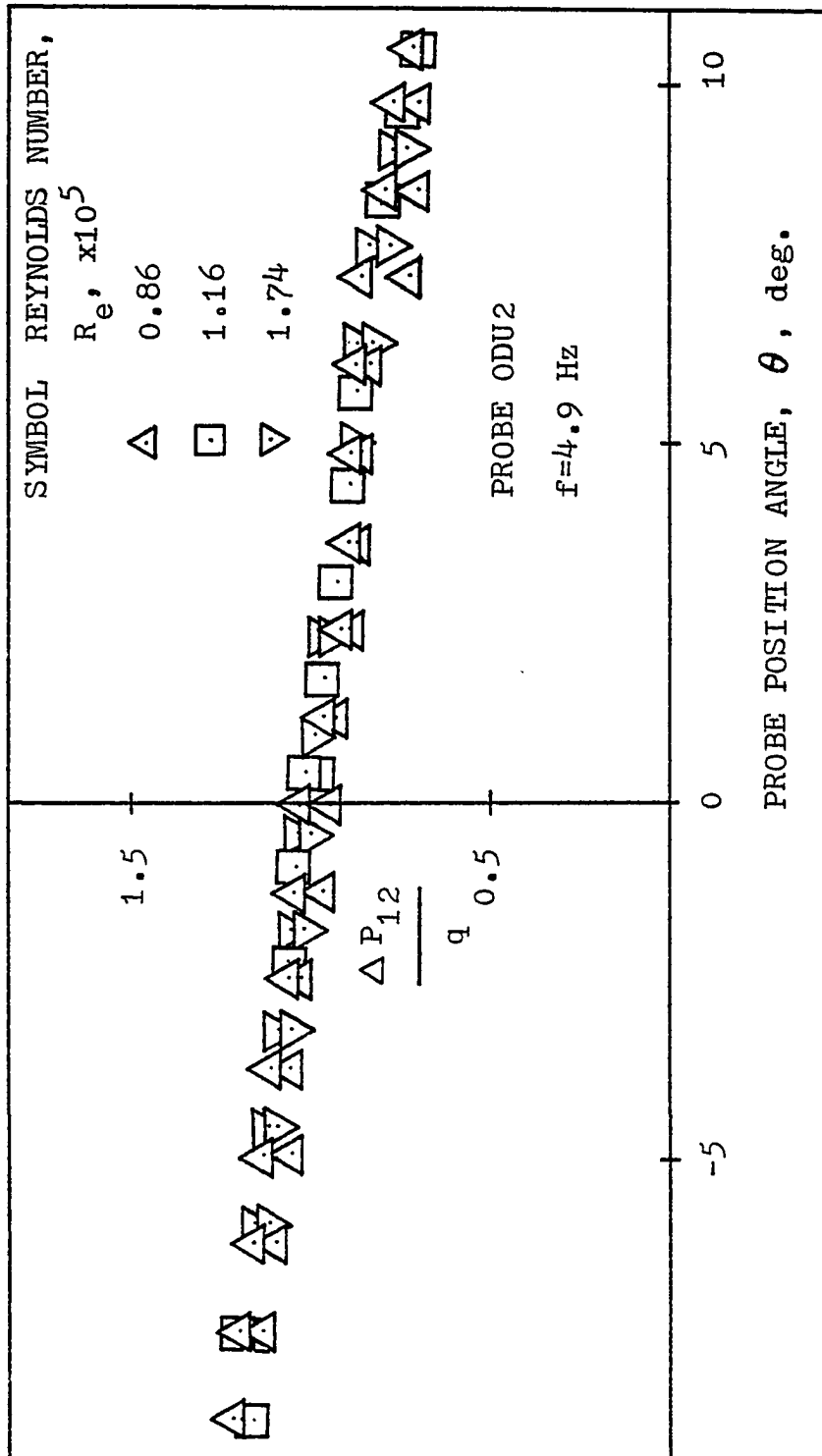
(b) $\Delta P_{12}/q$ versus θ

Figure 4.10 Continued



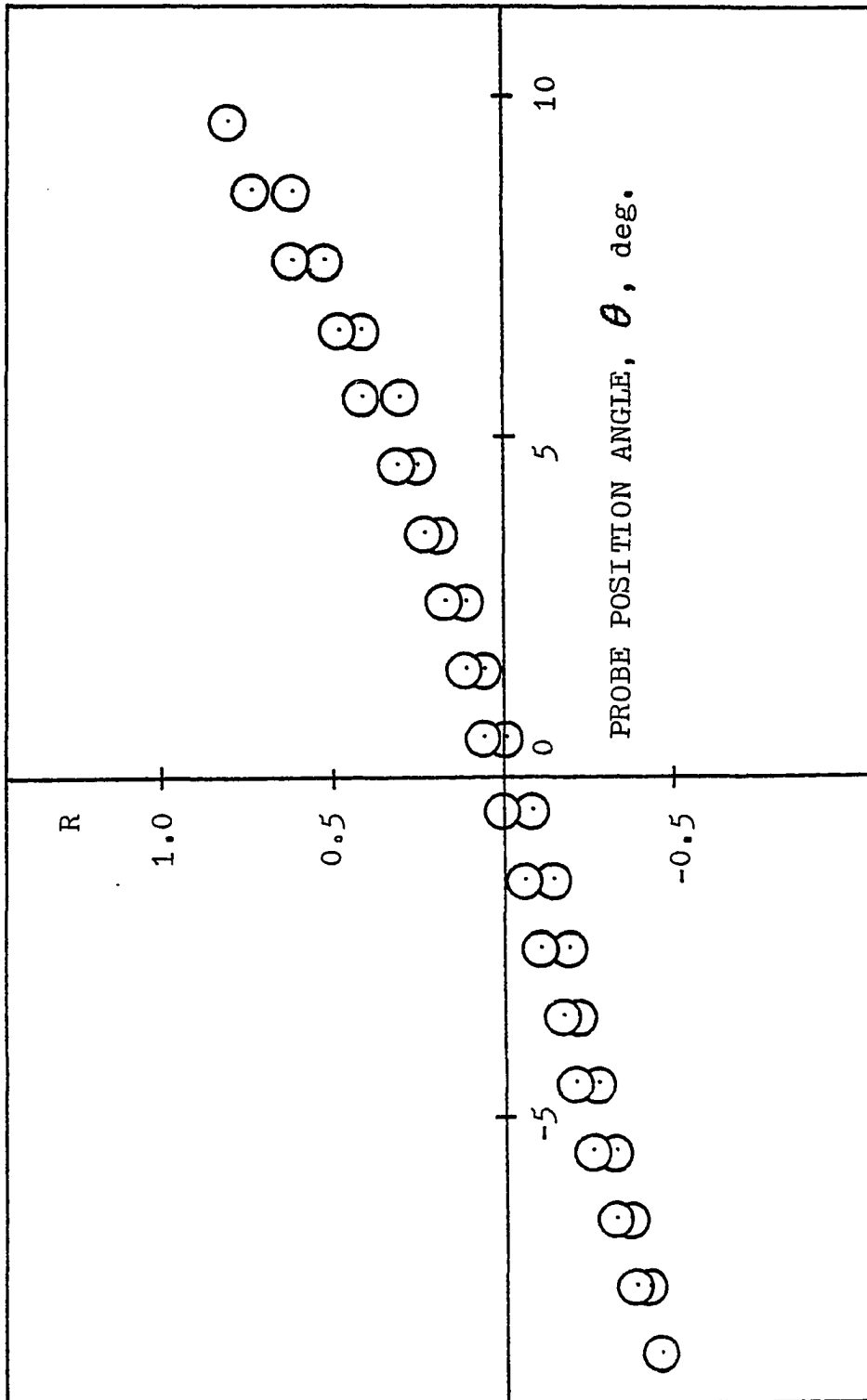
(c) $\Delta P_{23}/q$ versus θ

Figure 4.10 Continued



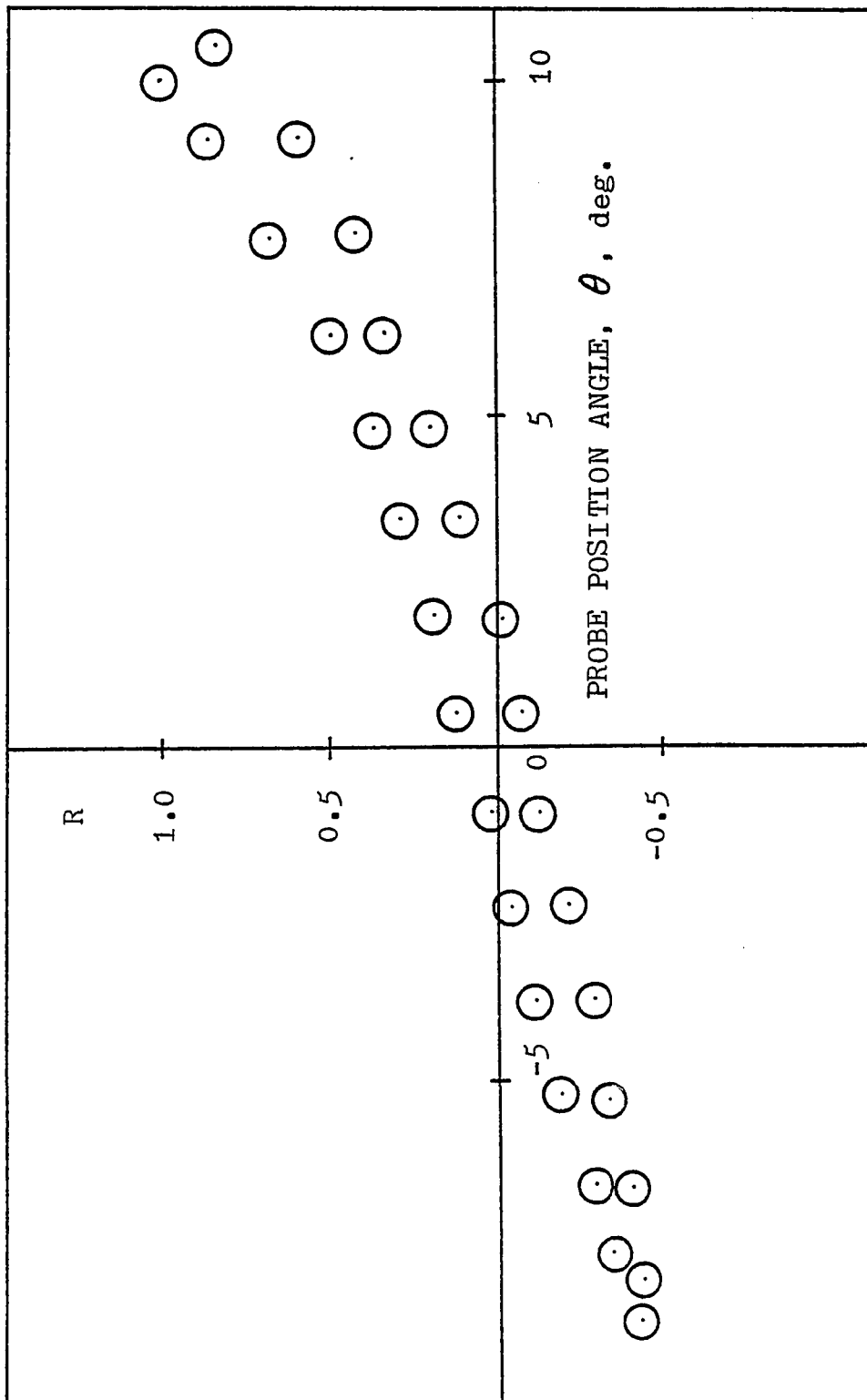
(d) $\Delta P_{12}/q$ versus θ

Figure 4.10 Concluded



(a) Test conditions: $R_e = 0.635 \times 10^5$ and $f = 1.84$ Hz

Figure 4.11 Variation of pressure differential ratio with probe angle



(b) Test conditions: $R_e = 1.74 \times 10^5$ and $f = 4.9$ Hz

Figure 4.11 Concluded

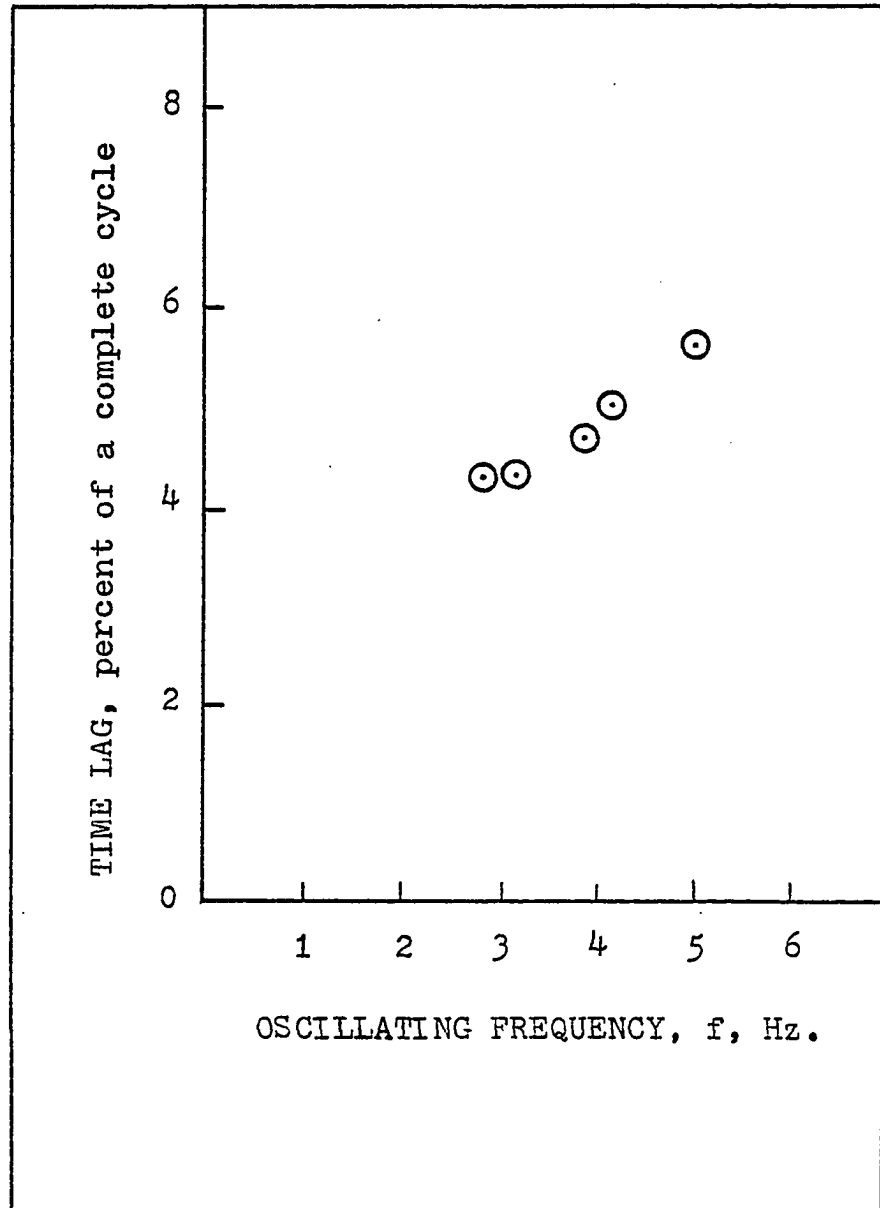
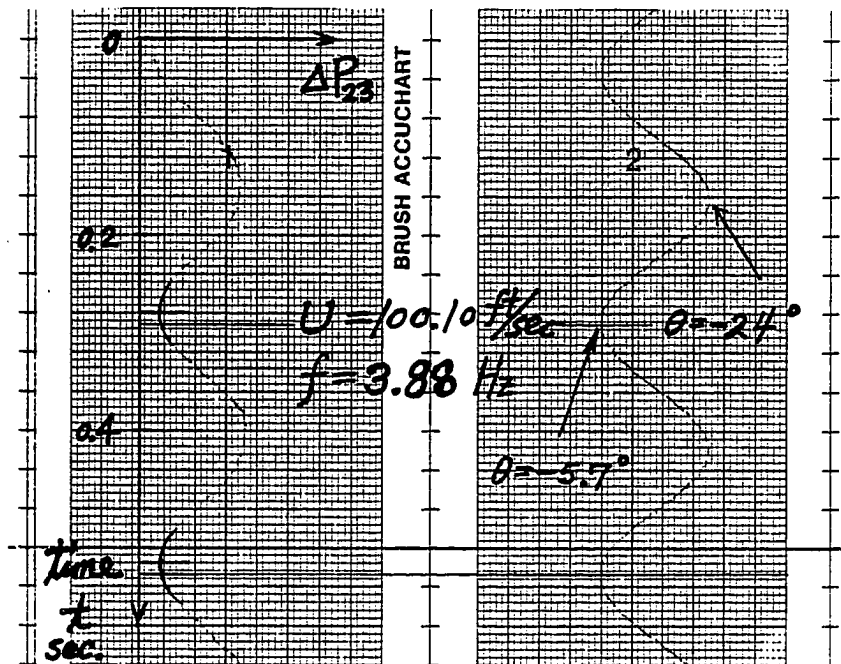


Figure 4.12 Variation of time lag with oscillating frequency, probe ODU2 and $U=30.5$ m/s.



$$\text{PEAK TO PEAK SHIFT} = 1.5/32.2$$

$$= 0.0466$$

$$\text{TIME INTERVAL FOR A PERIOD} = 0.258 \text{ seconds}$$

$$\text{ACTUAL TIME DELAY} = 0.012 \text{ seconds}$$

$$\text{TOTAL ANGULAR AMPLITUDE} = 18.3^\circ$$

$$\text{CORRESPONDING ANGULAR ERROR} = 0.86^\circ$$

Figure 4.13 Illustration of time lag phenomenon

varied from -5.7° to 24.0° , there was a time lag of 4.66 percent of a complete cycle. This corresponded to a 16.8° phase shift, or an angle error of 0.86° . The reasons for the observed time lag will be discussed in article 5.2. Similar phase shift behavior was observed at other test air speeds; this phase lag decreased as U increased.

V. TEST RESULTS ANALYSIS AND DISCUSSION

5.1 Static Test

From results presented in figure (4.2) and Appendix F, it is seen that the static pressure distribution curves for a sphere with cylinder tailfitted disagree significantly for $|\theta| > 35^\circ$. According to the potential flow solution for flow past a sphere, the pressure coefficient is given by

$$\frac{P - P_\infty}{(1/2)\rho U^2} = 1 - \frac{9}{4} \sin^2 \theta, \quad (5.1-1)$$

where θ is measured from the front stagnation point. When data in figure (4.5) were compared to the equation (5.1-1), as shown in figure (5.1), the following experimental differences were found: First, for probe ODU2 for θ from 5° to 20° , although the pressure differential data were below the theoretical curve, they were parallel to the theory. Second, for θ less than 5° , there was a large difference between the theory and experiment. The reason for this discrepancy can be seen from figure (4.2), where it is seen that for a point located at large angles from the stagnation point the difference between theory and experiment becomes significant. Third, for probe NASA60, figure (5.1b) shows that data between $-5^\circ \leq \theta \leq 12^\circ$ were close to the theoretical curve. For

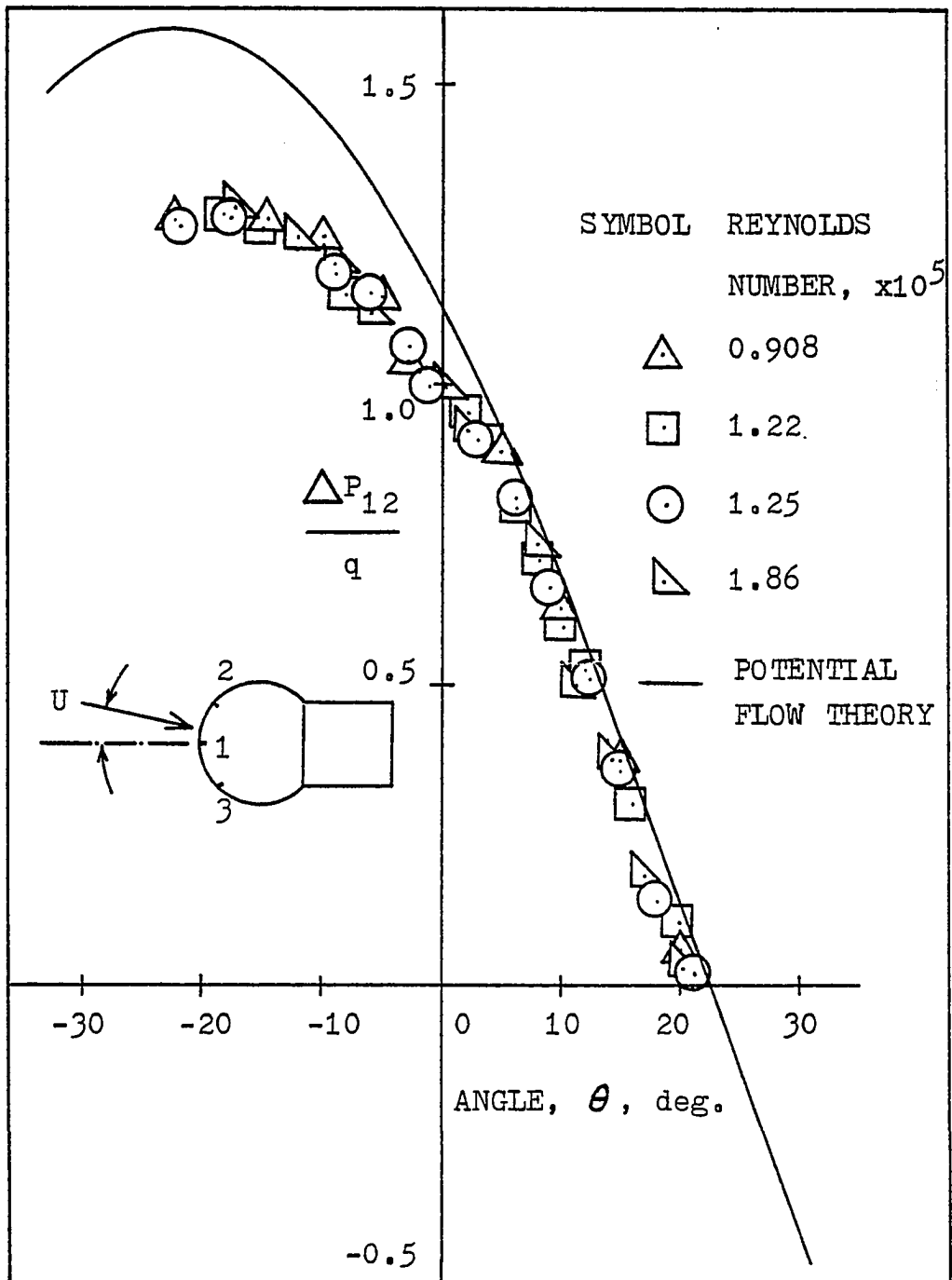
$\theta > 12^\circ$, the static pressure at port 2 became more negative than for the potential flow "sphere" condition. Hence, the value for $\Delta P_{12}/q$ fell below the theoretical curve due to the effect of the cylinder behind the spherical probe head, as discussed in Appendix F. In figures (5.1c, d), the non-dimensional pressure differentials, $\Delta P_{23}/q$, for both probe ODU2 and NASA60 have been compared to the static theory. The results for probe ODU2 in the angle range $-20^\circ \leq \theta \leq 20^\circ$ were in good agreement with theory, while the results for NASA60 probe were found to be less than the theory for positive θ .

5.1.1 Determination of Probe Coefficient from Steady Flow Results

The constant $9/4$ in the equation (5.1-1) is valid only for $|\theta| \leq 42^\circ$ for Reynolds number in the subcritical range and $|\theta| \leq 65^\circ$ for Reynolds number in the supercritical range due to the viscous effects and separation (Ref. 20). The actual values of b_{12} and b_{23} for the various probes need to be established from experiments. In a real fluid flow, because of the viscous effects and interference of the rear support of the probe head with the flow, equation (5.1-1) can be rewritten as

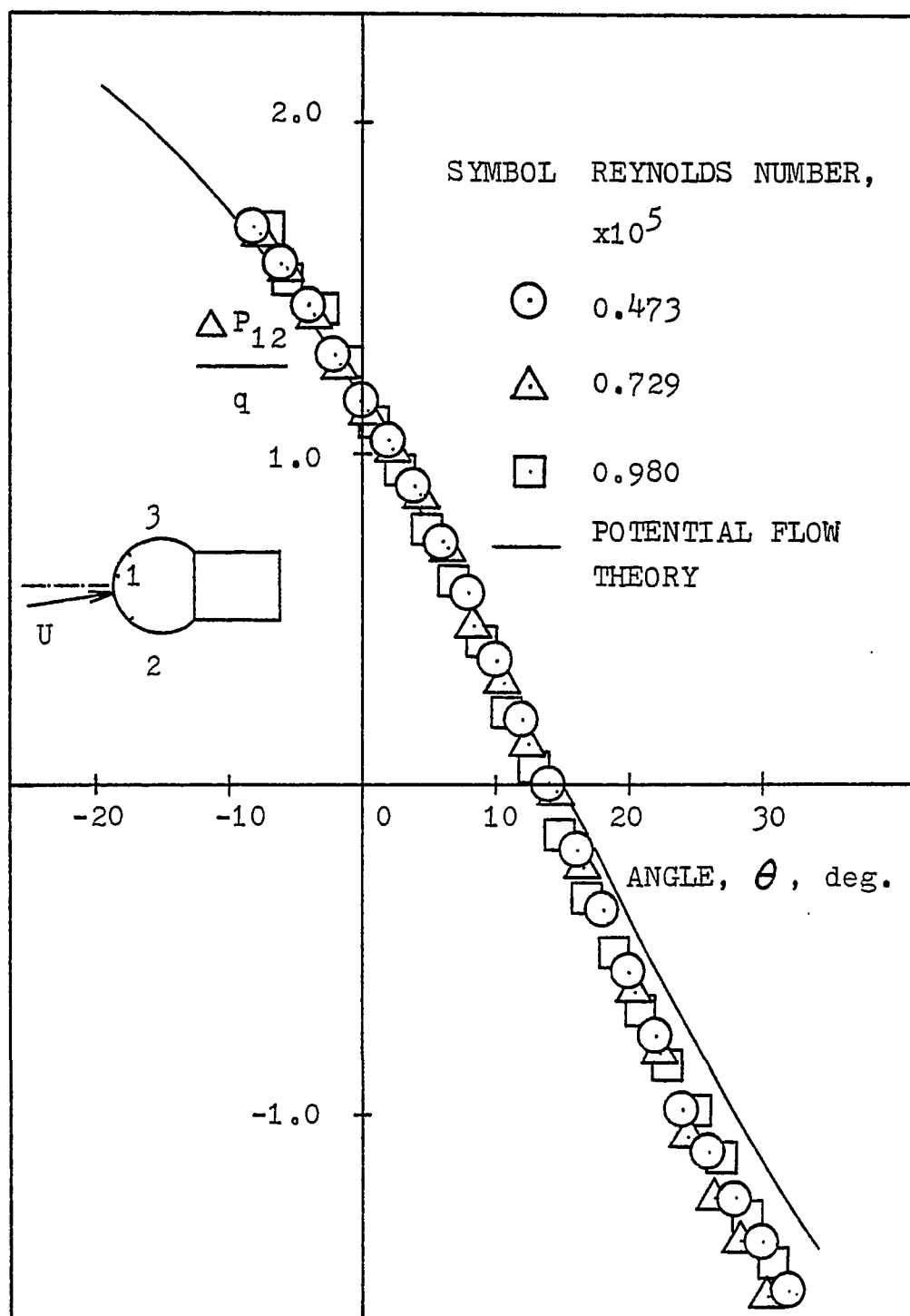
$$P_i = P_t - b q \sin^2 \theta_i,$$

where $P_t = P_\infty + (1/2)\rho U_\infty^2$, $q = (1/2)\rho U_\infty^2$, i denotes a point on the sphere surface, θ_i is the central angle between the stagnation point and point i , and b is the coefficient to be



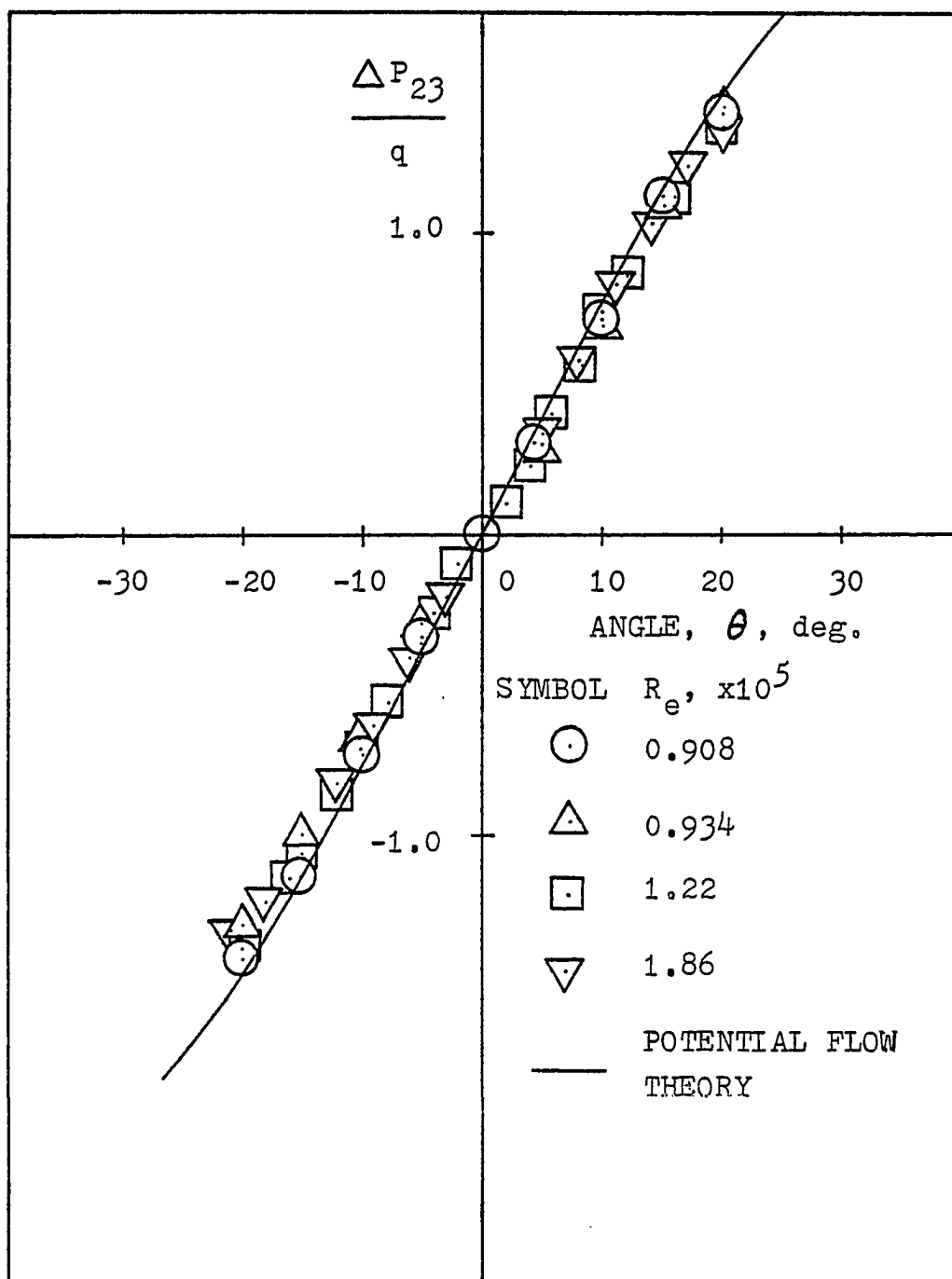
(a) PROBE ODU2, $\Delta P_{12}/q$ versus θ

Figure 5.1 Comparison of static test results with static potential flow theory



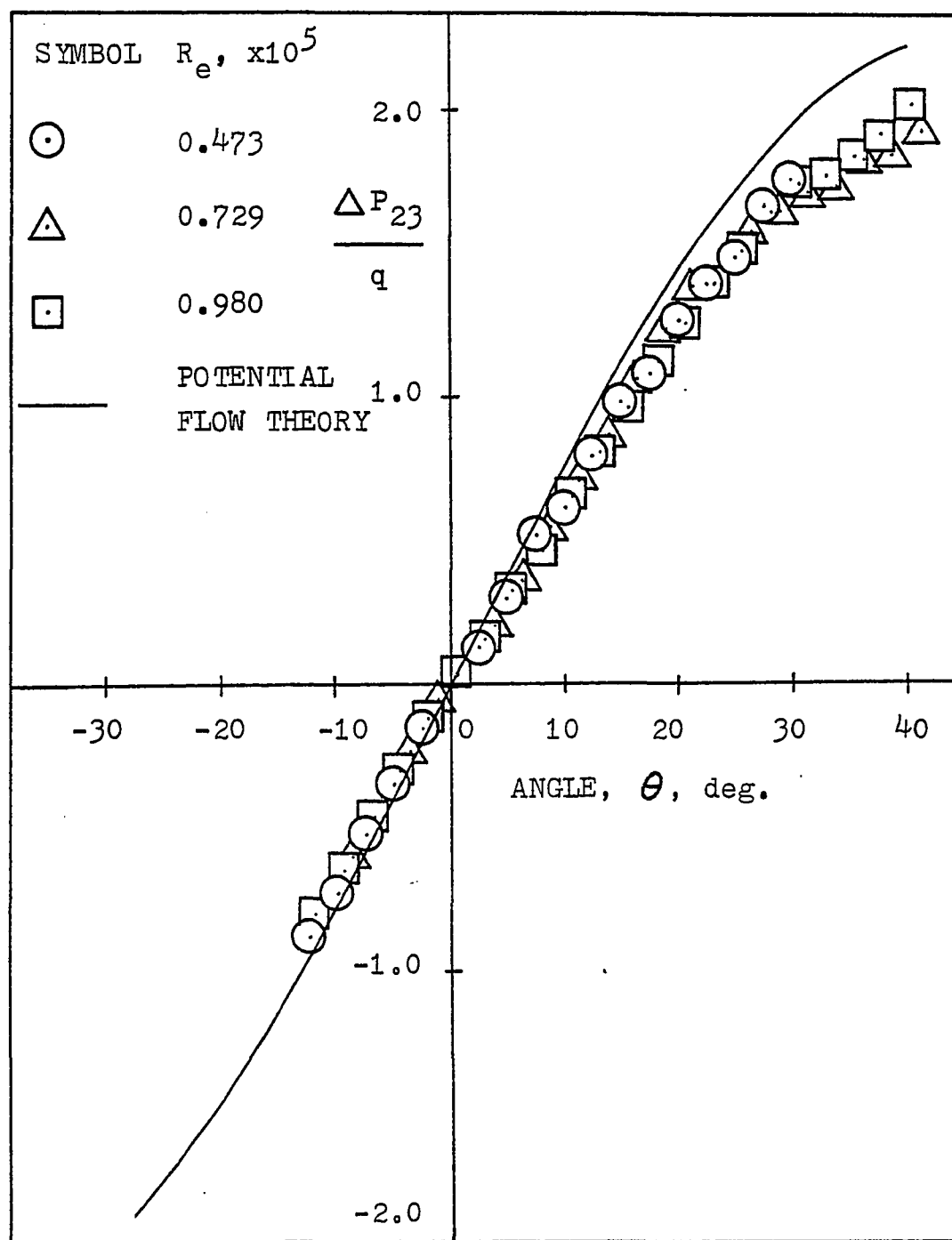
(b) PROBE NASA60, $\Delta P_{12}/q$ versus θ

Figure 5.1 Continued



(c) PROBE ODU2, $\Delta P_{23}/q$ versus θ

Figure 5.1 Continued



(d) PROBE NASA60, $\Delta P_{23}/q$ versus θ

Figure 5.1 Concluded

determined.

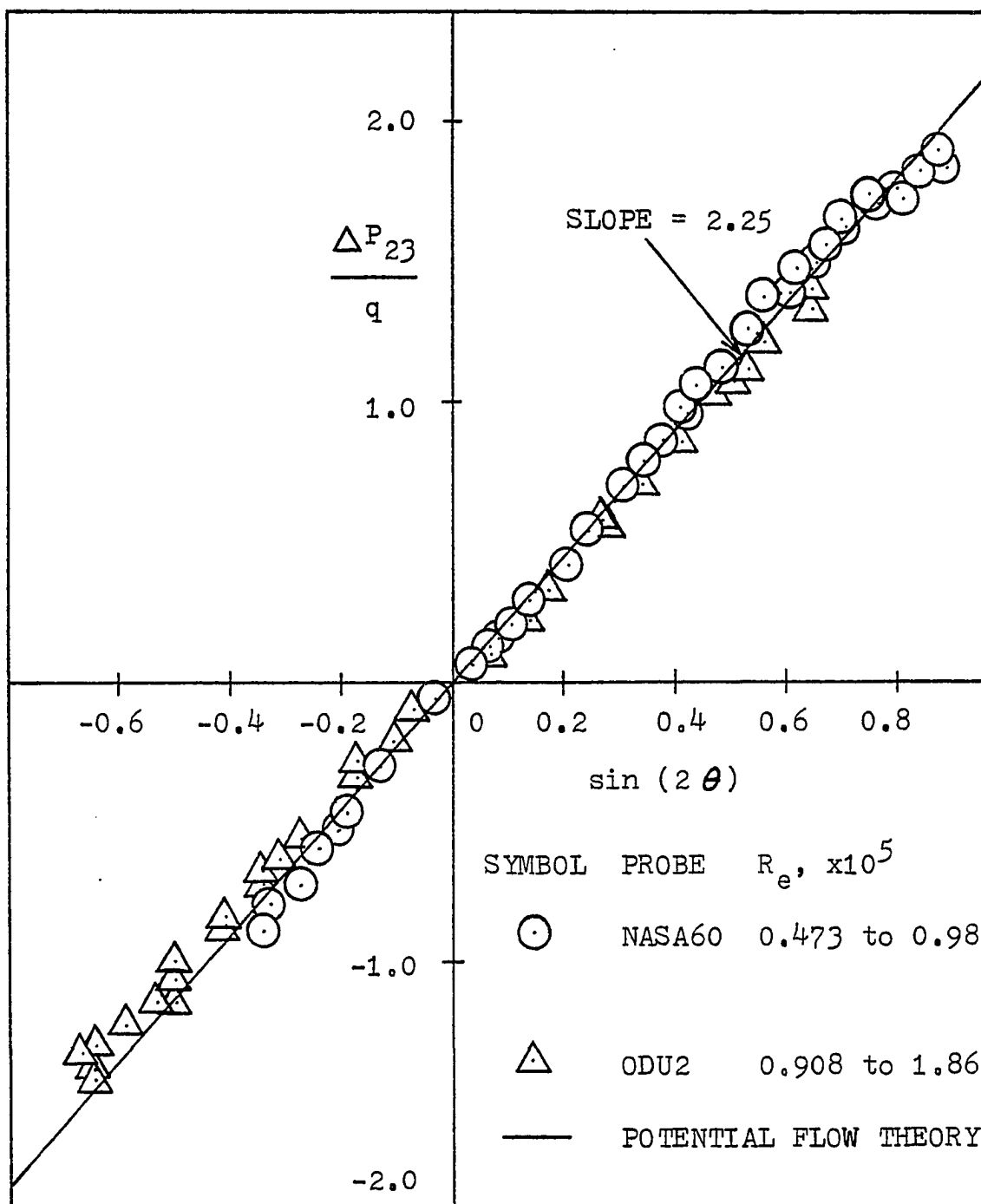
Applying equation (2.1-4) to the probe ODU2, let $\beta_2 = \pi/4$ and $\beta_3 = -\pi/4$, one obtains after some manipulation

$$\Delta P_{23} = P_2 - P_3 = b q \sin(2\theta) \quad (5.1-2)$$

Similarly, the pressure difference between ports 1 and 2 was found to be

$$\Delta P_{12} = b q \sin(\pi/4 - 2\theta) / \sqrt{2} \quad (5.1-3)$$

The experimental data presented in figure (4.5) were subsequently plotted into non-dimensional form, $\Delta P_{23}/q$ versus $\sin(2\theta)$, and $\Delta P_{12}/q$ versus $\sin(\pi/4 - 2\theta)/\sqrt{2}$, as shown in figure (5.2). The horizontal axis in figure (5.2c) was $\sin(\pi/6 - 2\theta)$ since the central angle between ports 1 and 2 for NASA60 was 60 degrees. Figure (5.2a) shows the non-dimensional relation between $\Delta P_{23}/q$ and $\sin(2\theta)$. The circular symbols correspond to probe NASA60, which yielded a slightly higher slope (2.34) than the theoretical slope of 2.25, while the triangular symbols for probe ODU2 yielded a smaller slope of 2.09. From figure (5.2b), for probe NASA60, the theoretical slope for pressure differences between ports 1 and 2 was $b\sqrt{3}/2=1.95$, while the experimental data yielded a slope of 2.57, which was 32 percent higher than the theory. In figure (5.2c) for probe ODU2 the theoretical slope was 2.25, while the experimental data yielded a slope of 1.97, which was 12.5 percent lower than the theory. The major factor for the large difference between these



(a) b_{23} , PROBES NASA60 AND ODU2

Figure 5.2 Non-dimensional comparison of the probe coefficient

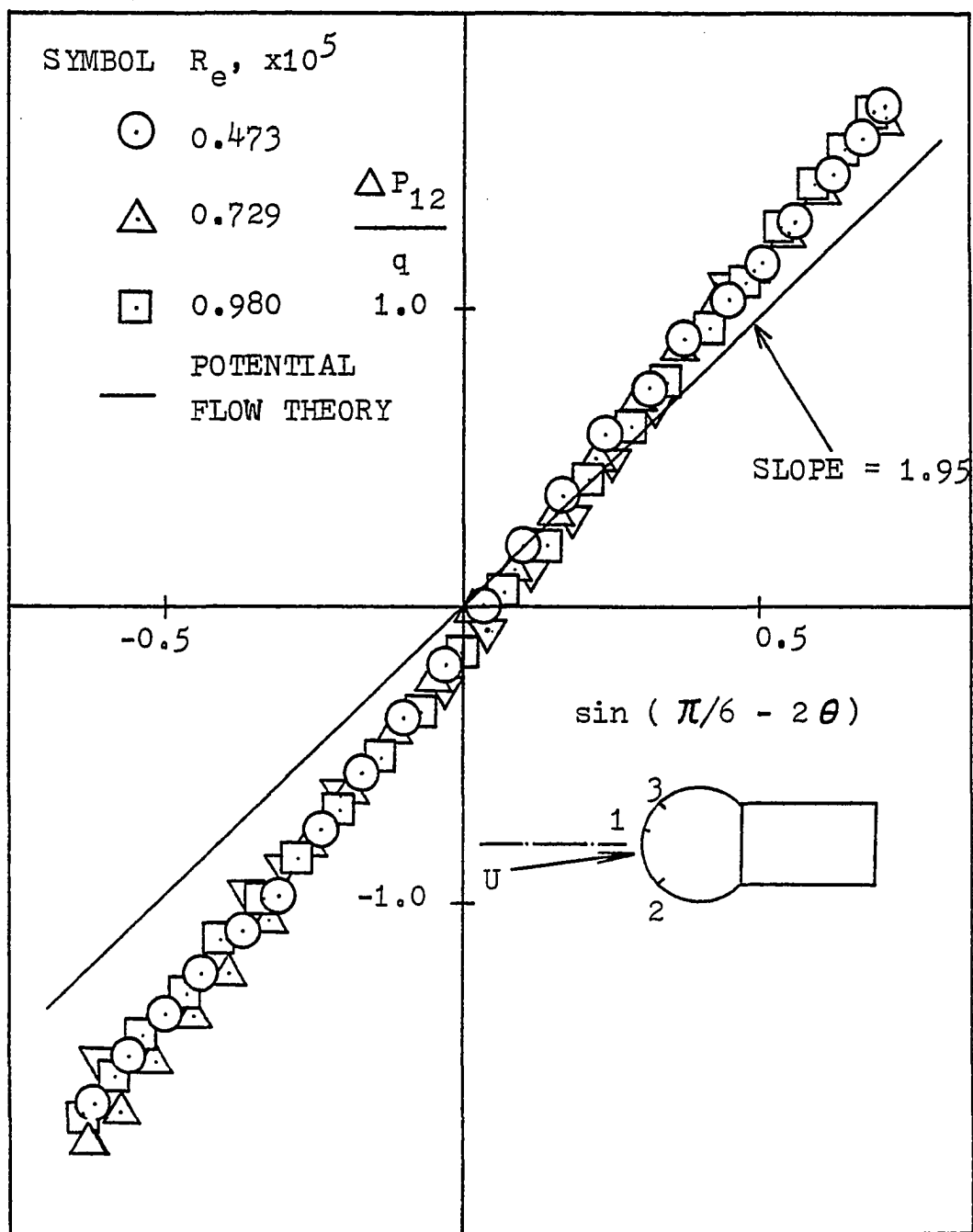
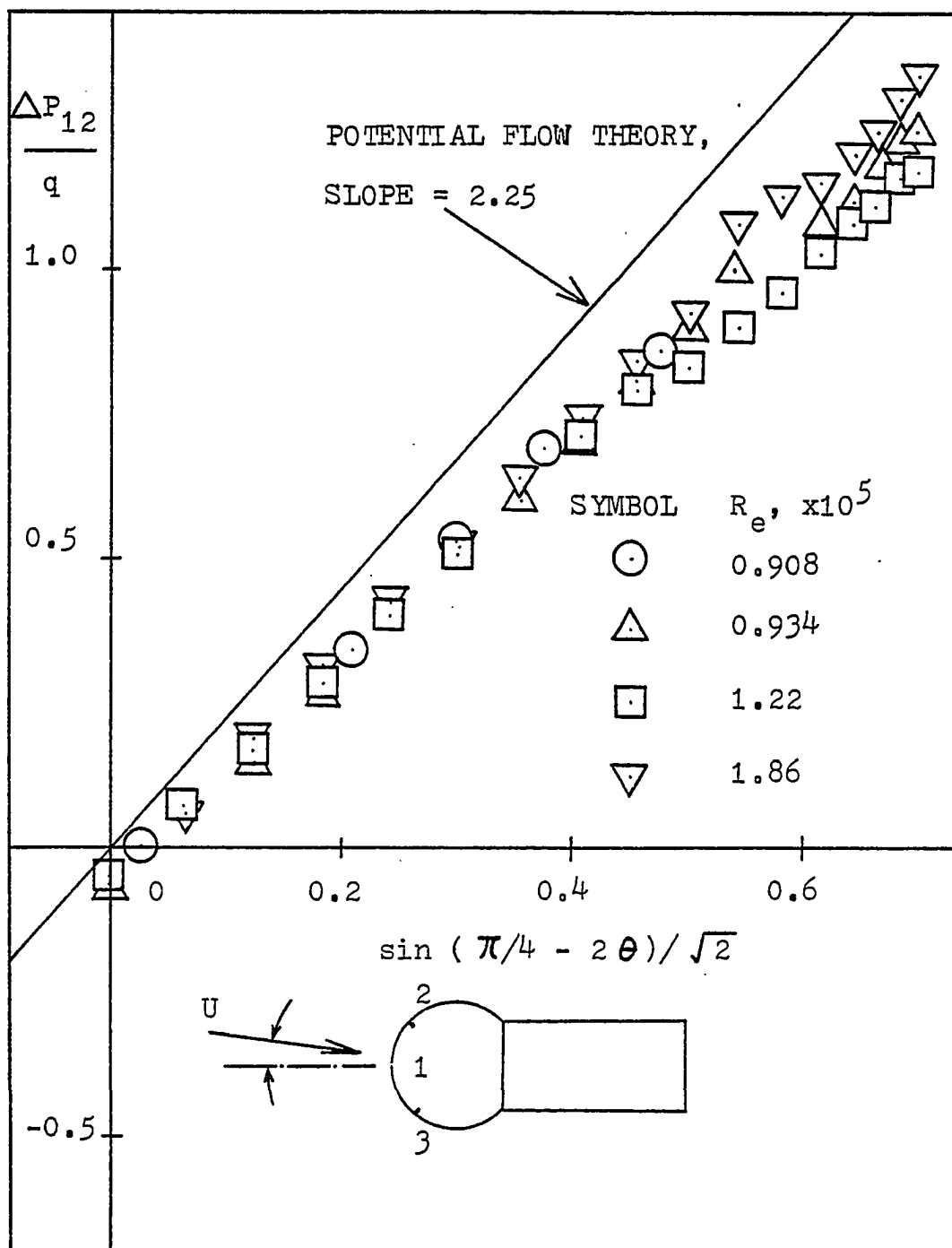
(b) b_{12} , PROBE NASA60

Figure 5.2 Continued



(c) b_{12} , PROBE ODU2

Figure 5.2 Concluded

two slopes was the different central angles between the ports 1 and 2.

Letting the coefficient between ports 2 and 3 be b_{23} and between ports 1 and 2 be b_{12} , figure (5.3) shows the variation of experimentally obtained probe coefficients b_{23} and b_{12} with Reynolds number based on the airstream velocity and the probe head diameter. It is seen that the probe coefficients depended on the central angle between the ports under consideration as well as the Reynolds number. For probe ODU2, b_{12} varied from 2.10 to 1.97 as Reynolds number increased, while b_{23} varied from 1.77 to 2.09. The open end tunnel results for b_{12} and b_{23} have been used in article 5.2 in the oscillating probe analysis, since the oscillating probe tests were done in the open end tunnel test section.

5.1.2 Direct Comparison between Theory and Static Test

Results for Determination of Static Angle of Attack
The relation between static angle of attack and pressure difference ratio was obtained from equation (2.1-4). For probe NASA60, the ratio of $\Delta P_{23}/\Delta P_{12}$ was found to be a function of angle only:

$$R = \frac{\Delta P_{23}}{\Delta P_{12}} = \frac{\sqrt{3} \sin(2\theta)}{2 \sin(\pi/6 - 2\theta)} \quad (5.1-4)$$

Figure (5.4a) shows the comparison between the equation (5.1-4) and experimental data for the NASA60 probe. The results were in good agreement. Similarly, for probe ODU2, one obtains

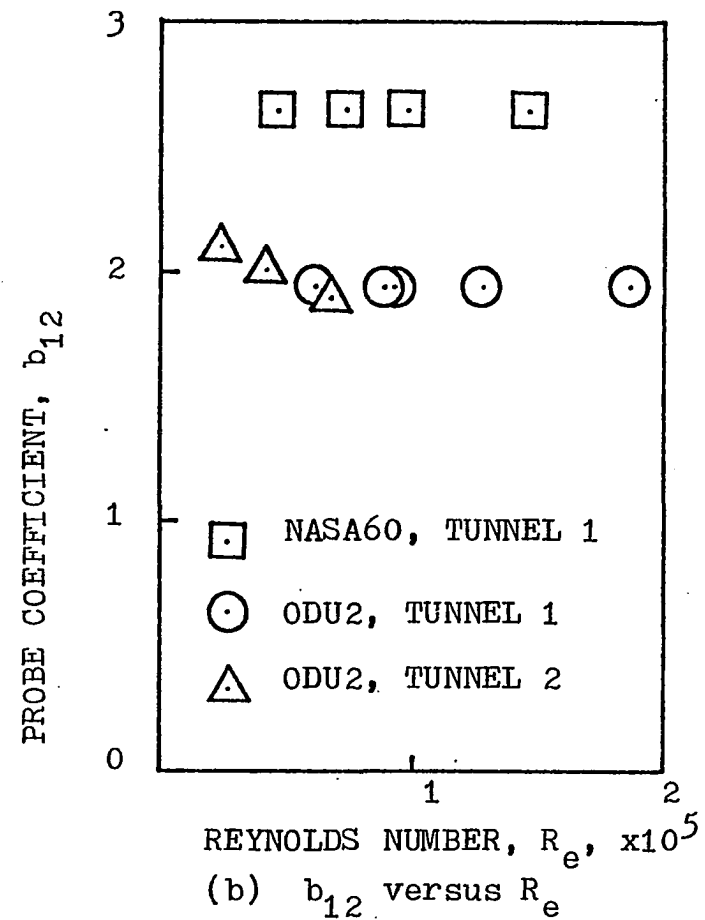
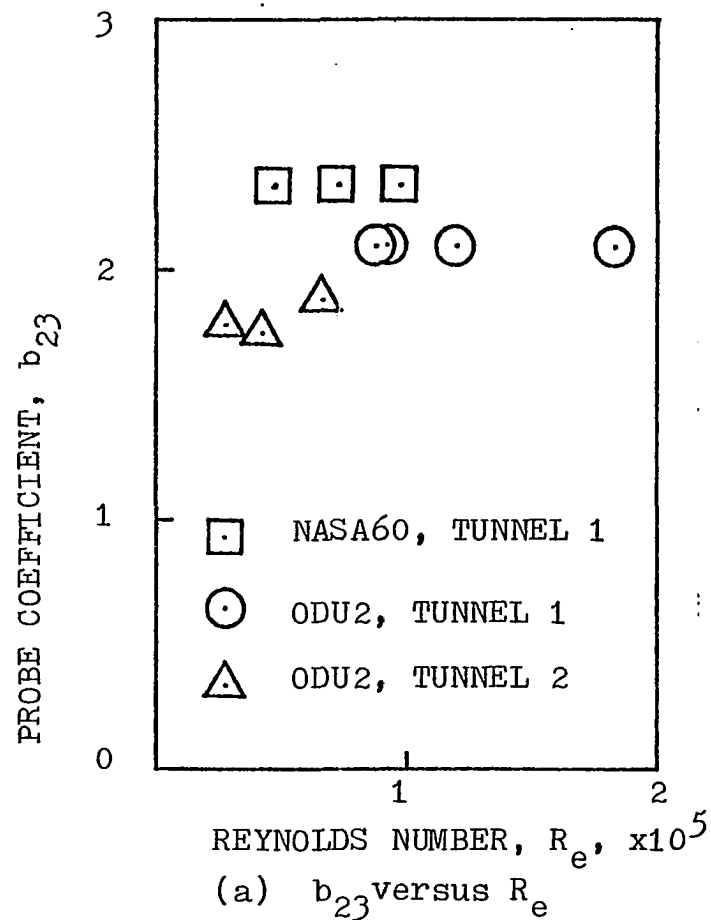


Figure 5.3 Variation of probe coefficients with Reynolds number, tunnel 1 - Induction Wind Tunnel, tunnel 2- Open End Wind Tunnel.

$$R = \frac{\Delta P_{23}}{\Delta P_{12}} = \frac{\sqrt{2} \sin(2\theta)}{\sin(\pi/4 - 2\theta)} \quad (5.1-5)$$

Figure (5.4b) shows the results for probe ODU2. The experimental data were again in good agreement with equation (5.1-5). The ODU1 probe had a different pressure differential arrangement than the ODU2 probe; hence, the theoretical relations for pressure differentials yielded

$$\frac{\Delta P_{13}}{\Delta P_{12}} = \frac{\sin(\pi/4 + 2\theta)}{\sin(\pi/4 - 2\theta)} \quad (5.1-6)$$

Figure (5.4c) shows the results for probe ODU1 and equation (5.1-6).

The observed differences between the static theory and experimental results were likely due to the effect of the cylinder behind the spherical probe head. For probe NASA60, the experimental data gave a maximum error of 3 degrees at $\theta = -22^\circ$. For $-16^\circ \leq \theta \leq 10^\circ$, the errors were less than 1° . For probe ODU2, the maximum error was 5 degrees at $\theta = -20^\circ$; for $-10^\circ \leq \theta \leq 12^\circ$, all errors were less than 1° . For probe ODU1, the maximum error was 1.8° at $\theta = 17.6^\circ$, and for $-18^\circ \leq \theta \leq 8^\circ$, all errors were less than 1° . For practical application, one could use the data points or the static theory based on superposition of velocity vectors to estimate the static angle of attack. It is expected that this estimation on θ would be accurate to within $\pm 2^\circ$ for $|\theta| < 20^\circ$ for the static theory or at least $\pm 1^\circ$ for a curve faired through the data.

In figure (5.5), the static input angle, θ_{in} , as measured by a clinometer to an accuracy of $\pm 0.1^\circ$ is shown for probe NASA60 versus the output angle as calculated by equation (5.1-7),

$$\theta_{out} = \frac{1}{2} \tan^{-1} \left[\frac{\Delta P_{23}}{\sqrt{3} \Delta P_{23} + 2(b_{23}/b_{12})\Delta P_{12}} \right] \quad (5.1-7)$$

where $b_{23}=2.34$ and $b_{12}=2.64$. These values of b_{12} and b_{23} are those shown in figure (5.3). It is seen that for $-6^\circ \leq \theta_{in} \leq 27^\circ$, calculated data points fell onto a straight line given by

$$\theta_{out} = 1.11 \theta_{in}.$$

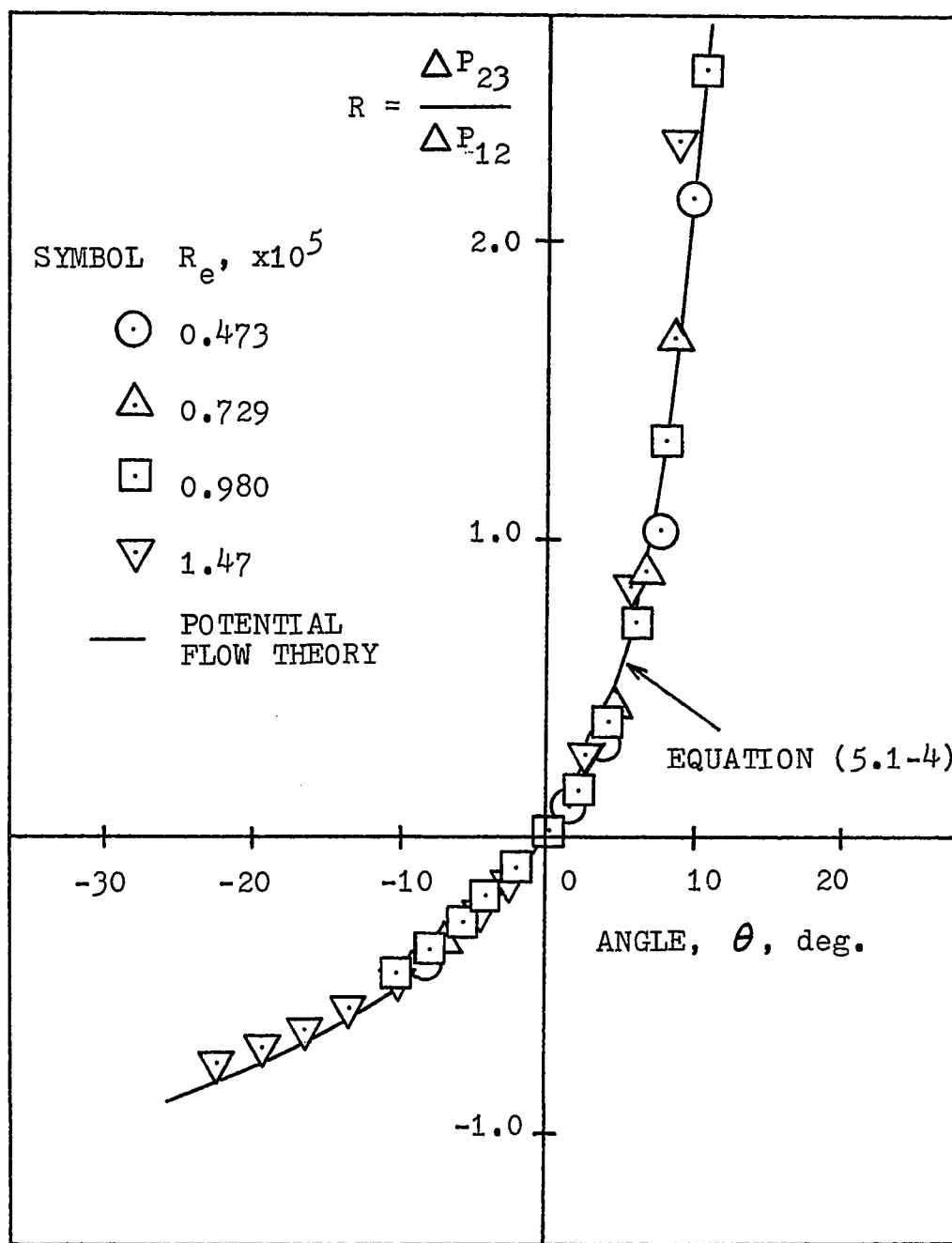
This linear equation was used to relate the calculated output angle to the actually measured input angle.

5.2 Oscillating Probe Test

While probe ODU2 was under the oscillating test condition, the pressure differentials ΔP_{12} and ΔP_{23} were automatically recorded through use of a two channel chart recorder. After data reduction, the probe response was plotted as either $\Delta P/q$ versus θ or $\Delta P/q$ versus t , where θ is the probe position angle which varied sinusoidally.

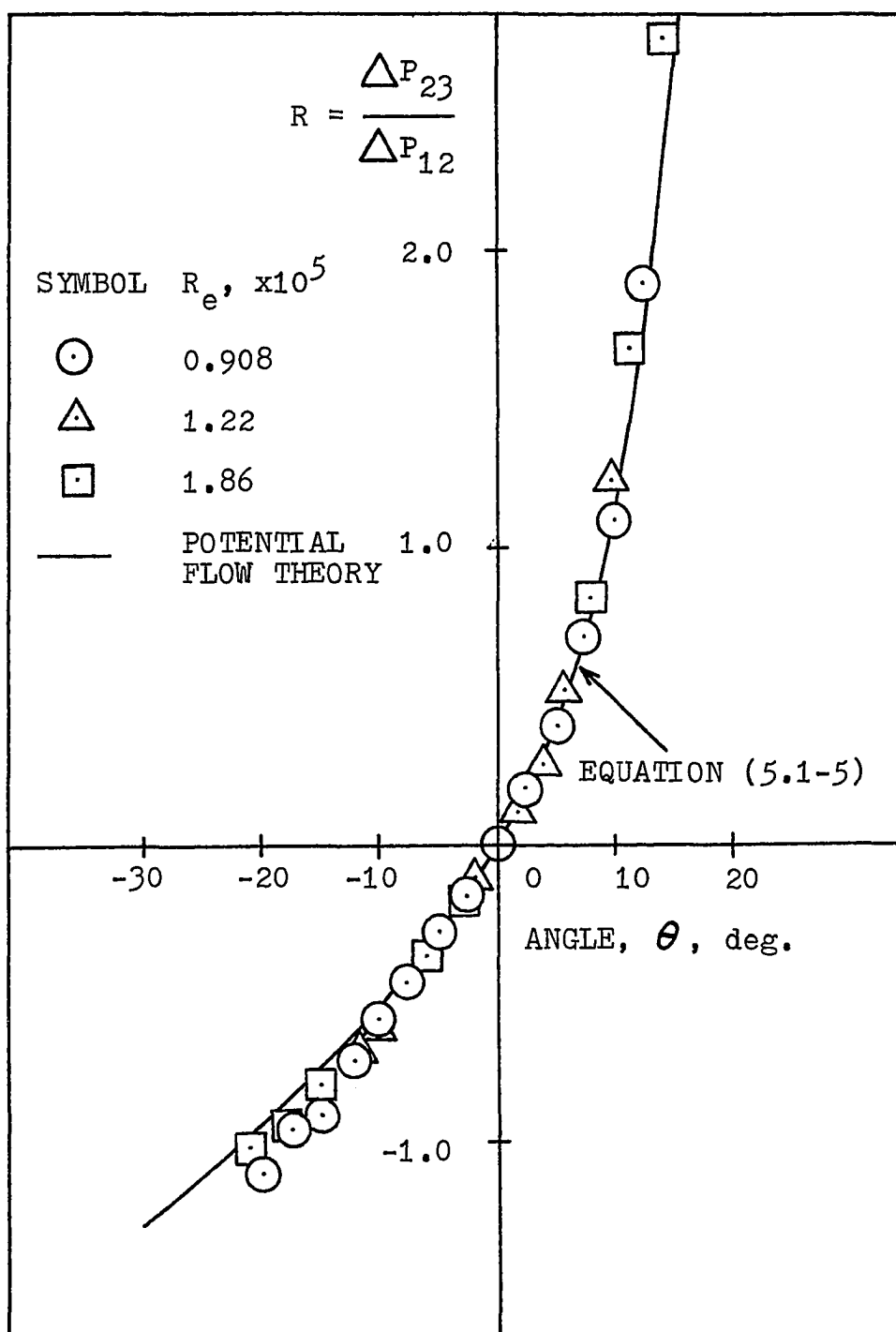
5.2.1 Oscillating Probe Data Analysis

Typical plots of $\Delta P_{23}/q$ versus θ for probe ODU2 in figure



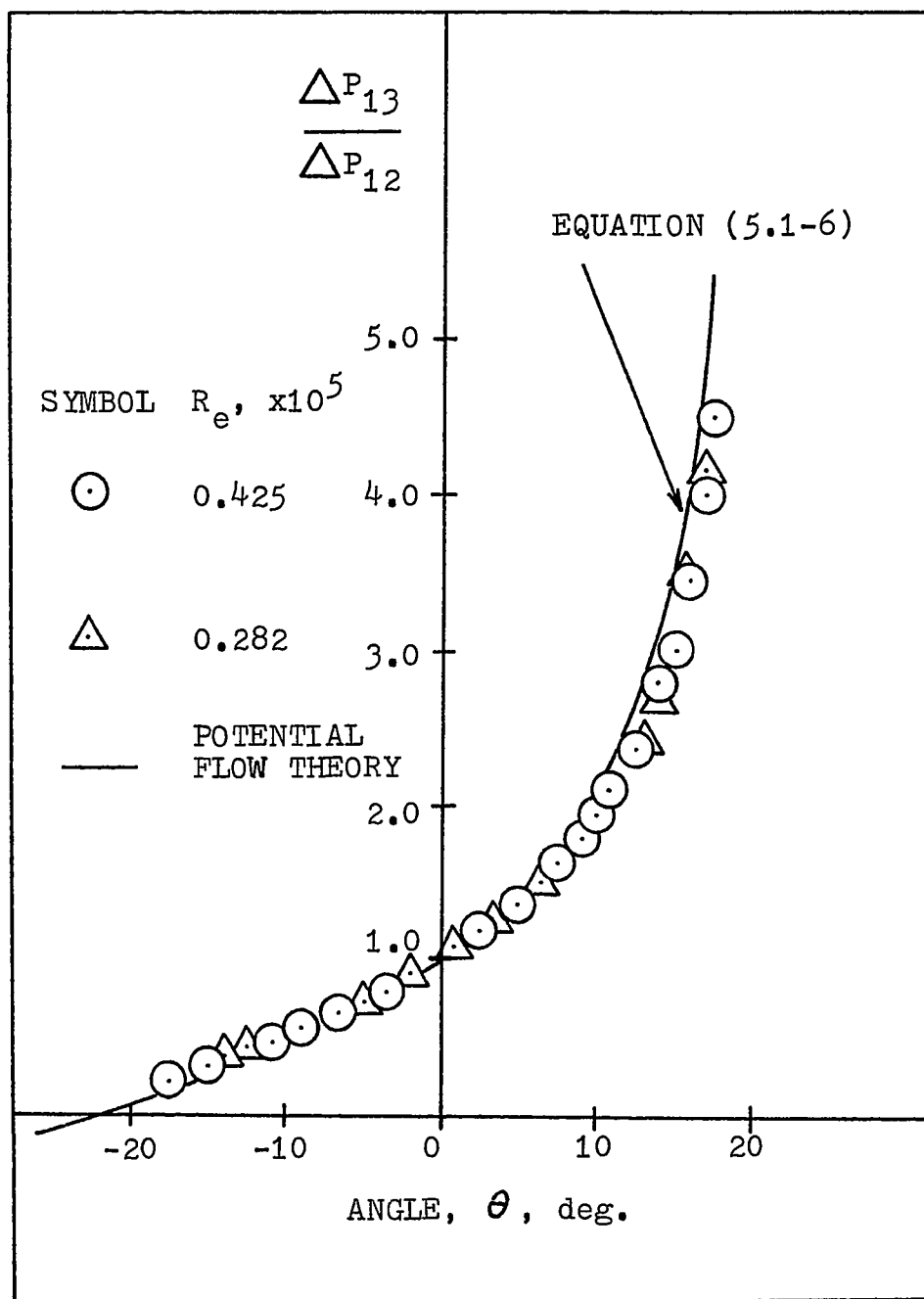
(a) PROBE NASA60

Figure 5.4 Variation of pressure differential ratio with airstream angle



(b) PROBE ODU2

Figure 5.4 Continued



(c) PROBE ODU1

Figure 5.4 Concluded

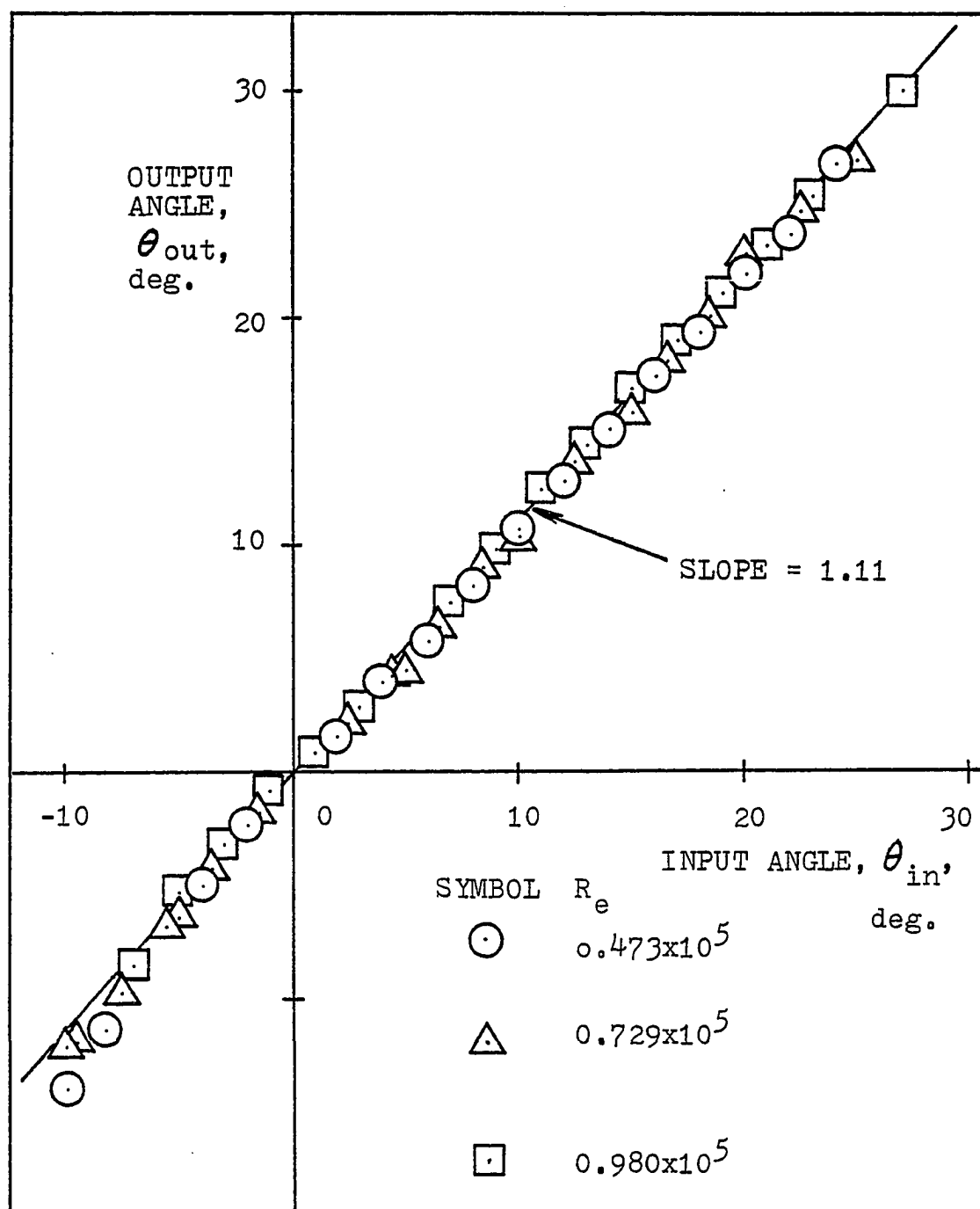


Figure 5.5 Variation of output angle with input angle,
probe NASA60

(5.6) showed that during the oscillating motion, the non-dimensional pressure differential was less than the value of $\Delta P_{23}/q$ under the static test condition when the probe moved upwards, i.e., as the probe moved from the lowermost position ($\theta = \theta_L$) to the uppermost position ($\theta = \theta_U$). However, when the probe moved downwards, the value of $\Delta P_{23}/q$ was larger than the value of $\Delta P_{23}/q$ under the static test condition. This can be explained by considering superposition of velocity vectors due to the airstream velocity, U_∞ , and the probe oscillating velocity, V_p . When the probe moved upwards to $\theta = 0^\circ$, the probe velocity caused an increase in the resultant velocity and increased the angle of attack, and hence the $\Delta P_{23}/q$ value also increased. When the probe moved downwards to the same $\theta = 0^\circ$ position, the resultant velocity increased but caused a negative angle of attack, and hence yielded a negative value for $\Delta P_{23}/q$. Figures (5.7a, b) show test results for $U = 30.5$ m/s (100 ft/sec), as the probe position angle, θ , was varied from 9.65° below to 8.5° above the horizontal reference line. In figure (5.7a), the non-dimensional pressure differential $\Delta P_{23}/q$ has been plotted against the probe position angle, θ , for oscillating frequencies $f = 1.84$ and 5.05 Hz. It is seen that all $f = 1.84$ Hz data were enveloped by the $f = 5.05$ Hz data, in qualitative agreement with the theoretical prediction by Theory II in figure (2.7a). The variation of $\Delta P_{12}/q$ with θ is shown in figure (5.7b), which was also in qualitative agreement with theoretical prediction of Theory II in

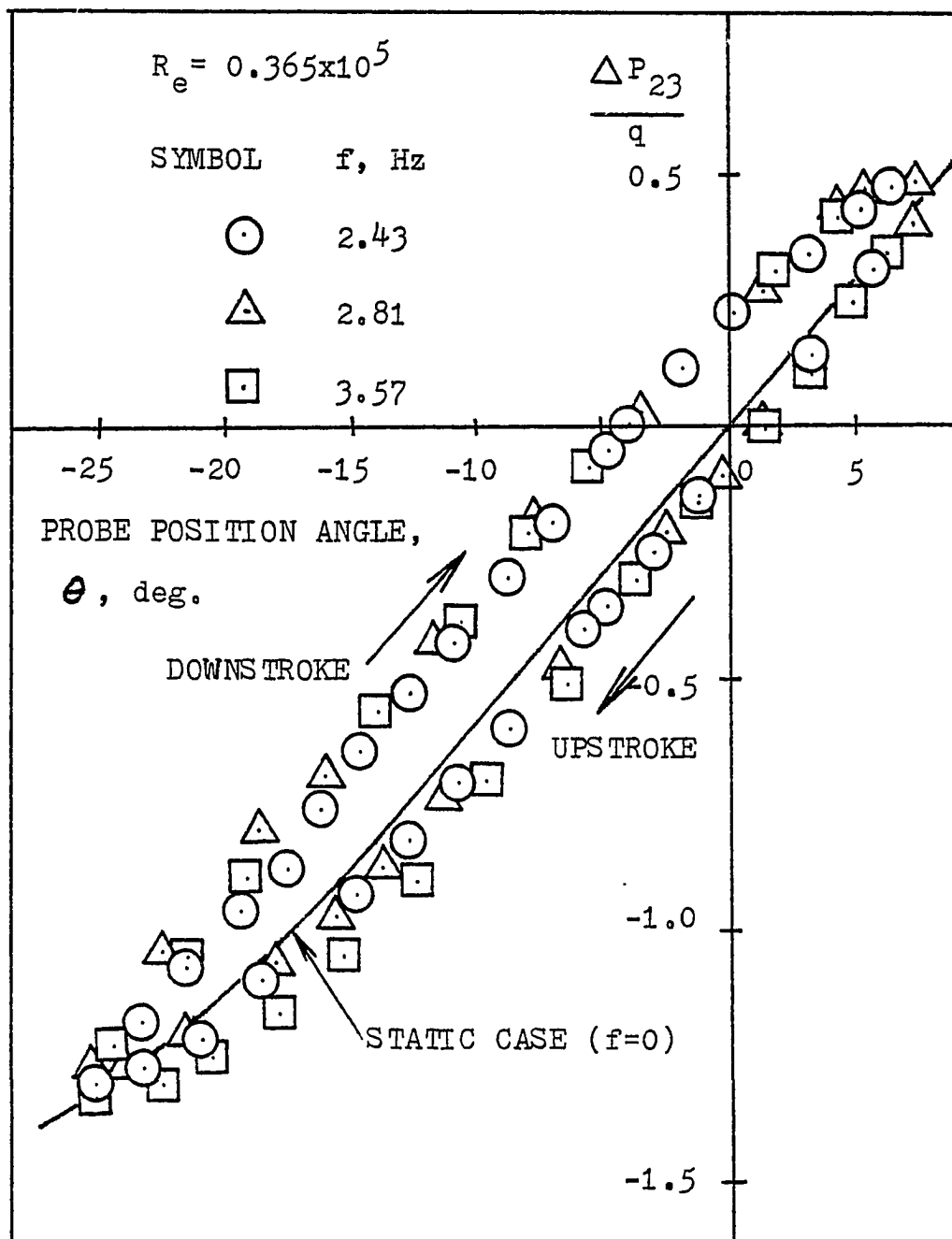


Figure 5.6 Variation of non-dimensional pressure differential, $\Delta P_{23}/q$, with probe position angle under different frequencies, probe ODU2.

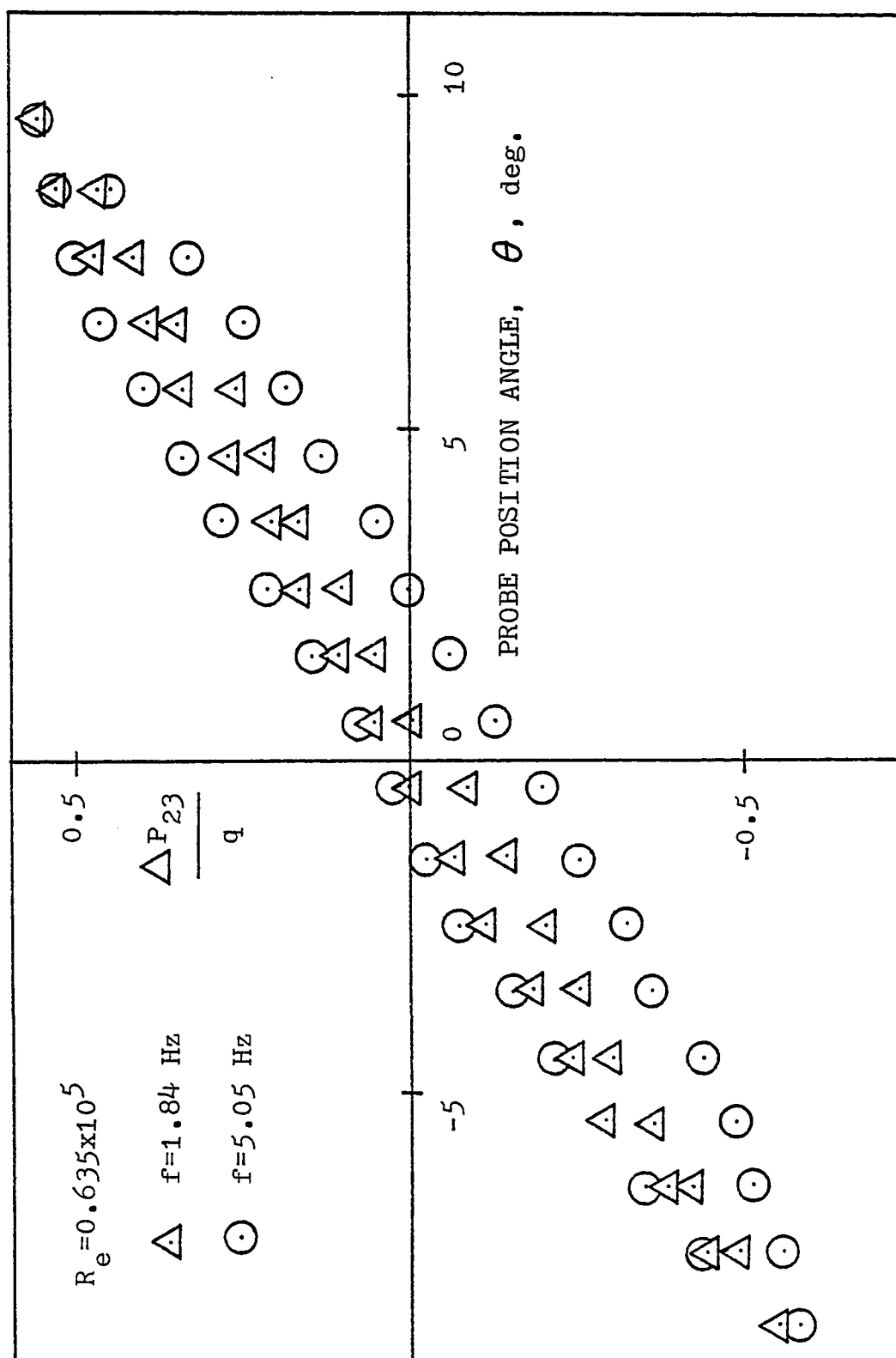


Figure 5.7 Experimental data on $\Delta P_{23}/q$ variation, probe ODU2.

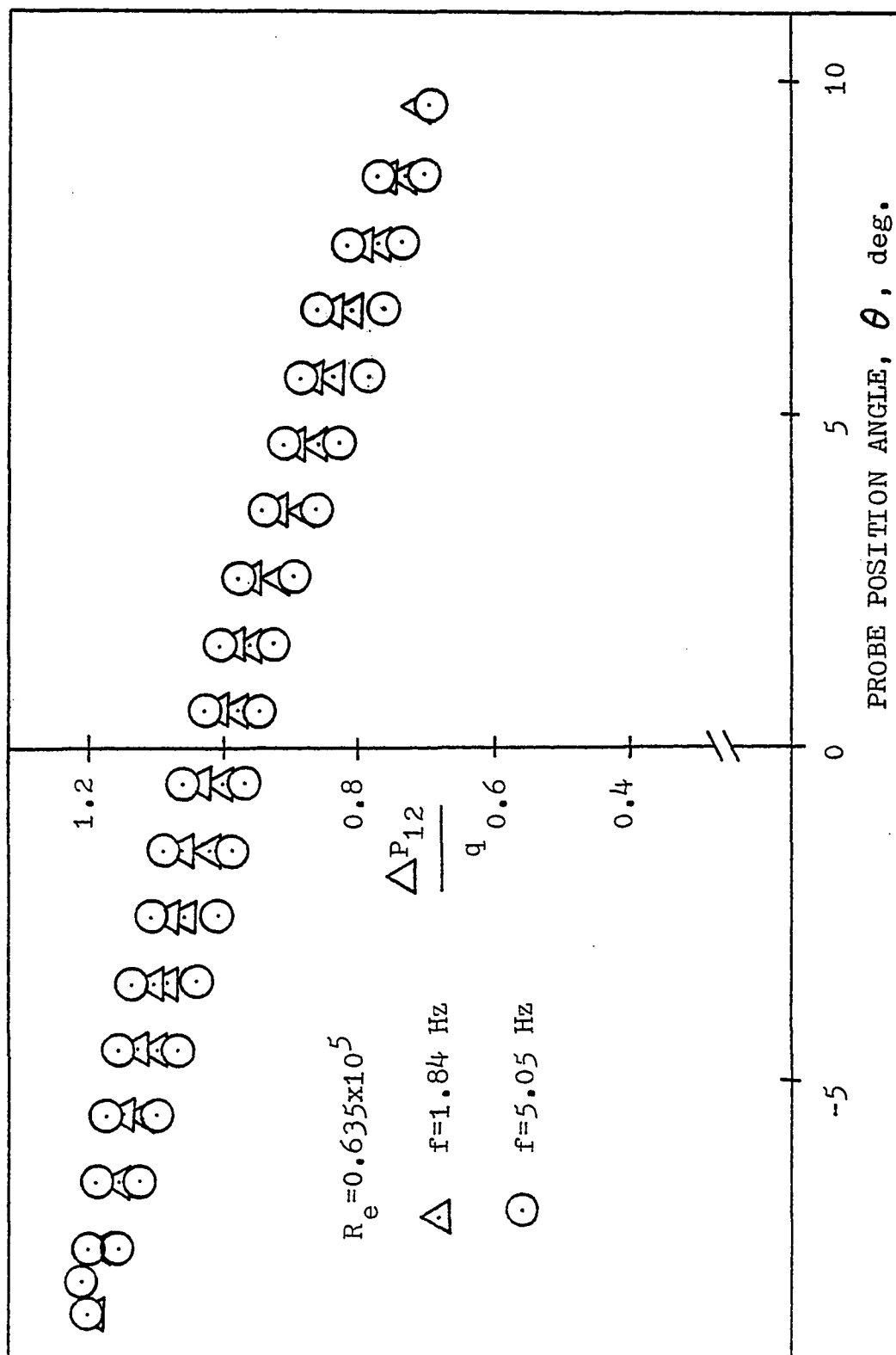
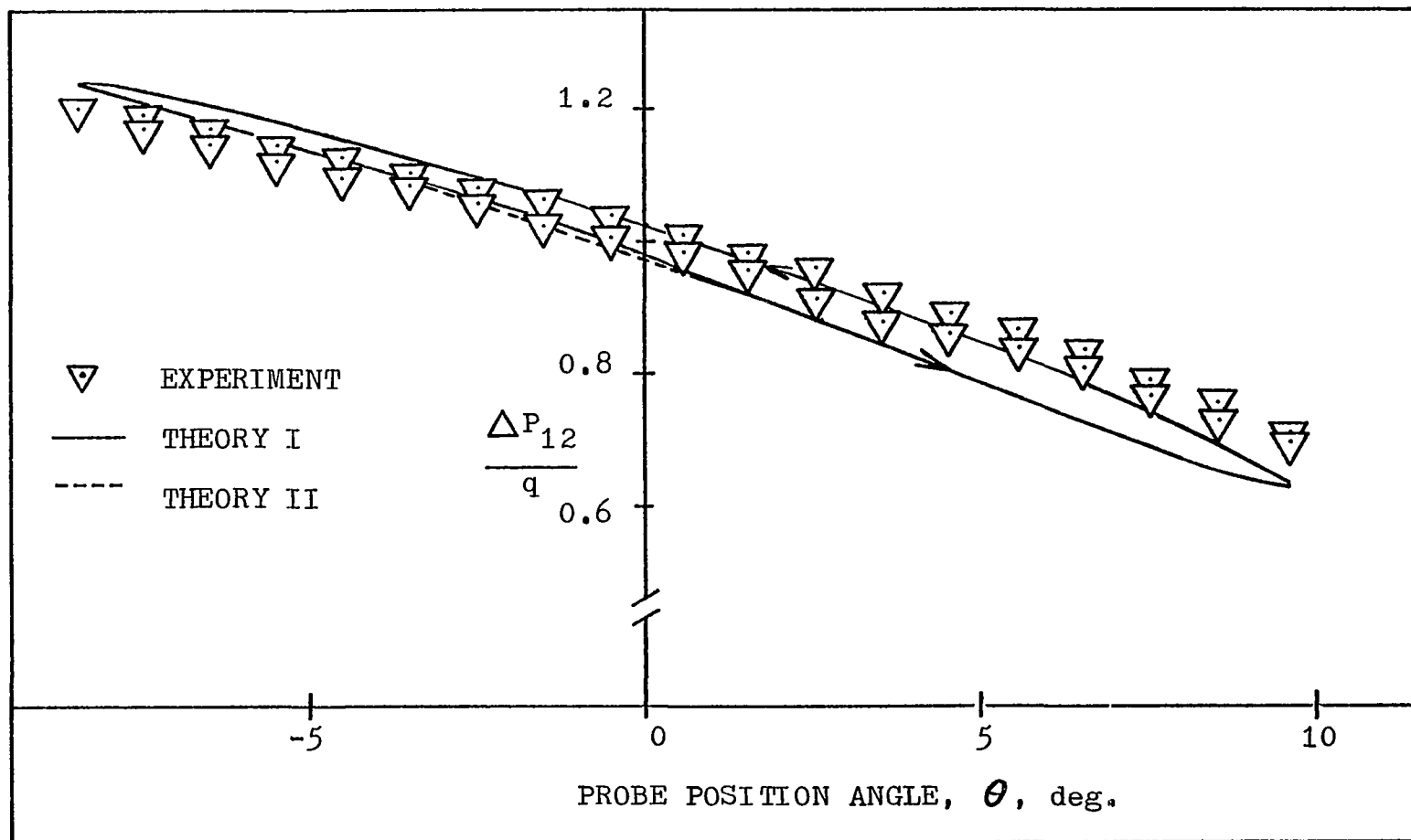
(b) $\Delta P_{12}/q$ VERSUS θ

Figure 5.7 Concluded

figure (2.7b). These data are also in qualitative agreement with predictions using Theory I.

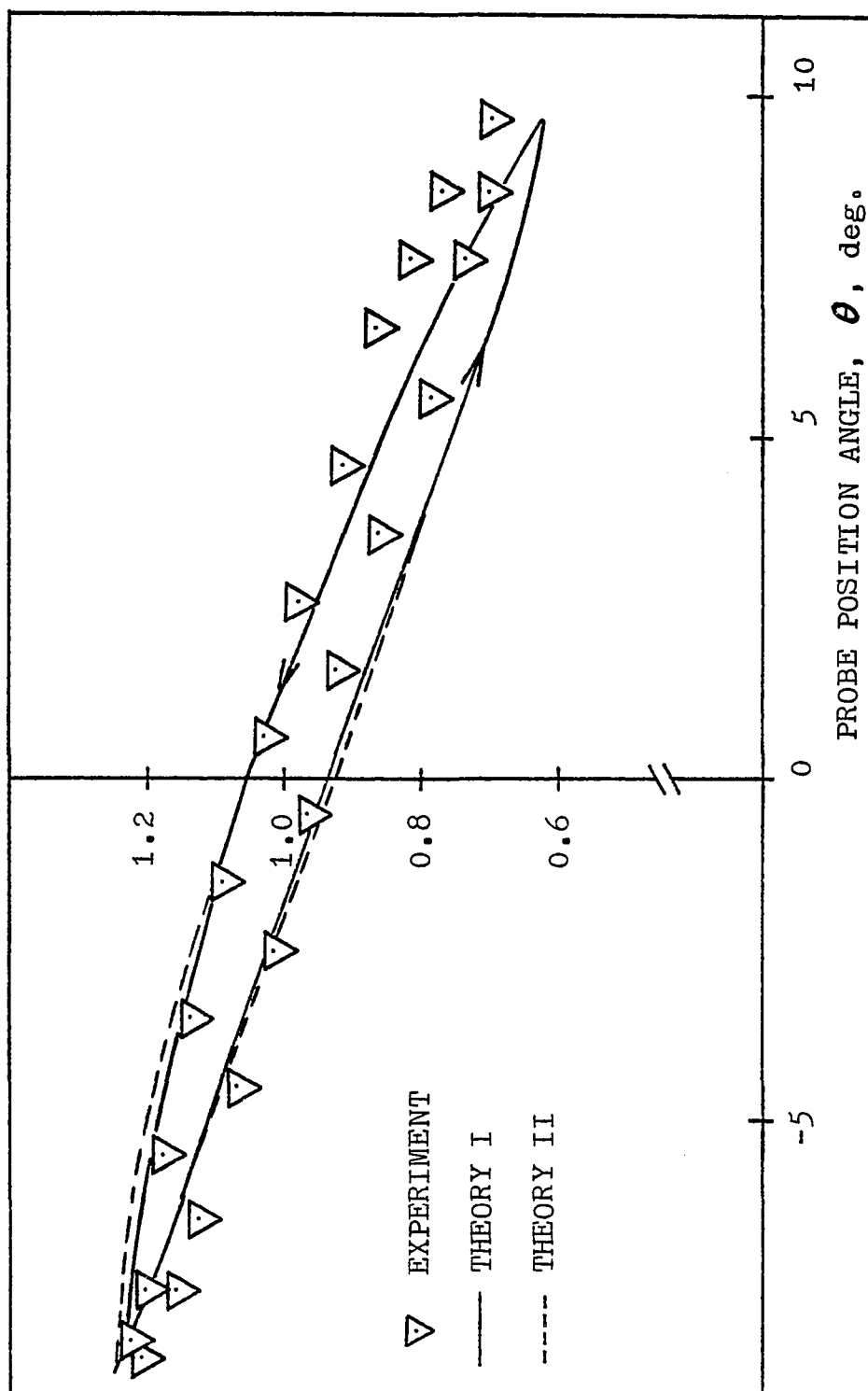
5.2.5 Comparison between Experiments and Theories

The theories presented in articles 2.4, 2.5, and 2.6 are now compared with the same experiment simultaneously. Various oscillating frequencies, airstream velocities, and ranges of probe angles were chosen for the purpose of comparison and the results are illustrated in figures (5.8) to (5.10). Figure (5.8) shows comparisons of experiment with Theory I and Theory II for $\Delta P_{12}/q$. The probe position angle varied from 9.65° to -8.5° . The airstream velocity was 30.5 m/s, corresponding to $R_e = 0.635 \times 10^5$, and oscillating frequencies were 1.84 and 5.05 Hz respectively. The discrepancy between the two theories was found small. The theories estimate smaller quantities for ΔP_{12} when the probe was near the lowermost position and higher values for ΔP_{12} when the probe was near the uppermost position. In figure (5.9), sample experimental results and theoretical prediction of $\Delta P_{23}/q$ variation have been plotted and compared. Figures (5.9a, b) show comparisons under test conditions of $U = 17.5$ m/s, for the probe position angle range $-25.5^\circ \leq \theta \leq 7.5^\circ$, with oscillating frequencies $f = 2.43$ and 3.57 Hz respectively. Theory I and Theory II fell very close to one another for $|\theta| < 10^\circ$, but differed for $-25.5^\circ < \theta < -10^\circ$ except at the extreme probe position. In these two figures, the experimental data and both theories were fairly close, the maximum error in θ



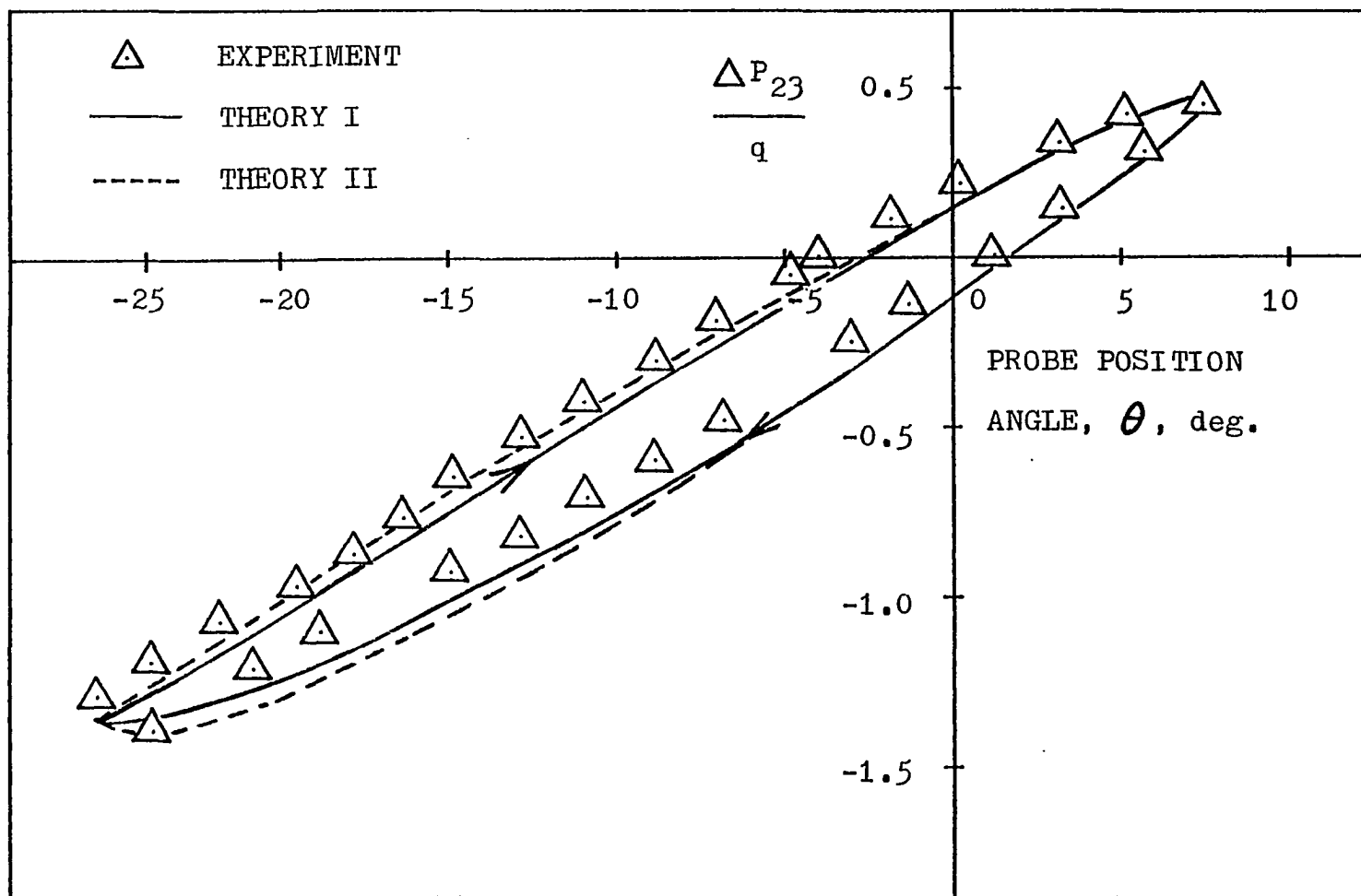
(a) $R_e=0.635 \times 10^5$, $f=1.84$ Hz, AND $b_{12}=2.03$

Figure 5.8 Comparison of experiment and theories, $\Delta P_{12}/q$ versus θ .



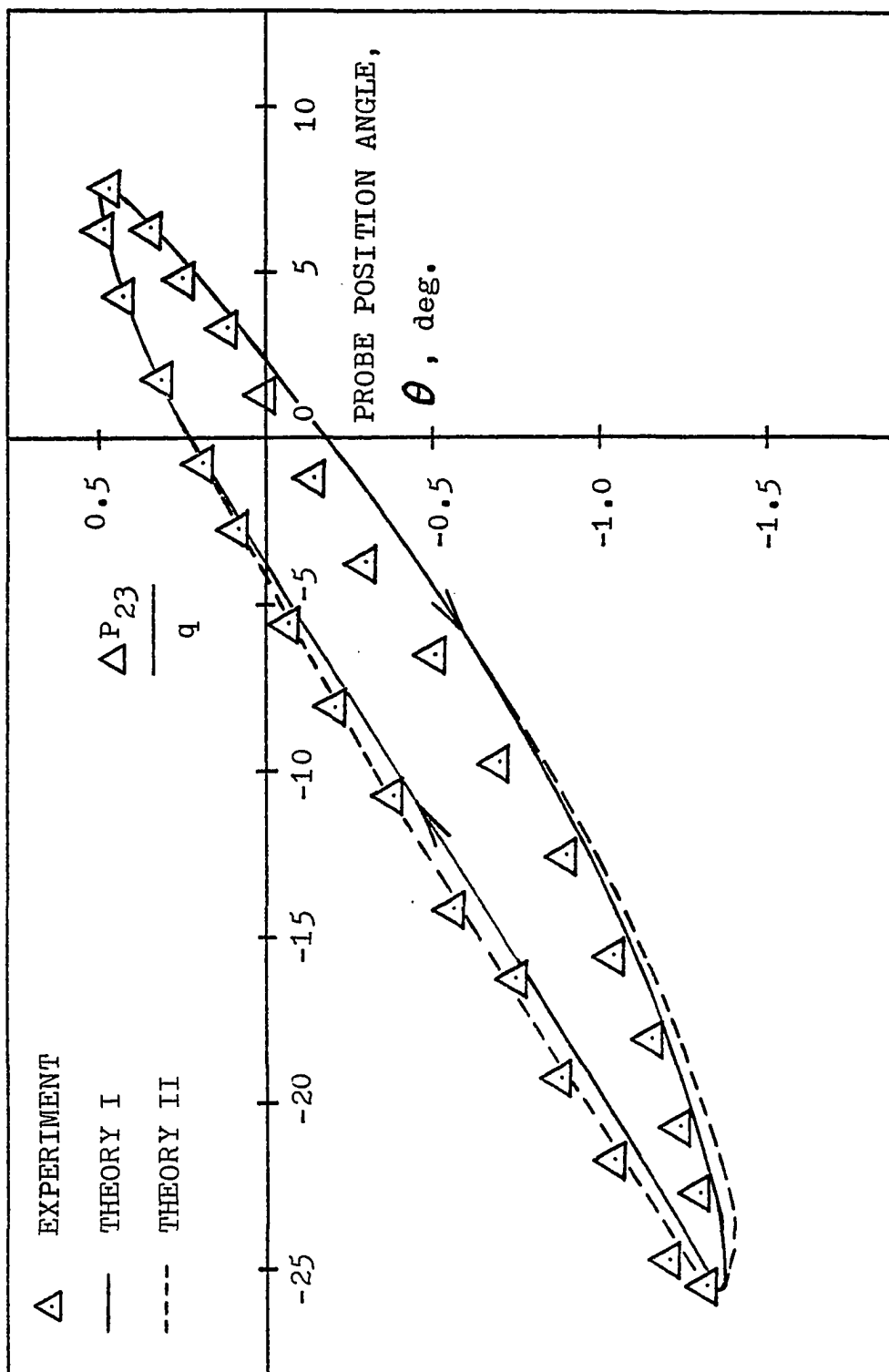
(b) $R_e = 0.635 \times 10^5$, $f = 5.05$ Hz, AND $b_{12} = 2.03$

Figure 5.8 Concluded



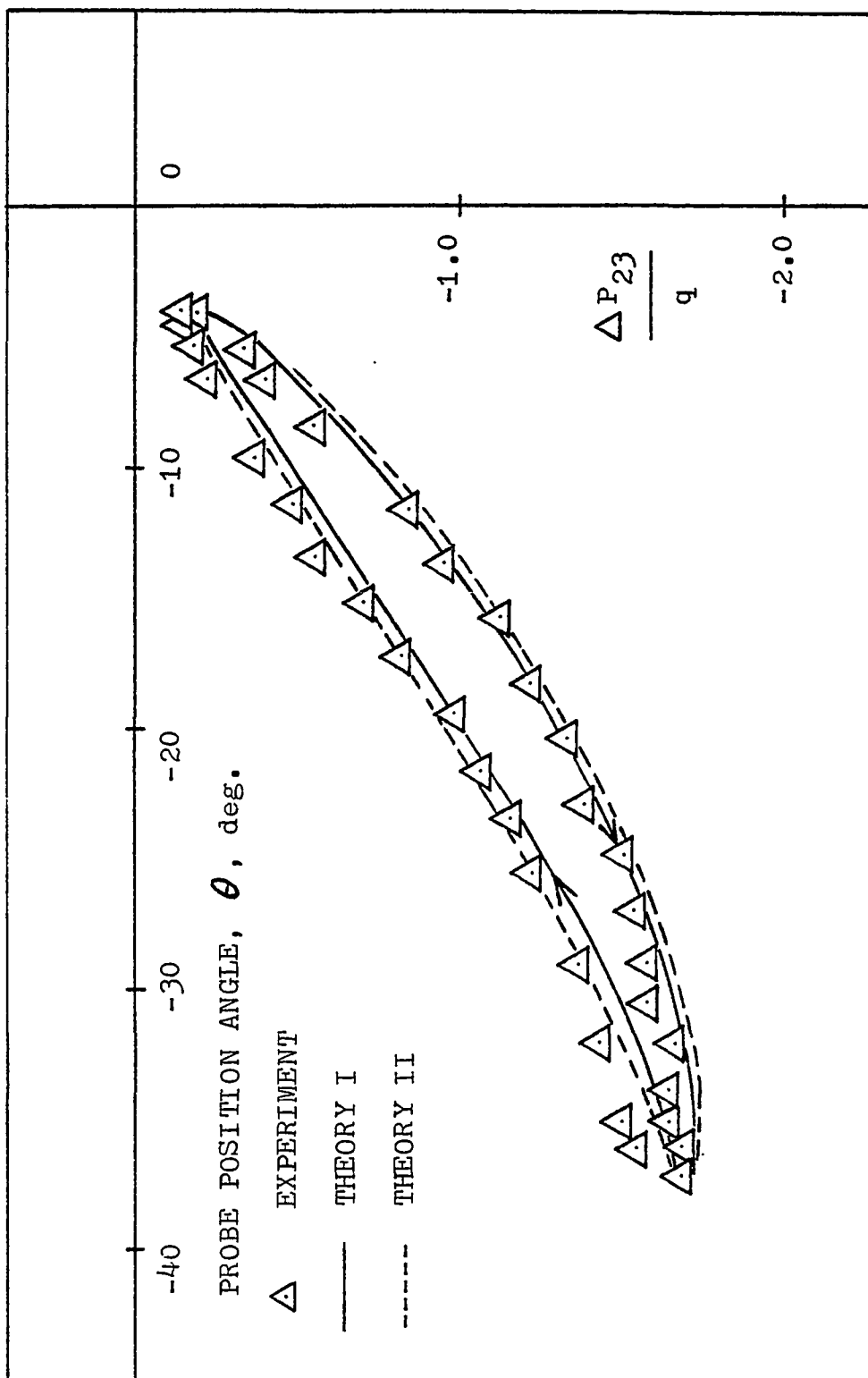
(a) $R_e = 0.365 \times 10^5$, $f = 2.43$ Hz, AND $b_{23} = 1.79$

Figure 5.9 Comparison of experiment and theories, $\Delta P_{23}/q$ versus θ .



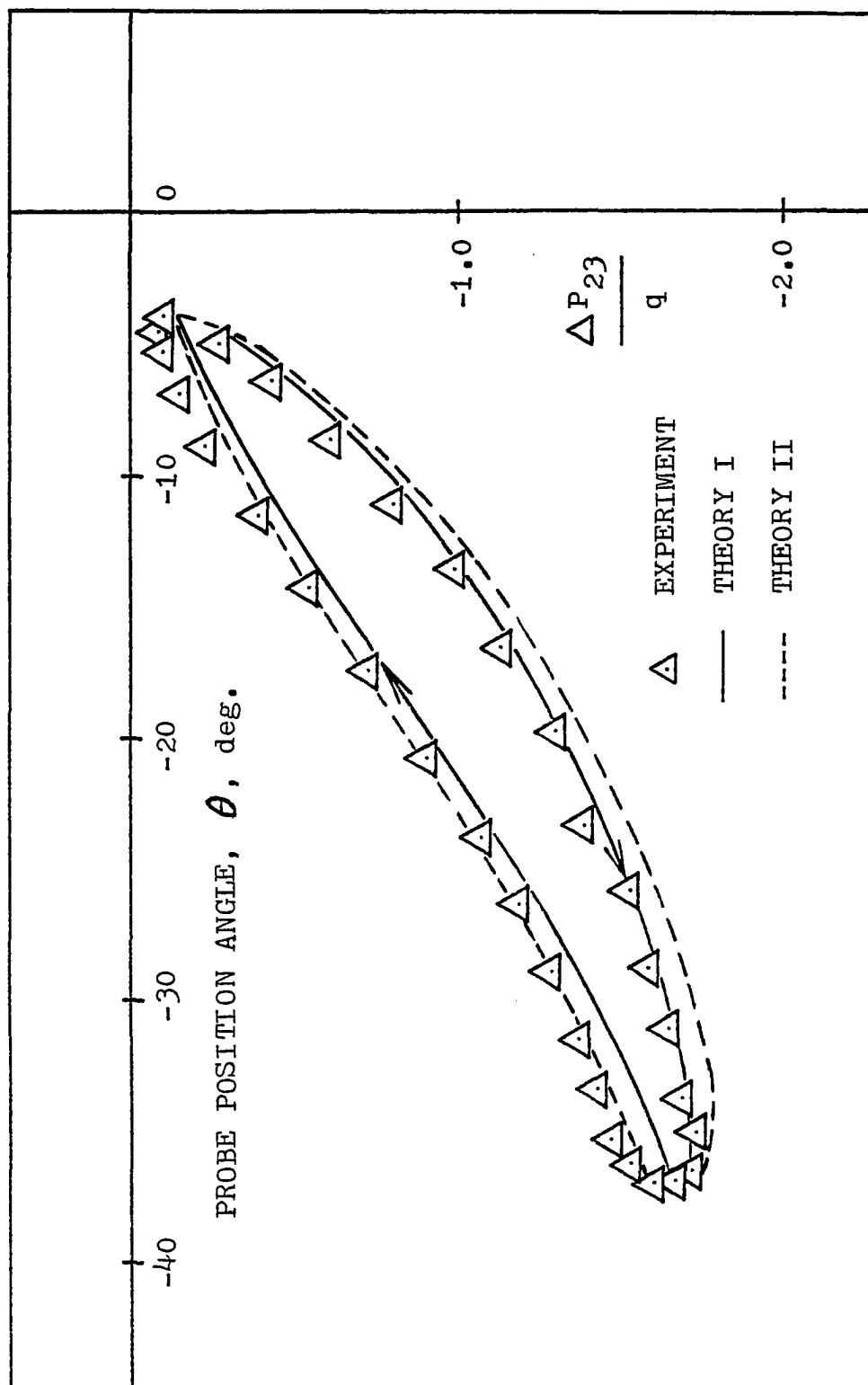
(b) $R_e = 0.365 \times 10^5$, $f = 3.57$ Hz, AND $b_{23} = 1.79$

Figure 5.9 Continued



(c) $R_e = 0.635 \times 10^5$, $f = 2.72$ Hz, AND $b_{23} = 1.79$

Figure 5.9 Continued

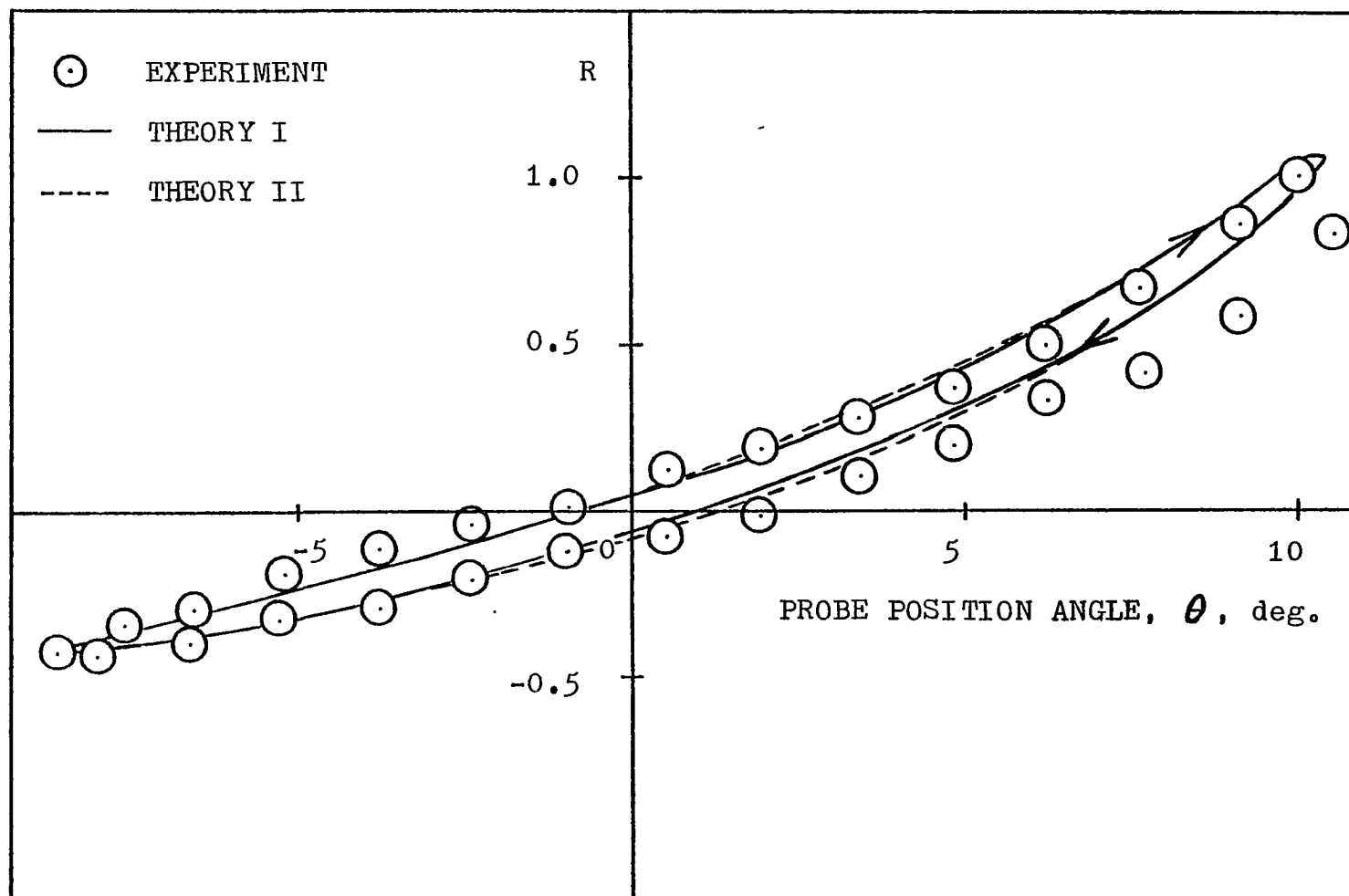


(d) $R_e = 0.635 \times 10^5$, $f = 4.03$ Hz, AND $b_{23} = 1.79$

Figure 5.9 Concluded

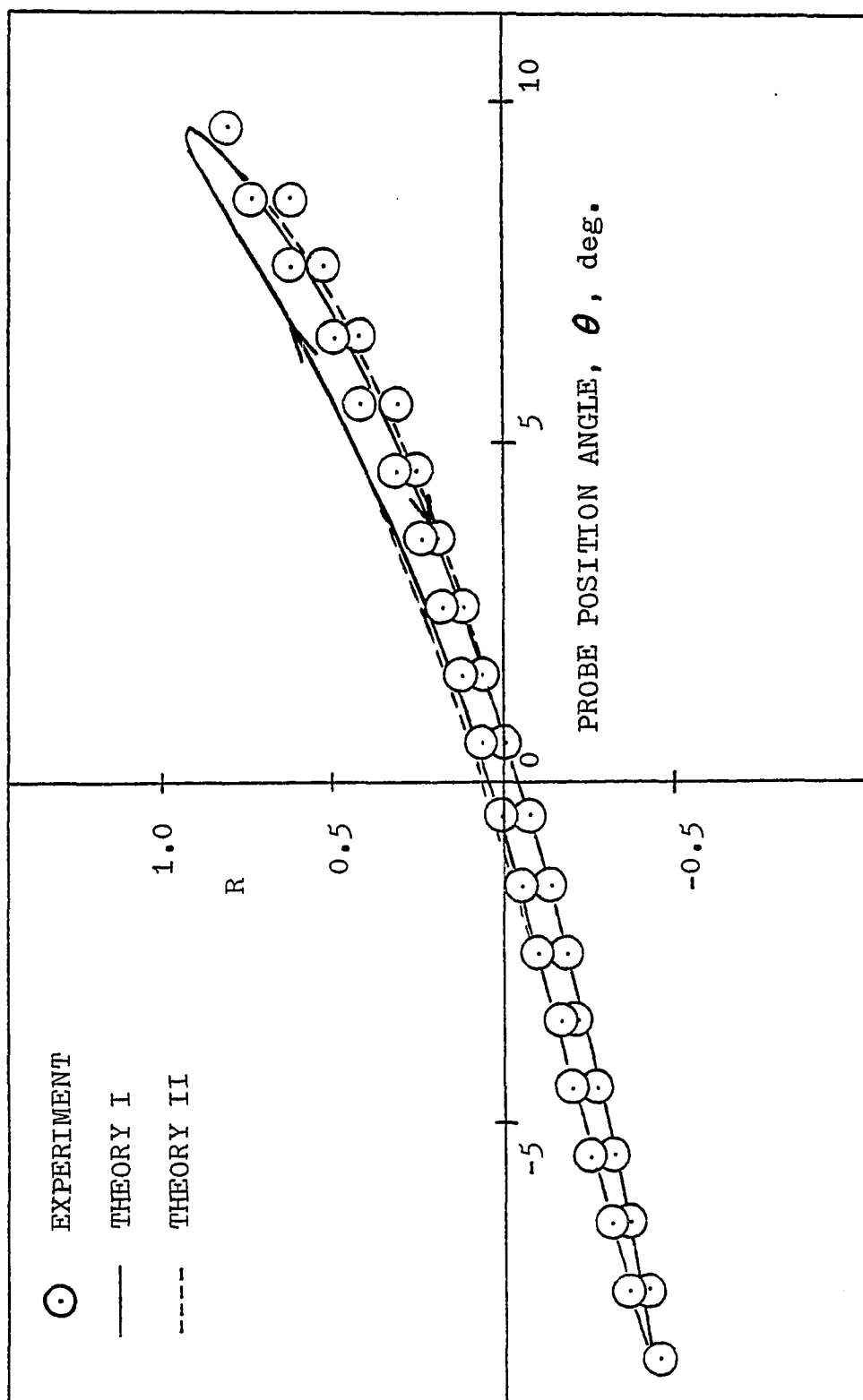
being about 2 degrees. Figures (5.9c, d) show comparisons under the test conditions of $U=17.5$ m/s for probe position angles of $-37.2^\circ \leq \theta \leq -4^\circ$, with oscillating frequencies $f=2.72$ and 4.03 Hz respectively. These two figures show that when probe position angle, θ , was large, i.e., $-37.2^\circ < \theta \leq -10^\circ$, the difference between the two theories was quite significant. Theory I agreed better with data for the oscillating motion from the lowermost position to the uppermost position, while Theory II agreed better when the probe moved downwards. Figure (5.10) shows the comparison of the pressure differential ratio, R , variation with both theories. Figure (5.10a) shows results for test conditions of $U=83.8$ m/s, $f=4.9$ Hz, and $-9.6^\circ \leq \theta \leq 10^\circ$. Figures (5.10b, c) show the results under test conditions of $U=30.5$ m/s, $-8.5^\circ \leq \theta \leq 9.65^\circ$, for $f=1.84$ and 5.05 Hz respectively. These three figures show no significant difference between the two theories; both theories overestimated the values of R for probe position angles below the horizontal reference line. Hence, for negative probe position angle, i.e., $0^\circ < \theta \leq \theta_U$, the theoretical R curves were close to experimental data, with a maximum error of about 2 degrees. For example, an upwards probe motion with $R=-0.23$ in figure (5.10c) corresponds to $\theta=-2.4^\circ$ on the Theory II curve, but the data corresponds to $\theta=-1.5^\circ$; hence, the error is 0.9° . As discussed in section 4.5, the experimentally observed time lag between the probe motion and pressure differential response is considered as the major reason for these errors. A

horizontal shift of $\theta = -0.5^\circ$ in figure (5.10c), equivalent to a time delay of 0.0055 seconds, will put most of the data near to the theoretical curves. This time lag phenomenon is believed to be due to local flow conditions which cannot instantaneously follow the probe motion. From Ref. 20, the maximum Reynolds number for laminar flow around a sphere is 3×10^5 based on the sphere diameter, a value larger than R_e for the current data. The laminar separation point for a sphere is about 110° from the front stagnation point for steady flow (Ref. 21). Hence, under the present oscillating test conditions, the probe head portholes appear to be far away from the separation point. The pressure time delay is believed to be due to inertial effects as the probe is under the oscillating motion. The air surrounding the probe head is either pushed ahead of or sucked in behind the probe according to the probe motion. When the probe moves upward, the upper half surface pushes the air above it and the air below the probe is pulled behind somewhat due to the probe's upward motion. When the probe stops its upward motion at the uppermost position, the air in the neighborhood of the probe head still has the tendency to follow its original motion. When the probe starts to move downward, the air flow then is forced to change its direction and follow the probe motion. However, there must be some finite time for the upward moving air to reverse its direction. Hence, the static pressure on the surface of the spherical probe head is influenced by the local air flow conditions near the probe head just outside



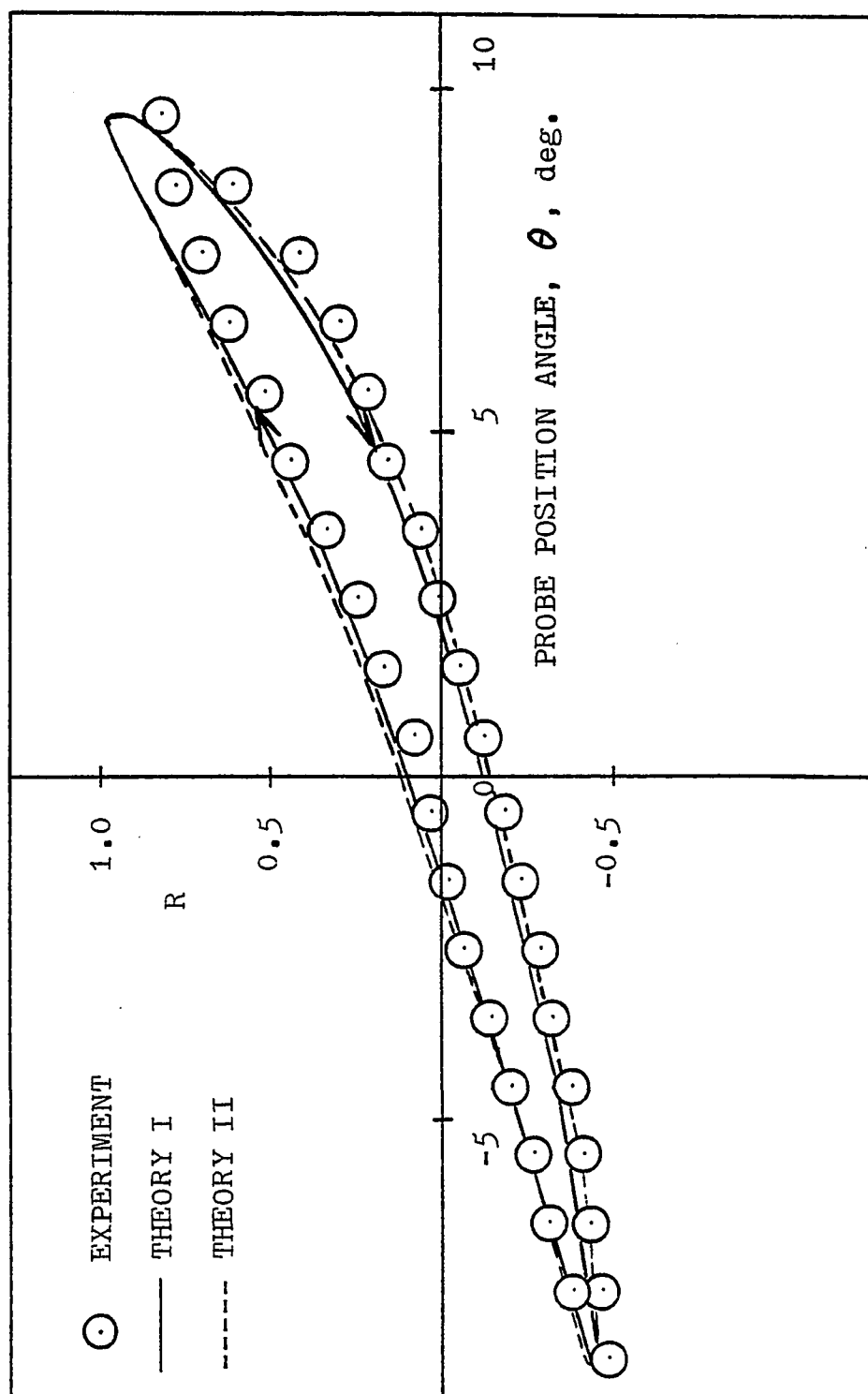
(a) $R_e = 1.74 \times 10^5$, $f = 4.9$ Hz, $b_{12} = 2.03$, AND $b_{23} = 1.79$

Figure 5.10 Comparison of experiment and theories, R versus θ .



(b) $R_e = 0.635 \times 10^5$, $f = 1.84$ Hz, $b_{12} = 2.03$, AND $b_{23} = 1.79$

Figure 5.10 Continued



(c) $R_e = 0.635 \times 10^5$, $f = 5.05$ Hz, $b_{12} = 2.03$, AND $b_{23} = 1.79$

Figure 5.10 Concluded

of the boundary layer. Since the air flow motion cannot follow the probe motion instantaneously, the transducers inside the probe then respond to the time delayed air motion, so that the pressure differential outputs show the observed time lag phenomenon. As observed in article 4.5, this time delay appears to increase linearly with increasing frequency for a fixed air speed. This is in agreement with unsteady aerodynamic theories developed for small reduced frequencies (Ref.22). The reduced frequency, k , is defined as $k=2\pi fD/U$. For the current study $D=0.0318$ m, while 9.99 rad/sec $\leq 2\pi f \leq 32.7$ rad/sec and 11.6 m/s $\leq U \leq 88.4$ m/s, so that $0.0036 \leq k \leq 0.090$. Thus, the current data has been obtained under the condition of small k values. Brune showed in Ref. 22 that unsteady aerodynamic problem for $k < 1$ could be solved approximately through expansion of the solution in a power series in k , where the lowest order solution solved a set of steady equations. The second order solution is proportional to the reduced frequency, k . In the current work Theories I and II are the lowest order solutions to the unsteady problem; in their formulation they do not permit any phase lag between the probe motion and the fluid motion. A second order solution is expected to improve the agreement between Theory II and experiment.

5.3 Theoretical Prediction of Time Dependent Angle of Attack

Theoretical prediction of time dependent angle of attack, α_a , is possible by using either Theory I or Theory II. These predictions are best for small f and large U , corresponding to small k . From article 2.7, the non-dimensional pressure differential ratio, R , is found to be a strong function of U , f , and θ . The relations between the probe position angle, θ , and the angle of attack, α_a , are given by equation (2.2-6) for Theory I and equation (2.3-30) for Theory II. A theoretical study using Theory II for the following conditions has been made:

$$\theta = -15^\circ - 5^\circ \sin(2\pi f t)$$

$$U = 61 \text{ m/s (200 ft/sec)}$$

and

$$f = 4, 5, 6, \text{ and } 7 \text{ Hz.}$$

The results have been plotted in figures (5.11) and (5.12), from which the approximate time dependent angle of attack can be obtained once the pressure differential ratio, R , is known from the probe pressure differential outputs.

Assume under the test conditions that the airstream velocity, U , the oscillating frequency, f , the test data ΔP_{23} and ΔP_{12} are known. From the R value calculated from the pressure differential data and figure (5.11) and the oscillating motion direction (upward or downward), one can find a corresponding θ value. From this θ value and figure (5.12), a corresponding angle of attack, α_a , can be found. For example, using probe ODU2 and field test conditions ($U=30.5 \text{ m/s}$

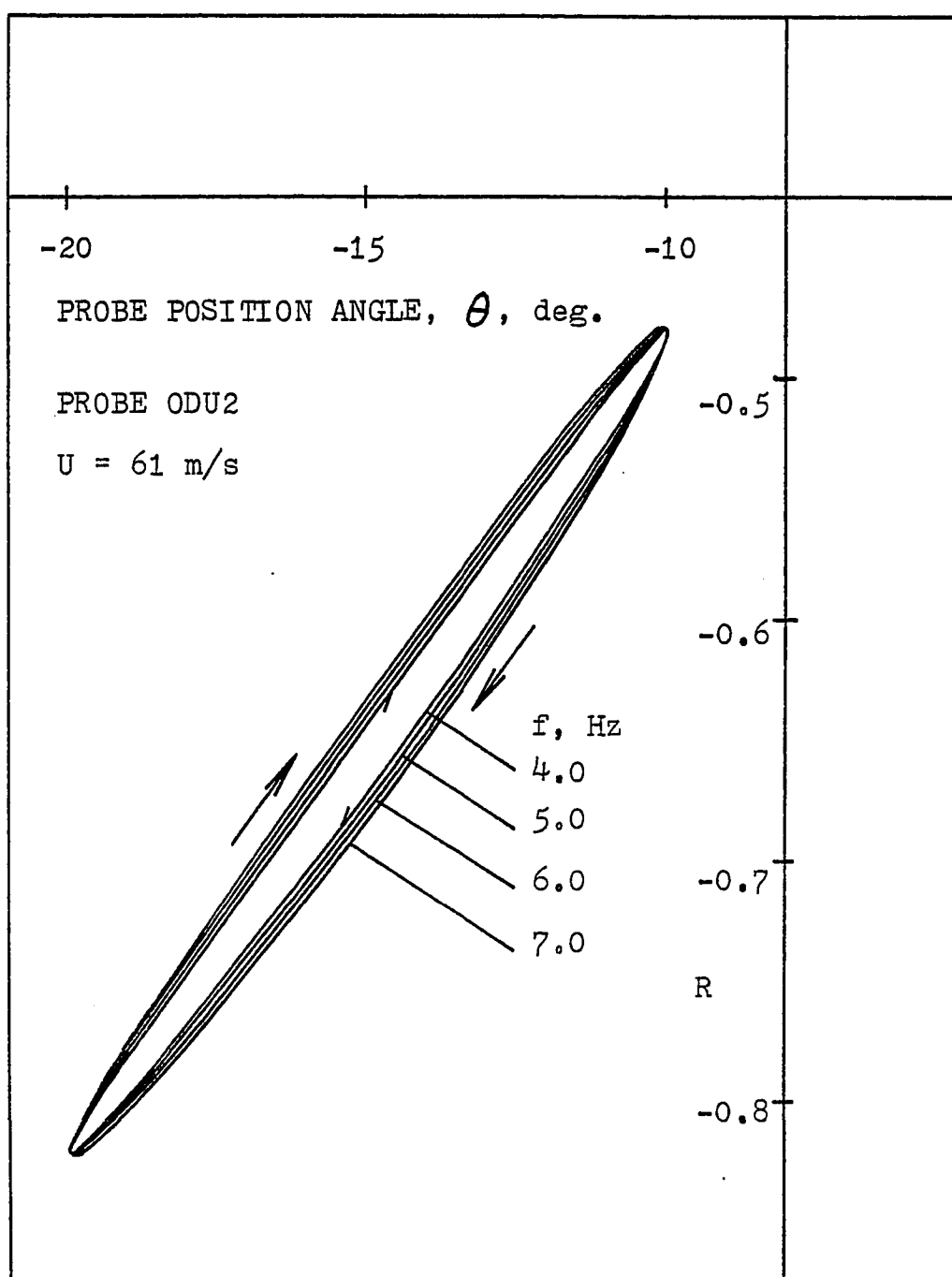


Figure 5.11 Theoretical prediction of R value as a function of θ , $R_e = 0.635 \times 10^5$, $b_{12} = 2.03$, and $b_{23} = 1.79$.

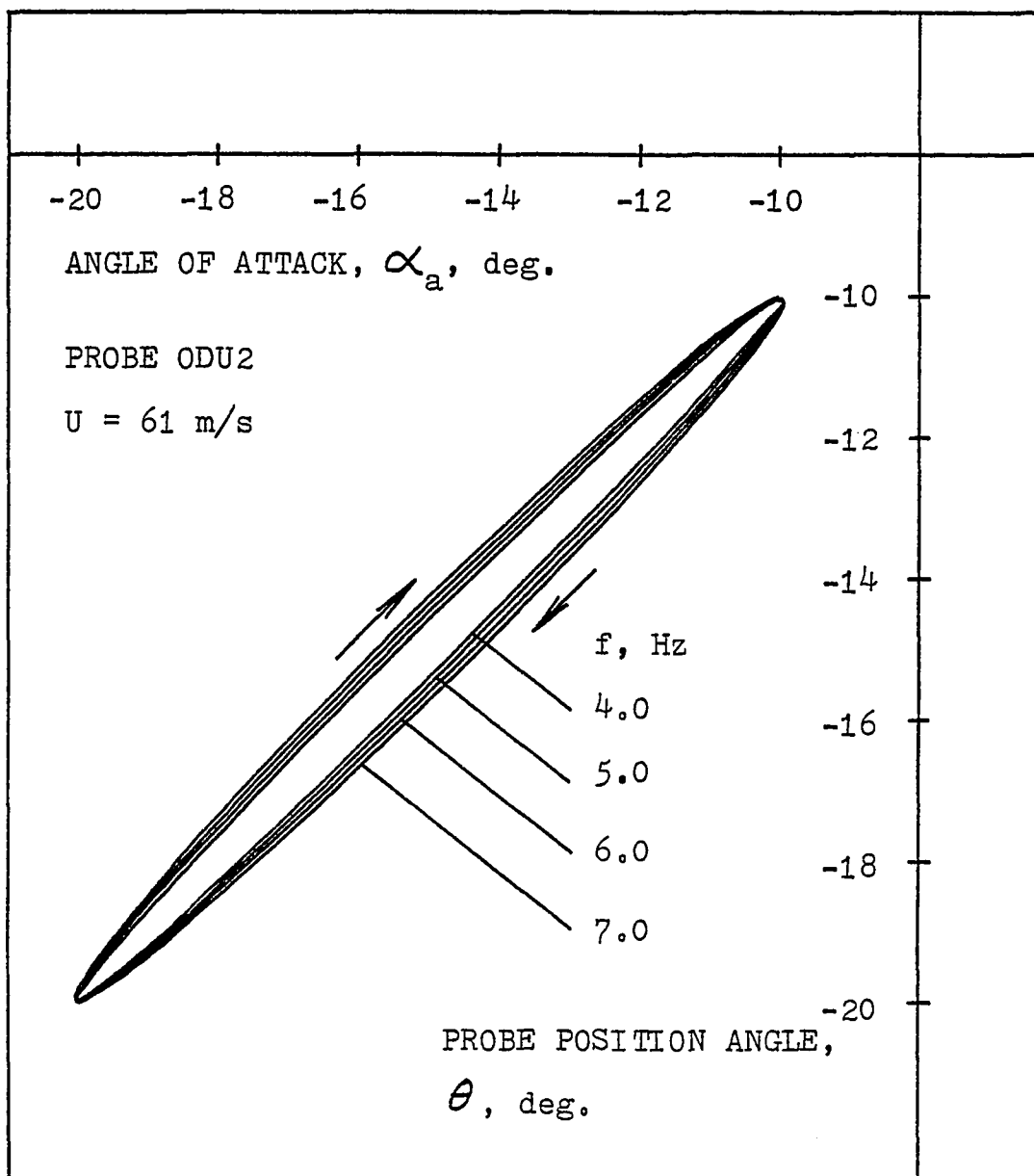


Figure 5.12 Theoretical prediction of angle of attack, α_a , $R_e = 0.635 \times 10^5$, $b_{12} = 2.03$, and $b_{23} = 1.79$.

and $f=1.84$ Hz), assume from the recorded ΔP_{23} and ΔP_{12} charts, one particular instant t^* yields an R value of 0.25 and indicates an upward motion. Then from figure (5.10b), a corresponding probe position angle $\theta=4.15^\circ$ is found from the Theory II curve, and from $\theta=4.15^\circ$ and upward probe motion, figure (5.13) yields an angle of attack $\alpha_a=3.5^\circ$. The experimentally measured θ at this value of t^* was 4.6° , yielding an error of 0.45° for θ and 0.5° for α_a .

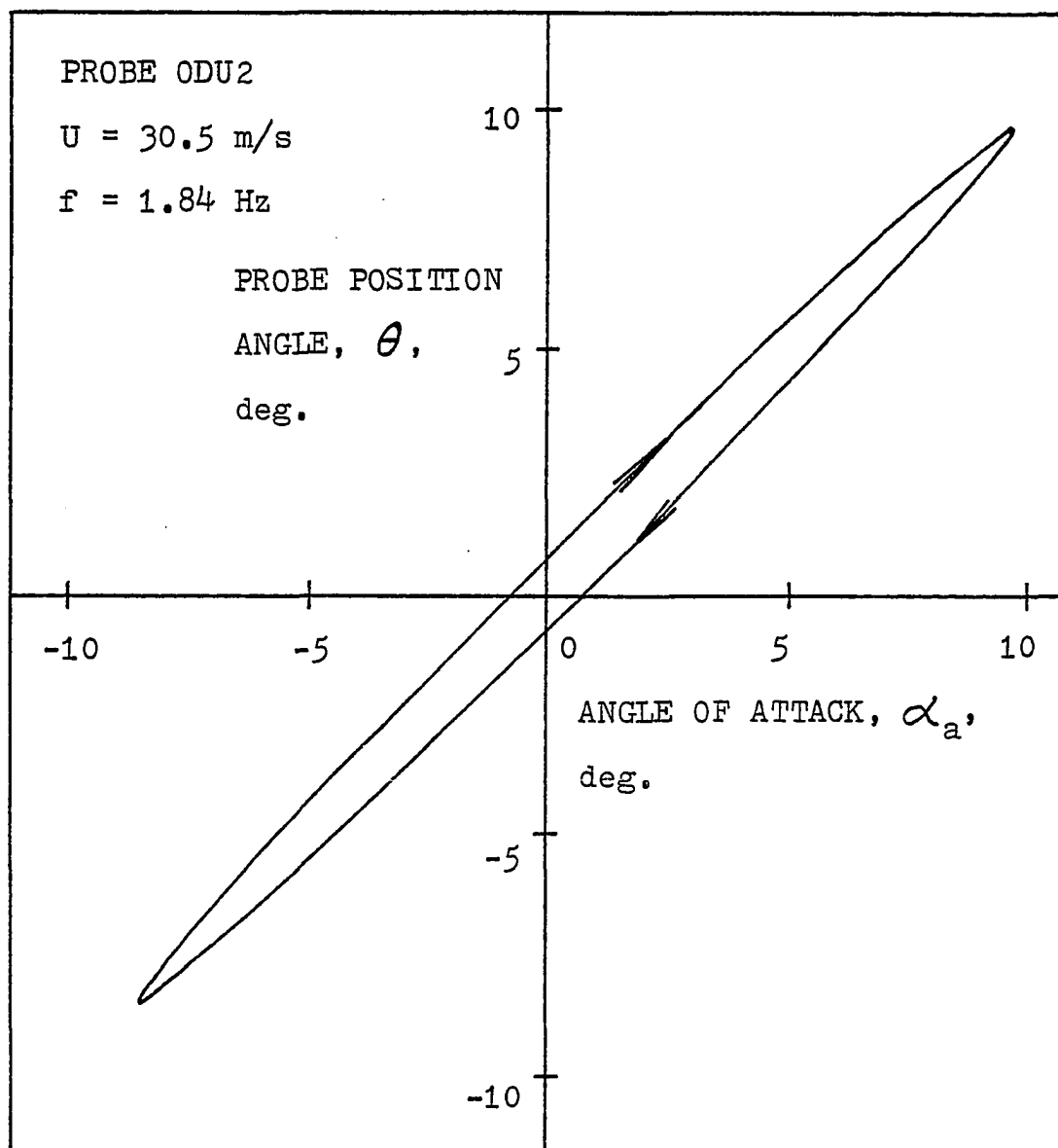


Figure 5.13 Theoretical prediction of angle of attack, α_a , $R_e = 0.635 \times 10^5$, $b_{12} = 2.03$, and $b_{23} = 1.79$.

VI. CONCLUSIONS

The objective of this study has been to design a pressure probe which can be used in a real helicopter blade system in flight. Totally five pressure probes were designed, and constructed either at NASA Langley Research Center or Old Dominion University. The calibration of probes has been carried out step by step experimentally. Both static and dynamic probe responses have been obtained and analyzed, and a theoretical analysis has been made to estimate the time dependent angle of attack through use of the experimental pressure differential responses.

The conclusions deduced from the theoretical and experimental results are as follows:

- 1) An influence of the cylindrical support behind the spherical head under the static test condition was found. The static pressure distribution curve was different when the probe position angle was larger than 35 degrees.
- 2) The experimentally determined probe coefficients were different from theoretical potential flow analysis assuming spherical geometry; these coefficients depend on the central angle between the two pressure ports, Reynolds number, as well as the probe geometry. The experimentally determined

probe coefficient based on the actual sphere-cylinder arrangement was always larger than the probe coefficient based on sphere only, largely due to the influence of the shank behind the probe head.

3) Static angle of attack calculation was close to the static theory. Using data points to predict the static angle of attack can yield a θ estimation to within $\pm 1^\circ$.

4) The experimentally determined probe coefficients have an important influence, as they are employed in the theoretical calculation of pressure differentials and R function. The best pair of coefficients b_{12} and b_{23} for probe ODU2, as judged by fitting the theories to the time dependent data, are found to be 2.03 and 1.79 respectively. These values lie within the ranges of probe coefficient values obtained from static tests at various Reynolds numbers.

5) The non-dimensional pressure differentials are functions of the airstream velocity, oscillating frequency, and probe position angle. Under a confined range of oscillation, i.e., $\theta_U \leq \theta \leq \theta_L$, for a constant airstream velocity, when the oscillating frequency, f , increased, the spread of the contour of $\Delta P/q$ versus θ also increased. For tests with a constant oscillating frequency, as the airstream velocity, U , increased, the contour separation of $\Delta P/q$ decreased. Hence, the effects of U and f on pressure difference were found to be opposite to one another. However, it is noted that either increasing f or decreasing U yields an increase in the reduced frequency, k . Thus, the contour spread

increases as k increases, or in other words as the probe velocity increases relative to the airstream velocity.

6) The variation of non-dimensional pressure differential $\Delta P_{23}/q$ with the probe position angle, θ , for Theory I, Theory II, and experimental data were found to agree to within 2 degrees for low oscillating frequencies (f less than 3 Hz) and high airstream velocities (U above 30.5 m/s).

7) The variation of pressure differential ratio, R , and pressure differential, $\Delta P_{12}/q$, with probe position angle, θ , for both Theory I and Theory II were found to be in error for probe angles near the lowermost position. R was overestimated there near the lowermost position due to the underestimation of $\Delta P_{12}/q$.

8) Time dependent angle of attack can be estimated by using either Theory I or Theory II from the pressure differential ratio, R . The experimental data are at most 2~3 degrees off the theoretical prediction for airstream velocities of 30.5 to 83.8 m/s and frequencies below 5.05 Hz.

9) This observed 2~3 degrees disagreement between the theories and experiment appears to be due to a time lag between the true probe motion and the probe pressure difference response. It is believed that this is a real time lag phenomenon, which is due to unsteady inertial and boundary layer effects, and which is not accounted for in the theories. Development of a more complete theory is likely to improve the agreement between experiment and theory and thereby improve the accuracy of the angle of attack prediction.

From the above conclusions, it appears possible to use probe ODU2 to measure the time dependent angle of attack of a helicopter blade system in flight to an accuracy of approximately $\pm 2^\circ$. With known flight velocity, rotor blade rpm, and maximum and minimum blade position angles, the continuous pressure differential outputs could be used to electronically calculate the pressure differential ratio and hence the time dependent angle of attack. Since actual helicopter blade motion would occur over a range of U larger than that of the current study, further reducing the k values perhaps this prediction might be made adequately using Theory I. However, since this would also correspond to larger R_e values and Mach numbers, it is recommended that further tests of the probe be conducted to cover these R_e and Mach number ranges to accurately determine b_{12} and b_{23} .

APPENDIX A

TESTS ON HEMISPHERICAL YAWMETERS

TESTS ON HEMISPHERICAL YAWMETERS

Three hemispherical yawmeters were tested under steady flow conditions. These yawmeters consisted of a hemisphere attached to a cylinder of the same diameter as shown in figure (A.1). Five portholes were drilled into the head: a center porthole located in the yawmeter axial axis and four holes at the side. Each side porthole had the same central angle, which varied for the various probes. The three probes had 45, 33 and 22.5 degrees central angles respectively.

The static tests were performed under similar conditions: first the pressure difference between portholes T and B or L and R was reduced to zero, then the yaw or pitch angle was varied. Figure (A.2) shows the variation of pressure differentials with yaw angle, β , for three yawmeters with different central angle γ . Figure (A.3) shows the variation of pressure differentials with pitch angle, θ .

The purpose of this investigation was to find the relation between the side port central angle γ and the probe response linear range. Although Wesely et al (Ref. 9) stated that smaller side port central angles have a wider acceptance angle, present experimental results for $-30^\circ \leq \beta \leq 30^\circ$ and $-30^\circ \leq \theta \leq 30^\circ$ showed the $\gamma=22.5^\circ$ probe to be no better than the $\gamma=33^\circ$ or 45° probes.

Important observations from this investigation were as follows:

- 1) These three hemispherical yawmeters were only satisfactory for static tests. The long tubing and manometer arrangement could not give a correct response for unsteady flow.
- 2) The stagnation point was displaced from the theoretical stagnation point based on a perfect sphere assumption. When the yawmeter was placed at an angle of attack α_a , the flow pattern around the hemispherical yawmeter became asymmetrical due to the large cylindrical support. (See a related discussion in Appendix F.)
- 3) Since the $\gamma=33^\circ$ probe did not have exactly 33° for side ports, both figure (A.2b) and figure (A.3b) yielded different slopes for $\Delta P_{\beta 3}$ and $\Delta P_{\theta 3}$ respectively.
- 4) The $\gamma=45^\circ$ yawmeter had a larger linear range than the $\gamma=33^\circ$ and 22.5° yawmeters.

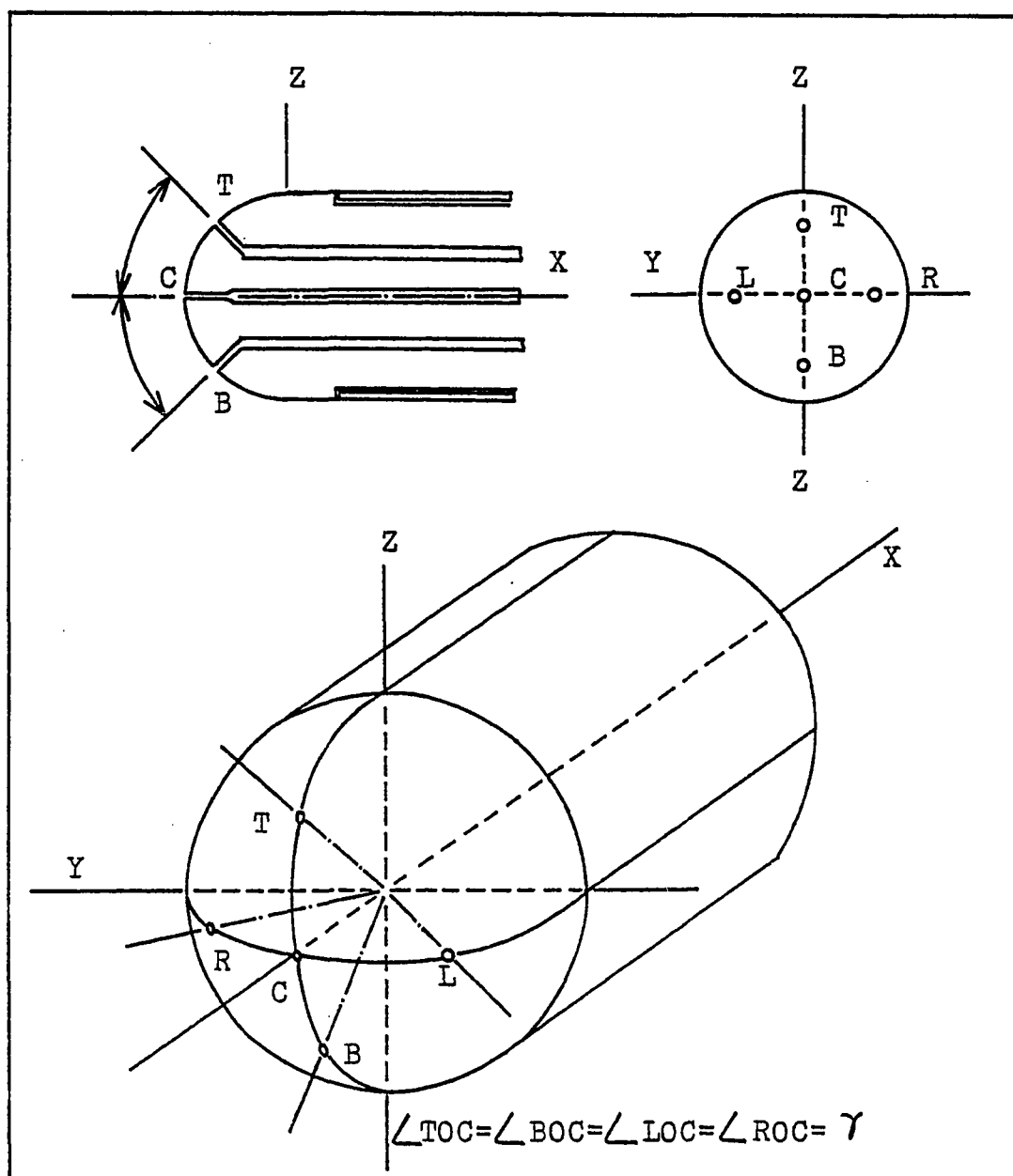
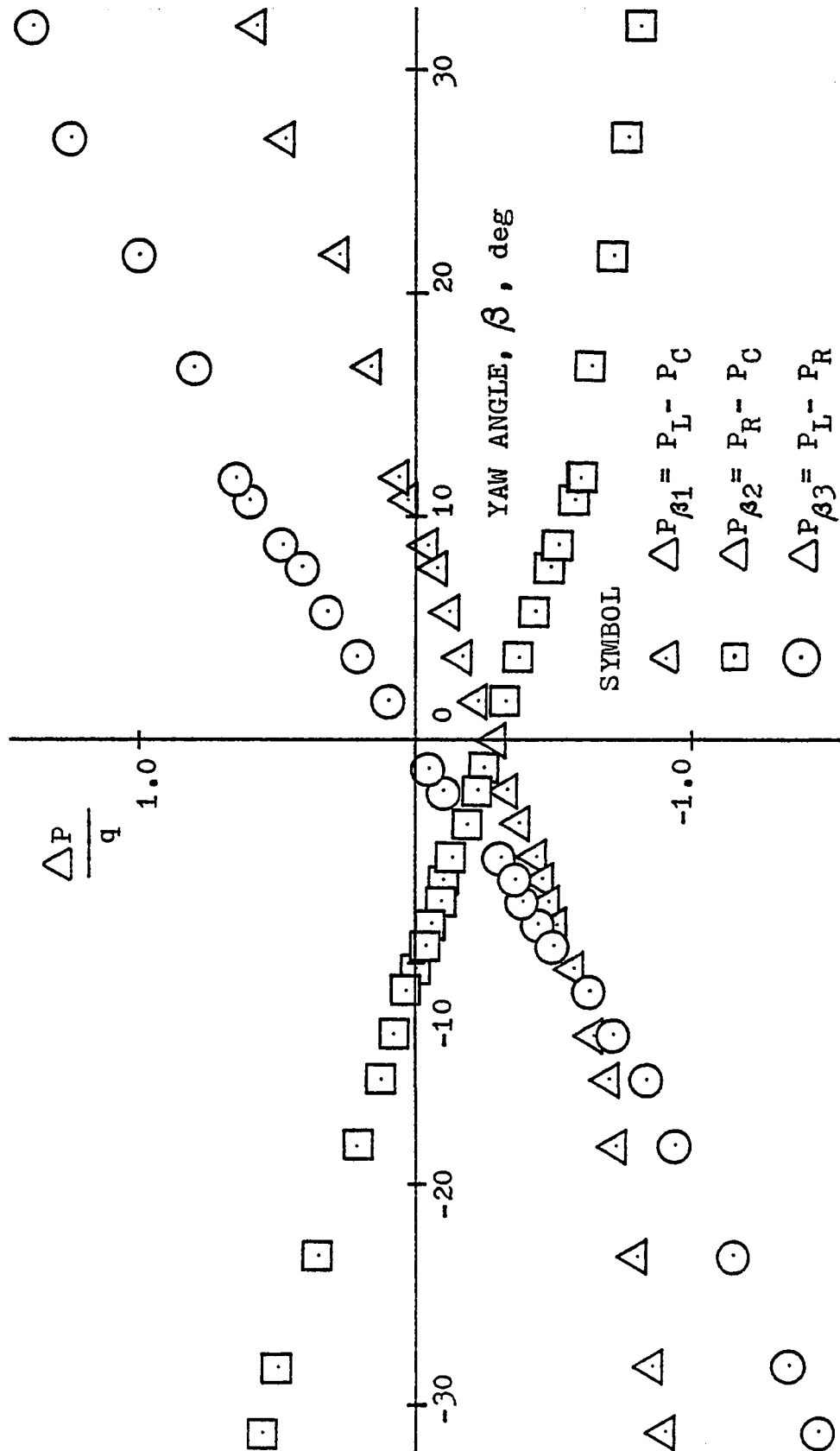
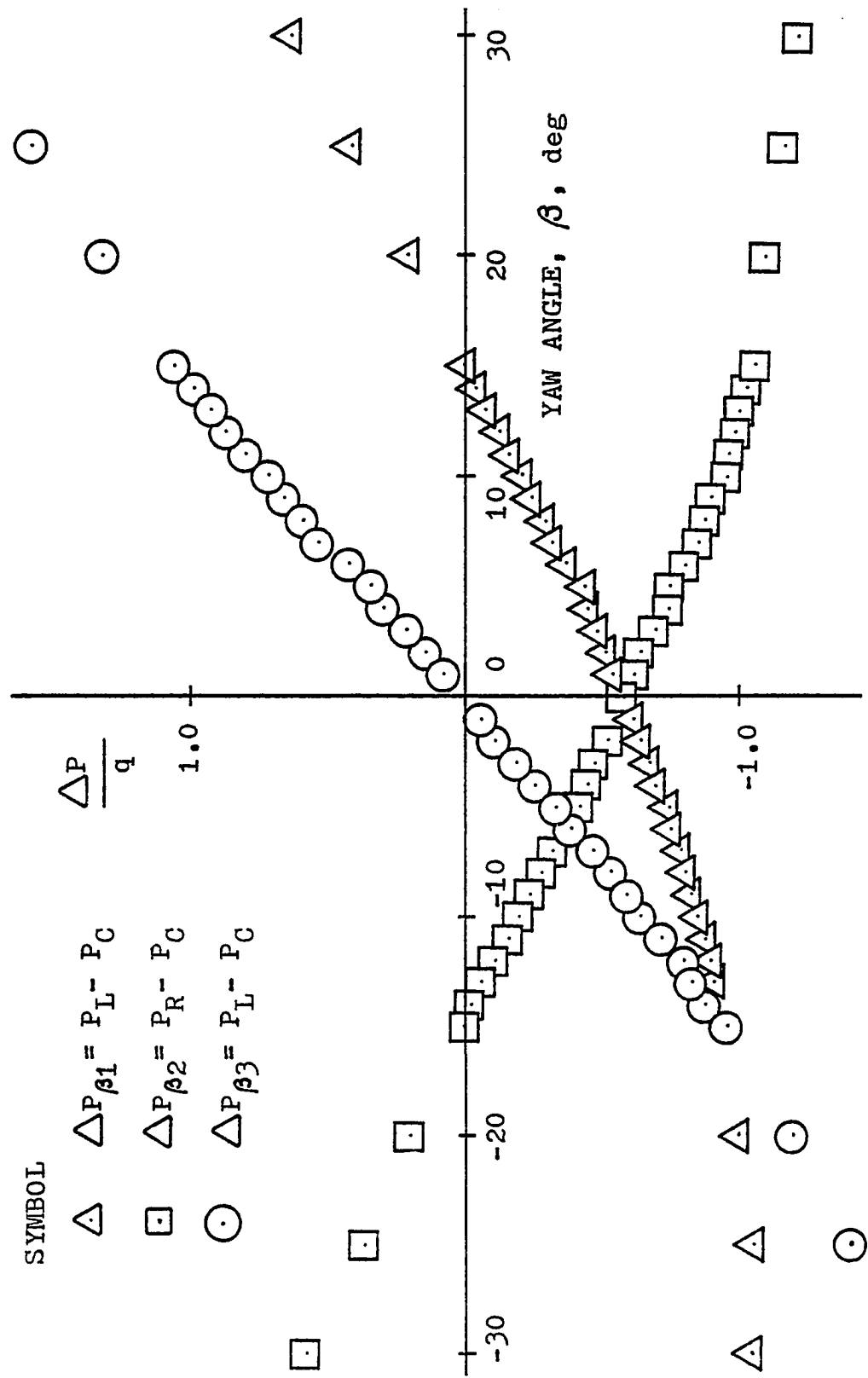


Figure A.1 Definition sketch of a 5-porthole hemispherical yawmeter.



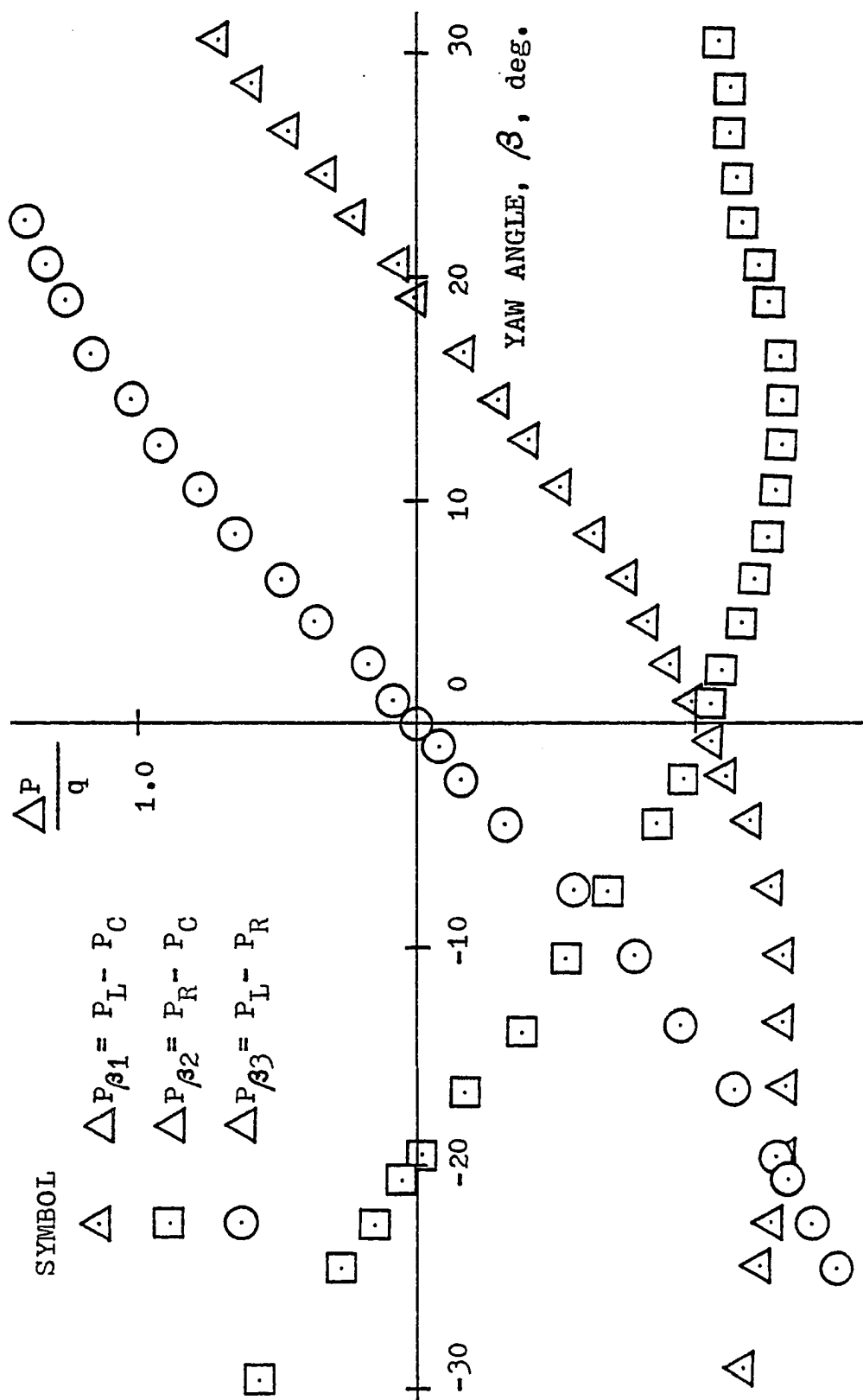
(a) $q=118$. newtons/m², $\gamma=22.5^\circ$

Figure A.2 Variation of pressure differentials with yaw angle.



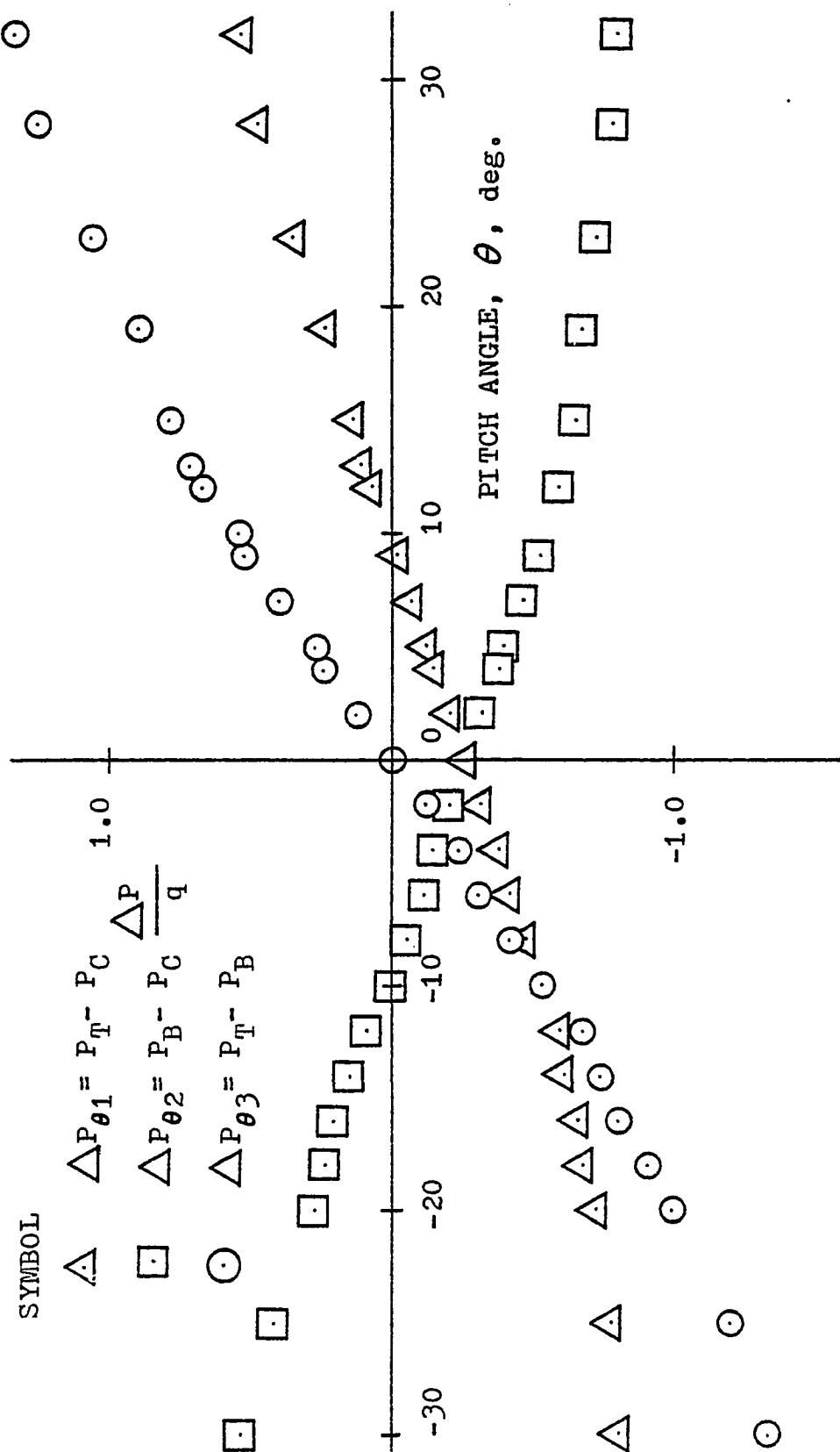
(b) $q=75.1$ newtons/m², $\gamma=33^\circ$

Figure A.2 Continued



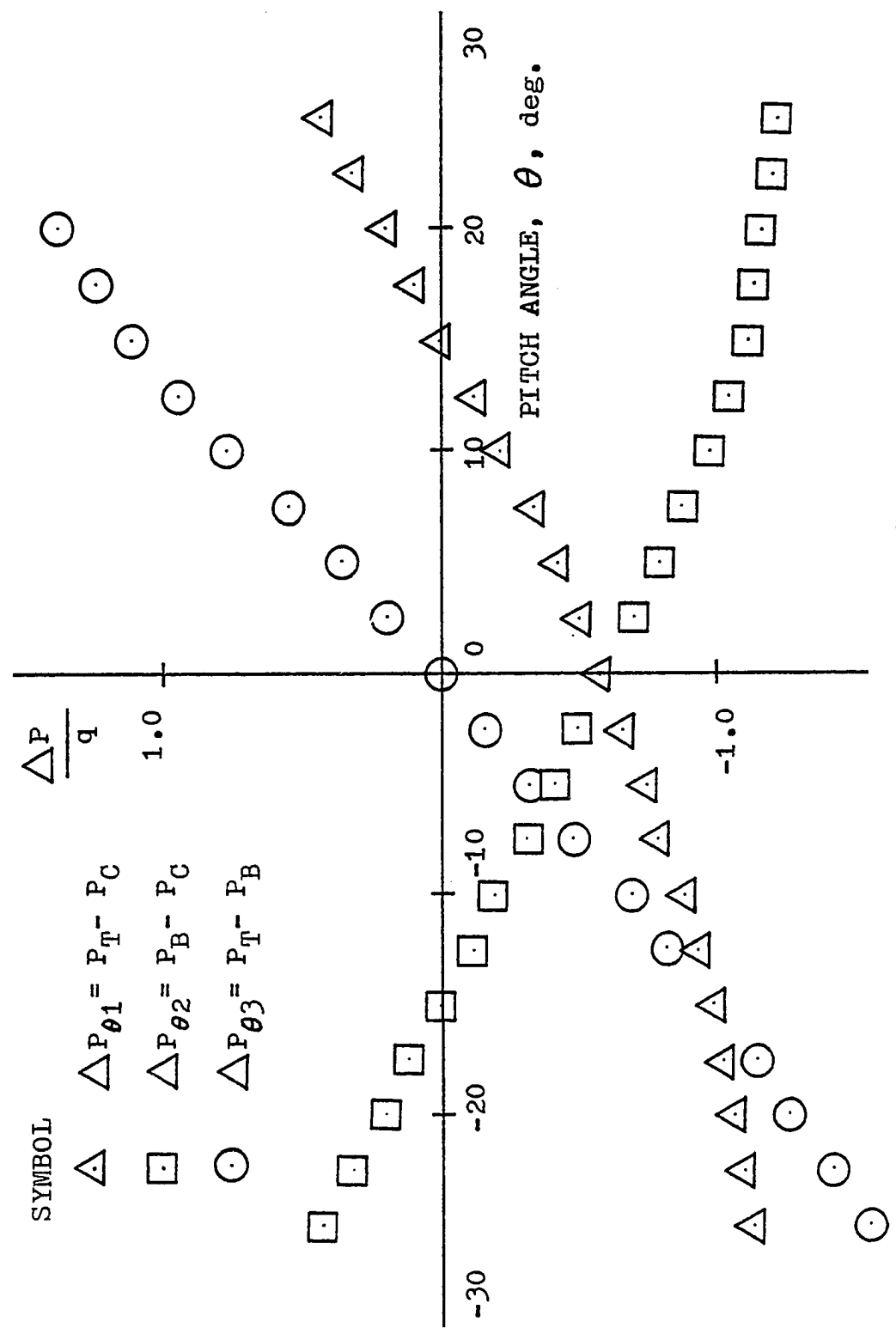
(c) $q = 90.8 \text{ newtons/m}^2$, $\gamma = 45^\circ$

Figure A.2 Concluded



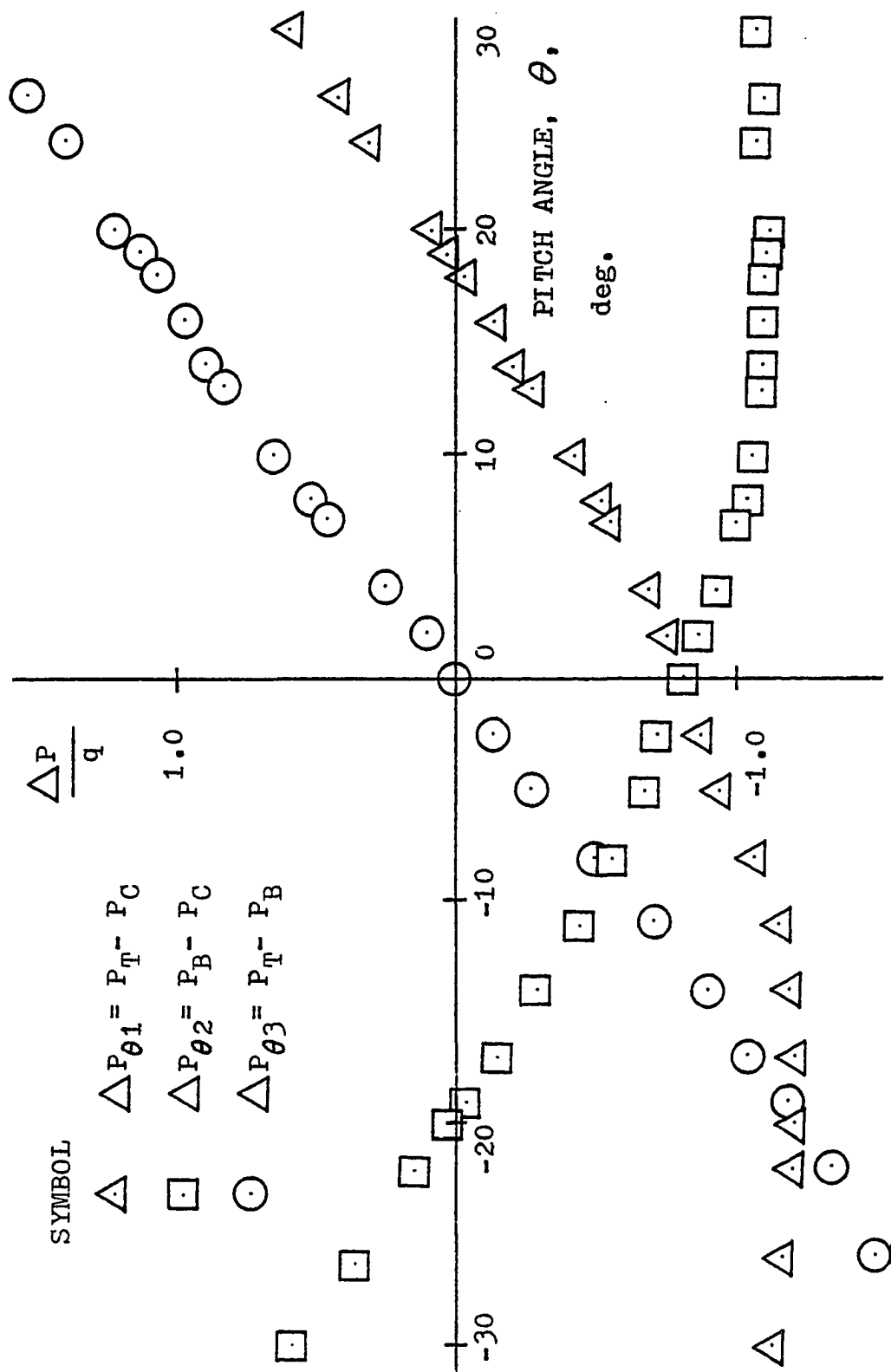
(a) $q = 59.4$ newtons/m², $\gamma = 22.5^\circ$

Figure A.3 Variation of pressure differentials with pitch angle.



(b) $q=101$. newtons/m², $\gamma=33^\circ$

Figure A.3 Continued



(c) $q=114$. newtons/m², $\gamma=45^\circ$

Figure A.3 Concluded

APPENDIX B

COMPUTER PROGRAM FOR THEORY I

COMPUTER PROGRAM FOR THEORY I

C DT INCREMENT OF TIME
 C A1 REFERENCE DISPLACE ANGLE
 C A2 HALF OF THE TOTAL ANGULAR AMPLITUDE UNDER
 OSCILLATION
 C TF TIME AT THE FINAL STEP OF CALCULATION
 C FREQ OSCILLATING FREQUENCY
 C NCASE NUMBER OF TEST CASE
 C UF FREE STREAM VELOCITY
 C B12 PROBE COEFFICIENT FOR PORTS 1 AND 2
 C B23 PROBE COEFFICIENT FOR PORTS 2 AND 3
 C A3 DISTANCE FROM PROBE HEAD TO CENTER OF
 ROTATION
 C VP PROBE VELOCITY
 C A7 INSTANTANEOUS ANGLE OF ATTACK
 C P12 PRESSURE DIFFERENTIAL BETWEEN PORTS 1 AND 2
 C P23 PRESSURE DIFFERENTIAL BETWEEN PORTS 2 AND 3
 C PP PRESSURE DIFFERENTIAL RATIO

DIMENSION FUNC1(200), FUNC2(200), FUNC3(200)

READ(2,24) NCASE

24 FORMAT(I5)

READ(2,26) A3

```
26  FORMAT(F10.5)
    READ(2,28) B12, B23
28  FORMAT(2F10.3)
    Z=1
1   READ(2,22) A1, A2, UF, FREQ, TF, TP, DT
22  FORMAT(2F10.6,5F10.4)
    A4=6.283185*FREQ
    WRITE(3,302) FREQ
302 FORMAT('1',//,10X, 'FREQUENCY=', F10.4,//)
    WRITE(3,304) UF
304 FORMAT(10X, 'UF=', 2X, F10.5,//)
    WRITE(3,306)
306 FORMAT(13X, 4HTIME, 7X, 5HANGLE, 9X, 3HP12, 9X, 3HP23, 10X, 2HPP)
    TF2=TF/2
    T=-1.570796/A4
    J=1
800 CONTINUE
    B=A1-A2*SIN(A4*T)
    VP=-A4*A3*A2*COS(A4*T)
    U=VP*SIN(B)
    V=VP*COS(B)
    IF(T.GT.TF2) GO TO 100
    IF(B.GT.0.) GO TO 200
    UT=UF+U
    A6=ATAN(V/UT)
    A7=57.2958*(B-A6)
    GO TO 600
```

```
200  UT=UF-U
      A6=ATAN(V/UT)
      IF(A6.GT.ABS(B)) GO TO 250
      A7=57.2958*(B-A6)
      GO TO 600
250  A7=57.2958*(A6-B)
      GO TO 600
100  CONTINUE
      IF(B.GT.0.) GO TO 300
      UT=UF-U
      A6=ATAN(V/UT)
      IF(ABS(A6).GT.ABS(B)) GO TO 350
      A7=57.2958*(B-A6)
      GO TO 600
350  A7=57.2958*(B-A6)
      GO TO 600
300  UT=UF+U
      A6=ATAN(V/UT)
      A7=57.2958*(B-A6)
      GO TO 600
600  CONTINUE
      BD=B*57.2958
      P12=B12*0.7071*SIN((45.-2.*A7)/57.2958)
      P23=B23*SIN(2.*A7/57.2958)
      TN=T/TP
      PP=P23/P12
      WRITE(3,308) TN,BD,P12,P23,PP
```

```

308  FORMAT(5X,5F12.3)
      T=T+DT
      FUNC1(J)=P12
      FUNC2(J)=P23
      FUNC3(J)=PP
      J=J+1
      IF(T.LT.TF) GO TO 800
      CALL PLOTA(104,DT,FUNC1,0,2)
      CALL PLOTA(104,DT,FUNC2,0,2)
      CALL PLOTA(104,DT,FUNC3,0,2)
      Z=Z+1
      IF(Z.LE.NCASE) GO TO 1
      STOP
      END

      SUBROUTINE PLOTA(NP,H,FUN,FACT,NSTEP)
      DIMENSION ALINE(120),DAS(120),SCALE(11),FUN(200)
      DATA DASH/'-'/,STAR/'*'/,BAR/'I'/,BLANK/' '/
      IF(FACT.EQ.0.) GO TO 30
      FACTOR=FACT
      GO TO 80
30    AMAX=1.0E-10
      DO 40 I=1,NP,NSTEP
      IF(ABS(FUN(I)).GT.AMAX) AMAX=ABS(FUN(I))
40    CONTINUE
      FACTOR=AMAX/50.
80    DO 95 I=1,11

```

```
95    SCALE(I)=-60.+10.*FLOAT(I)
      DO 100 I=1,120
100    DAS(I)=DASH
      DO 105 I=15,115,10
105    DAS(I)=BAR
      DO 110 I=10,120
110    ALINE(I)=BLANK
      ALINE(65)=BAR
      WRITE(3,200) FACTOR
200    FORMAT(1H1,2X,'TIME IN SECOND',33X,'SCALE FACTOR =',
           E11.4)
      WRITE(3,302) SCALE
302    FORMAT(1H0,11X,5(F4.0,6X),1X,6(F3.0,7X))
      WRITE(3,303) (DAS(I),I=10,120)
303    FORMAT(1H0,8X,114A1)
      DO 120 I=1,NP,NSTEP
      TIME=H*FLOAT(I-1)
      NPP=FUN(I)/FACTOR+65.
      ALINE(NPP)=STAR
      WRITE(3,304) TIME,(ALINE(J),J=10,120)
304    FORMAT(1H0,F8.3,111A1)
      ALINE(NPP)=BLANK
      IF(NPP.EQ.65) ALINE(65)=BAR
120    CONTINUE
      RETURN
      END
```

APPENDIX C

POTENTIAL FLOW SOLUTION PAST A TRANSLATING SPHERE

POTENTIAL FLOW SOLUTION PAST A TRANSLATING SPHERE

The Laplace equation for the velocity potential takes the form, for an axisymmetric case in spherical coordinates

$$\frac{\partial}{\partial r} (r^2 \sin \theta \frac{\partial \phi}{\partial r}) + \frac{\partial}{\partial \theta} (\sin \theta \frac{\partial \phi}{\partial \theta}) = 0 \quad (C.1)$$

Equation (C.1) can be solved by using the method of separation of variables, letting

$$\phi(r, \theta) = R(r) \Theta(\theta) \quad (C.2)$$

where R is a function of r only and Θ is a function of θ only. With (C.2), equation (C.1) may be separated into the form

$$\frac{1}{R} \frac{d}{dr} (r^2 \frac{dR}{dr}) = - \frac{1}{\Theta \sin \theta} \frac{d}{d\theta} (\sin \theta \frac{d\Theta}{d\theta}) = K \quad (C.3)$$

where K is a separation constant. Hence R and Θ solve

$$\frac{d}{dr} (r^2 \frac{dR}{dr}) - K R = 0$$

$$\frac{d}{d\theta} (\sin \theta \frac{d\Theta}{d\theta}) + K \sin \theta = 0 \quad (C.5)$$

The general solution of equation (C.4) is known to be of the form

$$R(r) = a_n r^n + b_n r^{-(n+1)} \quad (C.6)$$

where $K=n(n+1)$, and a_n and b_n are constants. Since the solution for ϕ should be finite as $r \rightarrow \infty$, it is required

to set a_n to zero.

Equation (C.5) can be written in a new form after setting $\cos \theta = \mu$ and $d(\)/d\theta = -(1-\mu^2)^{\frac{1}{2}} d(\)/d\mu$:

$$\frac{d}{d\mu} (1 - \mu^2) \frac{d\theta}{d\mu} + n(n+1)\theta = 0 \quad (C.7)$$

where θ now is a function of μ . This is Legendre's differential equation. The general solution of this equation is the form

$$\theta(\mu) = c_n P_n(\mu) + d_n Q_n(\mu) \quad (C.8)$$

where $P_n(\mu)$ and $Q_n(\mu)$ are Legendre functions (Ref.23) and c_n and d_n are constants. Since $Q_n(\mu)$ becomes infinite on the axis $\theta=0$ and $\theta=\pi$, it is required to set d_n equal to zero. Also, the function $P_n(\mu)$ becomes infinite on the axis if n is not an integer. Therefore n must be an integer and equation (C.8) becomes

$$\theta(\mu) = c_n P_n(\mu) \quad (C.9)$$

The function $P_n(\mu)$ is polynomial in μ of degree n .

The solution for the potential is the combined form of (C.6) and (C.9) and is of the form

$$\phi(r, \mu) = \sum_{n=0}^{\infty} \alpha_n P_n(\mu) / r^{n+1} \quad (C.10)$$

where the α_n 's may be a function of time. Equation (C.10) can be expressed explicitly as

$$\phi(r, \theta) = \alpha_0 \frac{1}{r} + \alpha_1 \frac{\cos \theta}{r^2} + \alpha_2 \frac{3 \cos^2 \theta - 1}{r^3} + \dots \quad (C.11)$$

The boundary condition requires the relation

$$\left. \frac{\partial \phi}{\partial r} \right|_{r=a} = -U \cos \theta$$

$$= -\frac{\alpha_0}{a^2} - 2\alpha_1 \frac{\cos \theta}{a^3} - \frac{3}{2} \alpha_2 \frac{3 \cos^2 \theta - 1}{a^4} - \dots \quad (\text{C.12})$$

must be satisfied. Hence, the coefficients

$$\alpha_0, \alpha_2, \alpha_3, \alpha_4, \dots = 0 \quad (\text{C.13})$$

and

$$\alpha_1 = \frac{U a^3}{2}$$

Then the solution for ϕ is

$$\phi(r, \theta) = A_0 - \frac{U a^3}{2} \frac{\cos \theta}{r^2} \quad (\text{C.14})$$

where A_0 is a constant and U , θ , and r all may vary with time. The unsteady Bernoulli equation may be written as :

$$\frac{\partial \phi}{\partial t} + \frac{1}{2} |\nabla \phi|^2 + \frac{P}{\rho_0} = H(t) \quad (\text{C.15})$$

As $r \rightarrow \infty$, we require

$$\frac{\partial \phi}{\partial t} \approx 0 \quad \text{and} \quad |\nabla \phi| \approx 0 \quad (\text{C.16})$$

hence

$$P_\infty / \rho_0 = H(t)$$

Equation (C.15) can be written as

$$P - P_\infty = -\rho_0 \frac{\partial \phi}{\partial t} - \frac{1}{2} \rho_0 |\nabla \phi|^2$$

Substituting equation (C.14), the above equation becomes

$$P - P_\infty = \frac{1}{2} \rho_0 a^3 \frac{\partial \phi}{\partial t} \left(\frac{U \cos \theta}{r^2} \right) - \frac{1}{2} \rho_0 \frac{U^2 a^6}{r^6} \cdot (\cos^2 \theta + \frac{1}{4} \sin^2 \theta) \quad (\text{C.17})$$

At $r=a$, the pressure difference on the surface of the sphere is

$$P - P_{\infty} = \frac{1}{2} \rho_0 a^3 \left[\frac{dU}{dt} \frac{\cos \theta}{a^2} - \frac{1}{4} U a^2 \sin \theta \left(\frac{d\theta}{dt} \right)_{r=a} - \frac{1}{2} a \cos \theta \left(\frac{dr}{dt} \right)_{r=a} \right] - \frac{1}{2} \rho_0 U^2 (\cos^2 \theta + \frac{1}{4} \sin^2 \theta) \quad (C.18)$$

where

$$\left(\frac{d\theta}{dt} \right)_{r=a} = \frac{U \sin \theta}{a} ,$$

and

$$\left(\frac{dr}{dt} \right)_{r=a} = - U \cos \theta .$$

Equation (C.18) can be further simplified to

$$P - P_{\infty} = \frac{1}{2} \rho_0 a \cos \theta \frac{dU}{dt} + \frac{9}{16} \rho_0 U^2 \cos 2\theta - \frac{1}{16} \rho_0 U^2 \quad (C.19)$$

or in coefficient form

$$\frac{P - P_{\infty}}{(1/2) \rho_0 U^2} = \frac{9}{8} \cos 2\theta + \frac{a \cos \theta}{U^2} \frac{dU}{dt} - \frac{1}{8} \quad (C.20)$$

APPENDIX D

COMPUTER PROGRAM FOR THEORY II

COMPUTER PROGRAM FOR THEORY II

C TF TIME AT THE FINAL STEP OF CALCULATION
 C FREQ OSCILLATING FREQUENCY
 C CEX1 PROBE COEFFICIENT FOR PORTS 1 AND 2
 C CEX2 PROBE COEFFICIENT FOR PORTS 2 AND 3
 C A1 REFERENCE DISPLACEMENT ANGLE
 C A2 HALF OF THE TOTAL ANGULAR AMPLITUDE UNDER
 OSCILLATING MOTION
 C A3 DENSITY OF AIR
 C A4 PROBE POSITION ANGLE
 C A11 DISTANCE FROM PROBE HEAD TO THE CENTER OF
 ROTATION
 C A13 RADIUS OF THE PROBE SPHERICAL HEAD
 C A20 ANGLE OF ATTACK
 C U AIRSTREAM VELOCITY
 C DT INCREMENT OF TIME

DIMENSION FUNC1(200), FUNC2(200), FUNC3(200)
 READ(2,205) NCASE
 205 FORMAT(I5)
 READ(2,207) CEX1,CEX2
 207 FORMAT(2F10.3)
 READ(2,209) A3,A11,A13

```

209  FORMAT(3F10.6)
      Z=1
150  CONTINUE
      READ(2,210) A1,A2,U,DT,FREQ,TF
210  FORMAT(2F10.6,F10.2,3F10.4)
      OMEGA=FREQ*6.283185
      A10=6.283185/OMEGA
      WRITE(3,305) U,OMEGA
305  FORMAT(1H1,10X,2HU=,F10.2,5X,6HOMEGA=,F10.4,/)
      WRITE(3,315)
315  FORMAT(13X,4HTIME,10X,2HA4,9X,3HA20,8X,4HPT23,8X,
      4HPT12,10X,2HPT,/)
      T=-DT
      J=0
20   T=T+DT
      J=J+1
      A4=A1-A2*SIN(OMEGA*T)
      A5=SIN(2.*A4)
      A6=COS(2.*A4)
      A7=0.5*A3*U*U
      A14=COS(OMEGA*T)
      A15=SIN(OMEGA*T)
      A16=COS(A4)
      A17=SIN(A4)
      DCDT=-OMEGA*A2*A14
      U1=A11*DCDT*A17
      DU1DT=OMEGA*A2*A11*(OMEGA*(A14**2)*A2*A16-OMEGA*A15*

```

```

A17)
U1SQ=U1*U1
A12=0.001168*U1SQ
P112=1.125*A12+0.14645*A3*A13*DU1DT
P123=0.0
V=A11*DCDT*A16
VSQ=V*V
DVDT=-OMEGA*A2*A11*(A15*OMEGA*A16+A17*OMEGA*A2*A14*A14)
P212=-0.5625*A3*VSQ-0.3536*A3*A13*DVDT
P223=0.7071*A3*A13*DVDT
A9=ATAN((DCDT*A13*A16+V)/(U+U1+DCDT*A13*A17))
A19=A4+A9
WSQ=(U+U1+DCDT*A13*A17)**2+(V+DCDT*A13*A16)**2
P12=0.5*A3*WSQ*CEX1*((SIN(A4+A9-0.7854))**2-(SIN(A4+
A9))**2)
P23=0.5*A3*WSQ*CEX2*((SIN(A4+A9+0.7854))**2-(SIN(A4+
A9-0.7854))**2)
PT12=(P12+P112+P212)/A7
PT23=(P23+P123+P223)/A7
TN=T/A10
A4=A4*57.2958
A20=A19*57.2958
PP=PT23/PT12
WRITE(3,300) TN,A4,A20,PT23,PT12,PP
300  FORMAT(5X,6F12.5)
FUNC1(J)=PT12
FUNC2(J)=PT23

```

```
FUNC3(J)=PP  
IF(T.LE.TF) GO TO 20  
Z=Z+1  
CALL PLOTA(100,DT,FUNC1,0,2)  
CALL PLOTA(100,DT,FUNC2,0,2)  
CALL PLOTA(100,DT,FUNC3,0,2)  
IF(Z.LE.NCASE) GO TO 150  
STOP  
END
```


APPENDIX E

ANALYTIC CALCULATION OF THE OSCILLATING PROBE MOTION

ANALYTIC CALCULATION OF THE OSCILLATING PROBE MOTION

The mechanism used to oscillate the probe has been described in section 1 of article 3.4, and has been shown in figure (3.12a). Assuming that there was no frictional loss due to the mechanical arrangement, the oscillatory motions of bar 1 and bar 2 would be identical. Hence, from the geometry of the mechanism, the instantaneous speed of the probe may be established.

Let X_0 and Y_0 be the distance of the crank axis measured from the pivotal center of the bar, where the origin of the coordinate system is located. For a point $Z_1(X_1, Y_1)$ at radius r of the crank circle

$$\begin{aligned} X_1 &= -X_0 - r \cos(\omega t) \\ Y_1 &= Y_0 + r \sin(\omega t) \end{aligned} \quad (E.1)$$

For $Z_2(X_2, Y_2)$ on the circular arc of radius R_0

$$\begin{aligned} X_2 &= R_0 \cos \beta \\ Y_2 &= R_0 \sin \beta \end{aligned} \quad (E.2)$$

Since the length L of the link is constant

$$L^2 = (X_2 - X_1)^2 + (Y_2 - Y_1)^2 \quad (E.3)$$

Substitution of equations (E.1) and (E.2) into (E.3) yields

$$C_1 \cos \beta - C_2 \sin \beta = C_3 \quad (E.4)$$

where

$$C_1 = 2R_0(X_0 + r \cos \omega t)$$

$$C_2 = 2R_0(Y_0 + r \sin \omega t)$$

$$C_3 = L^2 - R_0^2 - (X_0 + r \cos \omega t)^2 - (Y_0 + r \sin \omega t)^2$$

Upon differentiation of equation (E.4) with respect to time, t , and after some manipulation, one obtains the angular velocity of point Z_2 :

$$\frac{d\beta}{dt} = \frac{\frac{r\omega}{R_0} (C_2 \cos \omega t - C_1 \sin \omega t) - 2R_0 r \omega \sin(\omega t + \beta)}{C_1 \sin \beta + C_2 \cos \beta} \quad (E.5)$$

Hence the instantaneous velocity of the probe is

$$V_p(t) = L_p \frac{d\beta}{dt} \quad (E.6)$$

where L_p is the probe length, i.e., the distance between the probe head and the center of rotation.

For one set of experimental data:

$$X_0 = 0.177 \text{ m}$$

$$Y_0 = 0.0325 \text{ m}$$

$$R_0 = 0.0533 \text{ m}$$

$$r = 0.0056 \text{ m}$$

$$L = 0.278 \text{ m,}$$

equation (E.5) was employed to calculate the probe velocity and a computer program using the fourth order Runge-Kutta method was used to integrate forward in time. The computational method described was checked by a simple graphical method using the principle of instantaneous center of

rotation. The results of both methods were compared with the true sine curve as shown in figure (E.1).

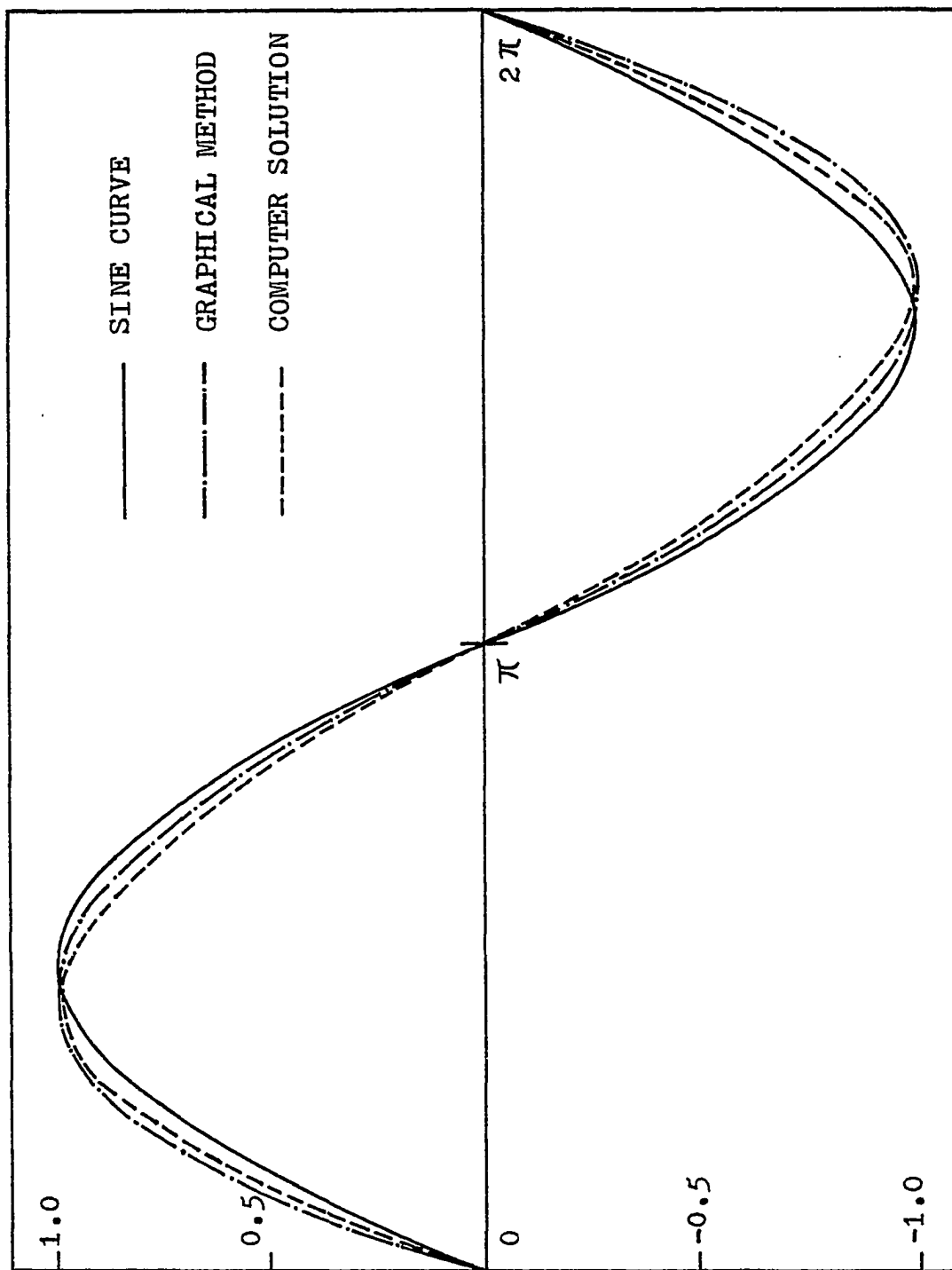


Figure E.1 Comparison of probe motion curves with the true sine curve

APPENDIX F

EFFECTS OF A CYLINDER BEHIND A SPHERE

EFFECTS OF A CYLINDER BEHIND A SPHERE

The effects of the cylinder tailfitted to the spherical probe are now described. The pressure distribution around a perfect sphere is well documented and can be found in Ref. 2. Very little information about the pressure distribution around a sphere with cylinder tailfitted was available at the time this investigation started.

A 0.0635 m diameter sphere, shown in figure (F.1), was placed in an open jet wind tunnel test section with an airspeed of 33.5 m/s. The sphere was rotated to make the porthole number 1 have an angle θ inclined to the horizontal airstream. The range of θ under consideration was from -80° to 80° . After the static pressures were measured within the θ range of interest, a 0.0445 m diameter, 0.153 m long cylinder was tailfitted into the rear portion of the sphere. Then the static pressures were measured again within the same θ range of interest. A comparison of experimental results between the sphere and sphere with cylinder tailfitted is illustrated in figure (F.2). It is seen that there is no difference on pressure distribution between the sphere with and without cylinder tailfitted for $-35^\circ \leq \theta \leq 35^\circ$, but when $|\theta| > 35^\circ$, a difference starts, and becomes very significant as $|\theta|$ increases. For the same sphere

with cylinder tailfitted mentioned above, the static pressure distributions for porthole number 2 and 3 within the range of interest are shown in figures (F.3) and (F.4) respectively. The static pressure was found very unstable in regions specified in figures (F.3) and (F.4).

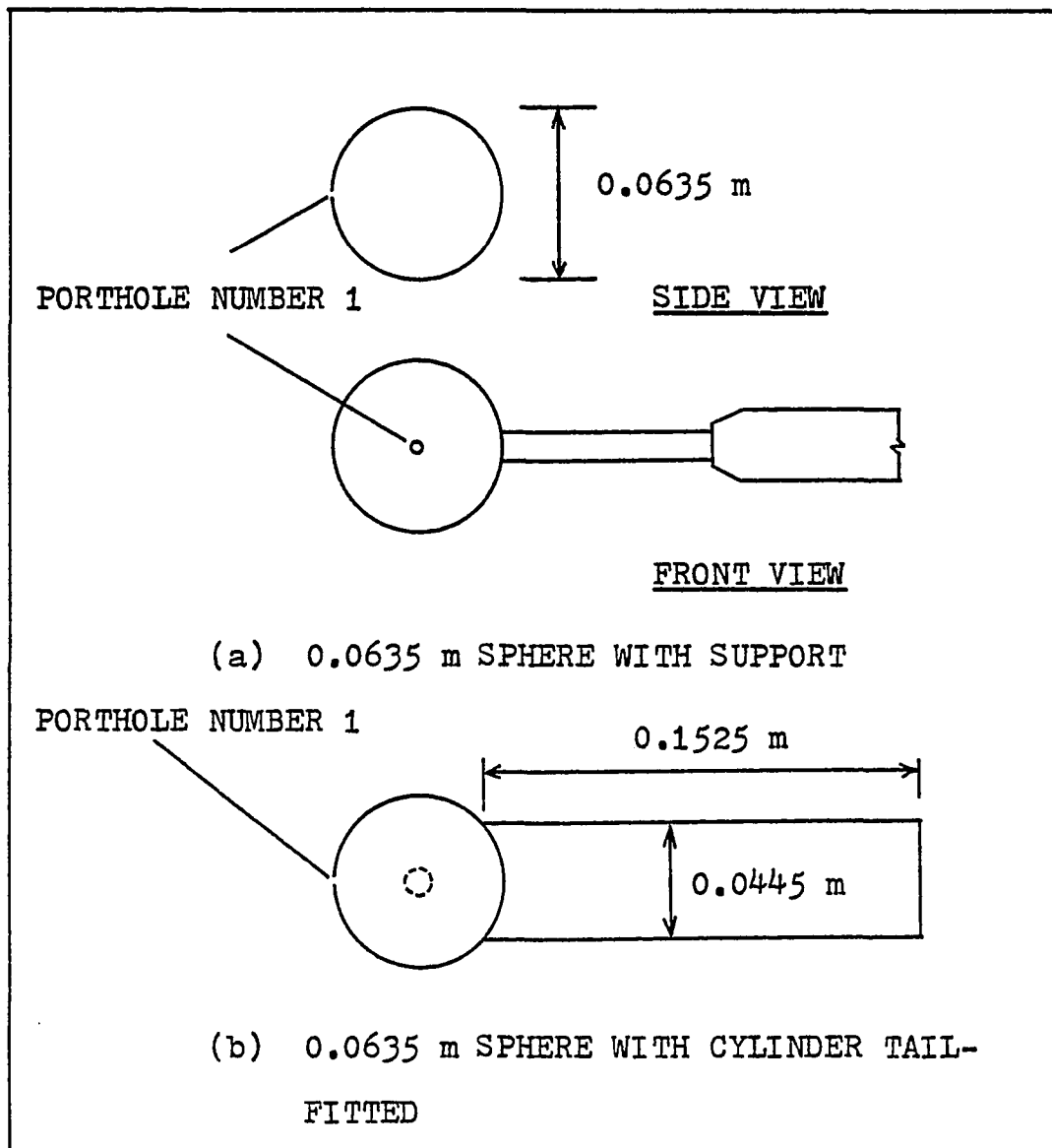


Figure F.1 Definition sketch of a 0.0635 m sphere with support and with cylinder tailfitted.

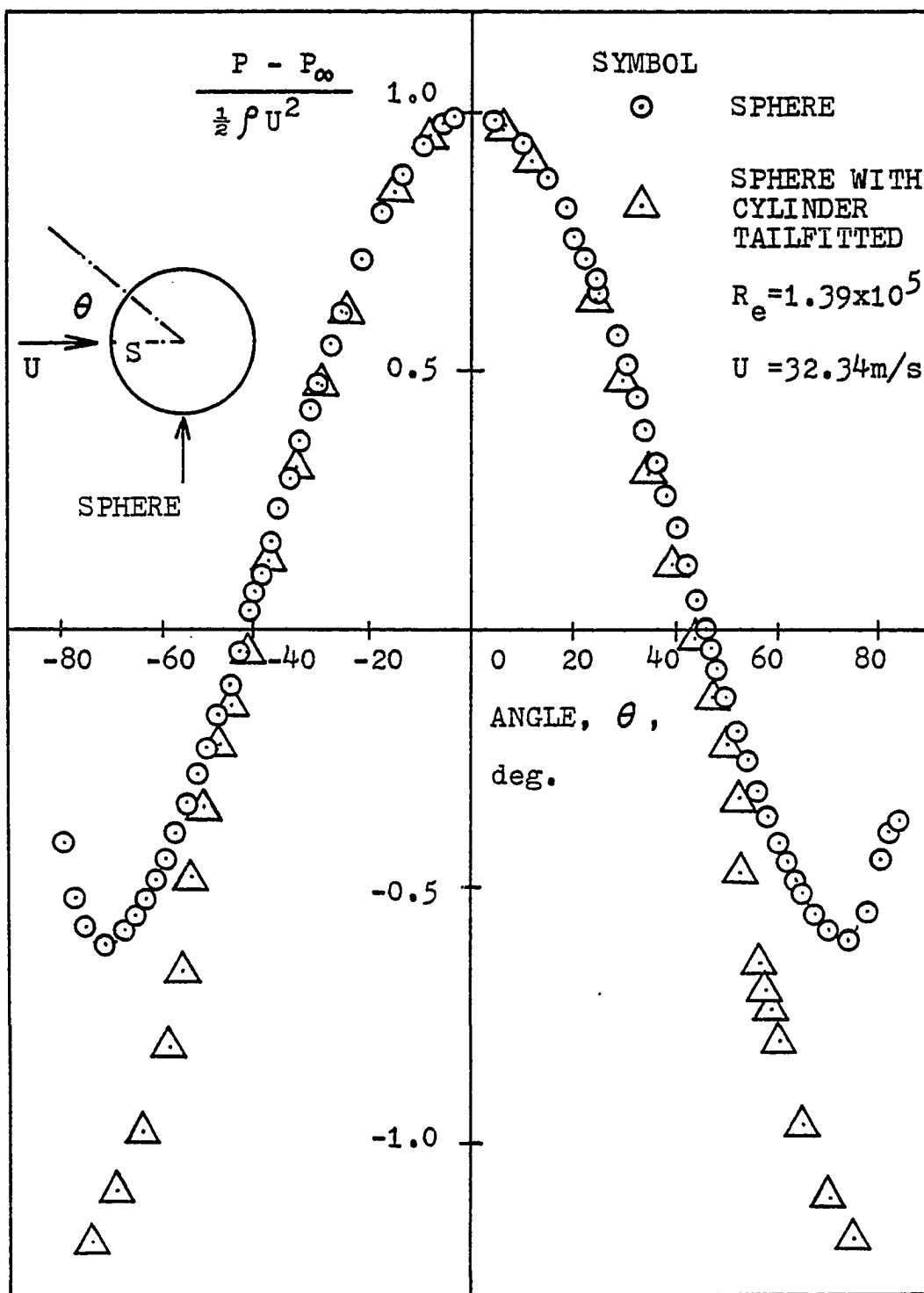


Figure F.2 Pressure distribution around a sphere with and without cylinder tailfitted.

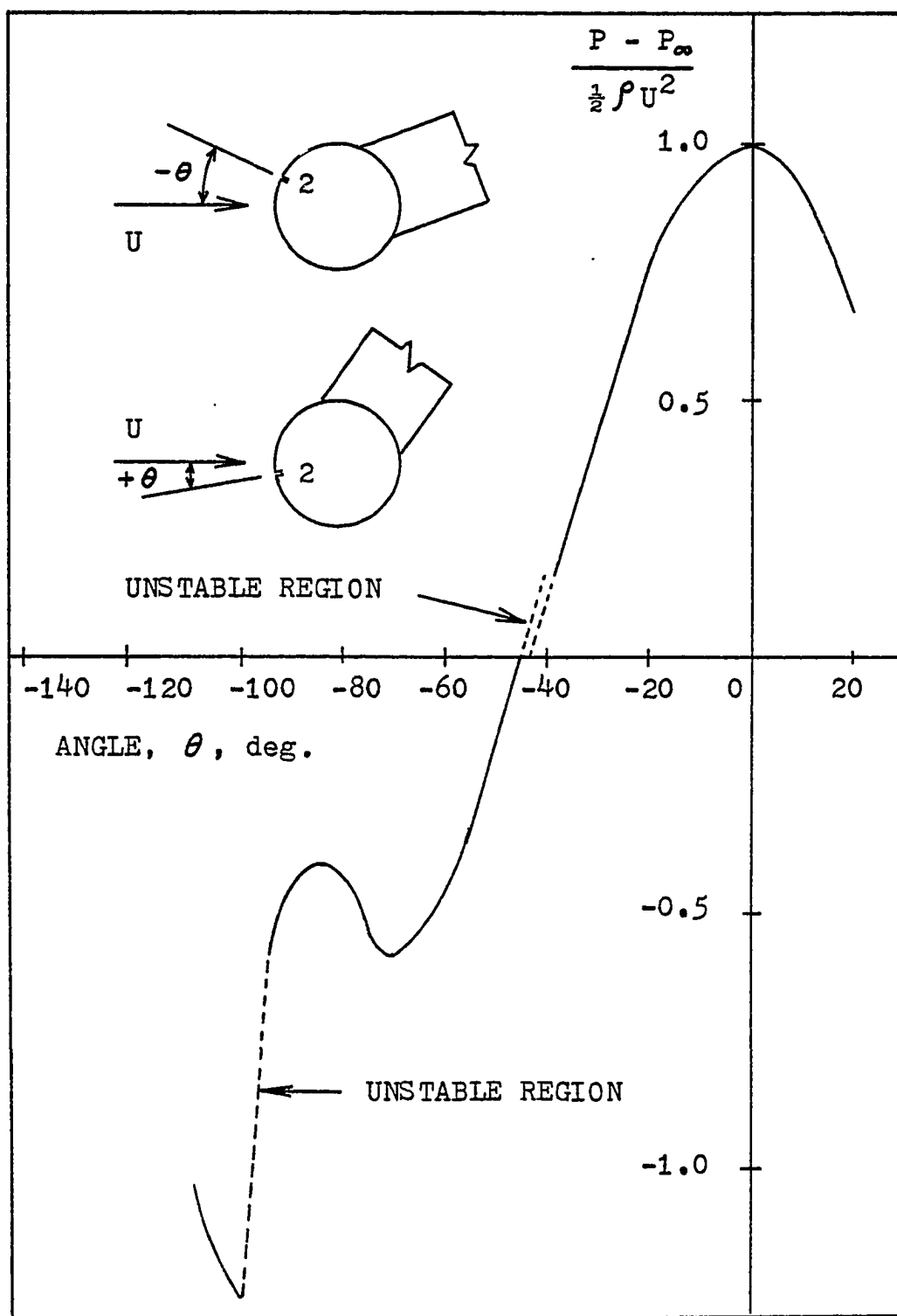


Figure F.3 Static pressure distribution of porthole number 2, $R_e = 1.39 \times 10^5$.

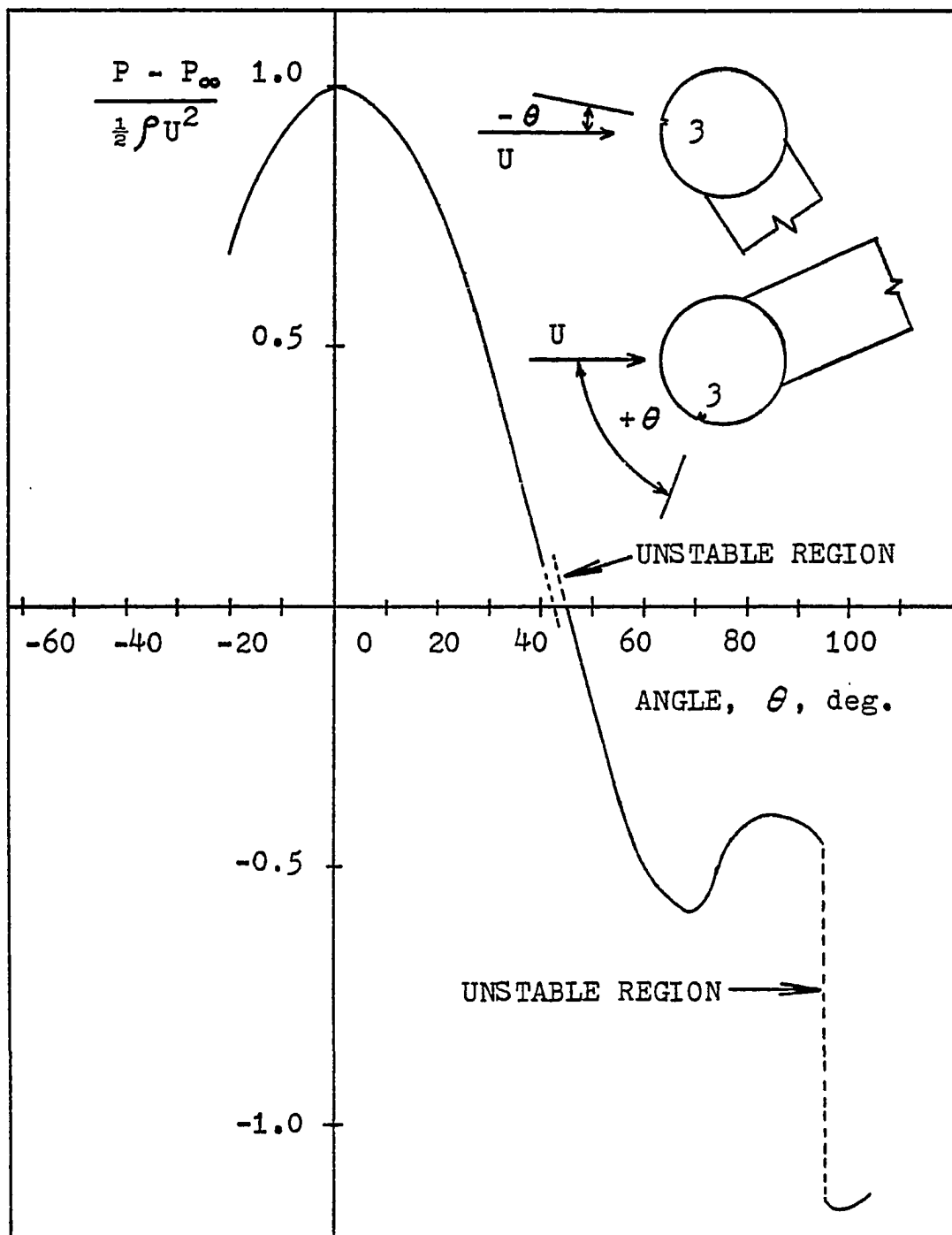


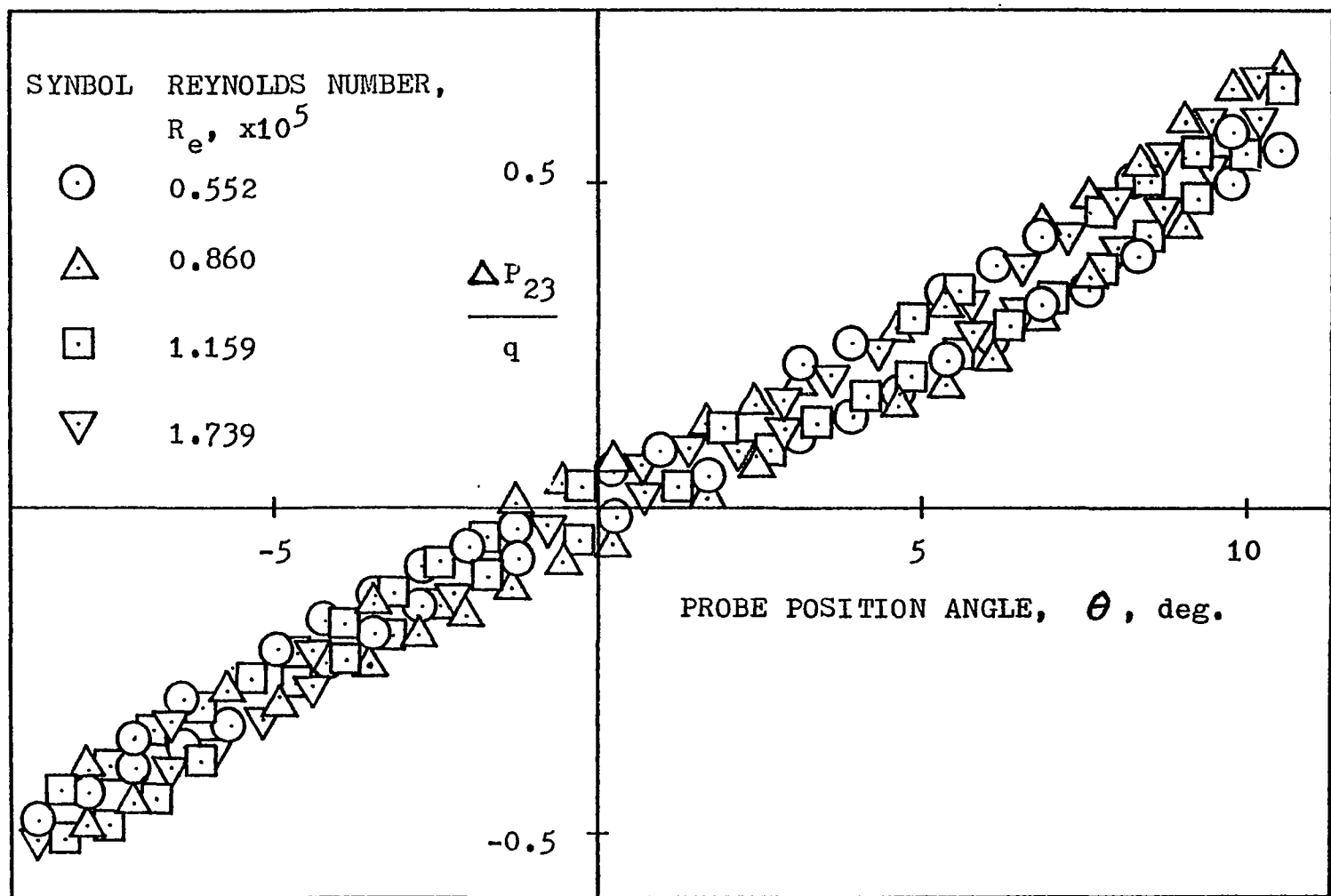
Figure F.4 Static pressure distribution of porthole number 3, $R_e = 1.39 \times 10^5$.

APPENDIX G

OSCILLATING PROBE TEST RESULTS

Table G.1 Oscillating Probe Test Results

Test Number	R_e range, $\times 10^5$	θ range, degree	f range, Hz.
1	0.552 to 1.739	-8.62° to 10.55°	1.59
2	0.552 to 1.159	-8.62° to 10.55°	2.92
3	0.552 to 1.739	-8.62° to 10.55°	3.46
4	1.159 to 1.739	-8.62° to 10.55°	2.92
5	0.635	-18.2° to 0.0°	1.88 to 4.81



(a) TEST NO. 1, $f=1.59$ Hz.

Figure G.1 Experimental data on $\Delta P/q$ variation, probe ODU2.

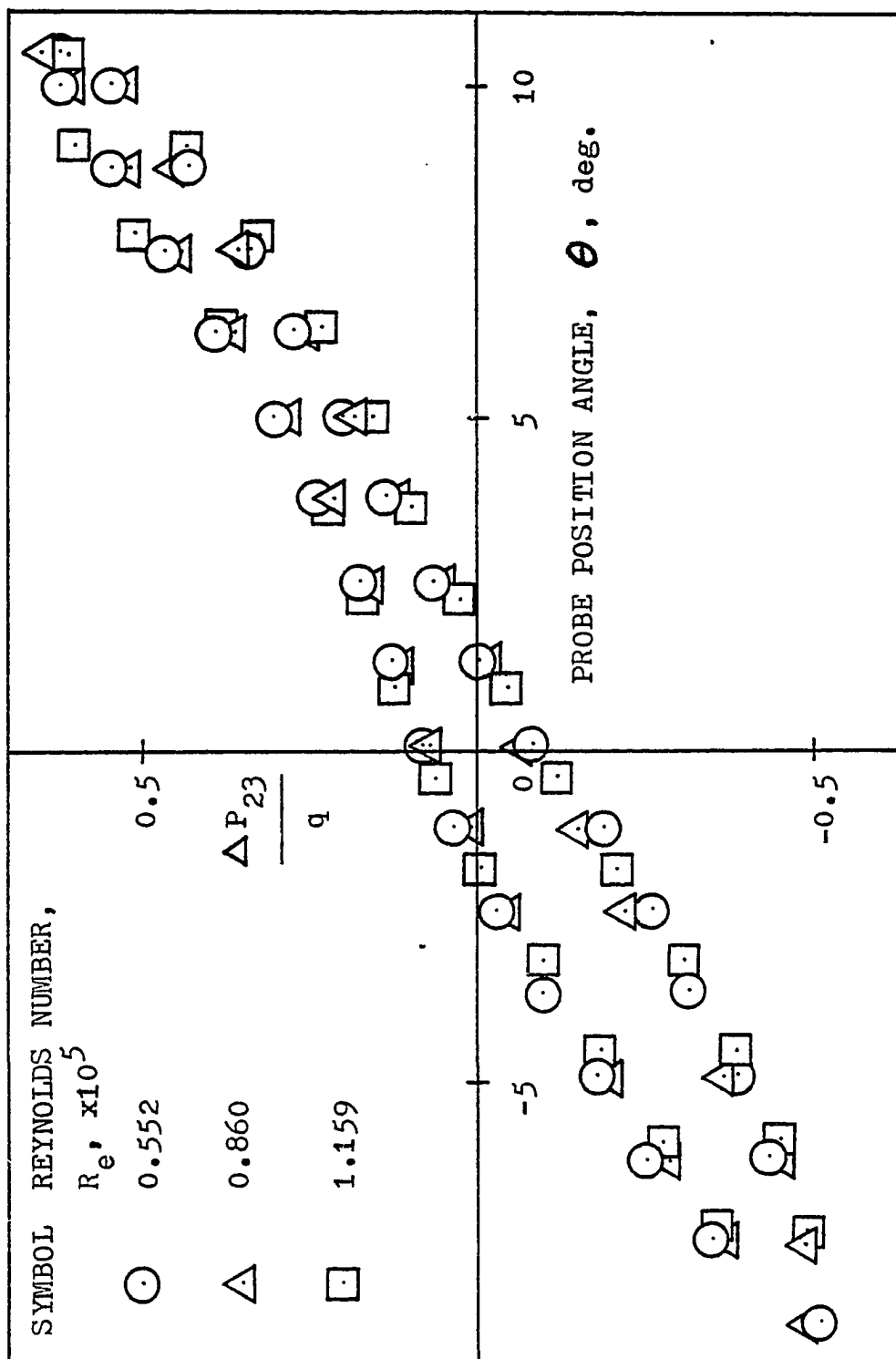
(b) TEST NO. 2, $f=2.92$ Hz.

Figure G.1 Continued

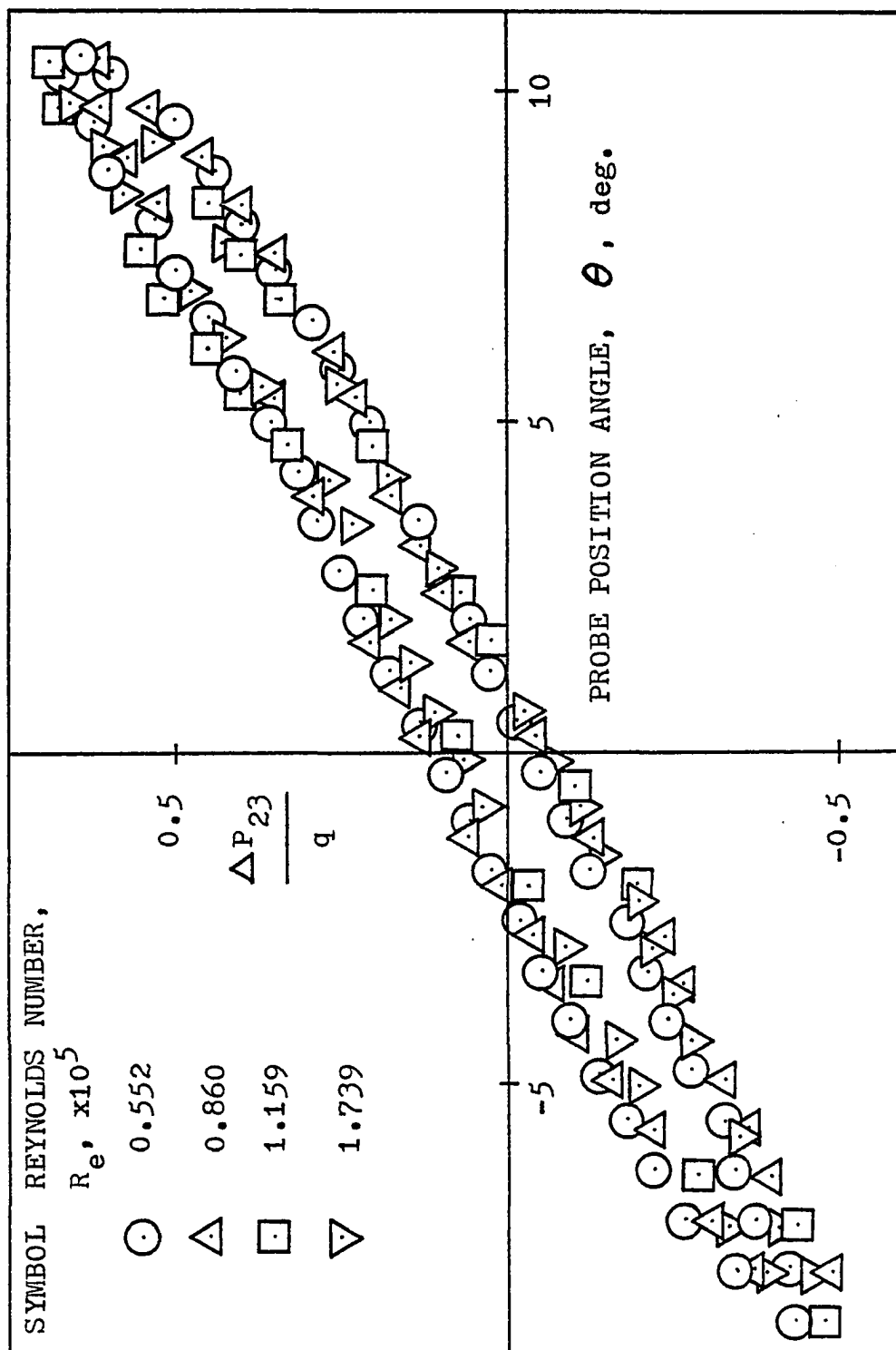
(c) TEST NO. 3, $f=3.46$ Hz.

Figure G.1 Continued

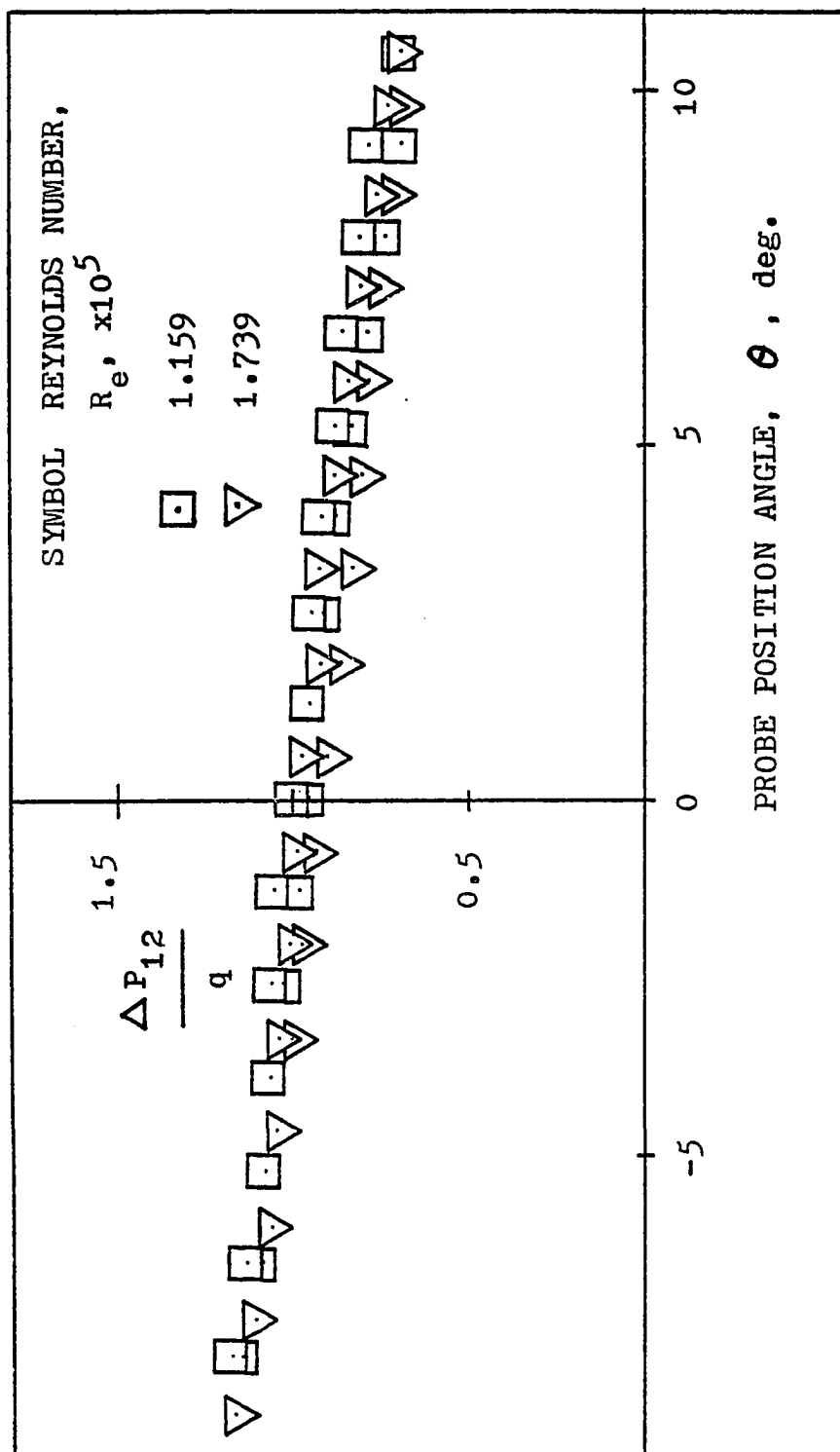
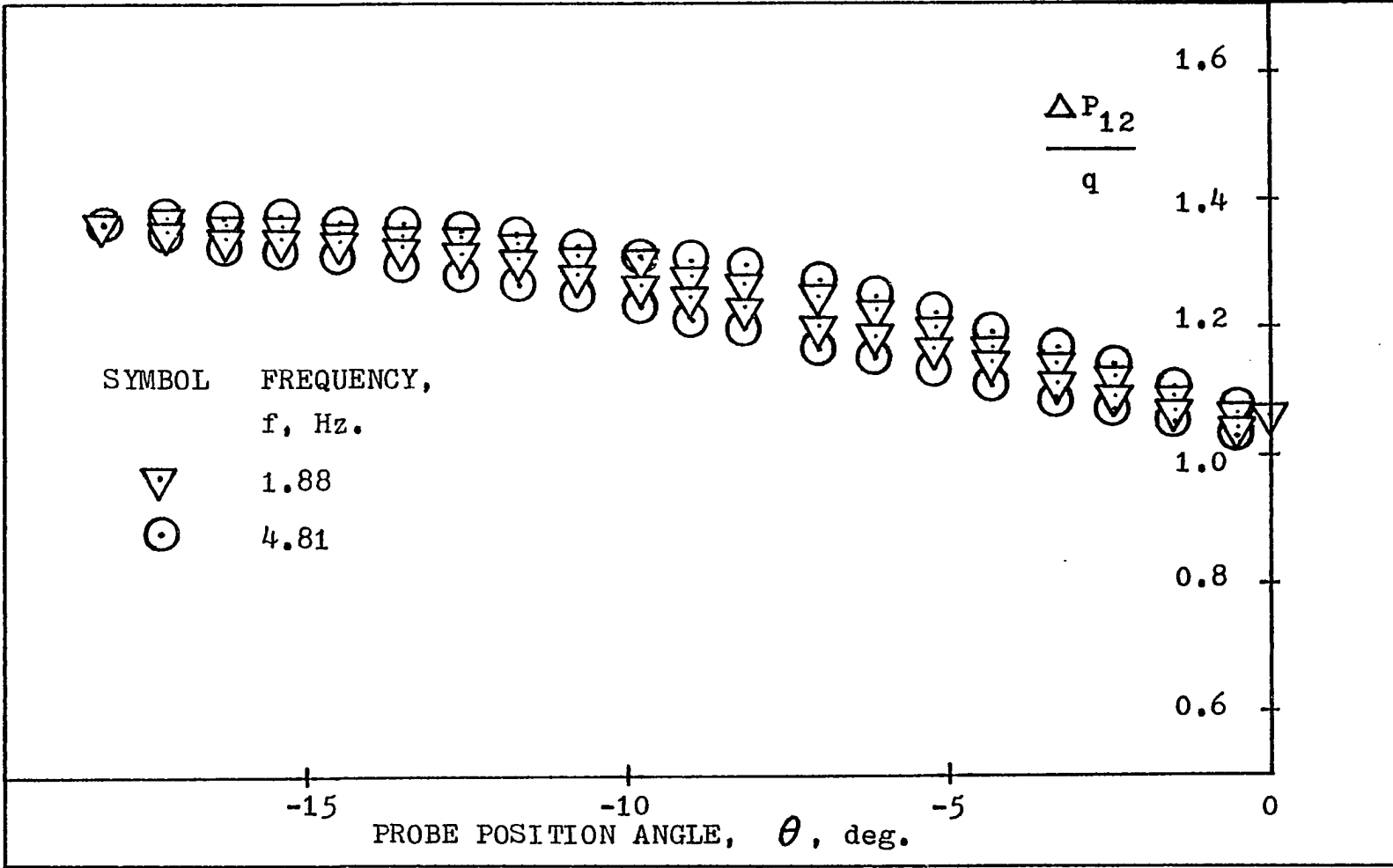
(d) TEST NO. 4, $f = 2.92$ Hz.

Figure G.1 Continued



(e) TEST NO. 5, $R_e = 0.635 \times 10^5$.

Figure G.1 Concluded

REFERENCES

- 1) Lavender, A. R. C., Report and Memoranda No. 844, 1923.
- 2) Bryer, D. W., Walshe, D. E. and Garner, H. C., "Pressure probes selected for Three-Dimensional Flow Measurement," Reports and Memoranda No. 3037, 1955.
- 3) Goldstein, S., Modern Developments in Fluid Dynamics, Vol. 1, Dover Ed., 1965, pp. 263-264.
- 4) Martinot-Lagarde, A., Fauquet, A. and Frenkiel, F. N., "The IMFL Anemoclinometer- An Instrument for the Investigation of a Fluctuating Velocity Vector," The Review of Scientific Instruments, Vol. 23, 1952, pp. 661-666.
- 5) Reichle, H. G. Jr., "Hemisphere-Cylinder Pressure Distribution At Subsonic, Transonic, and Supersonic Mach Numbers," MTP-AERO-62-30, NASA George C. Marshall Space Flight Center Report, 1962.
- 6) Martynor, A. K., Practical Aerodynamics, The Macmillan Company, 1965, p. 166.
- 7) Pope, A. and Harper, J. J., Low-Speed Wind Tunnel Testing, John Wiley & Sons, Inc., 1966, pp. 96-98.
- 8) Nowack, C. F. R., "Improved Calibration Method For A Five-Hole Spherical Pitot Probe," Journal of Physics E: Scientific Instruments, Vol. 3, 1970, pp. 21-26.

- 9) Thurtell, G. W., Tanner, C. B. and Wesely, M. L., "Three-Dimensional Pressure-Sphere Anemometer System," Journal of Applied Meteorology, Vol. 9, 1970, pp. 379-385.
- 10) Wesely, M. L., Tanner, C. B. and Thurtell, G. W., "An Improved Pressure-Sphere Anemometer," Boundary-Layer Meteorology, Vol. 2, 1972, pp. 275-283.
- 11) Montoya, E. J., "Wind-Tunnel Calibration and Requirements for In-Flight Use of Fixed Hemispherical Head Angle-of-Attack and Angle-of-Sideslip Sensors," NASA TN D-6986, 1973.
- 12) Yap, D., Black, T. A. and Oke, T. R., "Calibration and Tests of a Yaw Sphere-Thermometer System for Sensible Heat Flux Measurement," Journal of Applied Meteorology, Vol. 13, 1974, pp. 40-45.
- 13) Barna, S. P. and Liu, W. H., "Sensors for Measuring Instantaneous Angle of Attack of Helicopter Blades," Progress reports, NASA Grant NSG-1143, Old Dominion University Research Foundation, June 1975, July 1976, and August 1977.
- 14) Bennett, J. C., "Use of Five-Hole Pneumatic Probe in Unsteady Flows," Progress in Astronautics and Aeronautics, Vol. 53, 1977, pp. 71-82.
- 15) Yuan, S. W., Foundation of Fluid Mechanics, Prentice-Hall, Inc., 1967, pp. 233-236.
- 16) Lamb, H., Hydrodynamics, 6th Ed., The Macmillan Company, New York; reprinted by Dover Publications, Inc., New York, 1945, pp. 110-125.

- 17) Batchelor, G. K., An Introduction to Fluid Mechanics, Cambridge University Press, New York, 1967, pp. 449-453.
- 18) Karamcheti, K., Principles of Ideal-Fluid Aerodynamics, John Wiley & Sons, Inc., 1966, pp. 278-290.
- 19) Patterson, J. L., "A Miniature Electrical Pressure Gage Utilizing A Stretched Flat Diaphragm," NACA TN-2659, 1951.
- 20) Schlichting, H., Boundary Layer Theory, 6th Ed., McGraw-Hill Book Company, 1966.
- 21) Chang, P. K., Separation of Flow, Pergamon Press, 1970, pp. 203-204.
- 22) Brune, G. W., "Reduction of the Low-Frequency Unsteady Lifting-Surface Problem," J. Aircraft, Vol. 7, 1970, pp. 479-480.
- 23) Sokolnikoff, I. S. and Redheffer, R. M., Mathematics of Physics and Modern Engineering, 2nd Ed., McGraw-Hill Book Company, 1966.

BIOGRAPHY

PERSONAL

Name : Liu, Weiyuan Henry
Place of Birth : China
Date of Birth : January 14, 1948

PRESENT

Assistant Professor, Department of Mechanical Engineering,
Tatung Institute of Technology, Taipei, Taiwan, ROC.

EDUCATION

M.S. (Engineering), June 1973, Southern Illinois University
B.E. (Civil Engineering), June 1970, Chung Yuan College of
Science and Engineering, Taiwan, ROC.

HONORS

Member of the Honor Society of Phi Kappa Phi.
Research Assistant, Old Dominion University, from January
1975 to June 1978.
Teaching and Research Assistant, Southern Illinois Univer-
sity, from September 1971 to June 1973.

PUBLICATION

M.S. Thesis, "Investigation of A Confined Mixing Layer",
Southern Illinois University, June 1973.